Optimisation de la synthèse de nanotubes de carbone par dépôt chimique en phase vapeur assisté par micro-ondes : expérience et modélisation

Ahmed Andalouci

Université Sorbonne Paris Nord, Institut Galilée

THESIS

for the degree of

DOCTOR OF PHILOSOPHY

in Material science

Submitted by

Ahmed ANDALOUCI

24 January 2023

Title

Optimization of carbon nanotubes synthesis by microwave plasma-enhanced chemical vapor deposition: experiments and modeling

Thesis supervisors:

Samir FARHAT and Salim Mourad CHERIF

Jury Members:

Catherine Journet	Referee	Université Claude Bernard Lyon 1- LMI
Nicolas Vukadinovic	Referee	Dassault Aviation, Saint-Cloud, France
Pierre Legagneux	Member	Thales Research & Technology
Thomas Goislard	Member	Nawatechnologies
Khaled Hassouni	Member	Université Sorbonne Paris Nord- LSPM
Yves Roussigné	Invited	Université Sorbonne Paris Nord- LSPM
Samir Farhat	Thesis Advisor	Université Sorbonne Paris Nord- LSPM
Salim Mourad Chérif	Thesis co-Adviser	Université Sorbonne Paris Nord- LSPM

“People say to me: Are you looking for the ultimate laws of physics? No, I'm not. I'm just looking to find out more about the world, and if it turns out there is a simple ultimate law that explains everything, so be it, that would be very nice to discover. If it turns out it's like an onion with millions of layers, and we're just sick and tired of looking at the layers, then that's the way it is. But whatever way it comes out, nature is there and she's going to come out the way she is. And therefore when we go to investigate it we shouldn't pre-decide what it is we're trying to do, except to find out more about it. “

Richard Feynman

Table of contents

GLOSSARY OF ACRONYMS

(0D)	Zero-dimensional
(1D)	One-dimensional
(2D)	Two-dimensional
(BLS)	Brillouin Light Scattering
(CFD)	Computational fluid dynamics
(CNTs)	Carbon nanotubes
(CVD)	Chemical Vapor Deposition
(EELS)	Electron Energy Loss Spectroscopy
(fcc)	Face-centered cubic
(hcp)	Hexagonal close packed
(HRTEM)	High-resolution transmission electron microscopy
(LPCVD)	Low pressure CVD
(MWNT)	Multiwalled carbon nanotubes
(RF)	Radio frequency
(PAHs)	Polycyclic Aromatic Hydrocarbons
(PID)	Proportional–integral–derivative
(PECVD)	Plasma Enhanced Chemical Vapor Deposition
(SCCM)	Standard cubic centimeter per minute
(SWNT)	Single-walled carbon nanotubes
(SEM)	Scanning Electron Microscopy
(TEM)	Transmission Electron Microscopy
(T-CVD)	Thermal chemical vapor deposition
(UV)	Ultraviolet
(VSM)	Vibrating Sample Magnetometry
(VACNTs)	Vertically Aligned Carbon NanoTubes

General Introduction

Carbon nanotubes are the building blocks of nanoscience and nanotechnology. In addition to their historical importance in the genesis of carbon, they have shaped modern science in fields as varied as fundamental and applied physics, chemistry, materials science or biology. They form a model system for the study of electronic transport in one dimension and also constitute new challenges for the study of interfacial phenomena and the relationships between processes and use properties. Carbon nanotubes are nanoscale carbonaceous materials with (1D) symmetry. They paved the way for the study of other 1D nanostructures (BN and BCN nanotubes, nanowires) with significant implications in basic and applied research. This research focuses interest both on the knowledge of the fundamental properties of these nano-objects, both at the individual level, and their manipulation for the development of devices such as emission under field for forests of nanotubes.

One of the most coveted lines of research consists in developing processes for their synthesis. Chemical vapor deposition methods now allow the production of vertically aligned nanotubes (VACNTs). However, the controlled synthesis of these materials is essential to consider the targeted applications.

It is in this context that this thesis work takes place, the objective of which is to provide a better understanding of this process by adopting a methodology based on experimentation and modelling.

This manuscript is divided into four chapters. **Chapter I** is a state of the art to present carbon nanotubes, their structures, properties and synthesis processes. We will also introduce several concepts for modeling. **Chapter II** reports the work done in solid de-wetting of metals over substrates, nanotubes synthesis and filling as well characterization. In particular, the plasma enhanced PECVD reactor and the synthesis protocols will be described in detail including the techniques devoted to diffusion barrier and catalytic films deposition. In this chapter, we will investigate a range of parameters affecting the catalyst dewetting and the nanotube growth. We also present the optimal conditions elaborated to achieve dense vertically aligned carbon nanotubes. The gas composition is also studied by changing the O_2 and H_2 flow rates during nanotube growth, as well as the plasma power in plasma enhanced chemical vapor deposition

(PECVD) process. The variation of these parameters ends this section with an optimal protocol developed and customized to achieve high nanotube growth rate and dense vertically aligned carbon nanotubes (VACNTs). Finally, in-situ filling of VACNTs with a ferromagnetic material issued from various thicknesses of Co/Pd is presented. Temperature and plasma power are monitored to enhance the filling state of VACNTs and their vertical alignment. **Chapter III** is devoted to modeling the PECVD process for the nanotube growth. In particular, we will investigate by modeling supported by experiments the role of oxygen in carbon nanotubes (CNT) growth by plasma enhanced chemical vapor deposition (PECVD) process. **Chapter IV** presents some physical properties of the dewetted nanoparticles and synthesized VACNTs. In particular vibrating sample magnetometry (VSM) and Brillouin light scattering (BLS) techniques will be proposed to study both static and dynamic magnetic behaviors as well as mechanical properties of VACNTs. The **General Conclusion** allows us to come back to the main results of this thesis by giving some perspectives.

Chapter I:
Literature review

Since their discovery, carbon nanotubes (CNTs) have been the center of intense academic research activity and constitute today a major challenge in industry. This interest is justified by their nanometric size allowing miniaturization and by a combination of unique properties, modular and infinitely combinable. Extreme mechanical properties, electronic properties, emission properties under fields coupled with high thermal and chemical stability. The applications envisaged are then very numerous and range from materials composites, sensors, devices for active and passive electronics such as thermal interface materials for high performance microelectronics, devices for generating, converting and storing energy through the membranes for filtration, quantum technology etc... Chemical vapor deposition (CVD) methods now allow the production of vertically aligned nanotubes (VACNTs). Nevertheless, the controlled synthesis of these nanotubes is essential to envisage applications taking advantage of their unique properties. Indeed, the control of their diameter, the rate of defects, nanotube density and verticality impact the intended applications. Currently, these objectives has not yet been fully achieved because the mechanisms allowing the growth of defect-free nanotubes remain not yet fully understood. In particular, it is essential to master the processes of structuring and rebuilding the catalyst on the substrate and to control its mobility (diffusion) during the growth of the nanotubes. Hence, the "stabilization" of the catalyst prior to nanotubes growth appears as an important technological bottle-neck to the numerous applications. Barrier layers efficiently limit the diffusion of the catalyst into the mass of the support, and their low surface energy promotes the dewetting of the catalyst. The state of the art proposed in this chapter will be more focused on the general theory describing the kinetics of solid dewetting, nanotube growth and filling by chemical vapor deposition CVD and thermo-chemical modeling of the process in the objective to meet the specific demands of actual industrial applications.

1.1 Recent industrial developments

Advances in the synthesis and scalable manufacturing of carbon nanotubes remain critical to realizing many important commercial applications. Indeed, since their discovery 30 years ago, carbon nanotubes (CNTs) have attracted a lot of industrial interest because of their particular unidirectional geometrical characteristics, which give them interesting mechanical, electronic and thermal properties. They are light, flexible, mechanically strong, chemically inert, biocompatible and stable over a wide temperature range. Along their axis, CNTs have an axial Young's modulus of about 1 TPa and a maximum tensile stress of about 60 GPa. These exceptional values result from the high value of the C-C bonding energy among the highest

existing (>348 KJ/mol). The very high thermal conductivity of nanotubes of about 4000 W/(m.K) allows to functionalize composite materials to make them multifunctional. All these properties allow nanotubes to claim a wide range of applications and several manufacturers such as Arkema or Bayer have made at the beginning of this decade significant investments for the mass production of nanotubes that meet everyday applications. In 2011, Arkema opened a pilot plant in Mont (Hautes-Pyrénées-France) to produce 400 tons of carbon nanotubes per year. Similarly, China's CNano and Belgium's Nanocyl are able to produce several hundred tons per year of nanotubes by chemical vapor deposition (CVD) at lower costs. In 2010, Germany's Bayer opened a unit for the industrial synthesis of 200 tons of nanotubes per year, for an investment of 20 million euros. Japan's Showa Denko K. K. (SKD) opened a facility to produce 400 tons per year of VGCFTM-X, a class of carbon nanotubes used as reinforcement in composite resins. However, the initial enthusiasm has been confronted with numerous difficulties related mainly to the control of production costs and the non-conservation of properties observed at the nanoscopic scale at the macroscopic scale coupled with health uncertainties. For example, the German company Bayer shut down its nanotube synthesis subsidiary in 2013. Similarly, Japan's Showa Denko K. K. (SKD) has restructured its plant. That said, even if the promise of industrial applications for carbon nanotubes has slowed, more targeted applications in the space or energy storage fields remain niches to explore. In this direction, Nawatechnologies, a French start up, has completed in the first quarter of 2022 €18.3m fundraising in order to build a factory for the mass production of vertically aligned carbon nanotubes based ultracapacitors. Their technology is based on the deposition of vertically aligned carbon nanotubes on aluminum foils used as electrodes with unrivaled power density. In parallel, C12 Quantum Electronics, another French startup has raised in 2021, €10m for the funding of its quantum technology. A pure carbon nanotube that only contains the 12C isotope is suspended above a silicon chip in order to build a qubit. This required a high control of the structure and the semi-conducting properties of carbon nanotubes in order to build the ideal host material for a spin qubit with minimal intrinsic incoherence.

1.2 Properties and applications

Carbon nanotube is a one dimensional structured graphitic material, its intrinsic properties combined with its unique nanoscale shape made it one of the most researshed object in physics as represented in Figure 1.1. Although classified as “carbon nanotube” (CNT), this single term can encompass several structures with different characteristics including chirality, diameter, length, crystallinity, purity, packing and wall number.

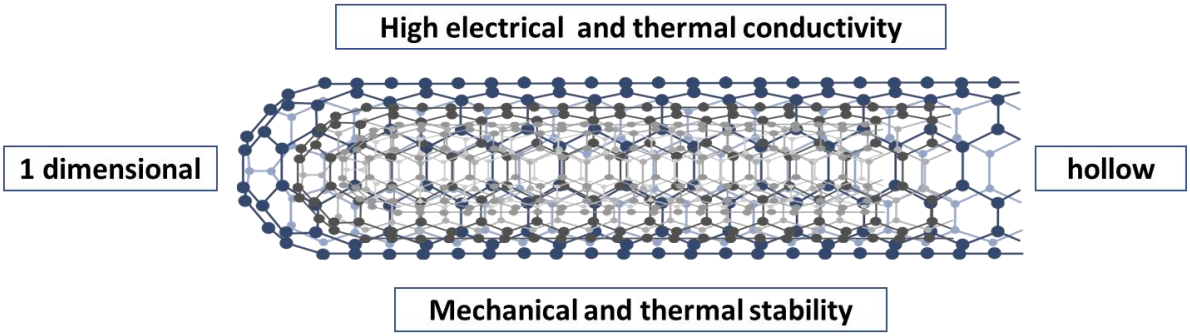

FIG 1.1 Structure and properties of a multiwalled carbon nanotubes.

Nanotubes can be classified in different families depending on:

- Wall number: multiwalled carbon nanotubes and single wall carbon nanotubes,
- Structure or chirality : zigzag , armchair or chiral
- Macroscopic organization : powder, fiber, sheets
- Nanoscopic organization:disorganized or VACNTs

Recent works have higlighted the wide range of application that versatility of CNTs offer due to their combined properties, including an excellent review [1].

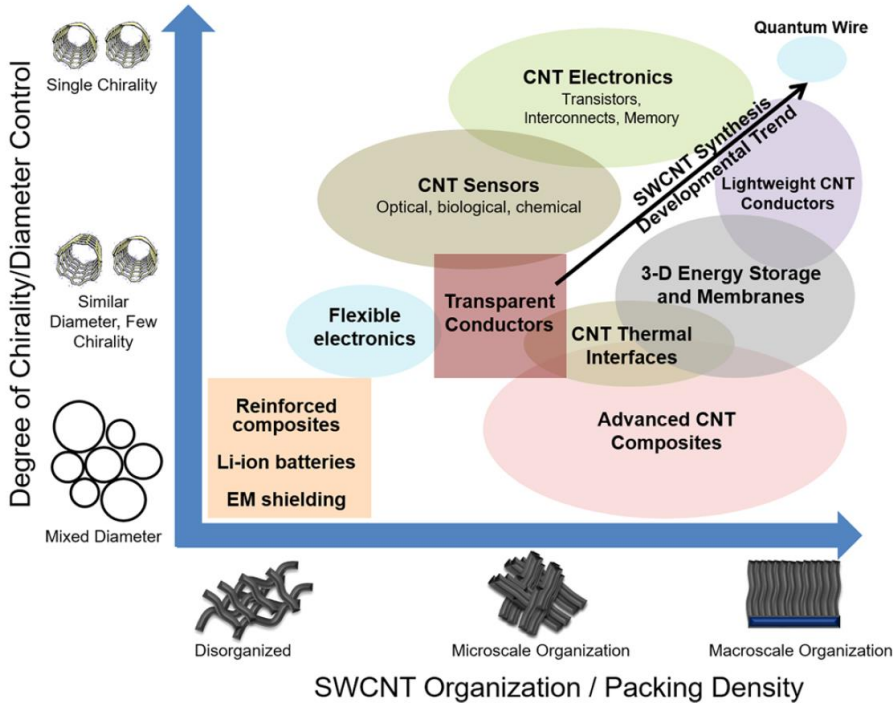

FIG 1.2 Wide range of application of carbon nanotubes. After [1].

As schematically summarized in Figure 1.2, depending of their organization and packing density, several potential applications of nanotubes have been proposed including but not

limited to microelectronics [2], spintronics [3] or sensorics [4]. More specifically, VACNTs assemblies represent particularly interesting systems in field emission cathods and data storage devices (Figure 1.3). For instance, such systems can represent a good thermal and mechanical material working at very low voltage for the next generation of field emission cathodes [5, 6], taking advantage of their unidimensional shape that can generate strong field electron emission effect [7]. The nanoscale size of CNTs and their large spin flip scattering lengths, combined to the fact that they behave as one-dimensional ballistic quantum conductors [8] makes them very attractive for spintronics applications. In the other hand, since vibration modes of ordered carbon nanotube arrays are correlated with nanotube lengths and diameters distribution in array, they was proposed as sensing elements of surface acoustic wave based sensors with increased sensitivity with respect to usually obtained values for the acoustic wave frequency range 0.1 – 1.0 GHz. [4]. Moreover, the applications of CNTs as reinforcing agents of polymer matrix composites are wide spread [4, 9, 10]. VACNTs are also highly attractive as potential stable supports for magnetic data storage arrays [11], Indeed, most catalysts for CNTs growth are ferromagnetic metals (Fe, Co, Ni), which makes such co-synthesis consisting of catalyst nanoparticles formation followed by CNTs growth, very promising route for the synthesis of aligned magnetic nanowires filled CNTs [12].

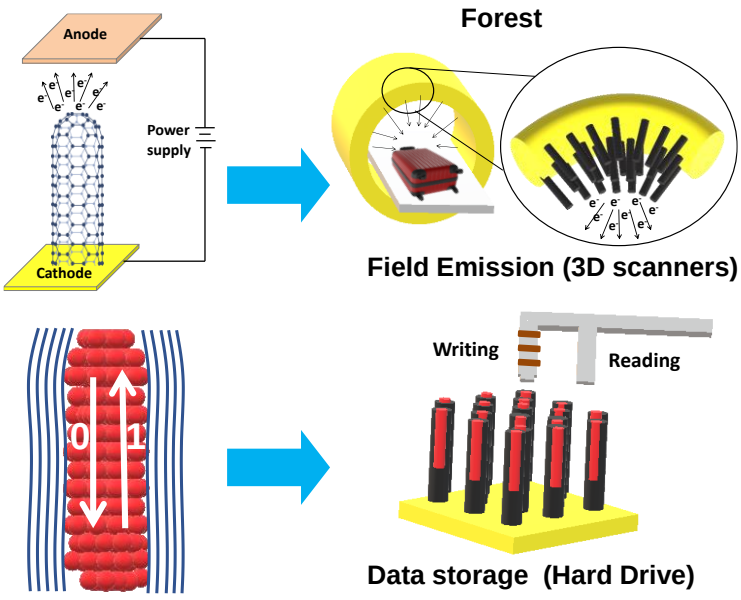

FIG 1.3 Applications of VACNTs in field emission cathods and data storage devices.

Such nanostructures are great physical objects to characterize and understand the growth of carbon nanotubes in general. Their vertical growth allow direct measurements of height,

alignment and surface density thereby allowing to estimate nanotube growth rate and catalytic life time [13, 14]. Non-destructive characterizations such as the estimation of an effective young modulus of the assembly which is not possible in a random oriented CNTs become possible, as proposed in the present study [15].

Indeed, both experimental and computational approaches are commonly used to investigate the elastic properties of CNTs [16, 17]. Despite the increase in experimental performances [18-20], a wide dispersion in the results is observed owing to the difficulty of the characterization at the atomic scale. The experimental measurement of their mechanical properties turns to be a tedious task. In this context, computational and modelling approaches have been regarded as powerful tools to predict the mechanical properties of CNTs [21-23] and the derived elastic properties such as Young's modulus, shear modulus and Poisson's ratio. An average value about 1 TPa is usually reported for the Young's modulus. It is to notice that many of the studies have focused mainly on the properties of individual CNTs and a little is down regarding the effective elastic properties of assemblies of VACNTs.

1.3 Synthesis methods

To use nanotubes in industrial applications, it is necessary to produce them in large scale with highly precise structure and morphology and at an affordable cost. Various methods are proposed in the literature, including arc discharge[24, 25], laser ablation and chemical vapor deposition (CVD) as represented in Figure 1.4. Due to its scalability and practicality to produce aligned nanotubes, chemical vapor deposition (CVD) becomes the most common method to produce nanotubes.

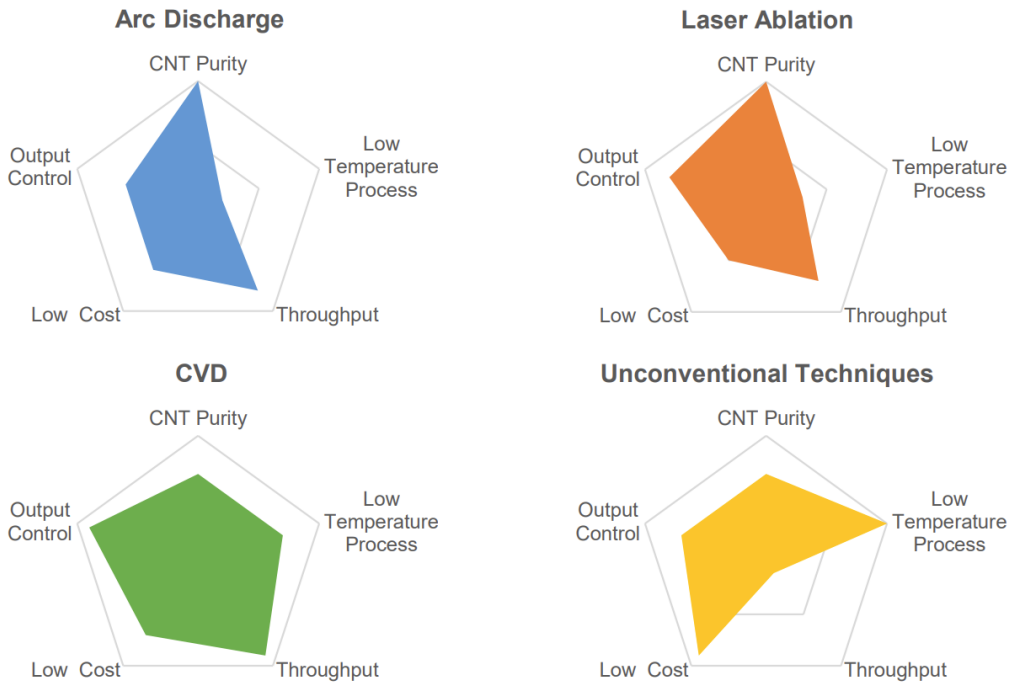

FIG 1.4 Radar charts showing a comparison between the common techniques for the synthesis of CNTs based on specific evaluation criteria. After [26].

The growth of VACNTs by chemical vapor deposition (CVD) consists in the decomposition of a gaseous carbon source (e.g. C_2H_2, CH_4) at relatively high temperature (500°C - 900°C) on the surface of a catalyst, typically a transition metal (e.g. Fe, Co, Ni) in the form of nanoparticles (Figure 1.5.a). The carbon atoms resulting from this dissociation diffuse "in" and "on" the surface of the catalytic nanoparticles (Figure 1.5.b) until saturation (Figure 1.5.c). The excess of carbon precipitates and organizes itself by covering the surface of the nanoparticles with one or more curved graphene layers. Even if the origin of the curvature in the plane of perfect hexagons is not yet elucidated, as for fullerenes (C_{60}), the creation of defects in the form of pentagons is necessary in adequacy with the Euler theorem. The pentagon would serve to transform the flat layer of otherwise hexagonal lattice to a nanotube cap. As the process continues, the addition of new carbon atoms forces this graphene layer to dissociate from the catalyst surface (Figure 1.5.d). This results in a tubular shaping of this graphitic structure (Figure 1.5.e) which grows freely. When the density of these nano-objects becomes important (typically $10^{11}cm^{-2}$), steric hindrance imposes that the only possible direction of growth is the direction perpendicular to the substrate and thus an alignment of the nanotubes is performed.

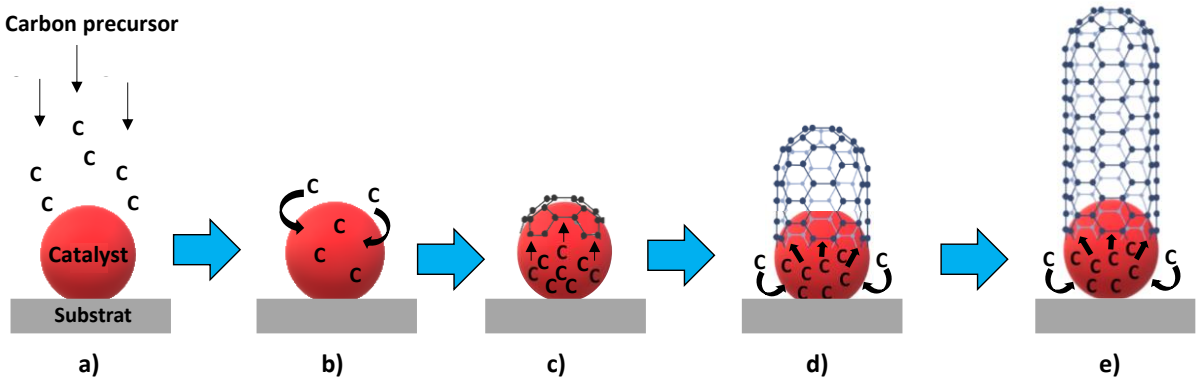

FIG 1.5 Stages of carbon nanotube growth by catalytic CVD: a) dissociation of carbon precursor, b) diffusion of carbon into/onto the catalyst, c) formation of graphitic layer(s) on the catalyst surface, d) nucleation of the carbon nanotube, e) growth of the carbon nanotube

It is worth to mention that VACNTs growth in a CVD process manifest in two mechanisms depending on the interaction between the catalyst and the underlying support, namely the well-known tip growth where the nanoparticle detach from the substrate due to weak interaction, this take off is driven by the growth of VACNTs on the lower part of the nanoparticle, on the other hand, base growth is characterizd by VACNTs growth on the superior part of the nanoparticle as represented in Figure 1.6 [14].

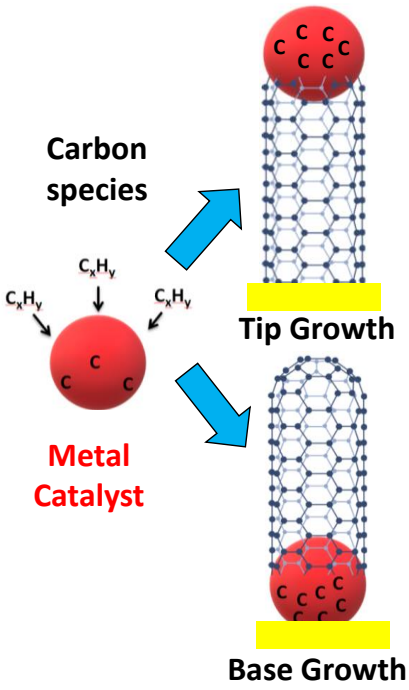

FIG 1.6 Mechanisms of carbon nanotubes growth.

The reason why chemical vapor deposition (CVD) remains the most suitable process for controlled synthesis of CNT arrays is that it allow enough time and a large set of parameters to control the structure of CNTs arrays as compared to arc discharge and laser ablation [27]. Indeed, Hata *et al.* has investigated the correlation between growth efficiency and catalyst structuring. Their results revealed that varieties of CNT forests and morphologies depend highly on the catalyst spacing and size as schematically represented in Figure 1.7. Therefore, a sweet spot can be identified using CVD parameters [28]. A radically opposite activation technique is to use plasma activation within plasma-enhanced chemical vapor deposition (PECVD). The ability of the plasma to support multiple reactive species concurrently is a key advantage in various technologies [29]. In PECVD of CNTs compared to thermal CVD, a large variety of species are activated in the plasma may contribute to the growth process, mainly radicals, ions and electrons[30]. The presence of electric fields and ion bombardments in the reactor favors ion-assisted precursor dissociation and accelerates carbon species transport to the catalyst nanoparticle surface thereby enabling a rapid, low-temperature growth of CNTs [31, 32].

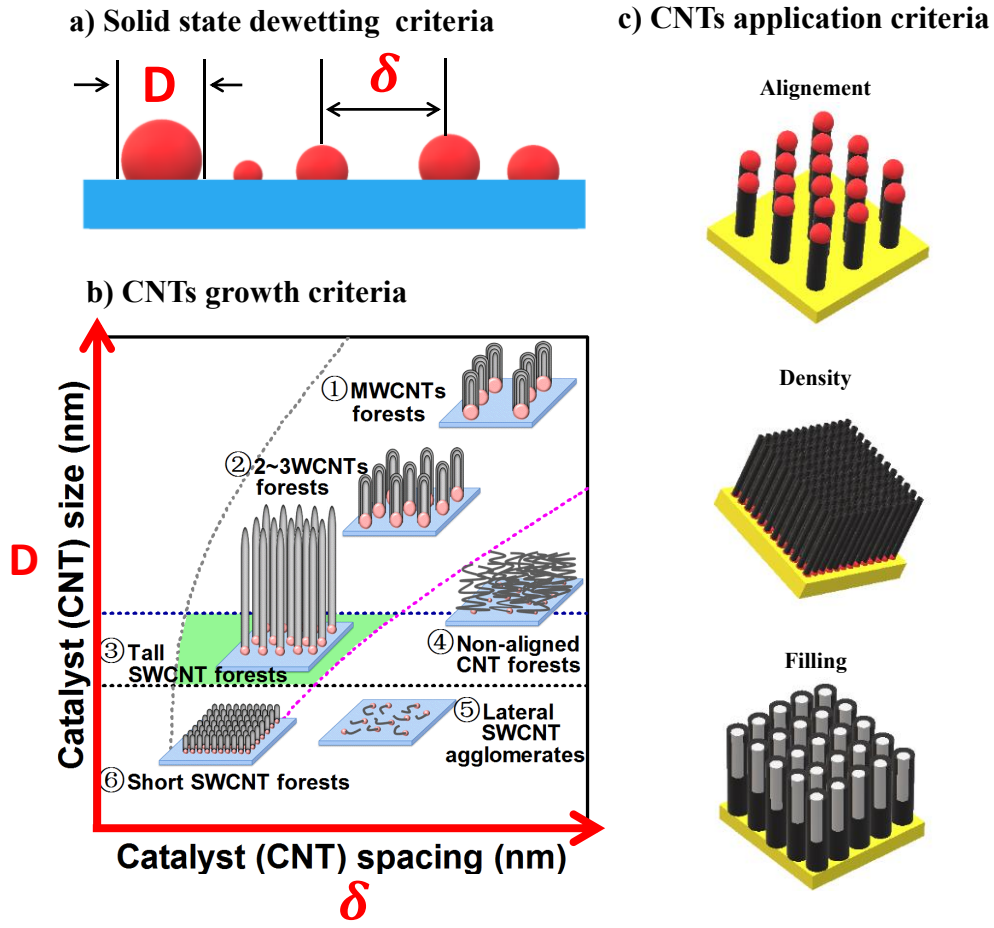

FIG 1.7 Correlation between catalyst structuring and VACNTs morphology. After [28].

Furthermore, CVD reactor performances (e.g. nanotube growth rate, number of walls, length, diameter, density, verticality, purity, chirality and uniformity) are related to the substrate and precursor nature, growth temperature, total pressure, gas flow rate, reactant relative concentrations, and geometry of the reactor which are the more important parameters to be controlled. Depending on the horizontal or vertical reactor position, gas phase temperature gradients can produce density variations leading to buoyancy driven secondary flows superimposed on the main flow. This adversely affects gas phase reactions and species spatial distribution. CNT growth can also be influenced by ppm-level changes in the concentration of H_2O vapor from moisture within the CVD reaction chamber leading to additional "hidden" factors. In what follows, we will discuss individually the effect of the most relevant growth parameters with the idea of optimizing them in the following chapters.

1.4 VACNTs Growth parameters

In contrast, PECVD processes implie a large number of parameters including intrinsic plasma parameters such as plasma power and reactor total pressure. Other parameters such as the gas flow and the concentration ratio between the different carbonaceous and carriers gases can affect the nanotube growth *via* important variations in concentration of neutral and ionic carbon precursors in the vicinity of the substrate.

1.4.1 Catalyst

The catalyst is the seed that absorbs the surrounding carbon atoms and transform them into the graphitic walls of nanotubes. The control of the size of the catalytic nanoparticles is hence fundamental since the diameter of the CNTs obtained is directly related to that of the catalytic particle [33]. As already mentioned, the possibility of controlling the size of metal nanoparticles is a major challenge for the controlled growth of nanotubes. According to the variants of the catalytic CVD growth process, the catalyst can either be pre-deposited on the substrate before the temperature increase and the injection of the reactive gases (so-called two-step process), or it can be injected together with the reactive gases at the synthesis temperature (so-called one-step process).

In our case the catalyst is pre-deposited on the form of a thin film of nanometric thickness and then heated to form catalytic nanoparticles whose size increases with the thickness of the thin film. The pre-treatment of this film consists of a thermal or plasma heating to pass from a continuous film to an assembly of nanoparticles by dewetting. The addition of

gases (H_2 or NH_3) during this heating step favours the organization of the film in the form of dense and distinct islands and thus exalts the catalytic activity during the growth.

1.4.2 Substrate

Substrates of different nature have been used for the growth of VACNTs, The nature of the substrate is a crucial factor in controlling these arrays and can vary depending on the desired application from semiconductors (Si [34, 35], Ge[36]), insulators (SiO_2 [37-39], Al_2O_3 [40-42], ZrO_2 [43], MgO [44], Si_3N_4 [45]) or conductive alloys (TiSiN [46], TiN [47], AlSi [48], $CoSi_2$ [49]). However, diffusion of the catalytic nanoparticle in the substrate at high process temperatures is still a major problem. Many techniques were proposed to limit diffusion of the catalytic nanoparticles into the substrate such as the use of metal oxides like SiO_2 and Al_2O_3 as nanoparticles supports; since dewetting is known to proceeds easier in substrates of low surface energy than in those of high surface energy. On oxides, diffusion can mostly be mitigated by using multiple step deposition of film to compensate the loss of mass after each heat treatment [50] or by depositing thick films. However, thick films may yield low density and large nanoparticles. Diffusion barriers are more effective solution to dewett few nanometers film thickness and especially have been attractive to achieve high area density of nanotubes as represented in Figure 1.8. Yang *et al*. have proposed to use TiSiN supports as a refractory, amorphous, conducting material during nanotube growth from iron catalyst. They showed that TiSiN limits the diffusion of sub-nanometer metallic catalyst (Fe) in the bulk of the under layer support [46]. TiSiN substrates could also allow a more controllable dewetting, reducing the effect of undesirable processes mentioned earlier. However, little effort has been devoted so far to study the model of dewetting on TiSiN in particular, and conductive substrates in general. Figure 1.8 schematically shows the advantage of using a diffusion barrier in the context of catalyst dewetting and nanotube growth.

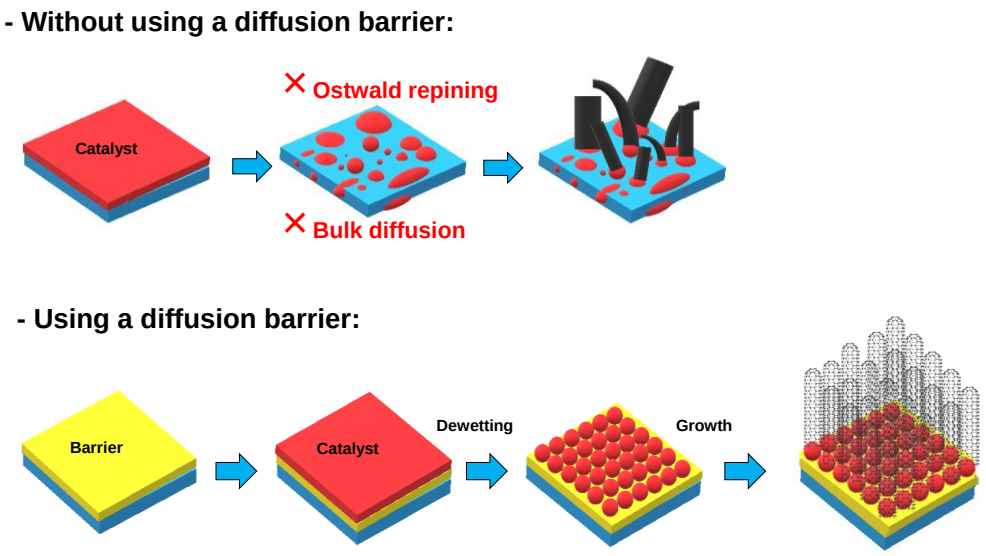

FIG 1.8 Advantages of using a diffusion barrier during the catalyst dewetting and subsequent VACNTs growth.

1.4.3 Carbon precursor

The dissociation of the feedstock mixture creates a reactive composition of radicals that leads to catalytic growth of CNTs on the nanoparticle surface. Hence, the composition of the feedstock greatly influences both nanotube growth rate and catalyst life time [51]. Gaseous mixture feed to the reactor mainly contains a carbonaceous precursor such as methane, acetylene, ethylene, and a carrier gas such as hydrogen or ammonia used also as reducing agents of the oxidized catalytic nanoparticles. While methane has reasonable stability at high temperatures, its thermal decomposition into atomic carbons and linear dimers/ trimers of carbon can be lowered around 700°C in the presence of a transition metal catalyst (Co, Fe, Ni) to produce CNTs. Higher temperatures are not recommended due to the over saturation of nanoparticles with carbon leading to fast catalyst deactivation[52]. This deactivation depends also on methane and hydrogen partial pressures [53]. Hence substrate temperature and hydrogen flow rate among other experimental parameters have to be optimized for high CNTs yield as studied in our previous work [54].

1.4.4 Temperature

Even if the decomposition of the carbon gases by the plasma electrons is independent of the substrate temperature, the abundant generation of radicals and ions in the plasma makes it possible to lower the temperature of the substrate even below 500°C. Below this temperature, nanofibers with a lower degree of graphitization are generally obtained [55]. The growth temperature of CNTs must be sufficiently low (to be compatible with microelectronics

processes) and sufficiently high to ensure sufficient decomposition of the carbonaceous gas. The technical challenge is hence to find this compromise for a given reactor geometry. This could be obtained through modelling.

1.4.5 Growth enhancers

Oxygen species are common used enhancers in CNTs growth, Hata *et al*. reported a water-assisted CVD of millimeter tall CNTs, using water to selectively remove amorphous carbon without damaging the nanotubes enabling what is described as "super growth" [56]. Highly efficient growth can be achieved using countless other growth enhancers beyond H_2O. For that the combination of two ingredients must be met: a growth enhancer must contains oxygen and a carbon source that must not contain oxygen as represented in Figure 1.9 [57]. To explore the conditions of highly efficient nanotube growth, Futaba *et al.* [55] studied 27 combinations of carbon sources (ethylene, acetylene, and carbon monoxide) and different growth enhancers summarized in Figure 1.9. For each combination, the optimized growth yield (forest height) is displayed in the two-dimensional map of Figure 1.9a. In summary, according to Futaba *et al.*, highly efficient growth is obtained when two fundamental rules are achieved i.e. (i) a growth enhancer containing oxygen, and (ii) a carbon source not containing oxygen. Thus, supergrowth is not limited to ethylene and water, but the concept can be expanded to what they call a ''generalized super-growth''. The results presented in Figure 1.9c demonstrate the broadness of the actual highly efficient growth with other growth possibilities not yet explored that could potentially transform the world of CNT synthesis [55]. However the role of oxygenated species has been described in different ways, Kohno *et al*. reported that alcohols are much better carbon sources due to the formed dangling bonds of OH radicals on the catalyst surface. These radicals are supposed to attack nearby amorphous carbon atoms to form CO [58]. The same effect has been reported in other works by adding separately very small amounts (0.1%) of oxygen to methane and hydrogen in conventional thermal CVD [59]. In Plasma Enhanced CVD, Ho Lee *et al* have demonstrated by optical emission that etching OH radical formed by addition of oxygen (0 - 12%) in the plasma is the key agent in improving nanotube quality [60]. In contrast, Hongjie Dai *et al* reported that the key role of oxygen in the plasma is balancing C and etching H radicals, *i.e*. providing a C-rich and H-deficient condition to favor the formation of sp^2-like graphitic structures [61].

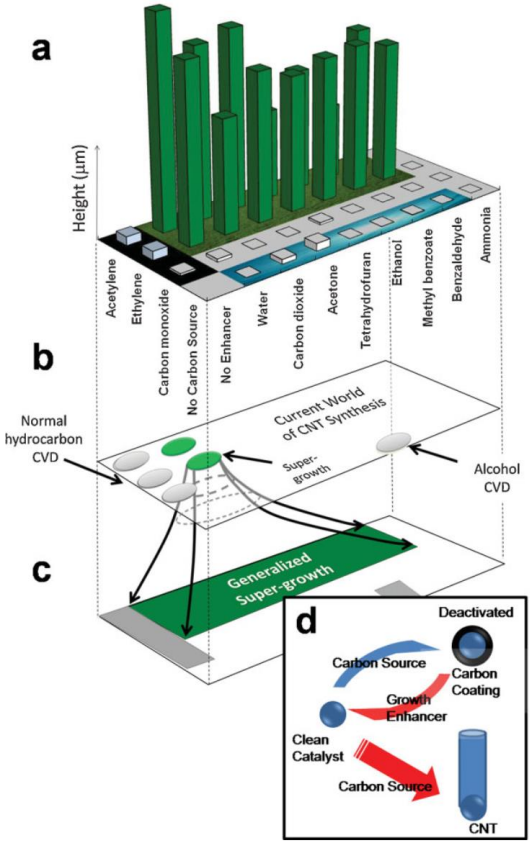

FIG 1.9 The expanded view of CNT synthesis. a) Carbon source–growth enhancer height mapping for all 27 combinations using a 10 min growth time. b) Mapping of the current world of CNT synthesis. c) Mapping of the expanded world of CNT synthesis with generalized super-growth. d) Scheme of the fundamental mechanism for highly efficient growth. After [57].

1.5 Solid state dewetting:

Metallic nanoparticles (MNPs) are considered to be the building blocks for many nanotechnology based devices [62]. The study of such materials structure and properties is therefore of great fundamental interest, especially since physio-chemical properties of MNPs are governed by their structure. For instance, both equilibrium and non-equilibrium magnetic properties of cobalt NPs, are known to on geometrical parameters such as particle size and shape. As example, the coercive field value H_c of the NPs is size and shape dependent [62-66]. MNPs can be disposed on a substrate and integrated in electronic and photonic devices fabrications [67, 68], bio-sensing [69], catalysis [70], and data storage applications [71, 72]. Moreover the surface density of these MNPs on a substrate is an important factor which must be considered for catalyzing carbon nanotubes growth [28], and to control their behavior as an

assembly for the fabrication of metamaterials [73]. However the control of these parameters on the nanoscale level is hampered by high cost techniques such as lithography [74]. Thereby, other innovative techniques have been developed to engineer these nanostructures such as nanoembeding [70], spatially confined dewetting[75] or templated dewetting [76]. In this sense, solid state dewetting of thin metal films is a promising strategy for MNPs controlled fabrication oriented towards different applications as represented in Figure 1.10.

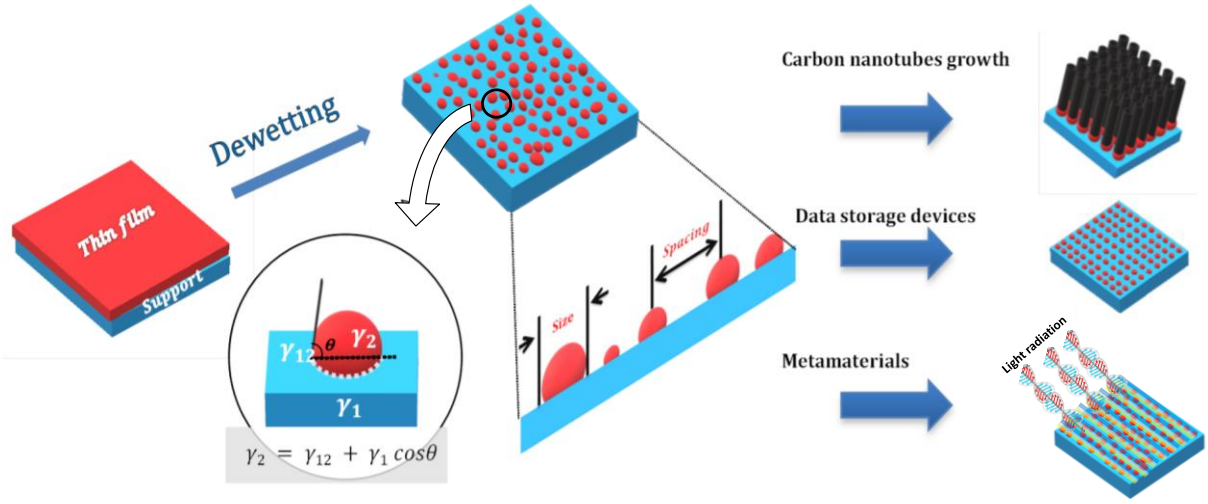

FIG 1.10 Scheme of the dewetting process of continuous metal films into isolated nanoparticles and possible applications in nano-electronics.

Solid-state dewetting is usually a common undesirable phenomenon found in thin film devices caused by heating leading their degradation and failure [77]. However, it could be also intentionally used as an effective cost friendly process to form ordered arrays of self-organized nanoparticles on a desired substrate [78, 79]. This process is driven by the difference in surface energy of the thin film and the underlying support and could be industrially scalable to morphologically transform continuous films (Cu [38], Au [80], Ag [81], Pt [82], Sn [83], Co [84]) into islands or droplets used to produce nano devices.

1.5.1 Origin of solid state dewetting

Solid state dewetting has the same origin as the dewetting of liquids *i.e.* a reduction of the energy of the surface/interface by shape change of the film. Indeed, continuous metallic

films are metastable when deposited on a substrate they do not wet. Their spontaneous evolution when thermally annealed at sufficiently high temperatures, results in very specific nanostructures. Annealing temperature is sometimes well below the film's melting temperature but could occur also above the melting temperature of the material, if laser irradiation [85, 86] or ion irradiation [87] are used. The physics of this morphological instability is quite different in the case of solids where the transport of atoms is caused by surface diffusion rather than by hydrodynamic flow as in liquids. The knowledge of diffusion paths is crucial since diffusive mass transport can occur along the surface, the interface or grain boundaries to form what was called by "grooves". Finally the propagation of these grooves results the formation of dispersed nanoparticles ideally of a spherical shape. This equilibrium shape of the nanoparticle (indexed "1") with a surface energy γ_1 on a substrate (indexed "2" as substrate) with a surface energy γ_2 is described by the Young-Laplace equation (1), [79]:

$$\gamma_2 = \gamma_{12} + \gamma_1 \cos\theta \quad (1)$$

Where γ_{12} is the energy of the nanoparticle-substrate interface and θ is the equilibrium contact angle. The balance of these three interfacial tensions is illustrated in Figure 1.10. If $\gamma_2 > \gamma_{12} + \gamma_1$, the film will be stable and will not dewett. However, if this condition is not satisfied, the film will dewett due to thermal annealing. In this case, atoms are sufficiently activated to overcome the energy barrier. The wettability of a given metal can be evaluated by the contact angle θ. Good wettability is insured when contact angle is smaller than 90° and the wettability becomes weak for a contact angle larger than 90°. The contact angle depends on the nanoparticle and substrate surface energies and could be affected by chemical reactions between liquid alloy and solid substrate as well as surface roughness [88]. Dewetting could be controlled by several parameters including : the initial film thickness [33], the annealing temperature [89] and treatment time [90] leading to controlled nanoparticle size and spacing.

Depending of its thickness, a flat film may dewett by hole nucleation on defects which is a random process that occur for relatively thick films, or by spinodal surface instability [91] resulting in specific dewetting patterns. Solid-state dewetting is indeed governed by the initial film thickness. Nuryadi *et al.* have demonstrated that the height h and the diameter d of agglomerated Si islands, as well as their surface density, are a function of the initial Si thickness [92]. Moreover experimental results indicate that, whatever the experimental conditions are, dewetting is closely related to the initial thickness of the films, with linear variation in the case of hole nucleation and growth [93, 94], and a 5/3 power variation in the case of spinodal dewetting [83, 95]. The density of nanoparticles varies as a function of the inverse of the square

of the initial thickness of the films, h^{-2}. The thickness effect on nanoparticles formation has been observed in preliminary experiments in this work using Ni thin films deposited on Si wafers and subjected to solid state dewetting as represented in Figure 1.11:

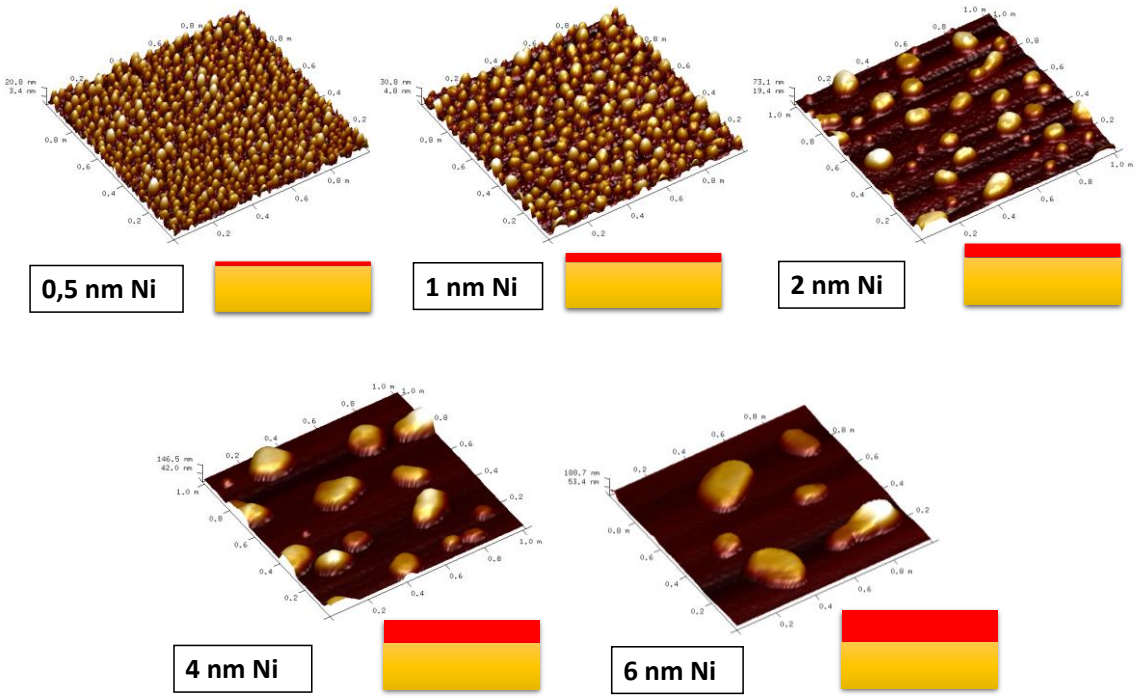

FIG 1.11 AFM characterization of dewetted Ni nanoparticles as a function of intial film thickness.

1.5.2 Dewetting models

To calculate the size and density of dewetted nanoparticles, three models are proposed in literature:

a. Mullins's model

The general theoretical framework describing solid state dewetting was put first by Mullins in the 1950s and was called "thermal grooving" [96]. Mullins proposed two distinct theories. The first is based on evaporation-condensation and the other on surface diffusion. The depth d of grain boundary groove for evaporation-condensation kinetics and surface diffusion mechanism was calculated by solving total mass conservation as represented in Figure 1.12. For the case of evaporation-condensation, the groove depth d (i.e., the distance from the groove root to the plane of the initial flat surface) vary with the square root of the time,

$$d = 1.13 \tan(\theta) \sqrt{\alpha t} \qquad (2)$$

While for the case of diffusion, atoms diffuse on the surface away from the triple junction, and d scales with the fourth root of the time,

$$d = 1.13 \tan(\theta) \sqrt[4]{\beta t} \quad (3)$$

In equations (2) and (3), t is the time, d is the instantaneous depth of grain boundary, h is the film thickness, θ is the angle at the triple point and α and β are constants depending on the temperature and given by:

$$\alpha = \frac{p_0 \gamma_s \Omega^2}{\sqrt{2\,\pi M_W\, kT}} \quad (4)$$

$$\beta = \frac{D_s \gamma_s \Omega^2 v}{kT} \quad (5)$$

where p_0 is the metal vapor pressure in equilibrium over the grain boundary, γ_s is the surface-free energy per unit area, Ω is the molecular volume, M_W is the molecular weight, D_s is the coefficient of surface diffusion and v is the number of atoms per unit area.

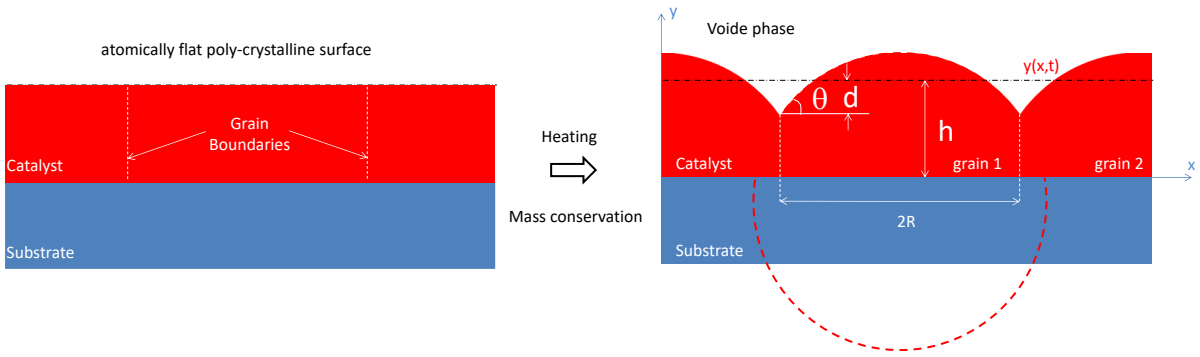

FIG 1.12 Schematic cross section of equilibrium circular grain boundary groove formed by heating atomically flat poly-crystalline surface. Time and horizontal coordinate evolution of the free surface area is labelled y(x,t).

Mullins's solution has been proposed to measure interfacial energies and surface diffusivities. Nevertheless, as shown in equations (2) and (3), Mullins's model predicts an unlimited variation of d when the time goes to the infinity.

b. Srolovitz and Safran model

To overcome this discrepancy in infinite size evolution, Srolovitz and Safran [97], proposed a new model to estimate the equilibrium groove depth for interconnecting spherical shape grain boundaries interacting with each other *via* surface diffusion. Grains are formed in between internal interfaces called grain boundaries. Due to their high energy in thin solid films, these grain boundaries junctions are primary sites for hole nucleation. Thermodynamic equilibrium requires that the groove angle θ is fixed. Figure 1.13 shows the equilibrium grain boundary groove configuration in the case of grains in the shape of a circular base with grain radius R and a spherical cap which intersects the grain boundary at an angle θ. The film thickness is h and the equilibrium groove depth d, measured with respect to the flat film rushes an equilibrium value given by,

$$d = R\,\frac{2-\cos(\theta)+cos^3(\theta)}{sin^3(\theta)} \quad (6)$$

For fully dewetting of the film, the groove must intercept the substrate and the groove depth d becomes larger than the film thickness h. However, this model does not consider the effect of initial height h, leading to a nanoparticle size independent of the initial catalyst volume.

c. Zhong model

In order to consider initial thickness effect, Zhong *et al.* [98] proposed a model based on the conservation of volume as well as the energy of the system before and after nanoparticle formation. Their model considers a truncated sphere formed by dewetting with a surface S_1 in contact with the atmosphere and a surface S_2 in contact with the support. Before the dewetting, the interfacial energy is given by

$$G_1 = A(\gamma_1 + \gamma_{12}) \quad (7)$$

where γ_1 is the catalyst surface energy, γ_{12} is the catalyst-support surface energy respectively and A is the support area per nanoparticle. After dewetting, the interfacial energy of aspherical nanoparticle of top surface area S_1 and a contact area S_2 is given by:

$$G_2 = (A - S_2)\gamma_2 + S_2\gamma_{12} + S_1\gamma_1 \quad (8)$$

Where S_{12} is the contact area and γ_{12} is the interface surface energy.

By introducing the contact angle θ given by the Young's equation (1) discussed above, and the radius R of the sphere formed by dewetting, we can calculate by geometrical considerations the surfaces S_1 and S_2:

$$S_1 = 2\pi R^2(1-\cos\theta) \quad (9)$$

$$S_2 = \pi R^2 \sin^2\theta \quad (10)$$

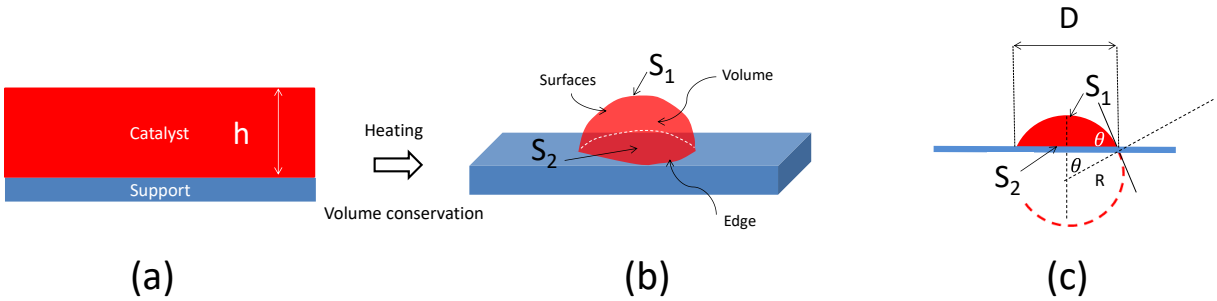

FIG 1.13 (a) Initial catalyst film. (b) Surfaces, volume and edge generated after heating. (c) Schematic cross section considered in Zhong *et al.* model. h: initial thickness of film. S_1: Top surface area. S_2: surface of the catalyst in contact with the support. θ: contact angle. R: radius of the hypothetical sphere. D: nanoparticle diameter.

Zhong *et al.* postulate that the minimum particle size occurs at $G_1 = G_2$ and estimated from metal volume conservation the diameter of the nanoparticle D as a function of the initial catalyst thickness h.

$$D = \frac{6h \sin\theta}{1-\cos\theta} \qquad for\ \theta < 90° \tag{11}$$

$$D = \frac{6h}{1-\cos\theta} \qquad for\ \theta > 90° \tag{12}$$

In the other hand, nanoparticle density N could be estimated from contact angle and nanoparticle diameter by the following equations, [81]

$$N = \frac{4\,(1+\cos\theta)}{\pi D^2(2+\cos\theta)} \qquad for\ \theta < 90° \tag{13}$$

$$N = \frac{4}{\pi D^2(1-\cos\theta)(2+\cos\theta)} \qquad for\ \theta > 90° \tag{14}$$

Nevertheless, the accuracy of this model depends highly on the mitigation of thermally activated processes mainly the migration of catalyst atoms into the bulk of the support and Ostwald repining at high temperatures which significantly reduce the efficiency of dewetting process [56]. Indeed, while bulk diffusion is described to lower the size of nanoparticles which is desirable on one part, this loss of mass and its interaction with the underlying substrate causes deactivation of the nanoparticles [99] and the forming of unwanted alloys [100]. On the other hand, larger particles grow in size at the expense of smaller particles and decreases the number density with time, a phenomenon known as Ostwald ripening, which consists of coarsening in which the particle size increases and particle density reduces after extended annealing [101, 102].

In the direction of suppressing these undesirable phenomena, different energy sources can be employed in order to furnish the energy necessary to activate the dewetting process of the film, other than thermal annealing. Many studies have been performed using electron and ion beam irradiation [94, 103, 104], laser induced dewetting [105, 106]. However, little research has been dedicated to plasma-induced dewetting [68]. During plasma treatment, energy is mainly transferred uniformly to the overall surface of the film by accelerated ions that carry more or less equivalent energy [107], which allows the control of nanoparticle size and distribution that depends on the density of radicals and ions which is tuned by plasma power and total pressure [108].

In Chapter II of this thesis, we will investigate a range of parameters affecting separately and combined, the dewetting of ultrathin cobalt films and formed nanoparticles properties. Our main motivation for the choice of cobalt catalyst is to study in Chapter IV the magnetic properties of multi-walled carbon nanotubes (MWCNT) with encapsulated Co nanoparticles. The effect of the diffusion barrier, plasma treatment as well the relationship between initial film thickness and dewetted nanoparticles diameter and density will be hence addressed from structural and magnetic point of views.

1.6 Filling of carbon nanotubes

Dealing with magnetic materials, they are characterized by the value of their remnant magnetization and that of the coercive field. The remnant magnetization is determined by the spontaneous magnetization of the material. Coercivity is linked in particular to magnetic anisotropy. The coercive field, the magnetization reversal and the interactions of the magnetic nanowires were widely studied [109-111]. Due to the high aspect ratio, the shape of these nanowires is the main contributor to magnetic anisotropy, having the easy axis along the wires axis. Thus, in the case of an elongated nanowire or ellipsoid, the direction of easy magnetization is the long axis of the particle and high aspect ratios lead to high form anisotropy fields. Thus, the shape anisotropy can be tailored to improve the magnetic properties of the material. Many techniques have been developed to fabricate ordered magnetic nanostructures with dimensions on the submicron to nanometer scale [112-115]. The investigation of promising pathway to directly integrate magnetic nanostructures with Si-based electronic devices is an exciting challenge in order to avoid all the heavy steps utilized in the usual lithography processes. Randomly and self-organized nanostructures are one of these approaches. For instance, the most

popular way of fabricating nanowire arrays is the electrodeposition in a porous alumina matrix being fast, inexpensive, and of high technological importance [116, 117].

Since the discovery of CNTs, the possibility of filling the central channel with various foreign elements or compounds, mainly metals and magnetic materials aiming at the synthesis of nanowires, has been considered. Nevertheless, capillarity and wetting remain the major limiting processes towards the use of the inner cavity. Since nanotube surface is a neutral support with high inertness to many chemical species, in addition it is electrically and thermally conductive, it can serve either as an anti-oxidation protection, electrical contacts, or for injection of spin current. Besides filling the central channel, intercalation in the intertubular space and functionalization of carbon atoms through addition reactions have been also proposed to improve CNTs integration in devices and advanced materials. Specifically, the template effect provided by the nanotube internal cavity can help inserted materials to adopt one-dimensional morphology with an alternative way to synthesize confined nanowires.

Besides the challenge of inserting foreign materials in a nanometric channel in diameter over micronic lengths, this opens the way to synthesize new materials with ultimate confinement. The understanding of the growth and filling mechanisms with a view to control selectivity and filling yield remain a great challenge towards the development of new hybrid materials for emergent applications. Filling methods can be classified into two main classes:

1.6.1 *ex situ* filling

In the *ex situ* route, the filling step takes place post-synthesis after the opening of the nanotubes [118-121]. Filling materials are in gaseous phase up to their vaporization or sublimation temperature (C_{60}, S, Se) [122-124] and halides, mixtures of halides and mixtures of halides together with chalcogenides (LiI, NaI, AgCl) [125]. This method can be applied to SWCNTs or MWCNTs and is not subjected to surface tension threshold, as opposed to the liquid route, allowing for high filling rates. Capillarity and diffusion of molecular species, such as fullerenes are the main filling processes. Nevertheless, this method is not applicable to the material with vaporization or sublimation temperature higher than 1000°C. When *ex situ* filling is induced by a liquid phase or molten material, capillary wetting represented by the Young-Laplace law become the dominant process [126]. In this direction, Ajayan and Iijima [127] reported the filling of CNTs with Pb by heating a mixture of CNTs and Pb above the melting point of Pb. Wet chemistry method is considered are an easy and scalable technique based on capillary filling. It consists of infiltrating metal precursor solutions into open ended CNTs as

represented in Figure 1.14. Hence depends mainly on internal diameters of CNTs, surface tension, viscosities of precursor solutions and length of CNTs [128-130]. pre-opened nanotubes were loaded with nanoparticles uses suspension of small nanoparticles (typically ~1nm in diameter) dispersed in a solvent [127, 131]. Since surface tensions of the usual solvents are less than 80 mN m^{-1}, wettability is not considered as a key factor in this case but the effect of the viscosity of the solvent could delay the filling process which can last several hours or even 3 days [125].

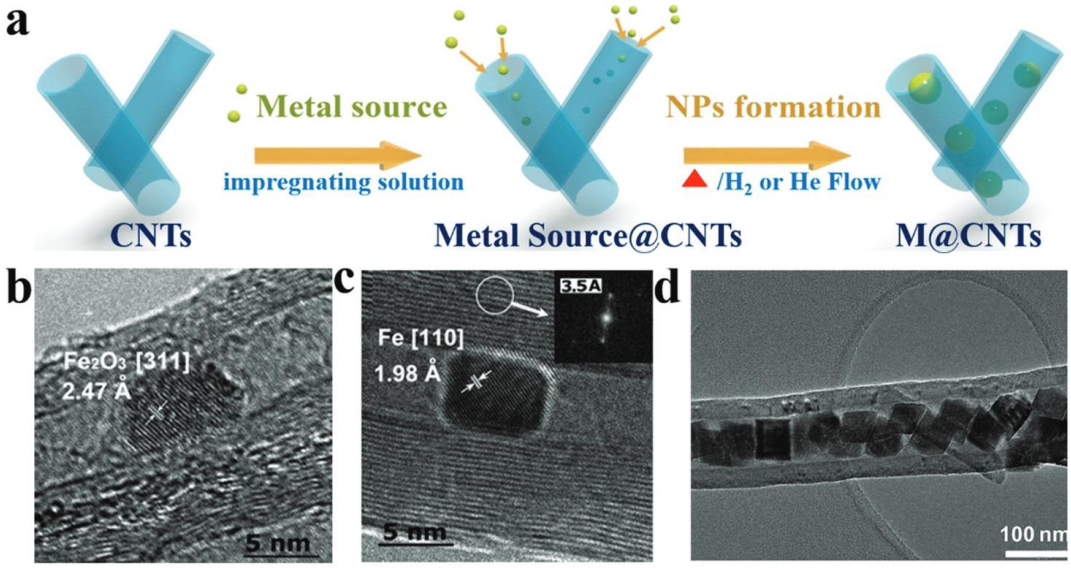

FIG 1.14 A schematic illustration for the fabrication of metal filled CNTs through the wet chemistry method. (b) Fe and (c) Fe2O3 and (d) Co inside CNTs After [130].

1.6.2 *in situ* filling

In the opposite direction, the *in-situ* route allows for faster and simultaneous nanotube growth and filling in the synthesis reactor with appropriate process parameters. Several metals have been filled in situ by arc discharge technique [132, 133]. In situ filling can also be achieved in chemical vapor deposition systems [12, 134-136]. During the growth of CNTs, the catalyst metal atoms can diffuse in the inner canal of via surface diffusion due to weak interactions between the metallic catalyst and the graphitic walls of CNTs [137]. This solid state diffusion takes place due to the dissociation of catalyst precursor. The continuous feeding of catalyst atoms through the root of CNT results in fragmented rod like structures confined by the inner walls as represented in Figure 1.15 [135]. Encapsulation of Co [138], Ni [139], Fe [140], and FeCo [141] in MWCNTs has been reported. Plasma Enhanced chemical vapor deposition was

proposed to encapsulate Pd [142] and Co [143] nanowires inside MWCNTs. For Co nanowires, the magnetic properties such as coercivity and saturation magnetization have been determined. Finally, Hayashi *et al*. reported PECVD synthesis of multiwalled carbon nanotubes (MWCNTs) filled with Co/Pd magnetic and nonmagnetic multi-metal nanowires using Co and Pd thin-layers deposited on Si using a bias-enhanced growth method [136, 144].

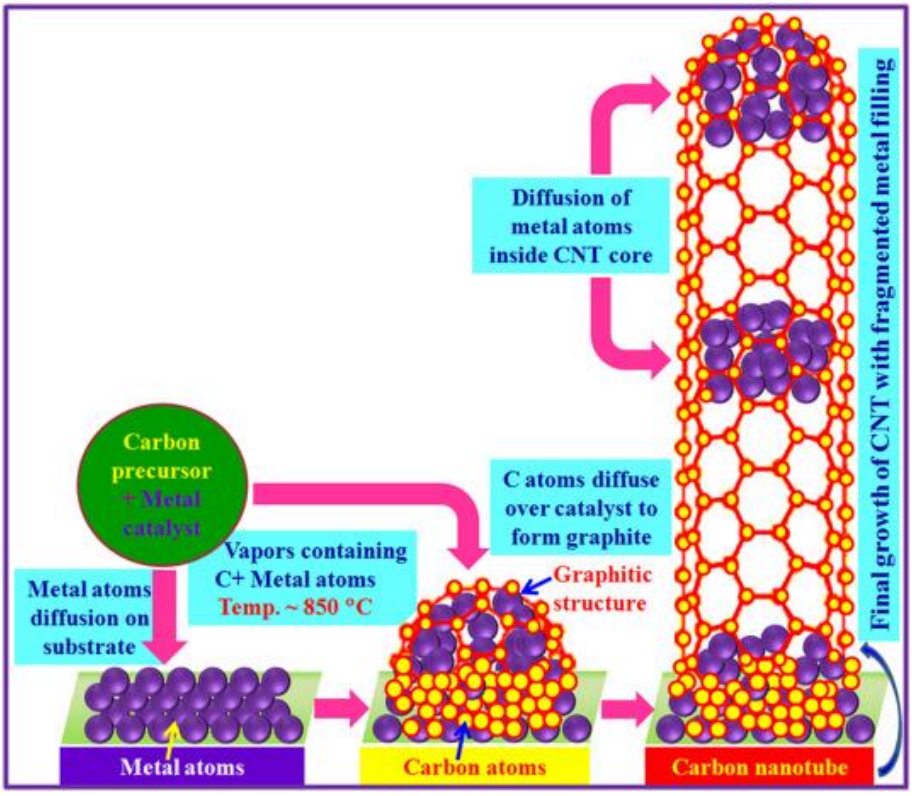

FIG 1.15 Schematic of growth and filling mechanism of filled CNT after [135].

However, despite many benefits, the PECVD process appears to be somewhat limited in the growth of hybrid CNTs. Not many works in the literature actually address the filling of carbon nanotubes with ferromagnetic materials by this technique. Indeed, to our knowledge, no detailed parametric studies of the combined effect of plasma, temperature as well as substrate nature and catalyst composition have been reported in order to find optimal conditions for the filling of VACNTs.

1.7 Modeling of CNTs growth

CVD parameters for the growth of VACNTs are interconnected through coupled mass transfer with hydrodynamics and heat transfer as well as gas and surface chemistries. Nevertheless, reactor design and operation have been performed quite exclusively by time consuming, tedious and expensive series of experiments. If these empirical trial-and-

error approaches have produced very interesting results, they begins to reach their limits and do not always provide convenient answers to the increasingly difficult CVD problems. They are time-consuming and expensive and their major inconvenience is their lack of generality and the difficulty to extend the results to different reactor configurations in scale-up context. Hence, in order to optimize the overall process, it is necessary to achieve a better understanding of the reaction mechanism at a molecular and reactor scale levels using mathematical models.

A radically opposite complementary modeling approach was proposed by Khalilov *et al.* [145] who used a computational method supported by experiments to study the plasma-based formation of nanotubes at the level of nickel nanoclusters. They first simulate *via* molecular dynamics the re-structuring of Ni thin films with a thickness in the range of 0.3-1.2 nm annealed onto semiconductor silicon substrates represented by Si_{3995} or Si_{8888} clusters, at temperatures between 600 K and 1200 K. Then, catalyzed CNT growth is simulated on Ni_{55} physisorbed on silicon by combining molecular dynamics and time-stamped force-bias Monte Carlo simulations. They conclude on the importance of H atoms in both the re-structuring of the initial Ni film and the subsequent CNT nucleation and growth. As represented in Figure 1.16, during CNT nucleation and growth, gas-phase hydrocarbon species C_xH_y impinge on the catalyst while they gradually dissociate (step 1 in Figure 1.16). It is thought that free H atoms radicals interact with adsorbed C_xH_y, resulting in H_2 desorption. The remaining C adatoms dissolve into the metal cluster and the adsorption/dissociation, C dissolution and H_2 desorption continues until the nanocluster is saturated (step 2). Subsequently, segregated C-atoms diffuse through the catalyst until recombining with other carbon atoms in order to form carbon structures such as C_2 dimers, sp^2 and sp^3 carbon atoms and short polyne chains without or with H-terminations (step 3). Appearance of a carbon cap on the cluster allows CNT nucleation (step 4), followed by CNT growth through direct adsorption of partially dehydrogenated hydrocarbon fragments near the catalyst/cap interface (steps 5 and 6).

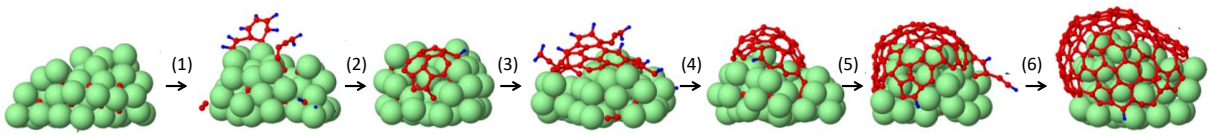

FIG 1.16 Schematic representation supported by molecular dynamic simulations of nucleation and growth of a CNT from C_xH_y species on a metallic catalyst in green color. C and H atoms are in red and blue colors, respectively. After [145].

Since sampling the atomic positional fluctuations in a picosecond molecular dynamics simulations are computationally very expensive, only 9 plasma-generated carbon precursors (C, C_2, C_2H, CH_3, CH_4, C_2H_2, C_6H_6, C_7H_8, and C_8H_{10}) were considered by Khalilov *et al.* [145], while 134 plasma species are considered in our model. Nevertheless, to initiate CNT growth, the most efficient intermediates are expected to be first produced in the gas phase and then diffuse on the catalyst surface to be chemisorbed and/or physisorbed to nucleate the nanotube [146]. In our approach exposed in Chapter III, taking advantage of the low computational time involved in thermochemical modeling, to better represent the number of carbon atoms provided for CNT formation, the decomposition of methane coupled with oxygen is calculated with the largest variety possible of gas phase intermediates including reactive species, free radicals, organic compounds and polycyclic aromatic hydrocarbons. Indeed, the CNTs growth efficiency in microwave PECVD process strongly depends on their relative concentration and reactivity. Then, for more accurate engineering optimization in larger multidimensional model, this mechanism could be easily reduced *via* sensitivity and uncertainty analyses. This allows the calculation of the overall uncertainty of simulation results and the identification of the most important input parameters to reduce chemical system without losing important kinetic and dynamic details.

Carbon nanotube synthesis by CVD process implies a huge number of interdependent variables, making the process optimization in such high-dimensional space-exploration very complex. In addition, the lack of a quantitative understanding of the gas-phase chemistry as well as the growth mechanism limited the approaches of so-called knowledge modeling. In an opposite direction, Chang *et al.* proposed a machine learning (ML) in combination with Raman *in-situ* characterization in a closed-loop fashion, to explore the large parameter space during CVD nanotube growth. An adaptive sequential algorithm is proposed in order to find the global optimum of black-box functions using Bayesian optimization to maximize CNTs growth rate from ethylene/hydrogen/water decomposition on 2 nm-thick Co film deposited on 10 nm alumina acting as a barrier layer, [147]. The advantage of this approach lies in the reduced number of experiments to achieve the optimum (100 experiments in ~8 hours). Despite these advantages, since (ML) are autonomous, they are highly susceptible to errors. Massive data sets are required to choose among different kernel and acquisition functions in order to let the algorithm learn and the convexity of the objective function is not guaranteed. For these reasons, we propose, as a complementary alternative, to develop a knowledge-based engineering modeling to assess the intrinsic parameters of nanotube growth. This approach supported by

experiments as represented in Figure 1.17, is illustrated in this thesis by studying the role of oxygen in carbon nanotube CNT growth during plasma enhanced chemical vapor deposition (PECVD) process.

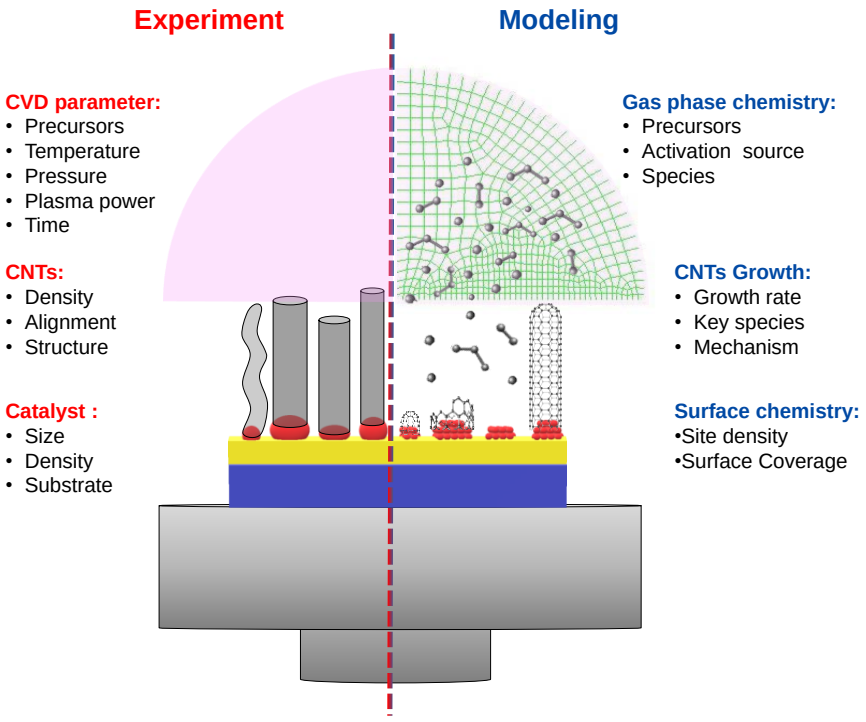

FIG 1.17 Experimental and modeling approach for studying carbon nanotubes growth.

An alternative approach has been proposed to better control vertically aligned nanotube growth by using phenomenological models inspired by equivalent electrical circuits providing qualitative insights underlying the main features of the nanotube growth mechanism. These models hypothesize that carbon precursor C_xH_y (or $C_xH_yO_z$ if oxygen is added) is subjected to reaction-diffusion in the boundary layer close to the metal catalyst surface as schematically illustrated in Figure 1.18. Since nanotube growth is a highly dynamic process, growth rate can be limited by several processes including: (i) diffusion and mass transfer in the gas or plasma phase, (ii) surface reactions on the catalyst surface, (iii) carbon diffusion through the catalyst bulk or over the catalyst surface. It was generally assumed that carbon diffusion through or over the catalyst nanoparticle was the rate limiting step [55, 148-152], but experimental observations based on the effect of factors such as the type of feedstock and the molecular dissociation render not consistent a solely solid-state diffusion-limited process, [153]. However, this kind of understanding is not comprehensive enough.

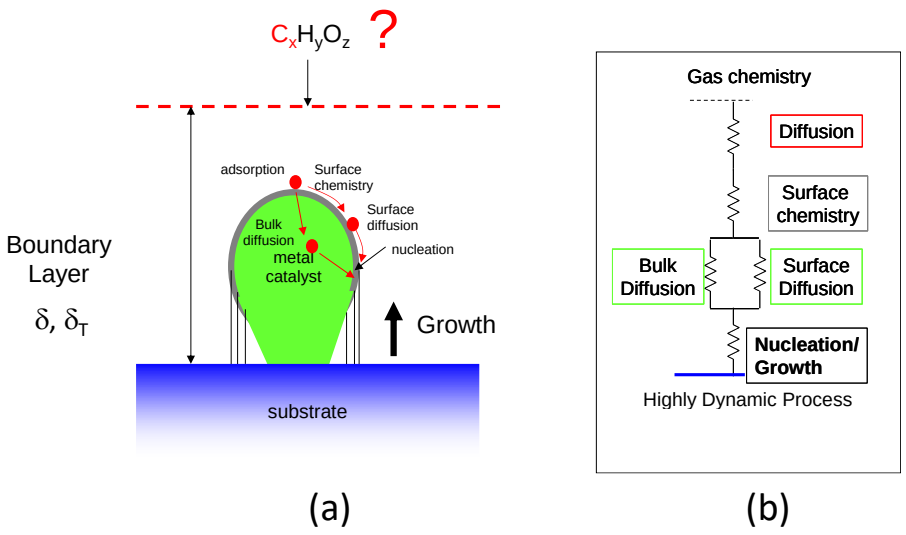

FIG. 1.18 (a) Phenomenological modeling of the main rate-limiting processes during CNT growth in the vicinity of metal catalyst nanoparticle located in the momentum and thermal boundary layers of thicknesses δ and $δ_T$ respectively. (b) The electrical equivalent circuit model of the transport of growth precursors from the bulk to the catalyst particle with resistances in either series or parallel.

In the nanotube context, computational fluid modeling are particularly attractive due their simplicity and minor computational effort as compared to atomistic simulations [30]. Puretzky *et al.* [13] and Naha and Puri [154] both developed kinetic models that describes the catalytic conversion of C_2H_2 into VACNTs in CVD, however the models disregarded the gas phase chemistry considering only the chemisorption of the inlet molecule C_2H_2 on the catalytic nanoparticle, surface and bulk diffusion of carbon atoms in the nanoparticle allowed to elucidate the temperature dependence of the growth rates and the terminal lengths and Naha and Puri model predicts the formation of longer CNTs with increasing C_2H_2 partial pressure [154], however this was rather interpreted from a catalyst size/carbon atom diffusion point of view. More sophisticated models have been developed incorporating mass and heat transfer equations as well as gas phase chemistry and surface chemistry in order to bridge the gap between the molecular scale and the macroscopic scale of the reactor, Grujicic *et al.* simulated the deposition of CNTs from the conversion of CH4 and H2 gas mixture in the presence of cobalt catalyst at the reactor length scale [155], the model included 13 species, 34 gas-phase reaction and 19 surface reaction, their optimization of the model aimed to maximize the deposition of carbon nanotubes and minimize the deposition of amorphous carbon. Lysaght and Chiu studied the

effect of temperature, CH4/H2 ratio as well as site density in a horizontal CVD reactor [156, 157], with only 7 species and 14 total reaction their model indicated that active site specification is a crucial parameter in deposition rate calculation and elucidated the role of H radicals adsorption and desorption in CNT growth. A more detailed modeling study was conducted by Hosseini *et al.* on the composition of the gas phase chemistry of CH_4/H_2 mixtures [158], with 13 species and 60 reversible reactions , They found that increasing the temperature and CH4 flow rate increase the CNTs growth rate due to the availability of more carbon molecules resulted from the dissociation of the gas mixture, except at high temperatures 800°C under insufficient H_2 flow rate, thereby, underlining the importance of balance between C and H atoms ratio in CNTs CVD synthesis. However, while many reports in experiments as well as modeling have investigated the effect of different parameters in CVD synthesis of CNTs, no modeling study to our knowledge has been conducted to identify the role of oxygen enhancers in gas composition as well as on the nanoparticle surface.

The nucleation and the growth mechanisms which can greatly influence the structure of carbon nanotubes, remain largely unexplored under oxygen plasma composition. This work contributes in quantitative and qualitative analysis of CNTs growth in order to understand the role of oxygenated species in plasma gas phase chemistry as well as in surface chemistry on cobalt nanoparticles.

1.8 Conclusions

In laboratory or industry, CVD growth systems have been long time developed by empirical ways. This is very clearly illustrated by Futaba's approach shown in Figure 1.9 of this state of the art. If this treatment has produced interesting results, it begins to reach some limits inherent to the increasing complexity of CVD systems in terms of reactor geometry or operating conditions. In contrast, theoretical analysis and modeling offer a more rational approach with new possibilities to better understand growth mechanisms with a particular emphasis on the analysis of chemical and physical phenomena in both the volume and the surface. This will constitute the roadmap that we have set to improve nanotube growth and filling and to provide a comprehensive understanding of these complex processes in the following chapters of this thesis. In Chapter II, we will investigate a range of parameters affecting separately and combined, the dewetting of ultrathin cobalt films and formed nanoparticles properties. The effect of the diffusion barrier, plasma treatment as well the relationship between initial film thickness and dewetted nanoparticles diameter and density will be hence addressed from

structural and magnetic point of views, indeed our main motivation for the choice of cobalt catalyst is to study in Chapter IV the magnetic properties of multi-walled carbon nanotubes (MWCNT) with encapsulated Co nanoparticles, along with magneto-optical properties of dewetted nanoparticles. The mechanical properties of VACNT assemblies will also be investigated. In Chapter III, we will study the quantitative understanding of the gas-phase chemistry as well as the nanotube growth mechanism using modeling approaches.

References

1. Rao, R., et al., *Carbon Nanotubes and Related Nanomaterials: Critical Advances and Challenges for Synthesis toward Mainstream Commercial Applications.* ACS Nano, 2018. **12**(12): p. 11756-11784.
2. Yuji Awano, S.S., Mizuhisa Nihei, Tadashi Sakai, Yutaka Ohno, and Takashi Mizutani, Fellow IEEE, *Carbon Nanotubes for VLSI: Interconnect and Transistor Applications.* 2010.

3. Titus, E., Krishna, R., Grácio, J., Singh, M., Ferreira, A. L., & Dias, R. G. , *Carbon nanotube based magnetic tunnel junctions (MTJs) for spintronics application. In Electronic Properties of Carbon Nanotubes.* IntechOpen, 2011.
4. V.V. Barkaline, A.S.C., P.V. Zhuchek, , *Acoustic properties of carbon nanotube arrays as chemical sensor elements.* Review of Advanced Materials Sciences, 2009. **20**: p. 28-36.
5. Giubileo, F., et al., *Field Emission from Carbon Nanostructures.* Applied Sciences, 2018. **8**(4): p. 526.
6. Jonge, N.d., et al., *High brightness electron beam from a multi-walled carbon nanotube.* Nature, 2002. **420**: p. 393-395.
7. Sun, Y., et al., *Field emission behavior of carbon nanotube field emitters after high temperature thermal annealing.* AIP Advances, 2014. **4**(7): p. 077110.
8. Frank, S., et al., *Carbon nanotube quantum resistors.* science, 1998. **280**(5370): p. 1744-6.
9. Kumar, A., K. Sharma, and A.R. Dixit, *Carbon nanotube- and graphene-reinforced multiphase polymeric composites: review on their properties and applications.* Journal of Materials Science, 2019. **55**(7): p. 2682-2724.
10. Imani Yengejeh, S., S.A. Kazemi, and A. Öchsner, *Carbon nanotubes as reinforcement in composites: A review of the analytical, numerical and experimental approaches.* Computational Materials Science, 2017. **136**: p. 85-101.
11. Liakakos, N., et al., *Solution epitaxial growth of cobalt nanowires on crystalline substrates for data storage densities beyond 1 Tbit/in2.* Nano Lett, 2014. **14**(6): p. 3481-6.
12. Rousseau, O., et al., *Elaboration and Magnetic Properties of Cobalt-Palladium Magnetic Nanowires Encapsulated in Carbon Nanotubes.* Journal of Surface Engineered Materials and Advanced Technology, 2017. **07**(01): p. 1-12.
13. Puretzky, A.A., et al., *In situ measurements and modeling of carbon nanotube array growth kinetics during chemical vapor deposition.* Applied Physics A, 2005. **81**(2): p. 223-240.
14. Takayuki Iwasaki, G.Z., Takumi Aikawa, Tsuyoshi Yoshida, and Hiroshi Kawarada, *Direct Evidence for Root Growth of Vertically Aligned Single-Walled Carbon Nanotubes byMicrowave Plasma Chemical Vapor Deposition.* J. Phys. Chem. B, 2005. **109**(42): p. 19556–19559.
15. Andalouci, A., et al., *Low frequency vibrations observed on assemblies of vertical multiwall carbon nanotubes by Brillouin light scattering: determination of the Young modulus.* Phys Condens Matter, 2020. **32**(45): p. 455701.
16. Wong, E.W., Sheehan, P. E., & Lieber, C. M., *Nanobeam mechanics: elasticity, strength, and toughness of nanorods and nanotubes. .* science, , 1997. **277**(5334): p. 1971-1975.
17. Salvetat, J.P., Bonard, J. M., Thomson, N. H., Kulik, A. J., Forro, L., Benoit, W., & Zuppiroli, L. (1999). *Mechanical properties of carbon nanotubes.* Applied Physics A, , 1999. **69**(3): p. 255-260.
18. Hall, A.R., et al., *Experimental measurement of single-wall carbon nanotube torsional properties.* Phys Rev Lett, 2006. **96**(25): p. 256102.
19. Kallesoe, C., et al., *3D mechanical measurements with an atomic force microscope on 1D structures.* Rev Sci Instrum, 2012. **83**(2): p. 023704.
20. Wang, L., Z. Zhang, and X. Han, *In situ experimental mechanics of nanomaterials at the atomic scale.* NPG Asia Materials, 2013. **5**(2): p. e40-e40.
21. A. Sakharova, N., et al., *Developments in the evaluation of elastic properties of carbon nanotubes and their heterojunctions by numerical simulation.* AIMS Materials Science, 2017. **4**(3): p. 706-737.
22. Rafiee, R. and R.M. Moghadam, *On the modeling of carbon nanotubes: A critical review.* Composites Part B: Engineering, 2014. **56**: p. 435-449.
23. Imani Yengejeh, S., S.A. Kazemi, and A. Öchsner, *Advances in mechanical analysis of structurally and atomically modified carbon nanotubes and degenerated nanostructures: A review.* Composites Part B: Engineering, 2016. **86**: p. 95-107.

24. Journet, C., Maser, W. K., Bernier, P., Loiseau, A., de La Chapelle, M. L., Lefrant, D. S., ... & Fischer, J. E., *Large-scale production of single-walled carbon nanotubes by the electric-arc technique.* nature, 1997. **388**(6644): p. 756-758.
25. Arora, N. and N.N. Sharma, *Arc discharge synthesis of carbon nanotubes: Comprehensive review.* Diamond and Related Materials, 2014. **50**: p. 135-150.
26. Colasanti, S., *Modeling and simulation of carbon nanotubes networks: Toward a multiscale approach* Doctoral dissertation, Technische Universität München, 2016.
27. Das, R., et al., *Can We Optimize Arc Discharge and Laser Ablation for Well-Controlled Carbon Nanotube Synthesis?* Nanoscale Res Lett, 2016. **11**(1): p. 510.
28. Chen, G., et al., *A sweet spot for highly efficient growth of vertically aligned single-walled carbon nanotube forests enabling their unique structures and properties.* Nanoscale, 2016. **8**(1): p. 162-71.
29. Eun Ju Bae, Y.-S.M., Donghun Kang, Ju-Hye Ko, Wanjun Park, *Low-Temperature Growth of Single-Walled Carbon Nanotubes by Plasma Enhanced Chemical Vapor Deposition.* Chemistry of Materials, 2005. **17**(20): p. 5141-5145.
30. Neyts, E.C., *PECVD growth of carbon nanotubes: From experiment to simulation.* Journal of Vacuum Science & Technology B, Nanotechnology and Microelectronics: Materials, Processing, Measurement, and Phenomena, 2012. **30**(3): p. 030803.
31. Denysenko, I., *Ion-assisted precursor dissociation and surface diffusion: Enabling rapid, low-temperature growth of carbon nanofibers.* Applied Physics Letters, 2007. **90**(25).
32. Neyts, E.C., et al., *Plasma Catalysis: Synergistic Effects at the Nanoscale.* Chem Rev, 2015. **115**(24): p. 13408-46.
33. Hofmann, S., et al., *Effects of catalyst film thickness on plasma-enhanced carbon nanotube growth.* Journal of Applied Physics, 2005. **98**(3): p. 034308.
34. Benkouider, A., et al., *Ordered arrays of Au catalysts by FIB assisted heterogeneous dewetting.* Nanotechnology, 2015. **26**(50): p. 505602.
35. Felici, R., et al., *In situ study of the dewetting behavior of Ni-films on oxidized Si(001) by GISAXS.* Surface Science, 2007. **601**(18): p. 4526-4530.
36. S Hajjar, G.G., L Josien, Jean-Luc Bubendorff, D Berling, A Mehdaoui,C Pirri, T Maroutian, C Renard, D Bouchier, et al., *Morphology and composition of Au catalysts on Ge(111)obtained by thermal dewetting.* Physical Review B, 2011. **84**(12): p. 125325.
37. Boragno, C., et al., *Critical thickness for the agglomeration of thin metal films.* Physical Review B, 2009. **79**(15): p. 155443.
38. Kwon, J.-Y., et al., *Comparison of the agglomeration behavior of Au and Cu films sputter deposited on silicon dioxide.* Journal of Applied Physics, 2003. **93**(6): p. 3270-3278.
39. P. R. Gadkari, A.P.W., R. M. Todi, R. V. Petrova, and K. R. Coffey, *Comparison of the agglomeration behavior of thin metallic films on SiO2.* Vacuum Science & Technology A, 2005. **23**(4): p. 1152-1161.
40. Cechal, J., J. Polcak, and T. Sikola, *Detachment Limited Kinetics of Gold Diffusion through Ultrathin Oxide Layers.* The Journal of Physical Chemistry C, 2014. **118**(31): p. 17549-17555.
41. Shi, W., et al., *Oxygen-promoted catalyst sintering influences number density, alignment, and wall number of vertically aligned carbon nanotubes.* Nanoscale, 2017. **9**(16): p. 5222-5233.
42. Kovalenko, O. and E. Rabkin, *Mechano-stimulated equilibration of gold nanoparticles on sapphire.* Scripta Materialia, 2015. **107**: p. 149-152.
43. Galinski, H., et al., *Agglomeration of Pt thin films on dielectric substrates.* Physical Review B, 2010. **82**(23): p. 235415.
44. Ye, J., *Fabrication of ordered arrays of micro- and nanoscale features with control over their shape and size via templated solid-state dewetting.* Sci Rep, 2015. **5**: p. 9823.
45. Niekiel, F., et al., *The process of solid-state dewetting of Au thin films studied by in situ scanning transmission electron microscopy.* Acta Materialia, 2015. **90**: p. 118-132.
46. Yang, J., et al., *Growth of high-density carbon nanotube forests on conductive TiSiN supports.* Applied Physics Letters, 2015. **106**(8): p. 083108.

47. Na, N., et al., *Simple and engineered process yielding carbon nanotube arrays with 1.2 × 10 13 cm −2 wall density on conductive underlayer at 400 °C.* Carbon, 2015. **81**: p. 773-781.
48. Yang, J., et al., *Comparison of carbon nanotube forest growth using AlSi, TiSiN, and TiN as conductive catalyst supports.* physica status solidi (b), 2014. **251**(12): p. 2389-2393.
49. Zhang, C., et al., *Growth of vertically-aligned carbon nanotube forests on conductive cobalt disilicide support.* Journal of Applied Physics, 2010. **108**(2): p. 024311.
50. Robertson, J., et al., *Chemical vapor deposition of carbon nanotube forests.* physica status solidi (b), 2012. **249**(12): p. 2315-2322.
51. Shah, K.A. and B.A. Tali, *Synthesis of carbon nanotubes by catalytic chemical vapour deposition: A review on carbon sources, catalysts and substrates.* Materials Science in Semiconductor Processing, 2016. **41**: p. 67-82.
52. Pinilla, J.L., et al., *High temperature iron-based catalysts for hydrogen and nanostructured carbon production by methane decomposition.* International Journal of Hydrogen Energy, 2011. **36**(13): p. 7832-7843.
53. Borghei, M., et al., *Kinetics of methane decomposition to COx-free hydrogen and carbon nanofiber over Ni–Cu/MgO catalyst.* International Journal of Hydrogen Energy, 2010. **35**(17): p. 9479-9488.
54. Hinkov, I., et al., *Microwave Plasma Enhanced Chemical Vapor Deposition of Carbon Nanotubes.* Journal of Surface Engineered Materials and Advanced Technology, 2014. **04**(04): p. 196-209.
55. Hofmann, S., Ducati, C., Robertson, J., & Kleinsorge, B., *Low-temperature growth of carbon nanotubes by plasma-enhanced chemical vapor deposition.* Applied Physics Letters, 2003. **83**(1): p. 135-137.
56. Kenji Hata, D.N.F., Kohei Mizuno, Tatsunori Namai,Motoo Yumura, Sumio Iijima, *Water-Assisted Highly Efficient Synthesis of Impurity-Free Single-Walled Carbon Nanotubes.* science, 2004. **306**(5700): p. 1362-1364.
57. Futaba, D.N., et al., *General rules governing the highly efficient growth of carbon nanotubes.* Adv Mater, 2009. **21**(47): p. 4811-5.
58. Kohno, S.M.R.K.Y.M.S.C.M., *Low-temperature synthesis of high-purity single-walled carbon nanotubes from alcohol.* Chemical Physics Letters, 2002. **360**(3-4): p. 229-234.
59. Hye Ryung Byon, H.L., Hyun Jae Song, and Hee Cheul Choi, *A Synthesis of High Purity Single-Walled Carbon Nanotubes from Small Diameters of Cobalt Nanoparticles by Using Oxygen-Assisted Chemical Vapor Deposition Process* Korean Chemical Society, 2007. **28**(11): p. 2056-2060
60. Ho, L., et al., *Hydrogen plasma treatment on catalytic layer and effect of oxygen additions on plasma enhanced chemical vapor deposition of carbon nanotube.* Journal of Alloys and Compounds, 2002. **330–332**: p. 569-573.
61. Zhang, G., et al., *Ultra-high-yield growth of vertical single-walled carbon nanotubes: Hidden roles of hydrogen and oxygen.* Proc Natl Acad Sci U S A, 2005. **102**(45): p. 16141-5.
62. Leslie-Pelecky, D.L. and R.D. Rieke, *Magnetic Properties of Nanostructured Materials.* Chemistry of Materials, 1996. **8**(8): p. 1770–1783.
63. Skomski, R., et al., *Multidomain and incoherent effects in magnetic nanodots.* Journal of Applied Physics, 2004. **95**(11): p. 7022-7024.
64. Fellah, F., et al., *Magnetic properties of ultrafine-grained cobalt samples obtained from consolidated nanopowders.* physica status solidi (a), 2011. **208**(8): p. 1942-1949.
65. Lee, J.S., et al., *Magnetic multi-granule nanoclusters: A model system that exhibits universal size effect of magnetic coercivity.* Sci Rep, 2015. **5**: p. 12135.
66. Lu, A.H., E.L. Salabas, and F. Schuth, *Magnetic nanoparticles: synthesis, protection, functionalization, and application.* Angew Chem Int Ed Engl, 2007. **46**(8): p. 1222-44.
67. Gentili, D., et al., *Applications of dewetting in micro and nanotechnology.* Chem Soc Rev, 2012. **41**(12): p. 4430-43.

68. *Sn particles produced by plasma-induced dewetting and its applications.* Doctoral dissertation, 2016.
69. Dreaden, E.C., et al., *The golden age: gold nanoparticles for biomedicine.* Chem Soc Rev, 2012. **41**(7): p. 2740-79.
70. Cavallini, M., et al., *Additive nanoscale embedding of functional nanoparticles on silicon surface.* Nanoscale, 2010. **2**(10): p. 2069-72.
71. Gu, M., Q. Zhang, and S. Lamon, *Nanomaterials for optical data storage.* Nature Reviews Materials, 2016. **1**(12): p. 16070.
72. Massimiliano Cavallini, F.B., Salvador Léon, Francesco Zerbetto, Giovanni Bottari, David A. Leigh, *Information Storage Using Supramolecular Surface Patterns.* Science, 2003. **299**(5606): p. 531.
73. José Dintinger, S.M., Carsten Rockstuhl, and Toralf Scharf, *A bottom-up approach to fabricate optical metamaterials by self-assembled metallic nanoparticles.* Optical Materials Express 2012. **2**(3): p. 269-278.
74. J.Y. Cheng, C.A.R., E.L. Thomas, H.I. Smith, R.G.H. Lammertink, G.J. Vancso *Magnetic properties of large-area particle arrays fabricated using block copolymer lithography.* IEEE Transactions on Magnetics, 2002. **38**(5): p. 2541 - 2543.
75. Gentili, D., et al., *Self-organization of functional materials in confinement.* Acc Chem Res, 2014. **47**(8): p. 2692-9.
76. Altomare, M., N.T. Nguyen, and P. Schmuki, *Templated dewetting designing entirely self organized platforms for photocatalysis.* Chem. Sci., 2016, 7, , 2016. **7**(12): p. 6865-6886.
77. Tiggelaar, R.M., et al., *Stability of thin platinum films implemented in high-temperature microdevices.* Sensors and Actuators A: Physical, 2009. **152**(1): p. 39-47.
78. Alburquenque, D., et al., *Dewetting of Co thin films obtained by atomic layer deposition due to the thermal reduction process.* MRS Communications, 2017. **7**(04): p. 848-853.
79. Thompson, C.V., *Solid-State Dewetting of Thin Films.* Annual Review of Materials Research, 2012. **42**(1): p. 399-434.
80. Seguini, G., et al., *Solid-state dewetting of ultra-thin Au films on SiO(2) and HfO(2).* Nanotechnology, 2014. **25**(49): p. 495603.
81. Araujo, A., et al., *Influence of the Substrate on the Morphology of Self-Assembled Silver Nanoparticles by Rapid Thermal Annealing.* The Journal of Physical Chemistry C, 2016. **120**(32): p. 18235-18242.
82. Strobel, S., et al., *Sub-10 nm structures on silicon by thermal dewetting of platinum.* Nanotechnology, 2010. **21**(50): p. 505301.
83. Choe, H.J., et al., *Sn microparticles made by plasma-induced dewetting.* Thin Solid Films, 2016. **620**: p. 165-169.
84. Oh, Y.J., et al., *Cobalt nanoparticle arrays made by templated solid-state dewetting.* Small, 2009. **5**(7): p. 860-5.
85. Henley, S.J., J.D. Carey, and S.R.P. Silva, *Pulsed-laser-induced nanoscale island formation in thin metal-on-oxide films.* Physical Review B, 2005. **72**(19): p. 195408.
86. Bischof, J., et al., *Dewetting Modes of Thin Metallic Films: Nucleation of Holes and Spinodal Dewetting.* Physical Review Letters, 1996. **77**(8): p. 1536.
87. Hu, X., D.G. Cahill, and R.S. Averback, *Nanoscale pattern formation in Pt thin films due to ion-beam-induced dewetting.* Applied Physics Letters, 2000. **76**(22): p. 3215-3217.
88. Tanaka, T., J. Lee, and P.R. Scheller, *Interfacial Free Energy and Wettability. In : Treatise on Process Metallurgy.* Elsevier, 2014: p. 61-77.
89. Carey, J.D., L.L. Ong, and S.R.P. Silva, *Formation of low-temperature self-organized nanoscale nickel metal islands.* Nanotechnology, 2003. **14**(11): p. 1223.
90. Shawat, E., et al., *What is below the support layer affects carbon nanotube growth: an iron catalyst reservoir yields taller nanotube carpets.* Nanoscale, 2014. **6**(3): p. 1545-51.
91. Thiele, U., M.G. Velarde, and K. Neuffer, *Dewetting: film rupture by nucleation in the spinodal regime.* Phys Rev Lett, 2001. **87**(1): p. 016104.

92. Nuryadi, R., et al., *Thermal agglomeration of single-crystalline Si layer on buried SiO2 in ultrahigh vacuum.* Journal of Vacuum Science & Technology B: Microelectronics and Nanometer Structures, 2002. **20**(1): p. 167.
93. Kwon, S.H., et al., *Synthesis of copper nanoparticles by solid-state plasma-induced dewetting.* Nanotechnology, 2011. **22**(24): p. 245608.
94. Kojima, Y. and T. Kato, *Nanoparticle formation in Au thin films by electron-beam-induced dewetting.* Nanotechnology, 2008. **19**(25): p. 255605.
95. Reiter, G., *Dewetting of thin polymer films.* Phys Rev Lett, 1992. **68**(1): p. 75-78.
96. Mullins, W.W., *Theory of Thermal Grooving.* Journal of Applied Physics, 1957. **28**(3): p. 333-339.
97. Srolovitz, D.J. and S.A. Safran, *Capillary instabilities in thin films. II. Kinetics.* Journal of Applied Physics, 1986. **60**(1): p. 255-260.
98. Zhong, G., et al., *Growth of Ultrahigh Density Single-Walled Carbon Nanotube Forests by Improved Catalyst Design.* ACS Nano, 2012. **6**(4): p. 2893 – 2903.
99. Maeda, F., et al., *Surface Reactions of Co on SiO2 thin layer/Si substrate Studied by LEEM and PEEM.* e-Journal of Surface Science and Nanotechnology, 2006. **4**: p. 155-160.
100. Joshua Pelleg and S. Zalkind , L.Z., B. M. Ditchek, *Silicide formation in the Co-Si system by rapid thermal annealing.* Thin Solid Films, 1994. **249**(1): p. 126-131.
101. Hasegawa, K. and S. Noda, *Moderating carbon supply and suppressing Ostwald ripening of catalyst particles to produce 4.5-mm-tall single-walled carbon nanotube forests.* Carbon, 2011. **49**(13): p. 4497-4504.
102. Kim, S.M., et al., *Evolution in Catalyst Morphology Leads to Carbon Nanotube Growth Termination.* The Journal of Physical Chemistry Letters, 2009. **1**(6): p. 918-922.
103. Meng, X., et al., *Microstructure analysis of ion beam-induced surface nanostructuring of thin Au film deposited on SiO2 glass.* Journal of Materials Science, 2012. **48**(2): p. 920-928.
104. Naik, J.P., et al., *Instabilities in Focused Ion Beam-patterned Au nanowires.* Microelectronic Engineering, 2011. **88**(9): p. 2840-2843.
105. Fowlkes, J.D., et al., *Self-assembly versus directed assembly of nanoparticles via pulsed laser induced dewetting of patterned metal films.* Nano Lett, 2011. **11**(6): p. 2478-85.
106. Ruffino, F., et al., *Formation and Evolution of Nanoscale Metal Structures on ITO Surface by Nanosecond Laser Irradiations of Thin Au and Ag Films.* Science of Advanced Materials, 2012. **4**(7): p. 708-718.
107. Kwon, S.H., et al., *Mechanism of Solid-State Plasma-Induced Dewetting for Formation of Copper and Gold Nanoparticles.* Journal of Nanoscience and Nanotechnology, 2013. **13**(9): p. 6109-6114.
108. Kwon, S.-H., et al., *Control of Size Uniformity of Cu Nanoparticle Array Produced by Plasma-Induced Dewetting.* Journal of Nanoscience and Nanotechnology, 2015. **15**(3): p. 2542-2546.
109. Zeng, H., et al., *Structure and magnetic properties of ferromagnetic nanowires in self-assembled arrays.* Physical Review B, 2002. **65**(13).
110. Ren, Y., et al., *The effect of structure on magnetic properties of Co nanowire arrays.* Journal of Magnetism and Magnetic Materials, 2009. **321**(3): p. 226-230.
111. Zagorskiy, D.L., et al., *Structure and Magnetic Properties of Nanowires of Iron Group Metals Produced by Matrix Synthesis.* Physics of the Solid State, 2018. **60**(11): p. 2115-2126.
112. Ebels, U., et al., *Ferromagnetic resonance studies of Ni nanowire arrays.* Physical Review B, 2001. **64**(14).
113. Gao, X., et al., *High-Density Periodically Ordered Magnetic Cobalt Ferrite Nanodot Arrays by Template-Assisted Pulsed Laser Deposition.* Advanced Functional Materials, 2009. **19**(21): p. 3450-3455.
114. Fellah, F., et al., *Magnetic properties of ultrafine-grained cobalt samples obtained from consolidated nanopowders.* physica status solidi (a), 2011. **208**(8): p. 1942-1949.

115. Guslienko, K.Y. and A.N. Slavin, *Magnetostatic Green's functions for the description of spin waves in finite rectangular magnetic dots and stripes.* Journal of Magnetism and Magnetic Materials, 2011. **323**(18-19): p. 2418-2424.
116. Chu, H., S. Yun, and H. Lee, *Fabrication of cobalt magnetic nanostructures using atomic force microscope lithography.* J Nanosci Nanotechnol, 2013. **13**(12): p. 8055-8.
117. Hamley, I.W., *Nanostructure fabrication using block copolymers.* Nanotechnology, 2003. **14**(10).
118. Ajayan, P.M., Ebbesen, T. W., Ichihashi, T., Iijima, S., Tanigaki, K. S., & Hiura, H. (1993). . *Opening carbon nanotubes with oxygen and implications for filling. .* Nature, 1993. **362**(6420): p. 522-525.
119. Tsang, S.C., Chen, Y. K., Harris, P. J. F., & Green, M. L. H., *A simple chemical method of opening and filling carbon nanotubes.* Nature, , 1994. **372**(6502): p. 159-162.
120. Ugarte, D., Chatelain, A., & De Heer, W. A., *Nanocapillarity and chemistry in carbon nanotubes.* Science, 1996. **274**(5294): p. 1897-1899.
121. Qiang, Y., et al., *High-Efficiency Ion Enrichment inside Ultra-Short Carbon Nanotubes.* Nanomaterials (Basel), 2022. **12**(19).
122. Smith, B.W., Monthioux, M., & Luzzi, D. E., *Carbon nanotube encapsulated fullerenes: a unique class of hybrid materials.* Chemical Physics Letters, 1999. **315**(1-2): p. 31-36.
123. Fujimori, T., et al., *Conducting linear chains of sulphur inside carbon nanotubes.* Nat Commun, 2013. **4**: p. 2162.
124. T. Fujimori, R.B.D.S., T. Hayashi, M. Endo, K. Kaneko, D. Tománek, , *Formation and properties of selenium double-helices inside double-wall carbon nanotubes: experiment and theory.* ACS nano, 2013. **7**: p. 5607-5613.
125. Brown, G., et al., *High yield incorporation and washing properties of halides incorporated into single walled carbon nanotubes.* Applied Physics A: Materials Science & Processing, 2003. **76**(4): p. 457-462.
126. Dujardin, E., Ebbesen, T. W., Hiura, H., & Tanigaki, K. , *Capillarity and wetting of carbon nanotubes. .* Science, 1994. **265**(5180): p. 1850-1852.
127. Ajayan, P.M., *Capillarity-induced filling of carbon nanotubes. Nature.* 361, 1993. **6410**(333-334).
128. Chen, W., Pan, X., Willinger, M. G., Su, D. S., & Bao, X. , *Facile autoreduction of iron oxide/carbon nanotube encapsulates. .* Journal of the American Chemical Society, , 2006. **128**(10): p. 3136-3137.
129. Baaziz, W., Florea, I., Moldovan, S., Papaefthimiou, V., Zafeiratos, S., Begin-Colin, S., ... & Pham-Huu, C. , *Microscopy investigations of the microstructural change and thermal response of cobalt-based nanoparticles confined inside a carbon nanotube medium. .* Journal of Materials Chemistry A, , 2015. **3**(21): p. 11203-11214.
130. Tabassum, H., et al., *Recent advances in confining metal-based nanoparticles into carbon nanotubes for electrochemical energy conversion and storage devices.* Energy & Environmental Science, 2019. **12**(10): p. 2924-2956.
131. Korneva, G., Ye, H., Gogotsi, Y., Halverson, D., Friedman, G., Bradley, J. C., & Kornev, K. G. , *Carbon nanotubes loaded with magnetic particles. .* Nano letters, 2005. **5**(5): p. 879-884.
132. Guerret-Piecourt, C., Bouar, Y. L., Lolseau, A., & Pascard, H., *Relation between metal electronic structure and morphology of metal compounds inside carbon nanotubes.* Nature, 1994. **372**(6508): p. 761-765.
133. Ajayan, P.M., et al., *Growth of manganese filled carbon nanofibers in the vapor phase.* Phys Rev Lett, 1994. **72**(11): p. 1722-1725.
134. Du, G., Li, W., & Liu, Y. , *Filling carbon nanotubes with Co9S8 nanowires through in situ catalyst transition and extrusion. .* The Journal of Physical Chemistry C, , 2008. **112**(6): p. 1890-1895.

135. Kumari, R., Singh, A., Yadav, B. S., Mohapatra, D. R., Ghosh, A., Guha, P., ... & Tyagi, P. K. , *Filled-carbon nanotubes: 1 D nanomagnets possessing uniaxial magnetization axis and reversal magnetization switching. .* Carbon, , 2017. **119**: p. 464-475.
136. Hayashi, Y., Inoue, H., Hayashi, T., Hada, M., Nishikawa, T., Tokunaga, T., & Amaratunga, G. A. J. , *Intentionally encapsulated metal alloys within vertically aligned multi-walled carbon nanotube array via chemical vapor deposition technique.* IEEE International Conference on Manipulation, Manufacturing and Measurement on the Nanoscale, 2017: p. 357-361.
137. Xiang, R., et al., *Encapsulation, Compensation, and Substitution of Catalyst Particles during Continuous Growth of Carbon Nanotubes.* Adv Mater, 2007. **19**(17): p. 2360-2363.
138. Bao, J., et al., *A Facile Method for Creating an Array of Metal-Filled Carbon Nanotubes.* Adv Mater, 2002. **14**(20): p. 1483-1486.
139. Bao, J., Zhou, Q., Hong, J., & Xu, Z. , *Synthesis and magnetic behavior of an array of nickel-filled carbon nanotubes. .* Applied physics letters, 2002. **81**(24): p. 4592-4594.
140. Kozhuharova, R., et al., *(FexCo1−x)-alloy filled vertically aligned carbon nanotubes grown by thermal chemical vapor deposition.* Journal of Magnetism and Magnetic Materials, 2005. **290-291**: p. 250-253.
141. Elias, A.L., Rodriguez-Manzo, J. A., McCartney, M. R., Golberg, D., Zamudio, A., Baltazar, S. E.,& Terrones, M. , *Production and characterization of single-crystal FeCo nanowires inside carbon nanotubes. .* Nano letters, 2005. **5**(3): p. 467-472.
142. Toh, S., Kaneko, K., Hayashi, Y., Tokunaga, T., & Moon, W. J. , *Microstructure of metal-filled carbon nanotubes.* Journal of electron microscopy, 2004. **53**(2): p. 149-155.
143. Fujita, T., et al., *Cobalt nanorods fully encapsulated in carbon nanotube and magnetization measurements by off-axis electron holography.* Applied Physics Letters, 2006. **88**(24): p. 243118.
144. Hayashi, Y., et al., *Encapsluation of Co and Pd multi-metal nanowires inside multiwalled carbon nanotubes by microwave plasma chemical vapor deposition.* Diamond and Related Materials, 2007. **16**(4-7): p. 1200-1203.
145. Khalilov, U., et al., *Nanoscale mechanisms of CNT growth and etching in plasma envirement.* Journal of Physics D: Applied Physics, 2017. **50**(18): p. 184001.
146. Skukla, B., et al., *Interdependency of Gas Phase Intermediates and Chemical Vapor Deposition Growth of Single Wall Carbon Nanotubes.* Chemistry of Materials, 2010. **22**(22): p. 6035-6043.
147. Chang, J., et al., *Efficient Closed-loop Maximization of Carbon Nanotube Growth Rate using Bayesian Optimization.* Sci Rep, 2020. **10**(1): p. 9040.
148. Klinke, C., J.-M. Bonard, and K. Kern, *Thermodynamic calculations on the catalytic growth of multiwall carbon nanotubes.* Physical Review B, 2005. **71**(3).
149. Chhowalla, M., et al., *Growth process conditions of vertically aligned carbon nanotubes using plasma enhanced chemical vapor deposition.* Journal of Applied Physics, 2001. **90**(10): p. 5308-5317.
150. Hofmann, S., et al., *Surface diffusion: the low activation energy path for nanotube growth.* Phys Rev Lett, 2005. **95**(3): p. 036101.
151. Raty, J.Y., F. Gygi, and G. Galli, *Growth of carbon nanotubes on metal nanoparticles: a microscopic mechanism from ab initio molecular dynamics simulations.* Phys Rev Lett, 2005. **95**(9): p. 096103.
152. Liu, K., et al., *A growth mark method for studying growth mechanism of carbon nanotube arrays.* Carbon, 2005. **43**(14): p. 2850-2856.
153. Wirth, C.T., Zhang, C., Zhong, G., Hofmann, S., & Robertson, J., *Diffusion- and Reaction-Limited Growth of Carbon Nanotube Forests.* ACS nano, 2009. **3**(11): p. 3560-3566.
154. Naha, S. and I.K. Puri, *A model for catalytic growth of carbon nanotubes.* Journal of Physics D: Applied Physics, 2008. **41**(6): p. 065304.
155. Grujicic, M., Cao, G., & Gersten, B., *Optimization of the chemical vapor deposition process for carbon nanotubes fabrication.* Applied surface science 2002. **191**(1-4): p. 223-239.

156. Lysaght, A.C. and W.K. Chiu, *The role of surface species in chemical vapor deposited carbon nanotubes.* Nanotechnology, 2009. **20**(11): p. 115605.
157. Lysaght, A.C. and W.K. Chiu, *Modeling of the carbon nanotube chemical vapor deposition process using methane and acetylene precursor gases.* Nanotechnology, 2008. **19**(16): p. 165607.
158. Hosseini, M.R., N. Jalili, and D.A. Bruce, *A time-dependent multiphysics, multiphase modeling framework for carbon nanotube synthesis using chemical vapor deposition.* AIChE Journal, 2009. **55**(12): p. 3152-3167.

Chapter II:
Dewetting, synthesis and filling of VACNTs

This chapter includes four parts. First, the methods of synthesis carbon nanotubes (CNT) used are presented, including the techniques devoted to diffusion barrier deposition as well as catalytic films deposition, the reactors used for the formation of catalytic nanoparticles and the synthesis of carbon nanotubes, and the characterization tools used to analyze nanomaterials structure and properties. Second, we investigate a range of parameters affecting separately and combined, the dewetting of ultrathin cobalt films into nanoparticles. The effect of the diffusion barrier, film nature, plasma treatment as well the relationship between initial film thickness and dewetted nanoparticles diameter and density are investigated from morphological and thermodynamic point of views. Third, we present the experiments plan elaborated to achieve dense vertically aligned carbon nanotubes. The optimization of the experimental protocol starts with the use of titanium silicon nitride TiSiN diffusion barrier, then by varying the catalyst nature and treatment. The gas composition is also studied by changing the O_2 and H_2 flow rates during nanotube growth, as well as the plasma power in plasma enhanced chemical vapor deposition (PECVD) process. The variation of these parameters ends this section with an optimal protocol developed and customized to achieve high growth rate and dense vertically aligned carbon nanotubes (VACNTs). The fourth and final section of this experimental chapter treats the subject of in-situ filling of VACNTs with a ferromagnetic material. Various thicknesses and Co/Pd ratios configurations of Co/Pd bilayers are tested. . Temperature and plasma power are monitored to enhance the filling state of VACNTs and their vertical alignment. Hence, the optimal parameters are presented in the end of this section and an attempt to explain the mechanisms responsible for the in-situ filling of VACNTs is proposed.

2.1 Materials and Methods

We introduce in this section the different experimental tools used to face the problematics presented in the previous chapter. This includes the deposition techniques dealing with the diffusion barrier layer, the catalytic layer as well as the treatment of the catalyst, and finally the growth and filling of carbon nanotubes. The characterization tools and the chosen features to assess the morphological and the structural state of the synthesized nanomaterials are also presented.

2.1.1 TiSiN deposition by thermionic vacuum arc

Thermionic vacuum arc (TVA) technology is developed at the NILPRP in Bucharest, Romania. This technique was proposed by Lungu *et al.* for highly uniform and nanostructured

surface coatings deposition and described in detail in [1, 2]. Even several techniques were proposed in the past to produce TiSiN including, physical vapor deposition, magnetic sputtering, ion beam assisted deposition and chemical vapor deposition [3], TVA technology remains well adapted to alloy film deposition of high purity and good adhesion, mainly due to the gas free evaporation in vacuum and the high density of the power per unit surface of the deposited metal. As represented in Figure 2.1, an electron beam is generated by a heated cathode composed by a tungsten filament and focused by a Wehnelt cylinder. The electrons are then accelerated to the anode containing a mixture of powder to be evaporated. In the case of TiSiN barriers, 3 moles of Ti and 1 mole of Si_3N_4 were used as anode. For this purpose, Ti powder 325 mesh from Alfa Aesar and Si_3N_4 powder 96+% 30-70 nm APS from Alfa Aesar were furnished by LSPM to NILPRP to deposit the barriers. An electrical arc is then ignited between the cathode and the anode in order to create a strong local heating. As a consequence, Ti and Si_3N_4 evaporation build up to the creation of a plasma in order to ensure the formation of high-density layer of titanium silicon nitride with a stoichiometry of ~ TiSiN and a thickness of ~50 nm.

The prepared samples were then subjected to the deposition of different catalysts by physical vapor deposition described in the next section.

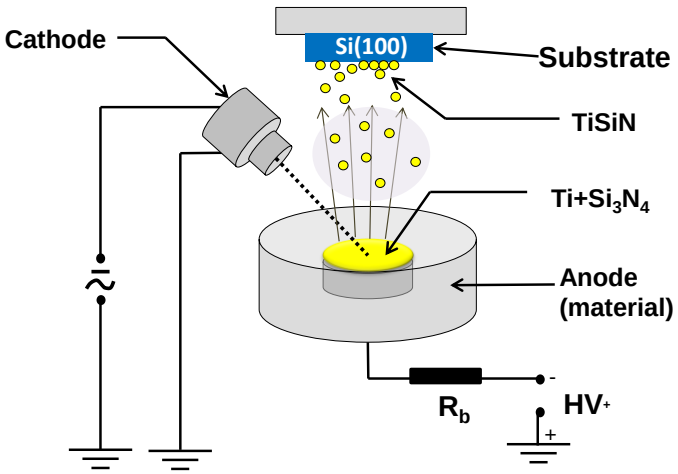

FIG 2.1 Thermionic vacuum arc TVA set-up of NILPRP used for TiSiN deposition.

2.1.2 Catalyst deposition

Physical Vapor Deposition (PVD) was chosen for the deposition of the catalyst layers using the electron beam Plassys MEB 550S type evaporator located in the clean room of the University of Paris Diderot (Laboratory of Quantum Materials and Phenomena, MPQ). This set-up is designed to deposit thin metallic layers of thickness between 1 and 100 nm by the evaporation of a material target (Co, Ni, Pd …) with an electron beam of maximum energy about 10 keV managed by an electric field operating between the anode and the cathode, as represented in Figure 2.2 The electrons flow is focused and controlled by magnetic coils that sweep the entire surface of the target, under high vacuum between 10^{-6} and 10^{-7} mbar, allowing evaporation to take place at lower temperatures around 1050° C. The molten material then vaporizes in the vacuum chamber and condenses on the substrate placed in front of the crucible. The PVD setup ensures better purity of the deposited layers and better control of the thickness of each film that is monitored with quartz balance equipment.

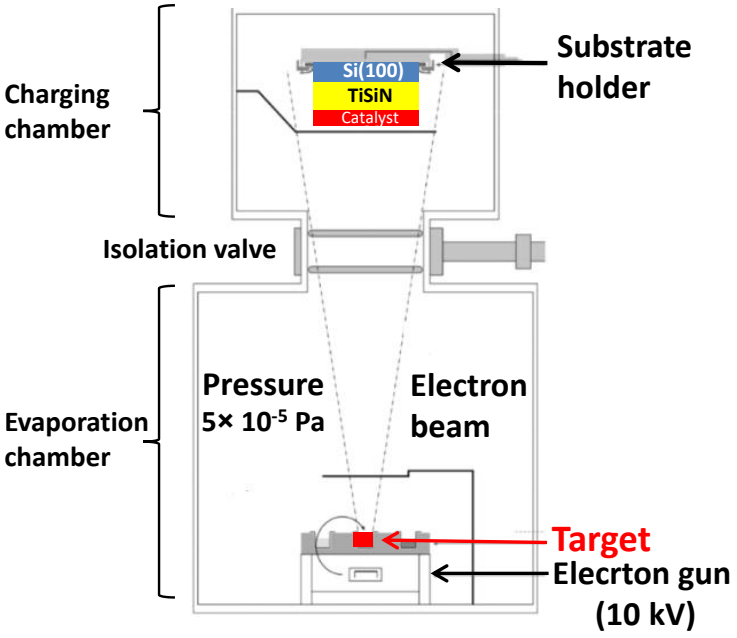

FIG 2.2 Scheme of the electron-beam physical vapor deposition chamber

The catalyst treatment and the VACNTs growth are then performed in the PECVD Bell jar reactor located in the LSPM laboratory shown schematically in Figure 2.3. We also occasionally used the THALES AIXTRON reactor located at TRT at Saclay site.

2.1.3 LSPM microwave PECVD reactor

Figure 2.3 report the different element constituting the PECVD reactor. As shown, it can be divided into 6 parts:

1) Reaction chamber

The growth process is carried out in a quartz bell where a molybdenum support, on which the substrates will be positioned, is placed in the central part. This substrate holder is of cylindrical geometry and moves along the vertical axis of the enclosure, allowing the plasma/substrate distance to be adjusted in order to perfect the hemispherical shape of the visible zone of the plasma and locate it just above the substrate.

2) Wave generator

To generate the plasma, we must create a static wave within the bell delimited by the Faraday cage. The maximum of the energy is then located in a hemispherical region above the substrate holder. The plasma excitation microwave frequency is 2.45 GHz. It is delivered by a SAIREM type microwave generator working in a range of powers varying from 0 to 1200 W. This power is transmitted through a rectangular waveguide fitted with an impedance adapter device. It is then applied by a coaxial metal antenna in a cavity delimited by the Faraday cage with the maximum of the electric field concentrated in the vicinity of the substrate.

3) Control panel

The control panel allows us to measure and regulate the microwave power, pressure and temperature of the substrate. But also, to control the gases flow rates entering the reactor. Gas lines available are methane, oxygen, hydrogen, and argon.

4) Pyrometer

The in-situ measurement of the substrate temperature is preformed using a bi-chromatic infrared pyrometer model IGAQ-10 from IMPAC. The sensor functions use two neighboring short wavelengths so as the degree of emissivity of the substrate will no longer influence the temperature measurement. The temperature measurement ranges between 350 and 1300°C with uncertainty about 0.5% (approximately 5°C to 800°C).

5) Heating system

The substrate holder is independently heated by passing a current through a graphite resistor located inside the molybdenum holder. A thermocouple inserted below the substrate holder allows determining the temperature in the middle of the heater. It should be noted that the radiation effects between the face of the substrate holder exposed to the graphite resistor and the latter can result in temperatures of the face of the molybdenum exposed to the plasma higher than those measured by the thermocouple (see Appendix AI.1 and AI.2). System stability tests were conducted for temperature as high as 1000°C.

6) Pumping system

The reactor is equipped with a primary pump which can reach 10^{-3} mbar, and a turbo molecular pump which can reach 10^{-7} mbar. The pressure is measured through an APG (active Pirani gauge) gauge for pressures between 10^{-3} and 1000 mbar, and an ARM (active reverse magnetron) gauge for pressures below 10^{-3} mbar.

2.1.4 Fundamental processes of plasma generation

The activation of the gas mixture (precursors) begins with the creation of the electromagnetic wave (EW) in the microwave generator. The EW is then carried through the waveguide and applied by the antenna above the substrate holder (see Figure 2.3 b, plasma region). The gas mixture is maintained under a predefined pressure which imposes a controlled particle density in the enclosure (see Figure 2.3 b, bell jar). The power-pressure couple must be precisely controlled to maintain and stabilize a given volume of plasma. The higher the pressure, the more power it will take to maintain the same volume of the visible plasma.

Energy transfer begins when a few free electrons in the gas are accelerated by the electric field of the EW. These electrons heat the gas by vibrational and rotational excitation of molecules when transferring part of their energy by collisions with other species. This causes the molecules to dissociate from the precursors, generating ions and neutral radicals necessary for the desired deposition such as carbon nanotubes growth in the present case.

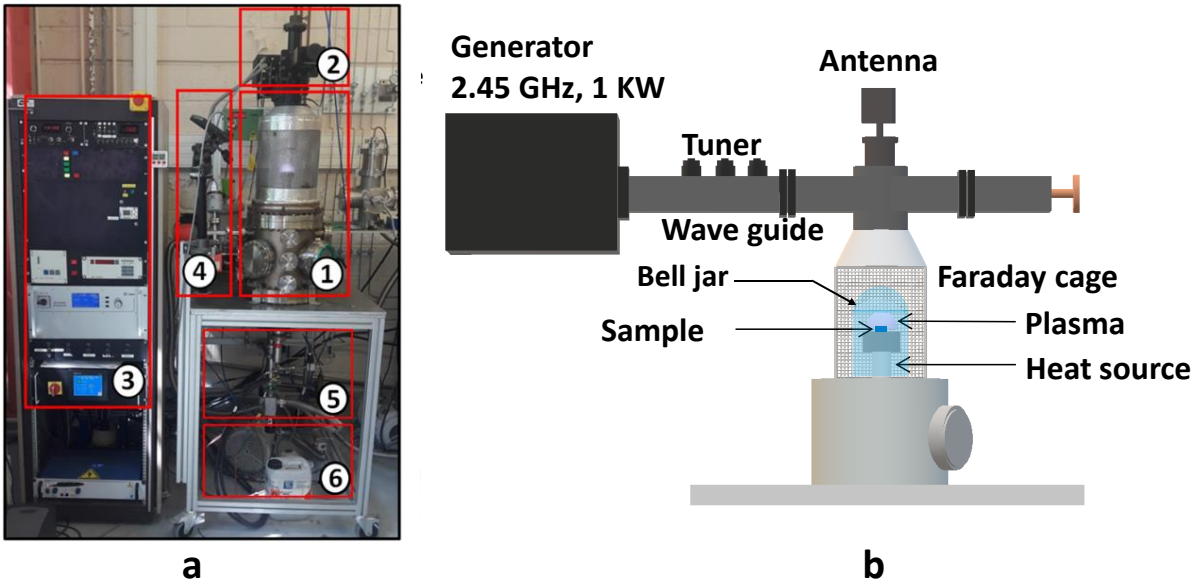

FIG 2.3 a) photo and; b) scheme of the LSPM's PECVD Bell jar reactor.

2.1.5 THALES DC-PECVD Reactor

The PECVD reactor located in Thales group facilities is similar to the LSPM PECVD reactor (Bell jar, graphite heating resistor and pumping system) except the fact that this reactor uses direct current power source. This source is connected to the cathode and the anode to generate a discharge plasma with a frequency of 11 kHz in the vicinity of the substrate holder as represented in Figure 2.4 c, the ionized plasma ensures the dissociation of the inlet gaseous species coming from the showerhead located in the top of the reaction chamber, the cathode on which the substrate are positioned is a graphite resistor that enables the heating of the substrate up to 1000°C , a thermocouple in contact with the substrate holder gives *in situ* measurement of the temperature profile.

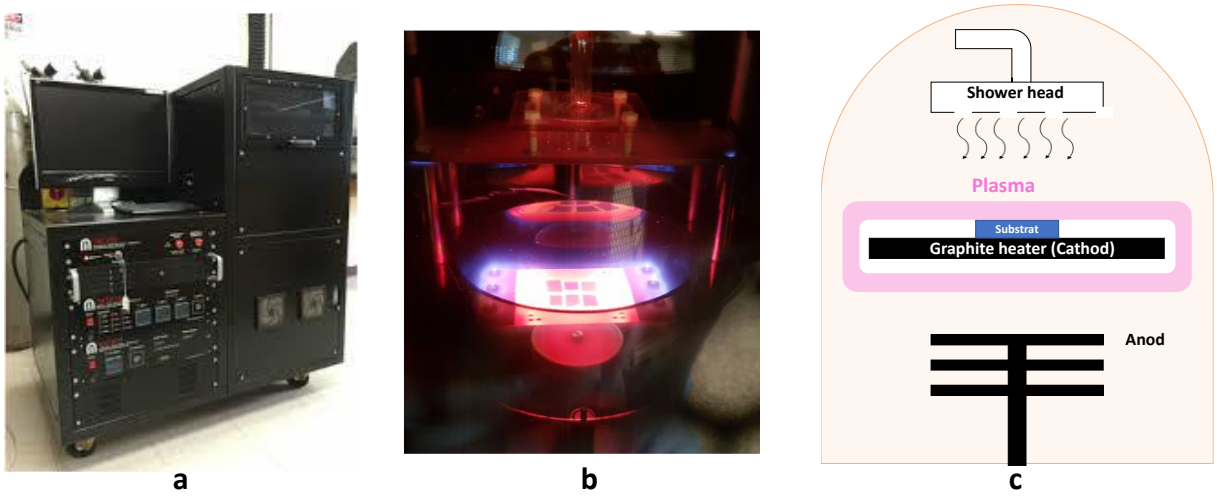

FIG 2.4 a) Photo of the PECVD AIXTRON reactor b) Photo of the reaction chamber c) scheme of the reaction chamber.

2.1.6 Characterization tools

The surface morphology of catalyst nanoparticles as well as the grown of VACNTs was first investigated using scanning electron microscopy (SEM). The SEM images were taken with a high-resolution Zeiss Supra 40 VP microscope with Schottky type field emission gun (W/ZrO filament heated to more than 1500°C). To collect the emitted electrons from the samples surface two main detectors were used. First, a secondary electron detector (SE) that makes possible to access information on the topography of the sample, allowing determination of the nanoparticles sizes and of VACNTs, as well as their shape and the thickness of the formed layers. Second, a backscattered electron detector (AsB) where the images obtained present strong contrasts due to the chemical composition of the visualized object. Indeed, the heavier the object the brighter the contrast is. This mode is useful when assessing the filling state of the VACNTs since the metallic encapsulated material has a larger atomic number.

The structural quality of VACNTs is derived using Raman spectroscopy technique (HR800, HORIBA Jobin-Yvon) operating in confocal mode in air with an excitation wavelength of 632.8 nm. Raman spectra of a given carbon nanotube structure is characterized by three peaks: i) a radial breathing mode (RBM) due the displacement of carbon atoms in the radial direction synchronously, it is a unique mode to few-walled carbon nanotubes that gives an effect similar to "breathing", RBM peak is observed between 100 and 250 cm^{-1} , ii) a disorder mode (D) mainly observed in MWCNTs due to the presence of disordered graphitic materials and located

between 1330-1360 cm^{-1}, iii) a graphitic mode (G) that corresponds to the stretching mode of the carbon - carbon bond in the graphite plane. This mode is observed at around 1580 cm^{-1}.

High resolution transmission electron microscopy HRTEM (JEM-ARM200F) (JEOL (Europe) SAS, Croissy-Sur-Seine, France) and spatially resolved electron energy loss spectroscopy (EELS) (JEOL (Europe) SAS, Croissy-Sur-Seine, France) and energy filtered elemental mapping was used. Quantitative high resolution (HRTEM) analyses were also performed using a JEOL JEMARM200F electron microscope. This microscope combines a cold field emission gun and an aberration corrector on the objective lens) to have clear statistics on walls number, constitutive tube diameters and integrity of the synthesized VACNTs.

2.2 Solid state dewetting

In this section, we investigate a range of parameters affecting separately or combined, the solid state dewetting of thin metallic films to form well-controlled nanoparticles. First, the effect of the diffusion barrier, of plasma treatment as well as the relationship between initial film thickness and dewetted nanoparticles size and density is addressed from investigation of the morphology of ultra-thin cobalt films of 1, 2 and 3 nm thickness. Second, the difference in the dewetting behavior of different metal catalyst (Co, Ni, Pd) is highlighted in the spectrum of surface energy values, Finally, the choice to use cobalt-palladium thin bilayers films is justified by the possible production of cobalt-palladium miscible nanoparticles in the eutectic region with lower melting point than cobalt and palladium thereby enhancing nanotube filling.

2.2.1 Experimental protocol

Substrates of silicon wafers with a (100) polished face were used initially to deposit 50 nm TiSiN layers by thermionic vacuum arc described above. Thin Co films of 1, 2 or 3 nm thickness were then deposited. Subsequently, the samples are introduced (air transfer) in the LSPM PECVD bell jar reactor. The synthesis process starts by sample annealing composed by two consecutive steps: (i) thermal annealing to disintegrate the continuous film onto isolated and randomly organized metal nanoparticles, followed by (ii) plasma annealing for cobalt oxide reduction due to the presence atomic hydrogen, ions, and excited states.

To study the dewetting process, we developed five experimental protocols using several variants of thermal and/or plasma annealing. In all protocols, hydrogen was used to reduce the residual oxides and to structure the cobalt nanoparticles. Due to the complex nature of a real arrangement of grains composing a film, it is difficult to estimate *a priori* the treatment time.

Nevertheless, according to Luber *et al.* [4], no significant changes in film morphology were observed after ~30 min dewetting of nickel films as measured by in situ time resolved reflectometry. Hence, we fixed the final treatment time from 20 min to 30 min. At the end of each experiment, the plasma, the heater and the gas feeding were switched off to cool down the sample. We performed the 5 protocols discussed below for three catalyst thickness (1, 2 or 3 nm) with (silicon (100) covered by ~2 nm of native oxide (SiO_2) or Titanium silicon nitride TiSiN with a thickness of ~50 nm) acting as nanoparticles support. The samples were labelled S_{ij} or T_{ij} where S and T refers to SiO_2 and TiSiN barriers respectively and i and j refers to the cobalt thickness (1, 2 or 3 nm) and protocol number (1, 2, 3, 4 or 5) respectively. All the other parameters are maintained at their standard values as represented in Figure 2.5.

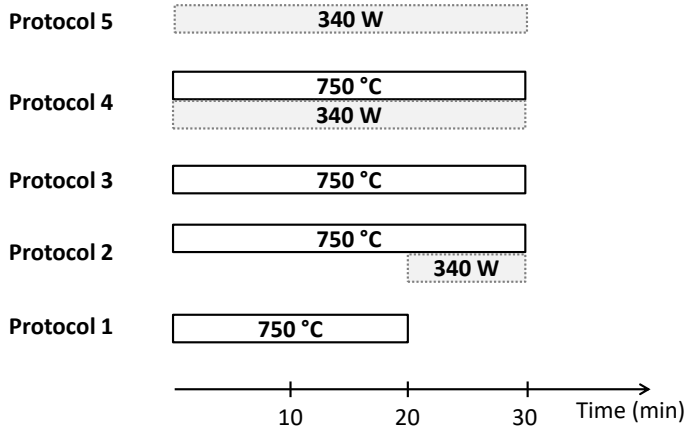

Parameter	Standard value
Substrate temperature	750°C
Pressure	10^3 Pa
Plasma power	340 Watt
H_2 flow rate	90 sccm

FIG 2.5 Five experimental protocols with process conditions used to test cobalt dewetting with combinations of H_2 thermal and/or H_2 plasma that lasted between 20 and 30 minutes.

2.2.2 Substrate nature effect

Figure 2.6 a and Figure 2.6 b show SEM pictures after the dewetting of 3 nm cobalt operated on TiSiN (sample T_{31}) and SiO_2 (sample S_{31}) barriers respectively using protocol 1. Figure 2.6 c and Figure 2.6 d show SEM pictures of the dewetting of 3 nm-thick cobalt layer on TiSiN (sample T_{32}) and SiO_2 (sample S_{32}) barriers respectively using protocol 2. These SEM pictures clearly show a spontaneous breakup of the continuous film into visible isolated nanoparticles.

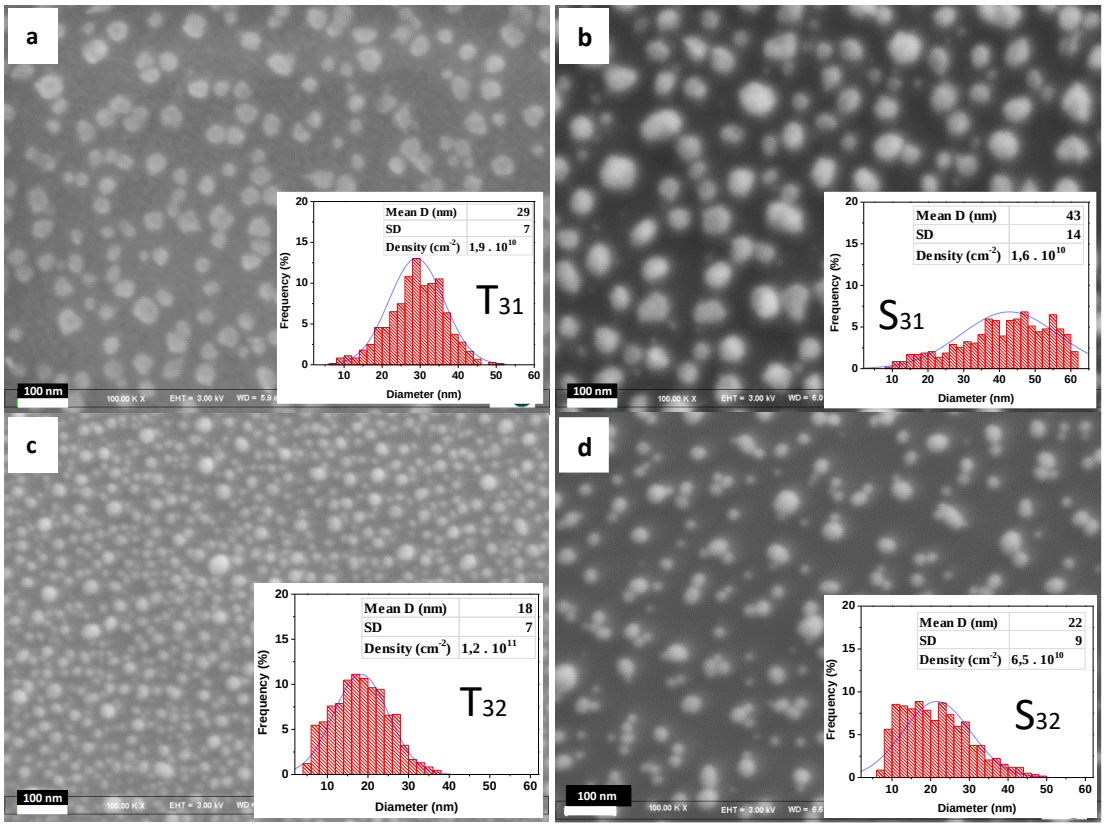

FIG 2.6 Top-view SEM images of cobalt nanoparticles formed by dewetting of 3 nm thickness Co films by applying two protocols from Figure 2.5. Protocol 1: a) Co 3 nm on TiSiN (sampleT_{31}), b) Co 3 nm on SiO_2 (sample S_{31}), and Protocol 2: c) Co 3 nm on TiSiN (sampleT_{32}), d) Co 3 nm on SiO_2 (sampleS_{32}).

Statistical analysis of these images was performed using ImageJ software and based on at least 300 nanoparticles taken in different regions of the sample. This allows the determination of the surface density N(cm^{-2}), and the diameter distribution (nm), as well as the standard deviation SD (nm) as represented in the insert of each SEM picture of Figure 2.6. The analysis of these data clearly shows that as compared to SiO_2, TiSiN barriers improves the surface density by ~25% for thermal annealing of 3 nm Co films, from 1.6×10^{10} cm^{-2} for SiO_2 to 2×10^{10} cm^{-2} for TiSiN, and by ~85% using combined thermal annealing and plasma treatment from 6.5×10^{10} cm^{-2} for SiO_2 to 1.2×10^{11} cm^{-2} for TiSiN. In the same time, mean metal diameter is reduced by ~48% by thermal annealing, from 43 nm SiO_2 to 29 nm for TiSiN, and by ~18% with combined thermal and plasma treatment, from 22 nm for SiO_2 to 18 nm for TiSiN. Smaller standard deviations are also obtained with TiSiN barriers leading to narrower size distributions shifted to small nanoparticle sizes.

As compared to SiO_2, TiSiN layer gives rise to higher nanoparticles surface density, lower particle diameter and higher distribution homogeneity. This is confirmed for both thermal and plasma treatments. To explain this notable difference, we used the respective surface energies of these two barriers. Comparing surface energies of TiSiN, SiO_2 and cobalt, respectively, $\gamma_{TiSiN} = 0.02\, J.m^{-2}$ [5] , $\gamma_{SiO_2} = 0.43\, J.m^{-2}$[6] $and\ \gamma_{Co} = 2.22\, J.m^{-2}$ [7] , one can observe that the surface energy difference $(\gamma_{Co} - \gamma_{TiSiN} = 2.20\, J.m^{-2}) > (\gamma_{Co} - \gamma_{SiO_2} = 1.79\, J.m^{-2})$, meaning that the driving force for dewetting is higher for Co on TiSiN than for Co on SiO_2. The reduction of the standard deviation when TiSiN is used as compared to SiO_2 could be explained by the Ostwald ripening effects on SiO_2. Indeed, this phenomenon increases the density of the large particles at the expense of the smaller ones thereby increasing the standard deviation of the diameter distribution as shown in Figure 2.6. As proposed by Robertson group for dewetting iron caralyst, TiSiN has proven to restrict iron atoms mobility which slows down Ostwald repining effects resulting in a small and narrow catalyst particle size distribution [8].

2.2.3 Plasma effect

From Figure 2.6, circular top view of Co nanoparticles and more homogeneous size distributions are clearly observed when submitting the samples to the Protocol 2 in comparison to the Protocol 1 described in Figure 2.5. This behavior highlights the role of the plasma treatment regardless of the substrate nature. In order to further investigate the plasma effect, three additional protocols with the same treatment time (Protocol 3, Protocol 4 and Protocol 5 as represented in Figure 2.5) were applied to dewett Co on TiSiN. Figure 2.7 shows SEM images and diameter distributions of these samples. From Figure 2.7 a, when the time of thermal annealing was increased to 30 minutes (sample T_{33}), we observe that the surface density drastically decreases, and that the nanoparticles average size is increased; another sign of Ostwald ripening phenomenon that is known to increases with time.

Let's now analyze plasma and thermal treatments in Protocol 4 applied simultaneously for the same time (30 min). SEM results and size distributions in Figure 2.7 b (T_{34}) show homogeneous nanoparticles size distribution. Nevertheless, lower surface density and higher particle size distribution are obtained as compared to Protocol 2, *i.e.* when the plasma is introduced after 20 min of thermal annealing (sample T_{32}).

Finally, using only plasma treatment to dewett 3 nm cobalt films (Protocol 5) has proven to be insufficient to obtain separate islands in 30 minutes as shown in in Figure 2.7 c (T_{35}).

Therefore, statistical analysis was not possible. This could be explained by the weak energy furnished to the cobalt film by atomic hydrogen. Indeed, temperature monitoring on the samples surface displayed a very slow slope of rising temperature that reached 350°C at the end of the treatment.

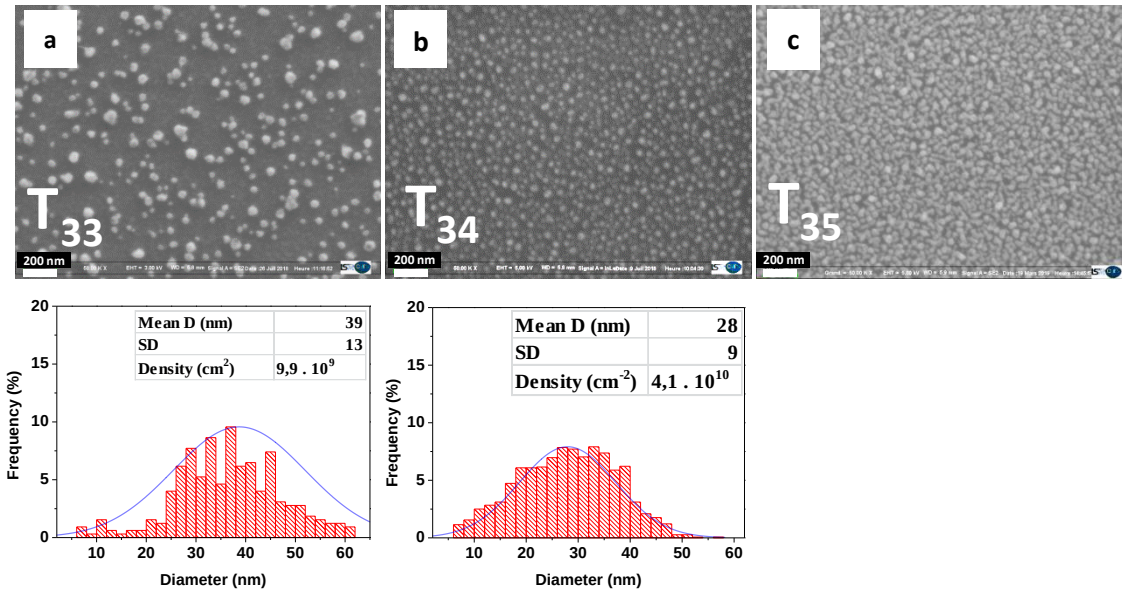

FIG 2.7 SEM images and cobalt nanoparticles diameter distribution formed by dewetting on TiSiN barrier at 750°C after: a) prolonged thermal annealing under hydrogen of 30 min (sample T_{33}) and b) after 30 min of simultaneous thermal annealing and hydrogen plasma treatment (sample T_{34}) and c) after 30 min of hydrogen plasma treatment only (sample T_{35}).

Bogarets *et al*. proposed recently an understanding on the effect of the H radicals present in H_2 plasma on metallic nanoclusters while preforming thermal annealing [9]. These H radicals bind strongly with metallic atoms making them more stable. As a result, the interaction between these nanoparticles becomes very weak and they cannot coalesce.

2.2.4 Thickness effect

In our conditions, Protocol 2 is found to be the best approach to optimize nanoparticles size distribution. We now investigate the effect of the initial film thickness on nanoparticles size distributions. For this purpose, we subjected the 2 nm and 1 nm-thick cobalt films, deposited on TiSiN as well as SiO_2, to the Protocol 2. SEM images and statistical analysis of dewetted nanoparticles are shown in Figure 2.8. For TiSiN substrates, as represented in Figure 2.8 a and Figure 2.8 c, decreasing the cobalt film thickness leads to an increase of the surface density. More precisely, for both films, the density is enhanced by 83% and up to 250%,

respectively, in comparison to the 3 nm-thick film. In addition, nanoparticle average size has been reduced as well to 12 nm and 8 nm for the 2 nm and 1 nm films, respectively. These results also show more homogeneous distributions. For the SiO_2 substrate, the decrease of the average nanoparticle size is less obvious, as shown in Figure 2.8 b and Figure 2.8 d. In addition, the nanoparticles density evolution as a function of thickness shows more or less constant values. These results are summarized in Figure 2.9. These behaviors are discussed within the frame of a model describing the nanoparticle size and density evolution as a function of the thickness, on TiSiN and SiO_2 substrates.

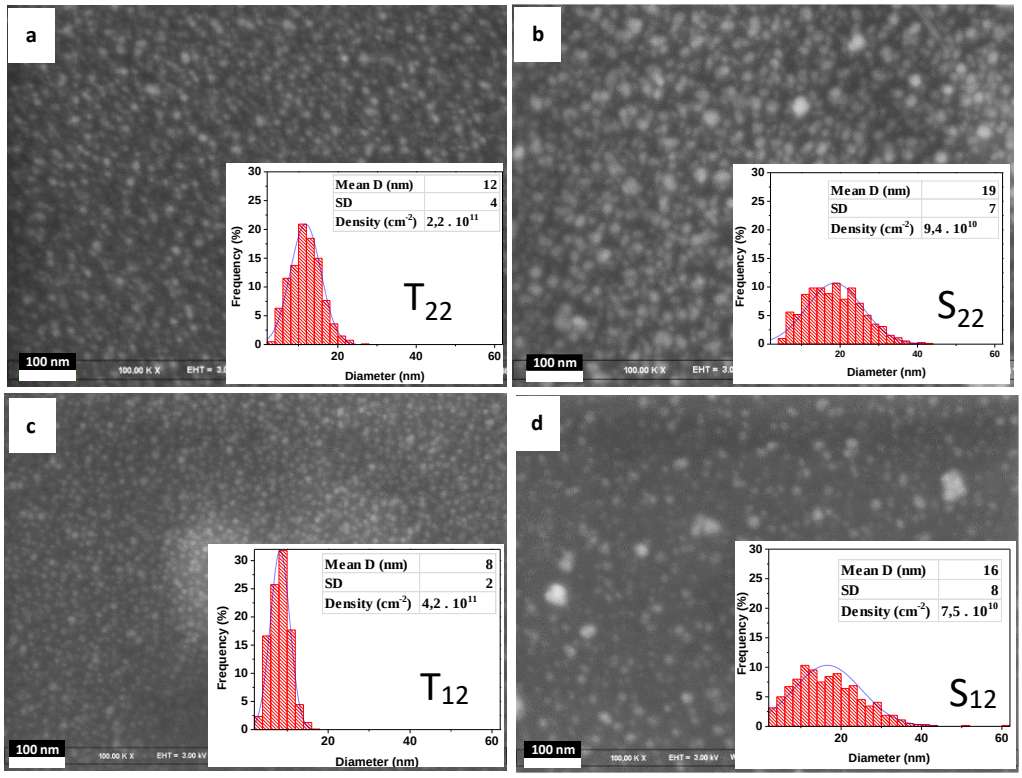

FIG 2.8 SEM images and diameter distribution formed by dewetting using protocol 2 on: a) Co 2 nm on TiSiN (sample T_{22}), b) Co 2 nm on SiO_2 (sample S_{22}), c) Co 1 nm on TiSiN (sampleT_{12}), d) Co 1 nm on SiO_2 (sampleS_{12}).

As shown in Figure 2.9, TiSiN substrates display far better performances in dewetting cobalt films to form smaller, high density and homogeneous nanoparticle arrays. Moreover the relationship between these three parameters are in well agreement with the model of Zhong *et al.*[10]. Using the conservation of the catalyst volume and the interfacial energy of an ideal thin film of thickness h on a substrate, Zhong *et al.* demonstrates that the diameter of the nanoparticle D, produced after dewetting, is determined from the contact angle θ from the two relationships:

$$D = \frac{6h \sin\theta}{1-\cos\theta} \quad \text{for } \theta<90°, \qquad (1)$$

$$D = \frac{6h}{1-\cos\theta} \qquad \text{for } \theta>90°, \tag{2}$$

For the dewetting of high surface energy metals on low surface energy oxides, the contact angle θ~ 90° leading to the relationship D~6h. Hence a typical initial catalyst thickness h of 1 nm would give nanotubes of diameter D ~ 6 nm.

Although this model is limited by kinetics, whereas cobalt nanoparticles on SiO_2 display very weak slope of a linear function with higher values that can be theoretically superior to 15 nm for sub nanometer film thickness ($D \sim 16h$). This disparity in dewetting efficiency between the two substrates is more highlighted by the surface density values. According to Zhong *et al.* model, surface density N varies as ($N = a\,.\,h^{-2}$) where a is a factor that depends on the contact angle, as plotted in Figure 2.9 b. To describe the evolution of the model for thicknesses higher than 3 nm, larger particle size will be more likely to form by Ostwald repining which increases with initial film thickness, as clearly described by Hofman *et al.* for Co, Ni and Fe [11].

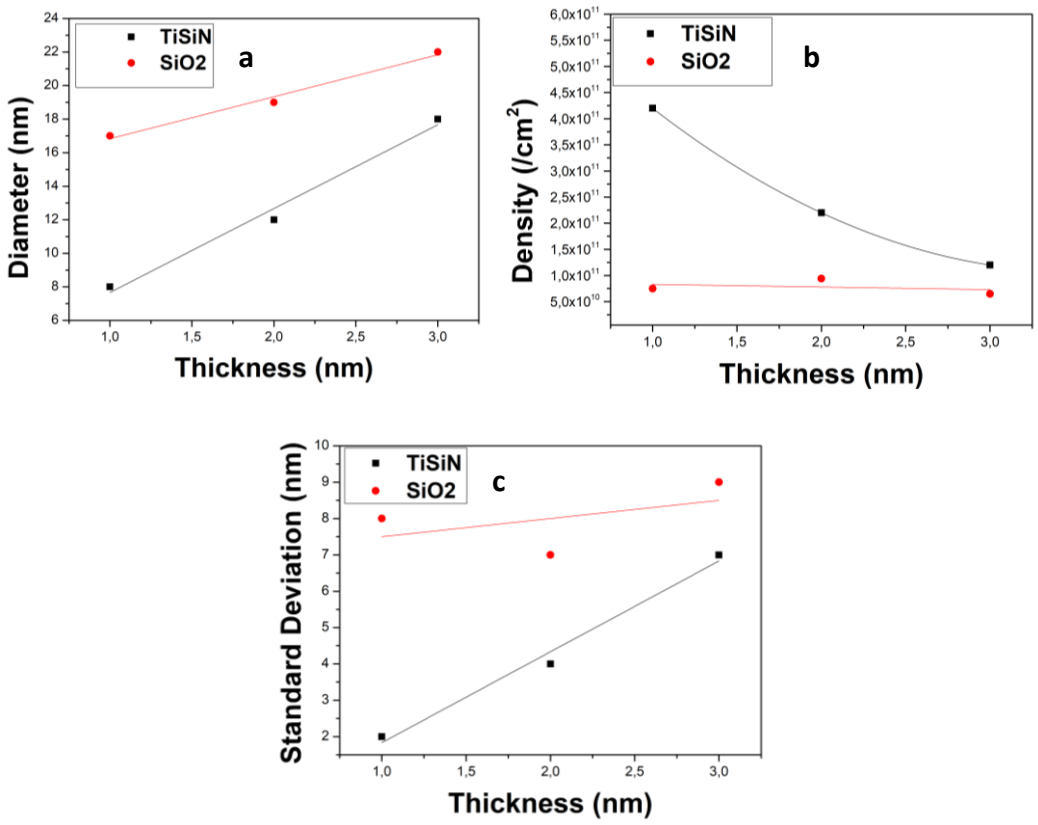

FIG 2.9 Evolution of : a) Diameter, b) Surface density, and c) Standard deviation of Cobalt nanoparticles as a function of initial film thickness dewetted on TiSiN and SiO_2 using Protocol 2.

The fitting curve of the density values of cobalt nanoparticles on TiSiN is in well agreement with the model. For the cobalt nanoparticles dewetted on SiO_2, surface density shows rather fluctuating values with a maximum for the 2 nm-thick film, demonstrating very weak dependence between density and initial thickness. This weak dependence could be explained by the competition between two main kinetic phenomena, namely bulk diffusion and Ostwald repining, while for the 1 nm thinner film, bulk diffusion is most likely the dominant phenomenon resulting in smaller nanoparticles. However, for the 3 nm thicker film, Ostwald repining may be the dominant phenomenon resulting in bigger nanoparticles. Though when either phenomenon is dominant, it results in low density values, the high density and low standard deviation values for 2 nm thickness could be considered as a result of the compensation between the two phenomena, *i.e.* bulk diffusion and Ostwald repining.

2.2.5 Metal nature effect

In this regard we compare the dewetting of cobalt to that of nickel. Nickel thin films were deposited on TiSiN coated Si substrates in order to compare the metal nature effect in dewetting between Ni and Co. For this purpose, two films with 3 nm thickness of Co and Ni underwent the optimized Protocol 2 discussed above. SEM images and related nanoparticle size distribution are presented in Figure 2.10.

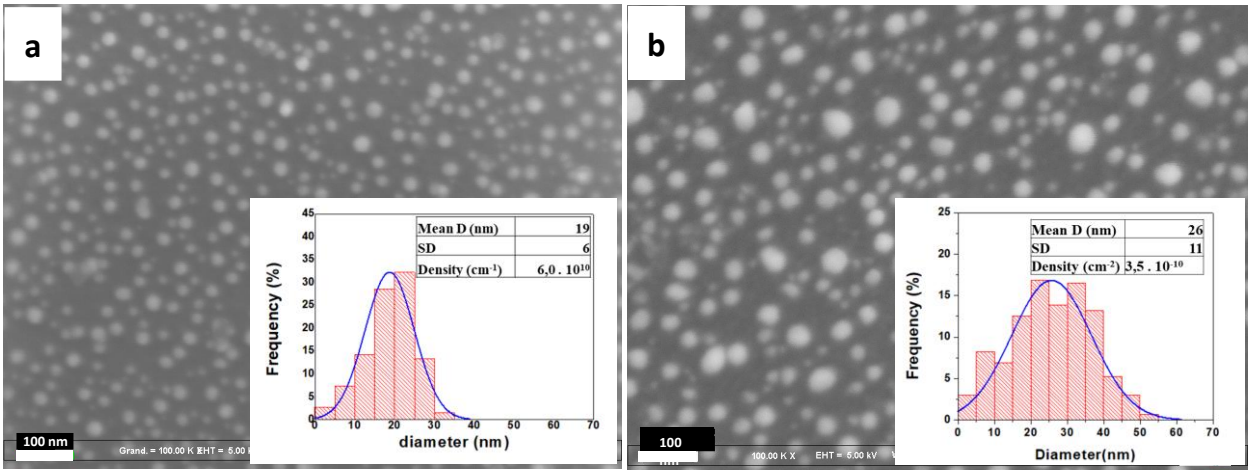

FIG 2.10 SEM images and diameter distribution formed by dewetting using Protocol 2 on: a) Co 3 nm on TiSiN, b) Ni 3 nm on TiSiN

Figures 2.10 a and 2.10 b show SEM images of the Co and Ni nanoparticle assemblies, respectively. The density of Co catalyst nanoparticles is higher than that of Ni nanoparticles produced by solid state dewetting. This density difference originates from the different dewetting behavior of Co and Ni on the TiSiN barrier layer, partially, due to the difference of

surface energy between Co and Ni. By comparing surface energies of Co, Ni and TiSiN, namely, $\gamma_{Co} = 2.22$ J/m ^{2}, $\gamma_{Ni} = 2.08$ J/m ^{2} [7], $\gamma_{TiSiN} = 0.02$ J/m ^{2} [5], respectively, one can calculate the surface energy difference for both systems: $(\gamma_{Co} - \gamma_{TiSiN} = 2.20$ J/m $^2) > (\gamma_{Ni} - \gamma_{TiSiN} = 2.06$ J/m $^2)$, meaning that the driving force for dewetting on TiSiN is higher for Co than for Ni. This results more dense cobalt nanoparticles. However, this small difference in surface energy might not explain the big difference in nanoparticles size (19 nm for Co vs 26 nm of Ni), as well as the lack of homogeneity of Ni assemblies on TiSiN substrates. This is likely an effect of nanoparticles migration and coalescence on the surface of the substrate. Co nanoparticles have smaller size distribution and better homogeneity due to their stable structure as they are more susceptible to have an oxide state as compared to Ni. Indeed O_2 and other oxidative agents such as Aluminum isopropoxide have added before to stabilize nanoparticles during VACNTs growth[12].

2.2.6 Partial conclusions

Morphological properties of dewetted cobalt nanoparticles were investigated. The use of a TiSiN layer as an effective diffusion barrier to well control the dewetting process has been proved to limit undesirable processes such as bulk diffusion and Ostwald repining in comparison to SiO_2 diffusion barrier. This allowed us to better control the size of cobalt nanoparticles and their distribution on the sample. Indeed, the model describing the size and density evolution of cobalt nanoparticles on TiSiN, as function of the initial film thickness, fits perfectly with theoretical demonstrations. Specific hydrogen plasma assisted dewetting protocol has been developed to reach optimal nanoparticles size and density as direct function of initial film thickness. Finally, metal nature effect was studied to identify a suitable catalyst for the growth of carbon nanotubes. Thus, dewetted Ni nanoparticles showed larger size distribution with lower density as compared to dewetted cobalt ones.

In summary, the complex nature of solid state dewetting has been discussed by studying process parameters. Since thermal activated phenomena (surface and bulk diffusion, Ostwald repining) enlarges nanoparticles size distribution and reduce areal density, we concluded that short time is advised for the formation of dense nanoparticles with small size distribution.
The dewetting process can also be considered as a rapid and interesting way to elaborate assemblies of self-organized magnetic nanoparticles, without using the lithography heavy approach, exhibiting interesting magnetic and magneto-optical properties that we will discuss in **Chapter IV**.

2.3 Synthesis of vertically aligned carbon nanotubes

This section deals with the synthesis of VACNTs from the dewetted catalytic nanoparticles. Process parameters such as O_2 and H_2 flow rates, plasma power, heat treatment times are varied in order to optimize growth rate, density and alignment of VACNTs. TiSiN diffusion barrier is compared to the SiO_2 one regarding nanotube growth.

The VACNTs growth implies a 3-step protocol presented in Figure 2.11 consisting of:

(i) thermal annealing for 20 min under hydrogen flowrate to dewett the catalytic film in isolated particles

(ii) hydrogen plasma annealing for 10 min to reduce the residual oxides and structure the catalyst in nanoparticles.

(iii) carbon nanotube growth by injecting ($CH_4/H_2/O_2$). Growth time was fixed for 5 minutes, after these three steps, the heater and the gas feeding were switched off to cool down the sample.

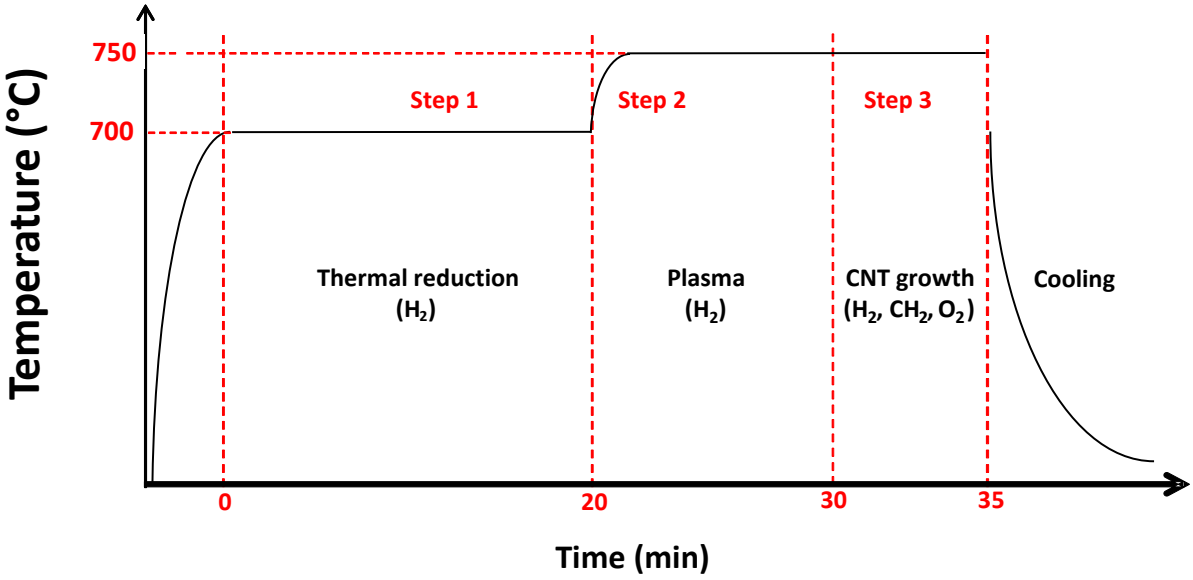

FIG 2.11 Experimental protocol number 1 for VACNTs growth in the bell jar reactor.

2.3.1 TiSiN Diffusion Barrier effect

3 nm-thick cobalt films were deposited onto SiO2 and TiSiN substrates and subjected to the growth protocol detailed above. After the CNTs growth, SEM cross section images (Figure 2.12) are realized and analyzed.

VACNTs with mediocre alignment and uniform height of 5.5 µm are observed on Co 3nm /TiSiN/SiO_2, indicating a growth rate approximately equal to 1.1 µm/min. On the other hand, only assembly of nanoparticles is observed in the case of SiO_2 barrier alone. No CNTs growth is observed probably due to the Cobalt silicide formation, thermally activated, especially at temperature higher than 600°C, this leads to catalytic nanoparticles deactivation as compared to Co nanoparticles obtained on TiSiN.

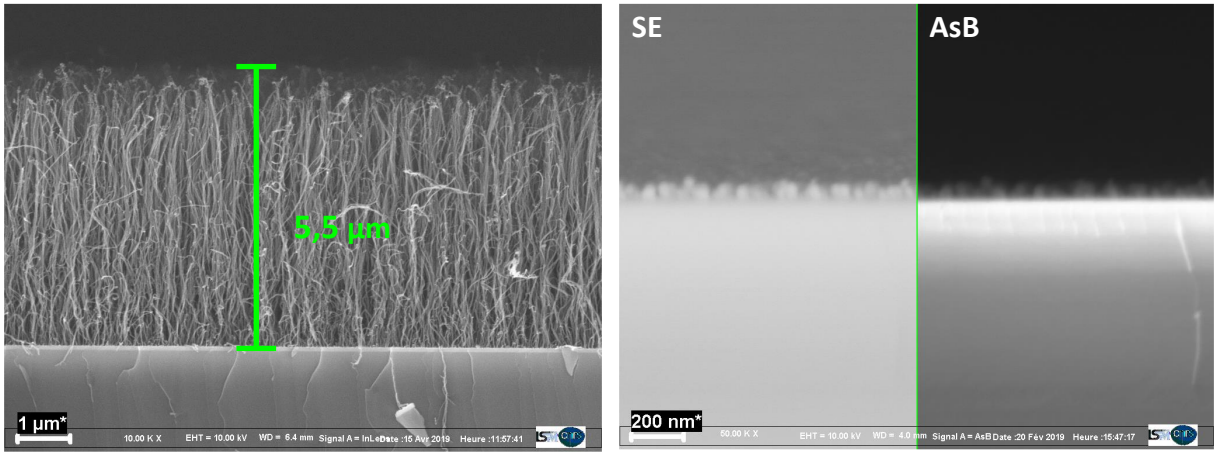

FIG 2.12 SEM cross section images of samples after VACNTs growth protocol: a) on Co 3nm /TiSiN/SiO_2 and b) on Co 3nm /SiO_2. Double images were recorded with Secondary Electron (SE) and Angle Selective Backscatter (AsB) detectors.

This behaviour highlights the efficient role of TiSiN in stabilizing Co nanoparticles for VACNTs growth by limiting catalyst-substrate interaction. Figure 2.13 with a higher magnification of the interface between the nanotubes and the substrate, clearly shows a TiSiN barrier of a thickness of ~50 nm where the integrity of the TiSiN diffusion barrier seems to be still preserved after the 3-step protocol. Cobalt nanoparticles are found at the contact point between nanotubes and TiSiN barrier, suggesting that the forests grow following the base growth mechanism. The spacing and size distribution of cobalt nanoparticles is in line with our previous work [13]. VACNTs misalignment is also apparent at the roots, may be due to the small spacing between the CNTs, originated from the low density of nanoparticles, thus allowing erratic growth in all directions.

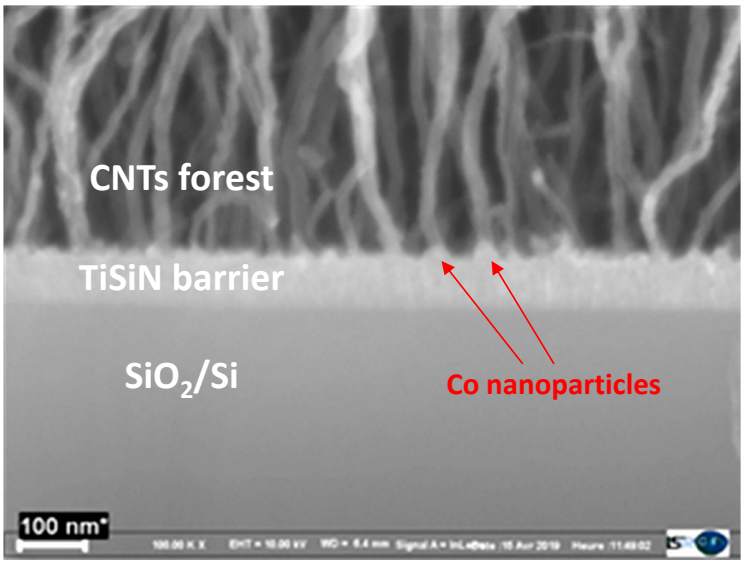

FIG 2.13 Zoom of SEM cross section image of VACNTs on Co 3nm /TiSiN/SiO_2.

2.3.2 Catalyst nature effect

In order to enhance the VACNTs density and alignment, the 3-step growth protocol was optimized (Figure 2.14) by reducing catalyst treatment time, based on the solid-state dewetting study that showed that thermally activated phenomena such as coalescence and Ostwald repining increasing with time.

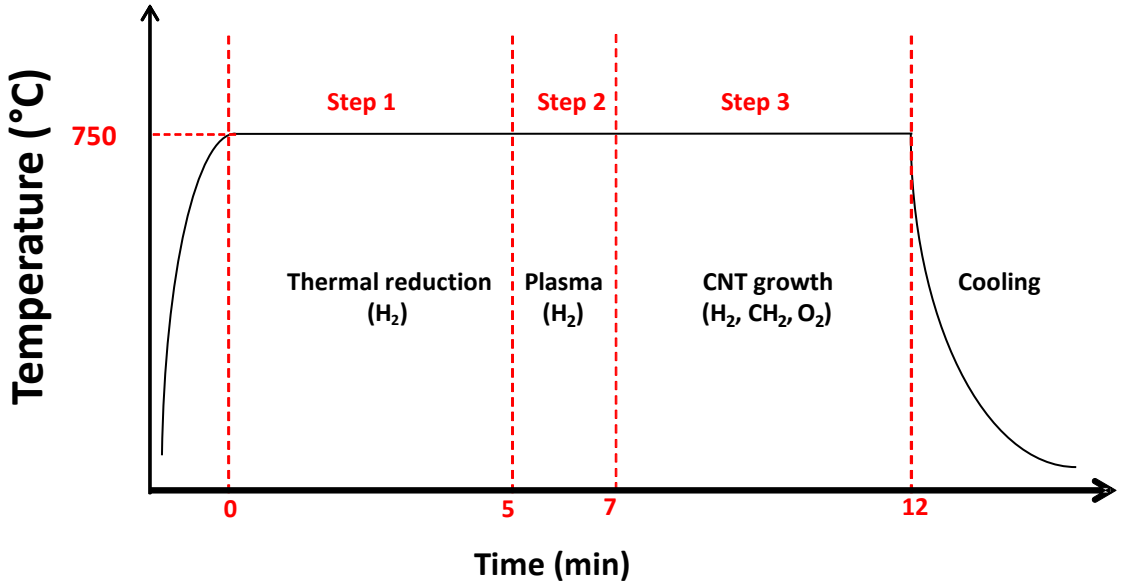

FIG 2.14 Improved experimental protocol 2 for VACNTs growth in the bell jar reactor.

After the protocol optimization, we studied the catalyst nature effect. Two TiSiN substrates with 3 nm Co and 3 nm Ni catalyst films were prepared and underwent the optimized 3-step protocol. The treated samples were named VACNTs/Co for the assembly issued from Co catalyst and VACNTs/Ni, for the one issued from Ni catalyst.

a) Morphology of VACNTs

Figures 2.15 a and Figures 2.15 b show SEM images of the VACNT/Co and VACNT/Ni assemblies, respectively. The height of the VACNTs/Co forests is about 6 μm and of the VACNTs/Ni is about 6.5 µm. The protocol optimization shows better VACNTs density, alignement and growth rate thereby confirming that it is recomanded to reduce the catalyst treatment time to minimize any interaction that may lead to lower density. The vertical orientation and density of VACNTs on the Co catalyst are better and higher than that of VACNTs on Ni catalyst. Since the areal density of nanotubes depends directly on the density of the catalyst nanoparticles produced by solid state dewetting, this is expected considering the results displayed in Figure 2.15, indeed higher nanoparticle densities were obtained for Co as compared to Ni.

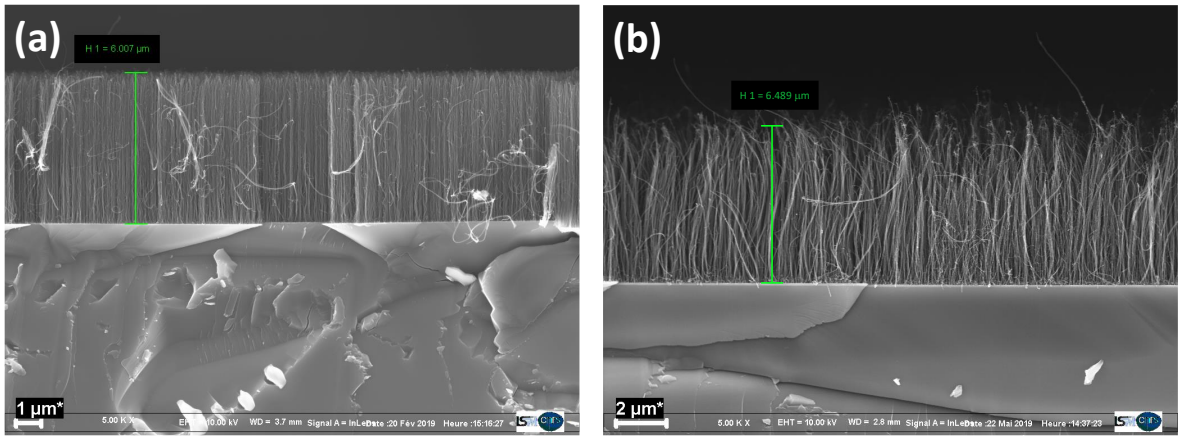

FIG 2.15 SEM images of assemblies of VACNTs from: (a) Co catalyst layer (VACNT/Co) and (b) Ni catalyst layer (VACNT/Ni).

b) VACNTs structure

Figure 2.16 shows the Raman spectra of the VACNTs presented in Figure 2.15. The intensity ratio between the graphitic G-band and the defect induced D-band (I_G/I_D ratio) is comparable for the two assemblies of VACNTs denoting equivalent structural quality. We can notice that the MWCNTs contain a high level of defects which are characteristic of MWCNTs grown by chemical vapor deposition (CVD) [14]. The relative intensities of D and G bands

depend on the average nanotube diameter, Kuznetsov *et al*. [15] suggested that curved graphene fragments can be considered as building blocks of CNTs and contribute to the defect band D.

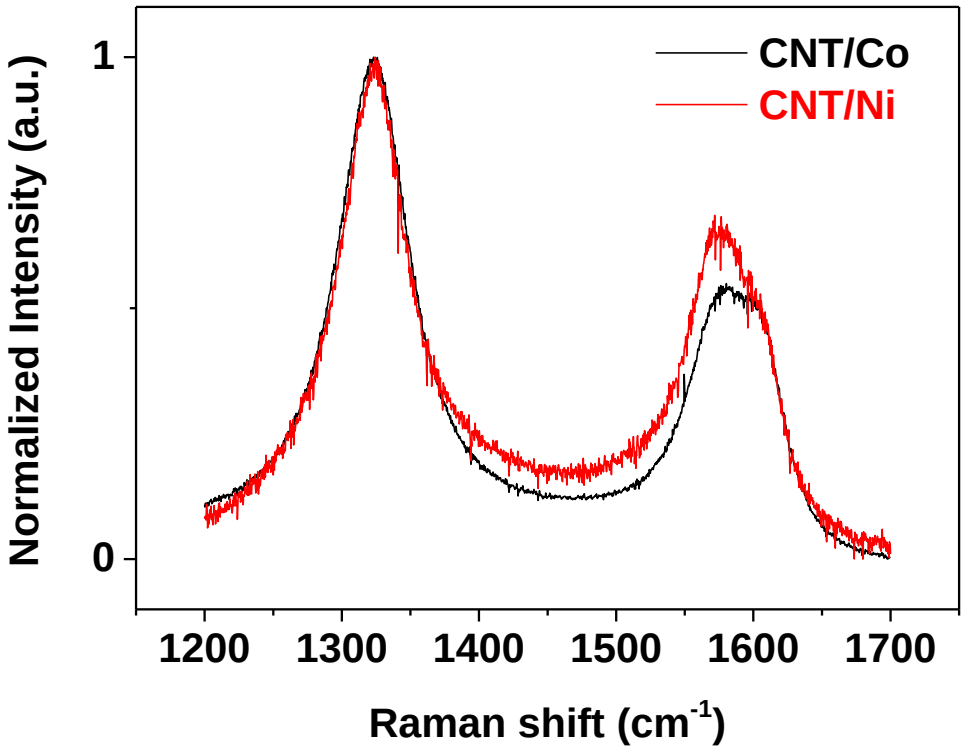

FIG 2.16 Raman spectra of VACNTs from: (a) Co catalyst layer (CNT/Co) and (b) Ni catalyst layer (CNT/Ni).

HRTEM images shown in Figure 2.17 revealed a good structural quality of the VACNTs for both assemblies issued from Co or Ni catalyst. Similar inner (about 7 nm) and outer (about 17 nm) diameters were measured from both VACNTs assemblies. From HRTEM of Figure 2.17 a, we can clearly distinguish on the top of the nanotube some of these graphene domains forming Moiré like hexagonal patterns with structure periodicity. Even constituted by large non-defective crystallites, they can be considered as building blocks of sp ^{2}-CNTs. Their polycrystalline nature, implies that defects are present in the boundaries that connect different grains with different orientations. These boundaries are mainly formed by strained pentagons and heptagons of carbon atoms in the edge of non-defective subdomains of average size La. A theoretical model supported by experimental results was proposed to correlate the I_G/I_D ratio to the domain size La using the following equation [16] :

$$La(nm) = 2.4 \times 10^{-10} \lambda^4 \ (I_G/I_D), \quad (3)$$

where lambda is the laser excitation in (nm). By applying it to the Co and Ni samples with

excitation wavelength of 632.8 nm, we estimated the in plane crystallite size (La) of 21 nm for Co and 25 nm for Ni.

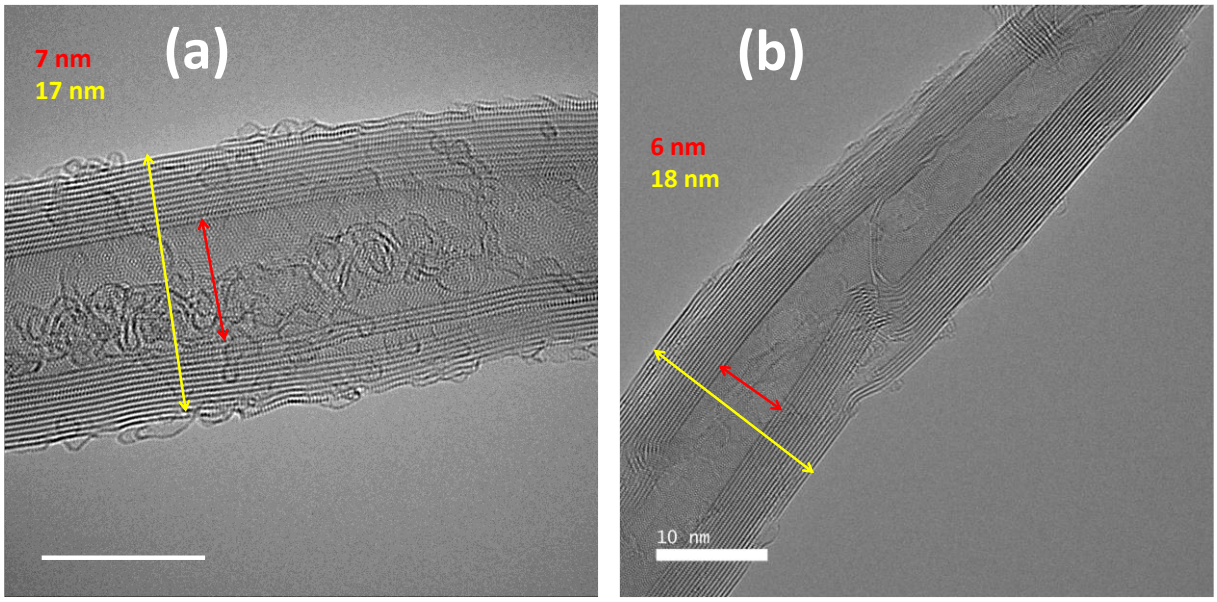

FIG 2.17 Super TEM images of CNT from: (a) Co catalyst layer (CNT/Co) and (b) Ni catalyst layer (CNT/Ni).

c) Discussion:

Regarding the difference in CNTs growth between Co and Ni, this is primarily determined by physical and chemical states of the catalyst during the growth. The $3d^7$ and $3d^8$ orbitals of Co and Ni respectively are between the most unstable electronic configuration Fe and the most stable one Cu. This allowed considering very similar catalytic activation for Co and Ni. Iron, leads to high nanotubes yield, which has attributed to the high solubility of carbon in iron. In contrast, carbon solubility in copper is much lower. But efficient carbon decomposition leads also to the formation of amorphous carbon, degrading the purity. To overcome this problem, iron-based bi-metallic catalyst like FeCu was proposed by the addition of inactive elements such as copper to iron. This lowers the yield but enhances the purity. A good tradeoff between purity and nanotube yield could be achieved by choosing mono metal catalysts such as Co or Ni as used in the present work. Physical state of these metals plays an important role in CNTs growth. The melting temperature of metallic Co and Ni catalytic particles with a radius r about 4nm is decreased by the Gibbs Thomson effect down to 570 ^{o}C and 720 ^{o}C, respectively as represented in Figure 2.18. Hence, Ni and Co nanoparticles annealed at about 750 ^{o}C should be partly in a liquid state providing the active sites in the

process of catalytic CNTs growth.

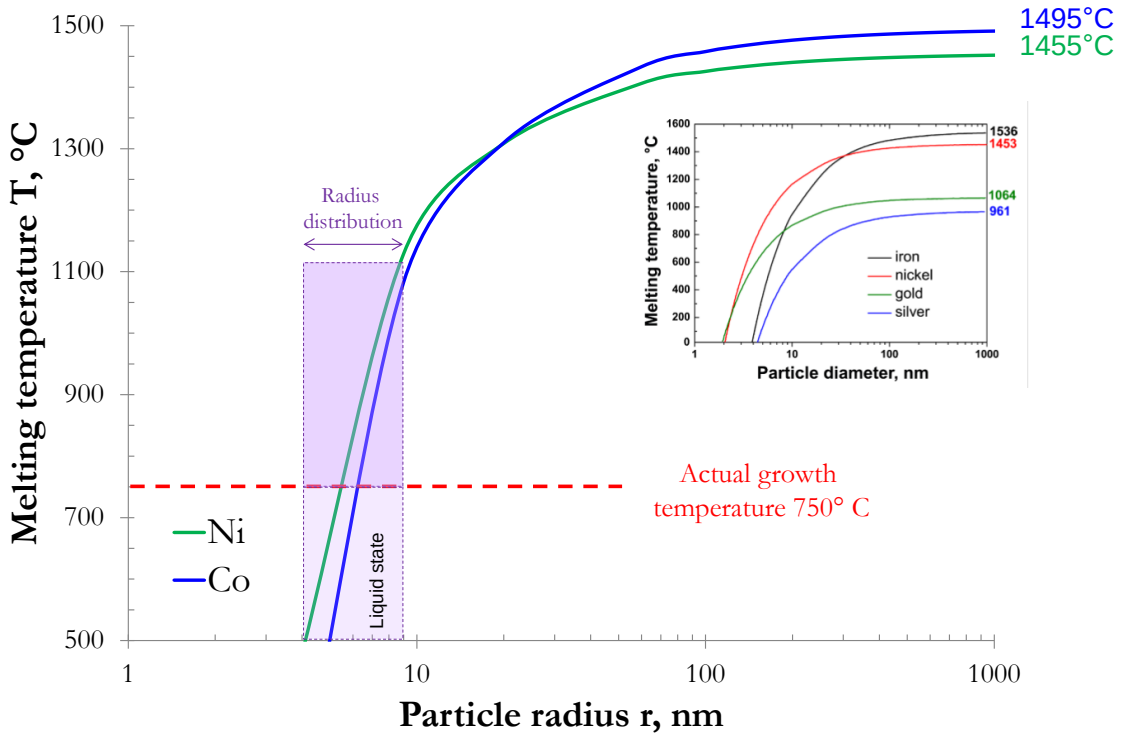

FIG 2.18 The melting temperature of nickel and cobalt particles as a function of the radius. Insert are the data reported in [17] for iron, nickel, gold and silver.

From a microscopic point of view, the kinetics of precipitation of the nanotubes is influenced by the diffusivity of C atoms, which have an activated dependence on temperature T

$$D = D_0 . exp\left(-\frac{E_a}{k_B T}\right), \quad (4)$$

with D_0 the pre-exponential factor, Ea the activation energy, and k_B the Boltzmann's constant. In our specific growth temperature of 750 °C, we estimated the bulk diffusion of carbon atoms in cobalt and nickel, respectively, at $D_{C\text{-}Co}$ about 2×10^{-9} cm ^{2} s $^{-1}$ and $D_{C\text{-}Ni}$ about 7×10^{-9} cm ^{2} s $^{-1}$. The slight higher carbon diffusion in Ni might explain the higher VACNTs height issued from Ni, however, as compared to bulk diffusion in other metals, they are in the same order of magnitude as represented in Figure 2.19.

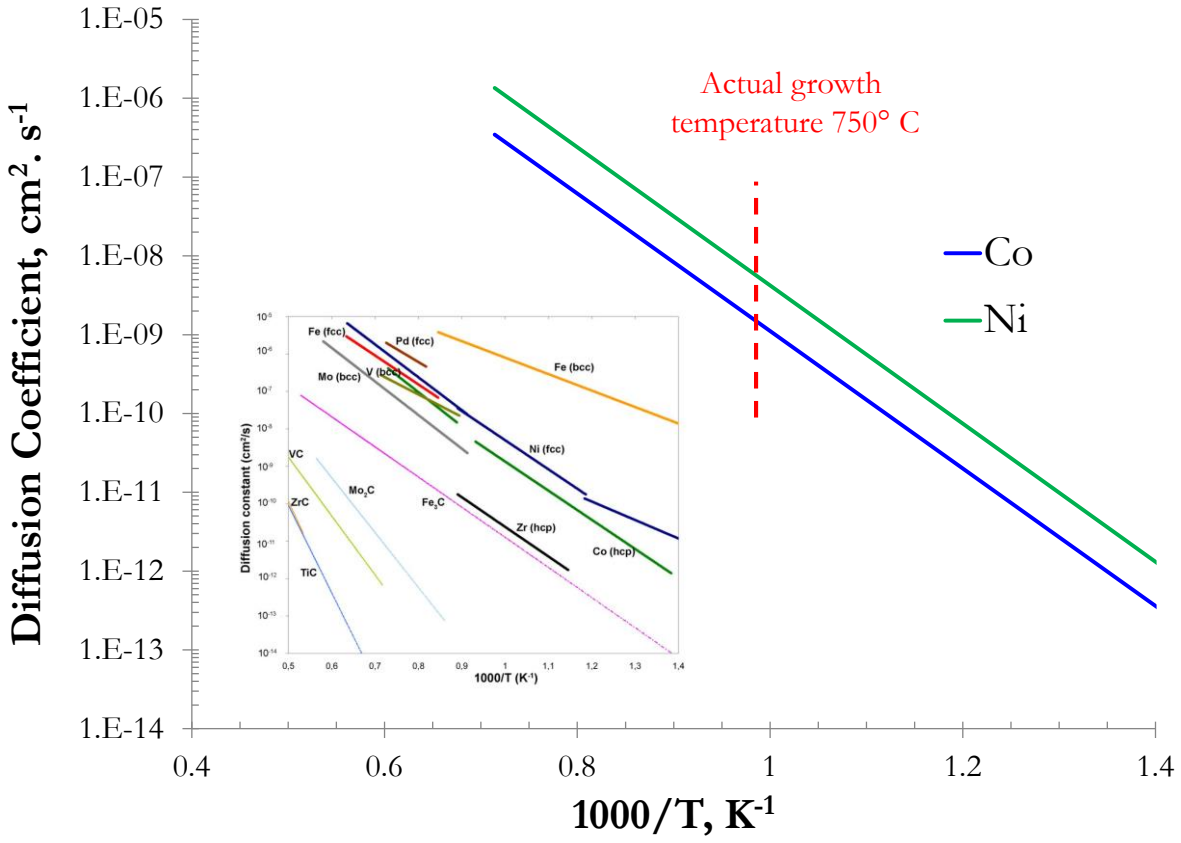

FIG 2.19 Bulk diffusion coefficients of carbon in cobalt and nickel a function of temperature. In insert the same property extended to various metals and metal carbides. [18]

2.3.3 O_2 flow rate effect

The effect of O_2 percentage in the gas inlet is studied here. CH_4 and H_2 flow rates are fixed at 90 sccm and 10 sccm respectively, and oxygen inlet value was changed from 0 to 4 sccm. The gas compositions as well as the other fixed process parameters are presented in Table 2.1.

Table 2.1: Parameters used to investigate O_2 flowrate in the inlet

Experiment	Substrate temperature	Pressure	Plasma power	CH_4 flow rate	H_2 flow rate	O_2 flow rate
Ox0	750°C	10 mbar	340 Watt	10 sccm	90 sccm	**0 sccm**
Ox1	750°C	10 mbar	340 Watt	10 sccm	90 sccm	**1 sccm**
Ox2	750°C	10 mbar	340 Watt	10 sccm	90 sccm	**2 sccm**
Ox3	750°C	10 mbar	340 Watt	10 sccm	90 sccm	**3 sccm**
Ox4	750°C	10 mbar	340 Watt	10 sccm	90 sccm	**4 sccm**

Cross-sectional SEM images of nanotube forests issued from cobalt nanoparticles dewetted on TiSiN barrier is shown in Figure 2.20. Although the five identical samples have been exposed to the same dewetting protocol, which leads to the formation of nanoparticles with close areal densities and size distribution, carbon nanotubes forests exhibit different densities and as a consequence different alignment. This behavior leads to believe that different oxygen concentrations added in the growth step has an effect on the catalytic activity of nanoparticles. Growth rate also exhibits a peak curve as a function of added O_2 quantities. Optimal growth, alignment and density point is identified at 2 sccm of O_2. Phenomenologically: this point might be situated between low oxygen intake, such as the case for (Ox0 and Ox1), that conducts to a not enough regeneration of the catalytic surface and too much oxygen intake leading to the deactivation of the nanoparticle by oxidative agents such as the case for (Ox3 and Ox4). From thermo-kinetic point of view, a modeling study is conducted in chapter 3 to unveil the role of oxygenated species on the chemical composition of the plasma and the VACNTs growth in our conditions.

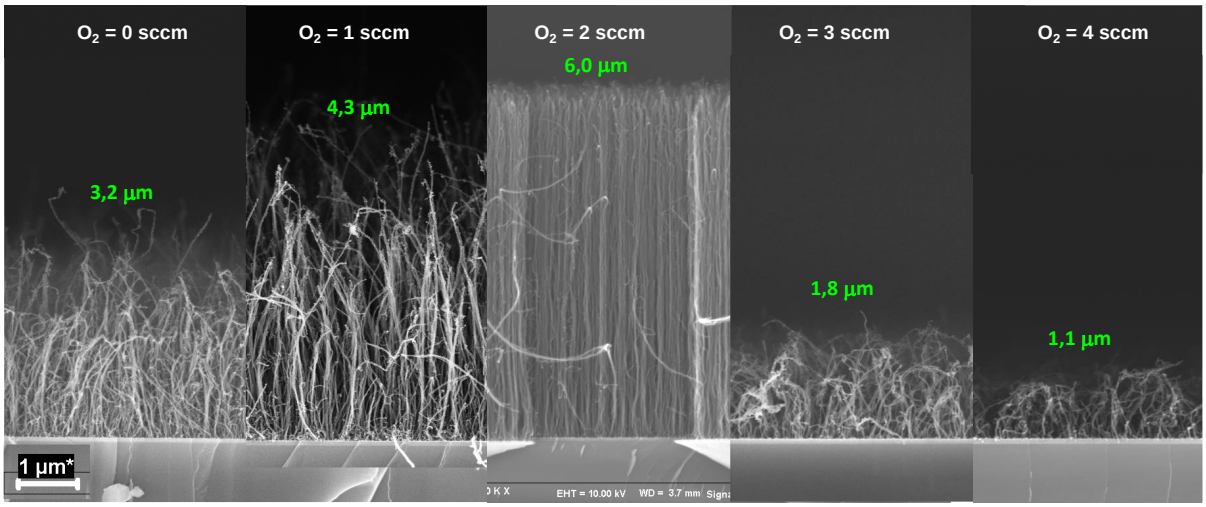

FIG 2.20 Cross-sectional SEM images of VACNTs formed after 5 min growth time for different inlet oxygen rates. The height of the forest is indicated in green.

2.3.4 H_2 flow rate effect

The effect of Hydrogen on VACNTs growth rate and morphology is studied in this section. H_2 flow rate is varied from 90 to 10 while keeping other parameters fixed. This also means that both ratios of CH_4 and O_2 in the gas composition are increased. The process

parameters are presented in Table 2.2. SEM images as well as VACNTs height are presented in Figure 2.21.

Table 2.2: Parameters used to investigate H_2 flowrate in the inlet

Experiment	Substrate temperature	Pressure	Plasma power	CH_4 flow rate	H_2 flow rate	O_2 flow rate
H1	750°C	10 mbar	340 Watt	10 sccm	**90 sccm**	2 sccm
H2	750°C	10 mbar	340 Watt	10 sccm	**60 sccm**	2 sccm
H3	750°C	10 mbar	340 Watt	10 sccm	**30 sccm**	2 sccm
H4	750°C	10 mbar	340 Watt	10 sccm	**20 sccm**	2 sccm
H5	750°C	10 mbar	340 Watt	10 sccm	**10 sccm**	2 sccm

The SEM images presented in Figure 2.21 indicate a direct influence of H_2 flow rate on the height of VACNTs. A maximum growth rate is observed for H_2 flowrate of about 20 sccm. Passing this value, the growth rate decreases again. As mentioned before, decreasing H_2 flow rate considerably means relative increasing of CH_4 and O_2 composition. However, we can conclude that a gas composition dominated by hydrogen might not be favorable to VACNTs growth. Increasing carbon species in the plasma due to high CH_4 ratios leads to higher growth rate. This might be a direct result of increasing carbon diffusion in catalytic nanoparticles. The complex nature of this ternary system ($H_2/CH_4/O_2$) requires the implementation of thermo-kinetic model coupled with surface chemistry in order to understand the changes of the concentration of key precursors leading to changes in growth rate. This is also discussed in the Chapter 3.

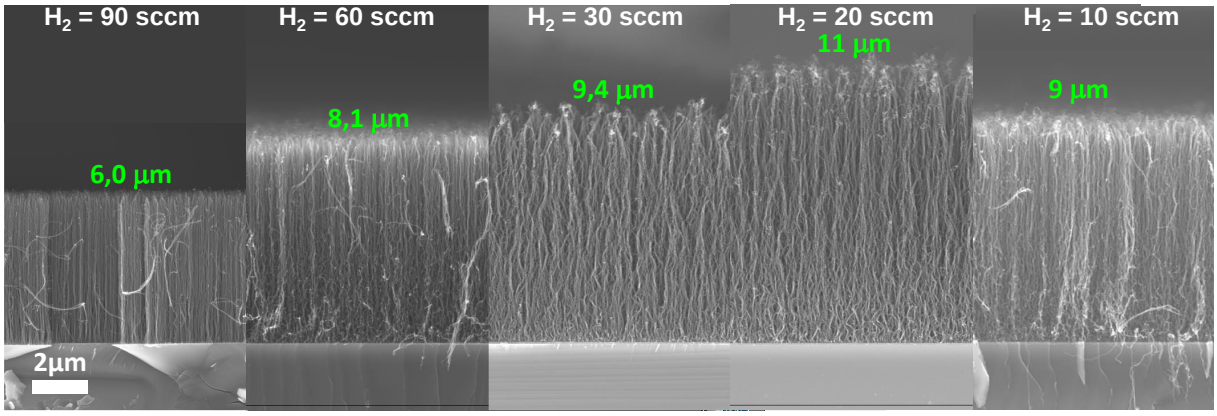

FIG 2.21 Cross-sectional SEM images of VACNTs formed after 5 min growth time for different inlet hydrogen flowrates. The height of the forest is indicated in green.

2.3.5 Plasma power effect

Plasma power was varied from 200 W to 430 W in order to enhance growth rate. However, pressure was kept constant through all experiments leading to slight change of the form and the volume of the plasma radiation. For experiments with a plasma power < 340 W, a less dense plasma hemisphere is created, while for power > 340 W, a denser plasma with a bigger volume is created. Process conditions for this study are presented in Table 2.3.

Table 2.3: Parameters used to investigate plasma power

Experiment	Substrate temperature	Pressure	Plasma power	CH_4 flow rate	H_2 flow rate	O_2 flow rate
Pl1	750°C	10 mbar	200 Watt	10 sccm	90 sccm	2 sccm
Pl2	750°C	10 mbar	240 Watt	10 sccm	90 sccm	2 sccm
Pl3	750°C	10 mbar	270 Watt	10 sccm	90 sccm	2 sccm
Pl4	750°C	10 mbar	300 Watt	10 sccm	90 sccm	2 sccm
Pl5	750°C	10 mbar	340 Watt	10 sccm	90 sccm	2 sccm
Pl6	750°C	10 mbar	370 Watt	10 sccm	90 sccm	2 sccm
Pl7	750°C	10 mbar	400 Watt	10 sccm	90 sccm	2 sccm
Pl8	750°C	10 mbar	430 Watt	10 sccm	90 sccm	2 sccm

Figure 2.22 shows the cross-section view of synthesized VACNTs according to each applied plasma power. The height, density and alignment of VACNTs show a maximum at 340W that appears as the optimal power at the applied pressure of 10 mbar. Lower plasma power yields shorter VACNTs probably due to the weak activation of the gas composition and the low concentration of precursors. Higher power densities yield shorter VACNTs with very low density and bad alignment. This is a sign of aggressive plasma etching of nanoparticles surface that could inhibited the nucleation of carbon nanotubes.

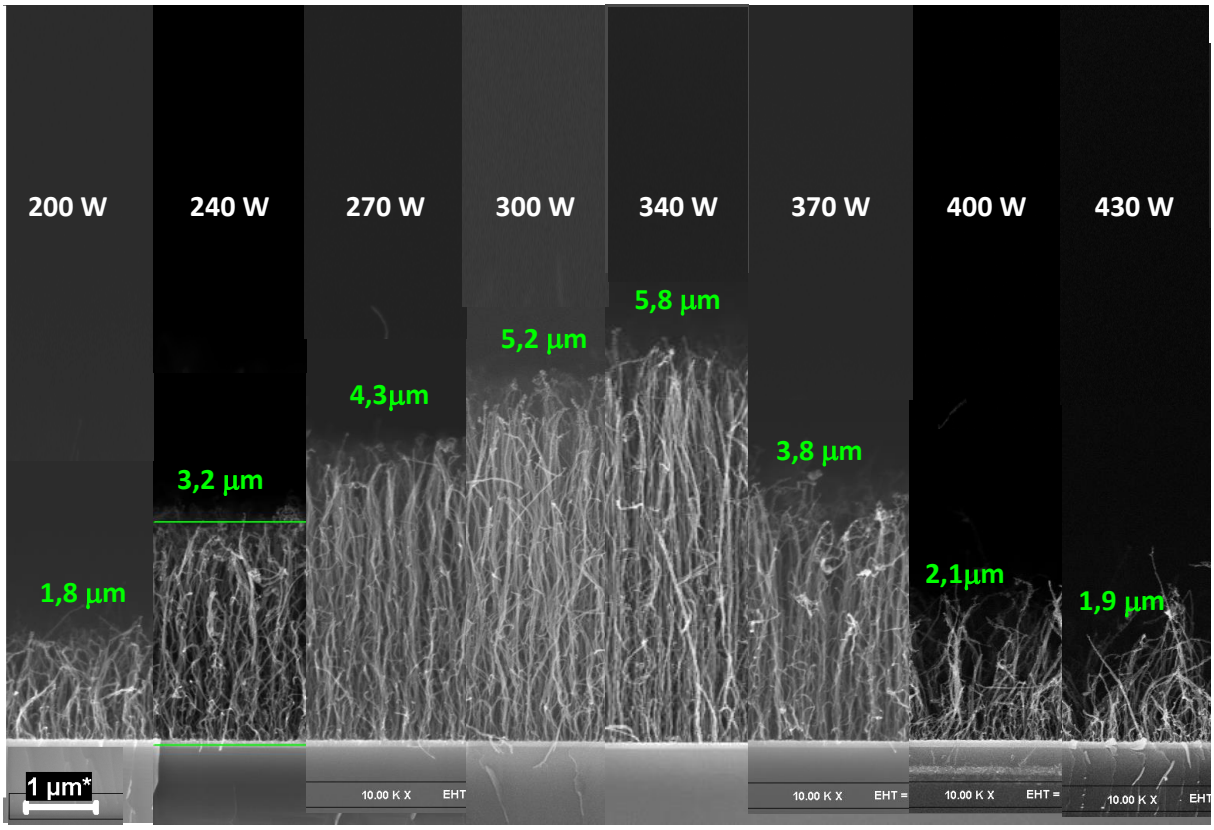

FIG 2.22 Cross-sectional SEM images of VACNTs formed after 5 min growth time for different applied plasma power. The height of the forest is indicated in green.

2.3.6 Optimal VACNTs growth conditions

The previous experimental results have revealed the influence of process parameters separately and combined on the morphology of the synthesized VACNTs. A customized protocol was thus derived with the aim to stabilize catalyst nanoparticles on the substrate, as well as to enhance growth rate, density and alignment of VACNTs. This 4-steps optimized experimental protocol is presented in Figure 2.23.

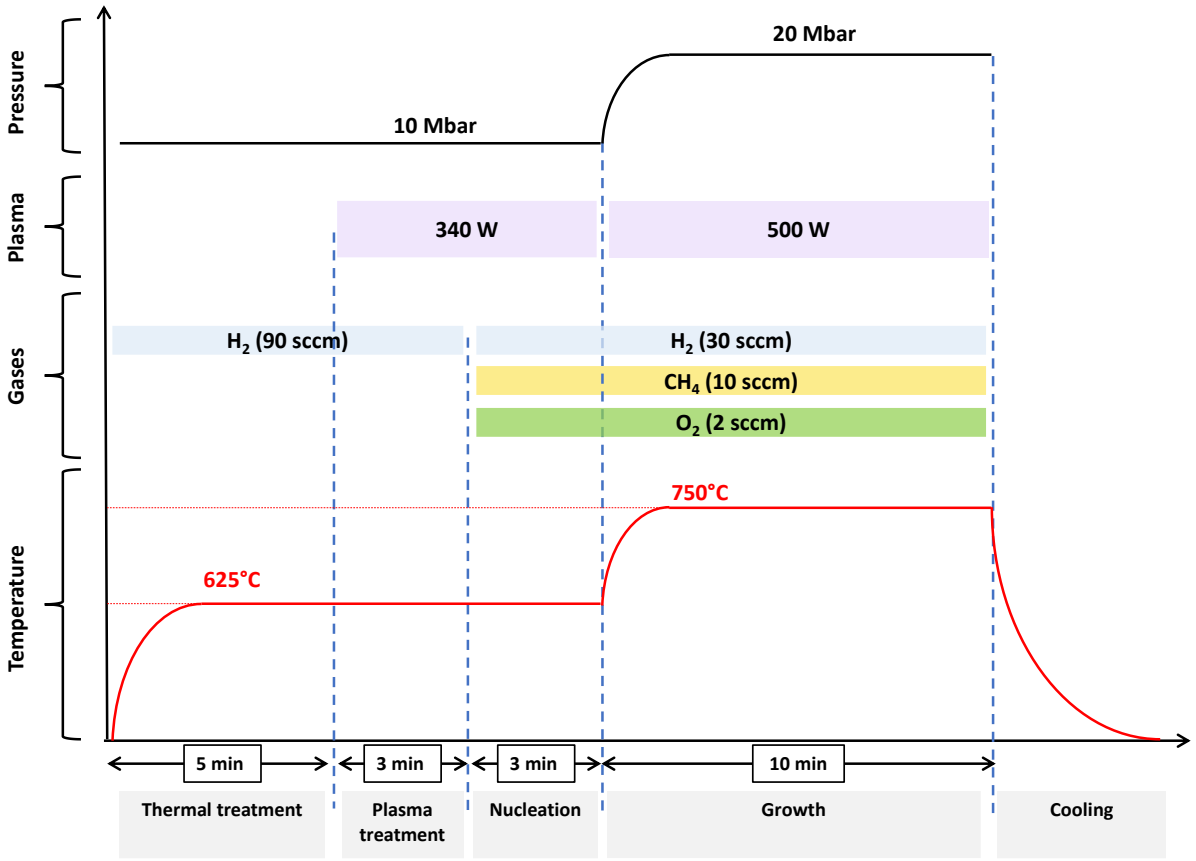

FIG 2.23 Optimized experimental protocol number 3 for VACNTs growth in the bell jar reactor.

As illustrated in Figure 2.23, our final optimized protocol consists of 4 steps,

(i) H_2 thermal treatment of the catalyst for 5 min at a lower temperature of 625°C in order to activate the dewetting of the thin film with a minimal effect of thermal phenomena that enlarge nanoparticles size.

(ii) H_2 plasma is activated for 3 min under constant 90 sccm H_2 to stabilize the plasma at 340 W and ensures the reduction of the formed catalytic nanoparticles.

(iii) A nucleation step is introduced to start VACNTs growth without aggressive etching, in this step a more optimal gas composition is set by reducing H_2 flow rate to 30 sccm while maintaining a 625°C substrate temperature.

(iv) A final growth step is started by increasing at the same time pressure to 20 mbar and plasma power to 500 W to generate more carbon precursors, temperature is also increased to 750°C, this increase of energy is implemented to maximize the growth rate for 10 min.

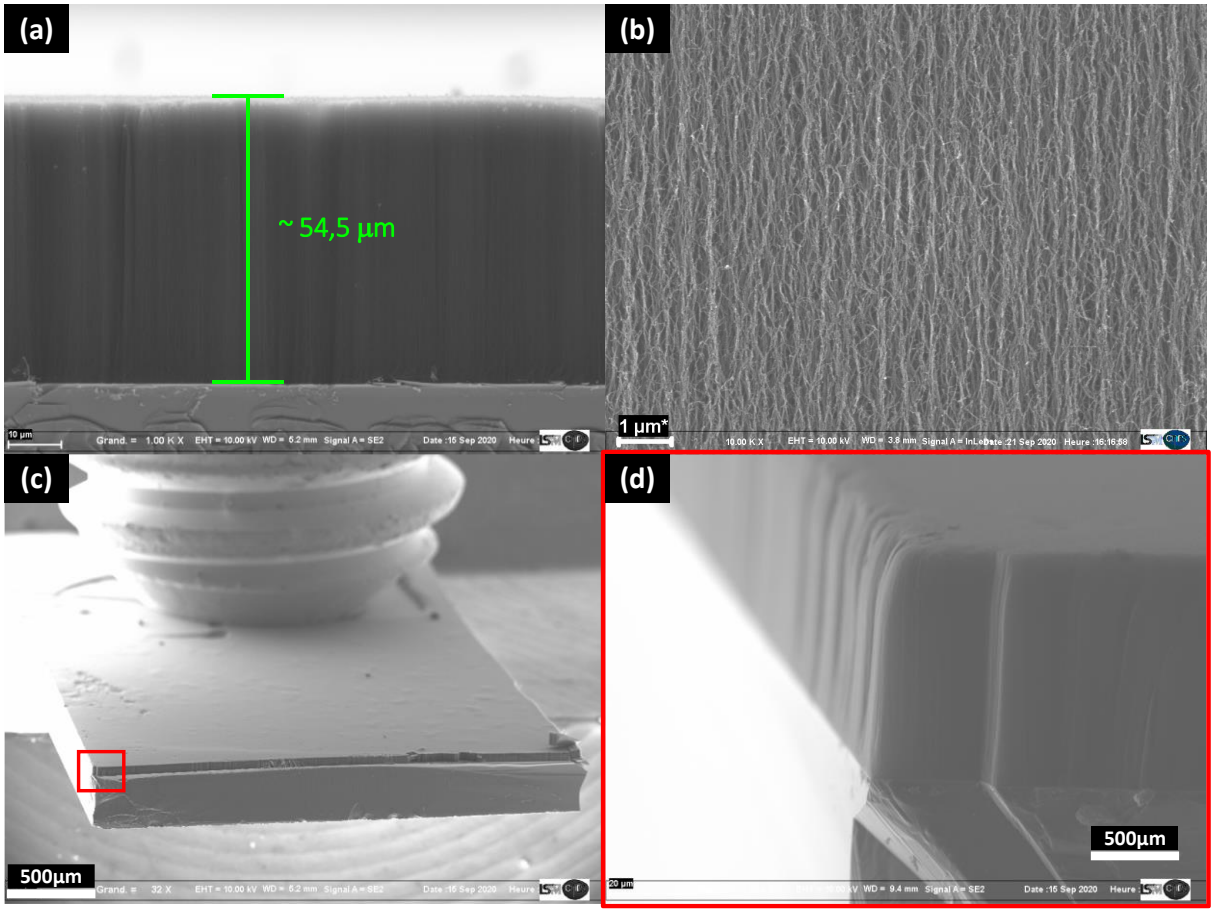

FIG 2.24 SEM cross section images of VACNTs issued from Co 3nm/TiSiN subjected to the optimized growth protocol: a) cross section of VACNTs, b) higher magnification of the grown VACNTs, c) tilt image of the substrate d) higher magnification of the edge of the substrate.

The optimized protocol was applied to the 3 nm Co/TiSiN sample. SEM images presented in Figure 2.24 show a very dense VACNTs forest with a height of 54.5 µm (Figure 24 a) for a growth time of 13 min and a growth rate of ~4.2 µm/min. The higher growth is reached when increasing the plasma power after the nucleation phase that doesn't affect nanoparticles directly since the nucleated VACNTs operate as a protective layer against etching. The synthesized VACNTs display a uniform height and surface distribution across the substrate as shown in the image of Figure 2.24 c. The higher magnification image of the sample shown in Figure 2.24 d confirms that this uniformity is displayed even at the edges of the sample.

2.3.7 Partial conclusions

Growth rate and morphology of synthesized VACNTs were investigated by varying the main process parameters. First, the use of a TiSiN barrier layer helped to stabilize Co nanoparticles and preserved their catalytic activity as compared to SiO_2 substrates. Second, the nature of the catalyst was discussed from morphological and structural point of views. For this purpose, both Ni and Co were used to grow VACNTs. Similar structural properties are observed but different densities are obtained due to different dewetting behavior as discussed in the previous section. O_2 and H_2 as well were varied in order to create a rich chemical environment for VACNTs growth. Keeping O_2 in small quantities, while reducing H_2, inlet creates a favorable environment to obtain a higher growth rate and dense VACNTs. Plasma power was also monitored to increase the growth rate. Lower plasma densities yielded shorter VACNTs and higher plasma densities might etch nanoparticles leading to short erratic carbon nanotubes. In summary, the need to customize the experimental protocol was highlighted by setting a 4-steps experimental protocol that yielded higher growth rate and densely packed VACNTs with a uniform structure over whole the substrate surface.

2.4 *In-situ* filling of vertically aligned carbon nanotubes

This section is dedicated to the elaboration of metal/VACNTs hybrid materials resulting from PECVD process. The study of the catalytic layer nanostructuring, into elongated nanowires encapsulated inside the grown VACNTs during the growth process, is detailed. First, we compare two different catalysts: single Co layer and Co/Pd bilayer, both of nanometric thicknesses, deposited onto SiO_2 as well as TiSiN serving as a diffusion barrier of the catalyst into the substrate. Thus, we sought to develop optimal growth conditions for hybrid nanotubes as well as their alignment by varying different experimental conditions, including the synthesis temperature, catalyst thickness and plasma power. The parametric study allowed us to highlight the role of Pd in enhancing the filling of the nanotubes as well as the effect of the TiSiN barrier layer as compared to SiO_2. Scanning electron microscopy (SEM) and Transmission electron microscopy (TEM) have been systematically used to image the morphology of the of the hybrid nanotubes. Finally, a statistic study was derived in order to have a better understanding of the filling mechanism and set up perspectives.

2.4.1 LSPM reactor filling experiments

In this first part, we present the experiments preformed in the PECVD bell jar reactor of the LSPM laboratory. Substrates with diffusion barrier SiO_2 or TiSiN were prepared following the same protocol. Co and Pd layers were deposited in the PVD reactor described in **section 2.1.2**. The Co layer thickness was fixed to 3 nm while the Pd one was fixed to 2 nm, following the stack:

- Pd 2 nm / Co 3 nm / SiO_2
- Pd 2 nm / Co 3 nm / TiSiN

These samples were then exposed to the standard growth protocol described previously.

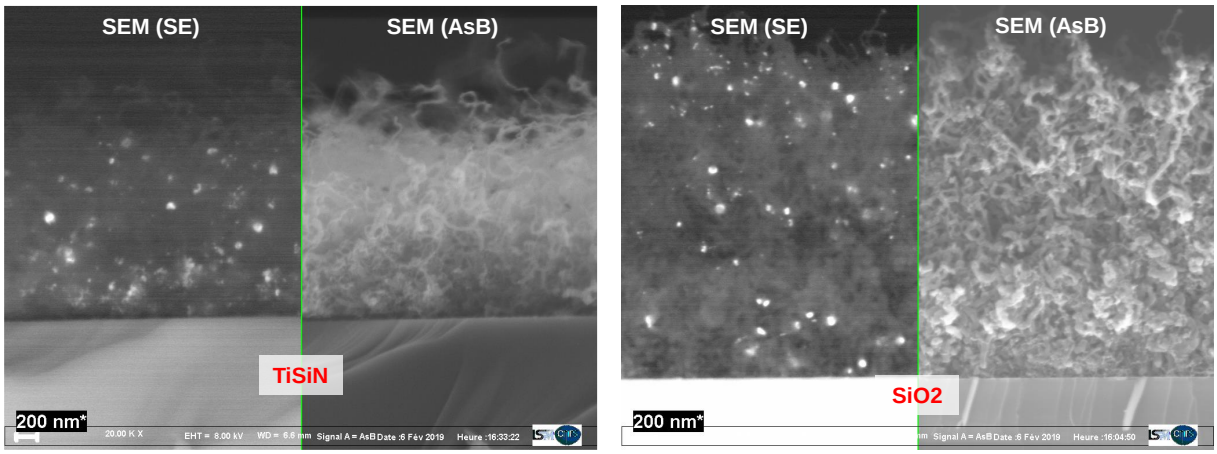

FIG 2.25 SEM cross section view of the grown CNTs on SiO_2 (right) and TiSiN (left). Double images were recorded with Secondary Electron (SE) and Angle Selective Backscatter (AsB) detectors.

Figure 2.25 shows an erratic growth of carbon nanotubes on both substrates with lower growth rate as compared to the samples with only 3 nm Co presented in the previous section. This behaviour is due to the presence of the bilayer thickness (5 nm), higher in this case, as well as the presence of Pd that probably changes the nanoparticle diameter distribution creating more space for nonlinear CNTs orientation during growth. It is to note an interesting result consisting in the growth of CNTs on SiO_2 for the first time to our knowledge. This means that the presence of Pd favors the growth of CNTs on SiO_2 substrates, either by limiting the diffusion of Co into SiO_2 or by enhancing the diffusion of carbon in the obtained miscible dewetted bimetallic nanoparticles. Regarding to the nanotubes filling, AsB detector images show the presence of metallic nanoparticles all over the CNTs forest with very little aspect ratio, meaning that addition of Pd do not lead to the enhancement of the filling.

Assuming the lack of metallic material deposited onto the substrate as the main reason behind the absence of filling effect, we deposited higher bilayer thickness as well as tried different configurations. Hence Co and Pd catalyst were deposited in the following configurations:

a) Pd 3 nm / Co 9 nm / TiSiN
b) Pd 3 nm / Co 9 nm / SiO_2
c) Pd 6 nm / Co 9 nm / TiSiN
d) Pd 6 nm / Co 9 nm / SiO_2

The prepared samples underwent the growth protocol. Since the catalyst thickness is higher in this case, higher dewetting time (Step 1 of 30 min + Step 2 of 30 min) was needed to obtain nanoparticles. The SEM cross section images of the grown CNTs forests are presented in Figure 2.26.

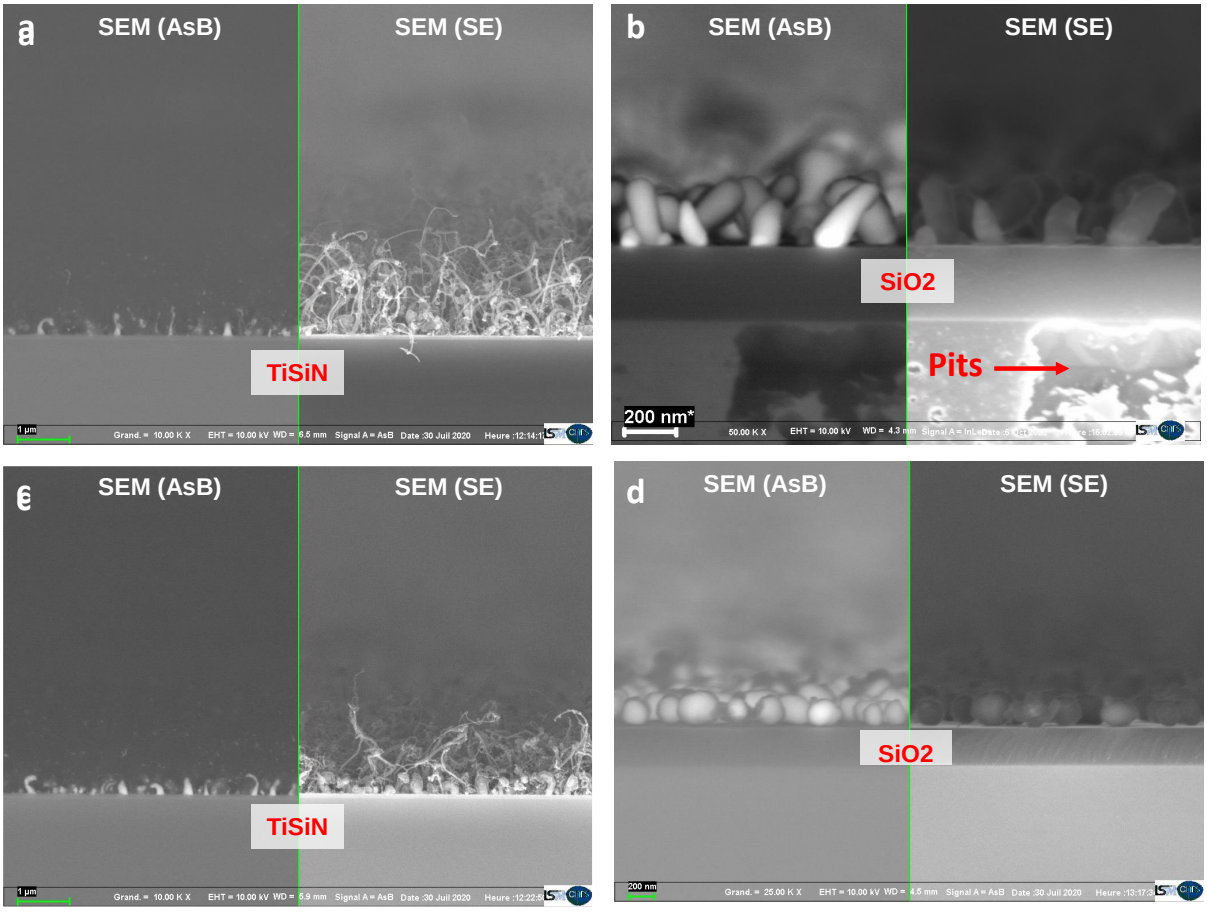

FIG 2.26 SEM cross section view of the grown CNTs on a) Co 9 nm / TiSiN , b) Pd 3 nm / Co 9 nm / TiSiN , c) Pd 6 nm / Co 9 nm / TiSiN , d)Pd 6 nm / Co 9 nm / SiO_2. Double images were recorded with Secondary Electron (SE) and Angle Selective Backscatter (AsB) detectors.

CNTs growth is observed in all samples with TiSiN barrier, while it is absent when using SiO_2 barrier. However, an erratic growth is still observed on TiSiN most likely due to the presence of Pd. Nevertheless, few metal filled carbon nanotubes, with higher diameter and erratic growth were observed on both Co 9 nm / TiSiN and Pd 6 nm / Co 9 nm / TiSiN samples (Figure 2.26 a and Figure 2.26 c, respectively). Conversely, with the SiO_2 barrier, the formation of nanoparticles with higher size (200 nm) is privileged (Figure 2.26 b and Figure 2.26 d, respectively). The absence of CNTs growth with SiO_2 barrier could be a result of the deactivation of the catalyst during the dewetting step. Indeed, the thermal treatment of Pd in the presence of H_2 over a prolonged time could lead to the diffusion of silicon Si into Pd to form Pd_2Si [19]. The SEM cross section image of the sample (Pd 3 nm / Co 9 nm / SiO_2: Figure 2.26 b) shows the presence of pits in the layer of Si which could be the evidence of Si diffusion to the surface through the porous SiO_2 layer. The nanoparticles formed show elongated forms with a vertical orientation that looks like growth of silicon nanowires. We tried applying a negative electric field (bias) to the substrate to improve the filling. These experiments were inconclusive due to electrical instabilities in LSPM reactor. Hence, we conducted these experiments at Thales reactor as part of the Labex DEFIS-CNT project (Démouillage de Films Solides pour la Croissance de Nanotubes) between LSPM and THALES TRT.

2.4.2 THALES reactor filling experiments

In order to enhance the VACNTs filling rate and to get a better alignment of the nanotubes forest, we preformed experiments in Thales laboratory. Indeed, the available Aixtron reactor allows the use of a negative bias electric field. Applying a bias is known to well control the CNTs growth direction [20]. We also expanded the Co and Pd catalyst configurations with the following 7 conditions:

a) Co 6 nm / TiSiN
b) Pd 2 nm / Co 6 nm / TiSiN
c) Pd 3 nm / Co 6 nm / TiSiN
d) Pd 4 nm / Co 6 nm / TiSiN
e) Pd 6 nm / Co 9 nm / TiSiN
f) Pd 3 nm / Co 9 nm / TiSiN
g) Pd 6 nm / Co 9 nm / TiSiN

The samples underwent the growth protocol employed in Thales Aixtron reactor. For confidential purposes, some details of the experimental protocol will be disclosed. The

general process parameters are presented in Table 2.4. Similarly, to our experimental protocol, the samples were subject to a treatment step where nanoparticles were formed by solid state dewetting, then, a mixed gas composition of (NH_3/C_2H_2) was injected in the plasma to generate the species necessary for the VACNTs growth. Here, the VACNTs were subject to a bias voltage during the growth for better alignment. The growth temperature, as well as the plasma power, was changed in order to understand the filling mechanisms.

Table 2.4: Parameters used in the Aixtron reactor

Substrate temperature	650° C - 950° C
Pressure	6 mbar
Plasma power	75 W -200 W
NH_3 flow rate	195 sccm
C_2H_2 flow rate	55 sccm

2.4.3 Temperature effect

The configuration of the catalyst bilayer as well the grown VACNT at 650°C and 100 W are presented in Figure 2.27.

As compared to CNTs grown in LSPM reactor, better alignment and larger diameters are observed for the VACNTs grown at 650°C in THALES reactor. The VACNTs forests heights remain low, about 1 µm, for all the samples. In contrast to LSPM experiments, the images obtained with an AsB detector show a top growth mechanism of VACNTs with more elongated nanoparticles at the tip of the nanotubes. This indicates a lower catalyst/substrate interaction. Interestingly, using a higher temperature of 850°C do not lead to substantial differences related to the different catalyst configurations as shown in Figure 2.28.

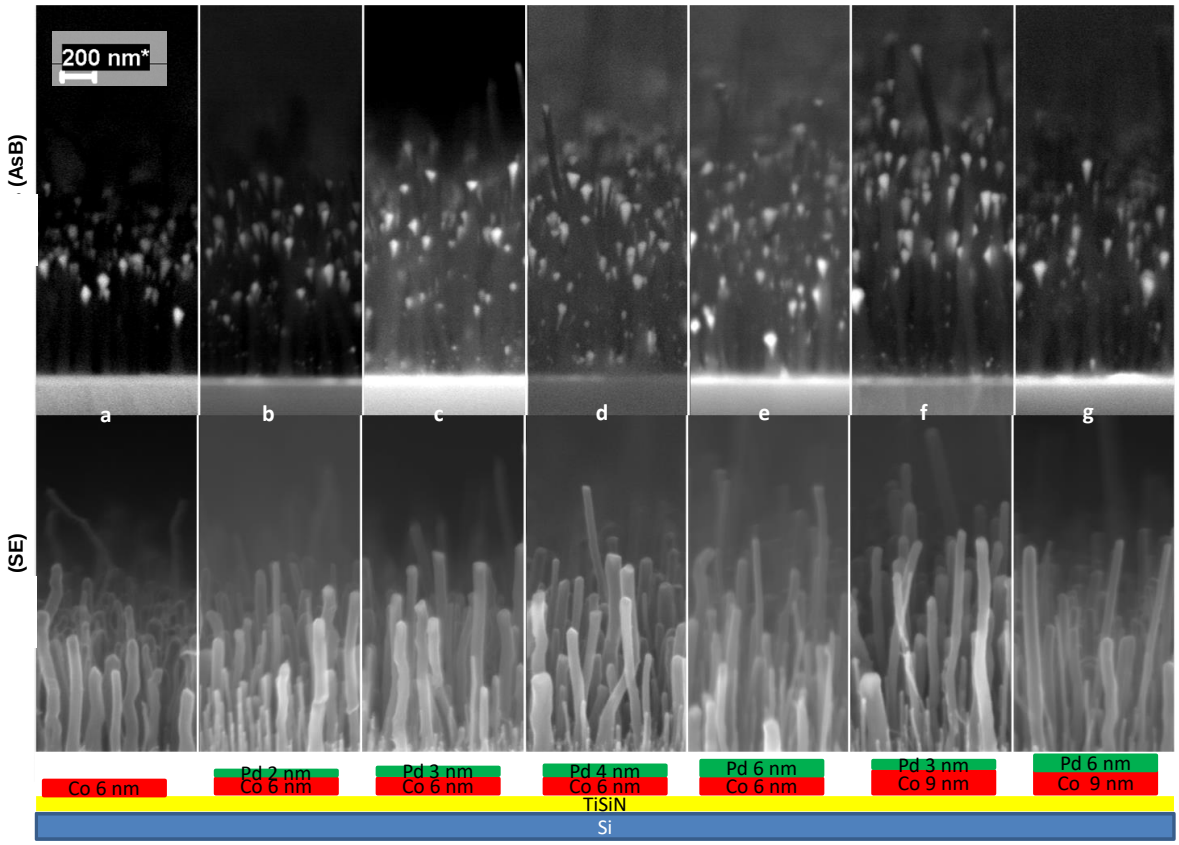

FIG 2.27 SEM cross section view of the grown CNTs on TiSiN at 650° C. a) Co 6 nm , b) Pd 2 nm / Co 6 nm c) Pd 3 nm / Co 6 nm , d) Pd 4 nm / Co 6 nm , e) Pd 6 nm / Co 6 nm ,f) Pd 3 nm / Co 9 nm, g) Pd 6 nm / Co 9 nm

By increasing the growth temperature, higher VACNTs growth rates were observed with a wavy morphology of the nanotubes. The overall VACNTs height is about 3 µm for all samples, except the sample with only Co as catalyst. This higher growth rate could be either a result of the presence of Pd or simply due to the higher catalyst layer thickness.

Increasing process temperature has a clear effect on the filling state of VACNTs; this effect reinforces the capillary filling theory since higher temperature decreases cohesive force and increase capillary flow. Capillary filling enhancement could also be a result of large canals of obtained VACNTs, indeed large diameter of VACNTs is observed at 850°c as compared to VACNTs obtained at 650°, this might be a result of thermally activated phenomena (Ostwald ripening and coalescence) that enlarges catalytic nanoparticles size as discussed previously.

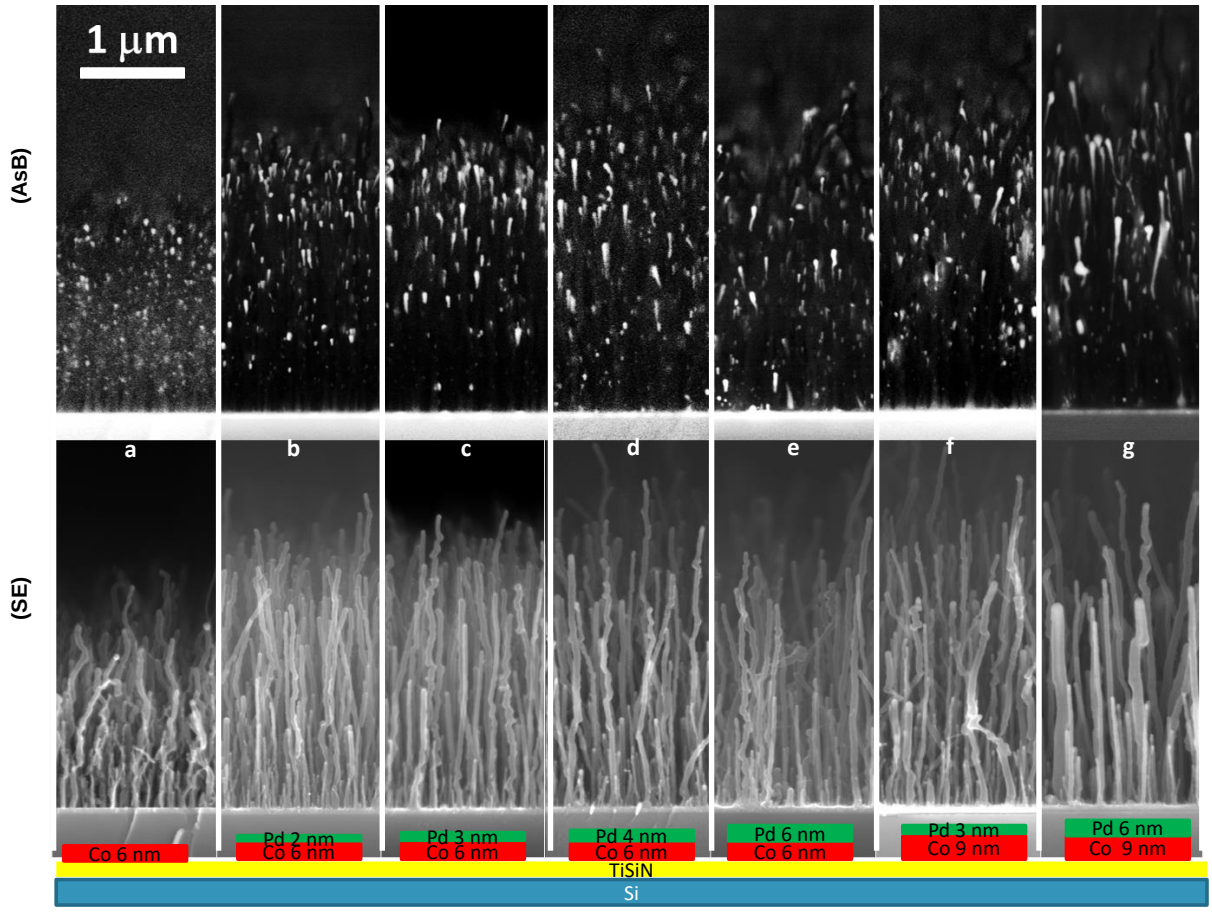

FIG 2.28 SEM cross section view of the grown CNTs on TiSiN at 850°C : a) Co 6 nm , b) Pd 2 nm / Co 6 nm c) Pd 3 nm / Co 6 nm , d) Pd 4 nm / Co 6 nm , e) Pd 6 nm / Co 6 nm ,f) Pd 3 nm / Co 9 nm, and g) Pd 6 nm / Co 9 nm.

2.4.4 CoPd Bilayer configuration effect

By comparing the filling state of different samples as a function of the bilayer configuration, increasing Pd/Co ratio seems to not have a substantial effect on samples with 6 nm Co layer (Figures 2.28 (b-e)); indeed, the elongated shape of nanoparticles is similar in all of them. However, increasing Pd thickness in these samples results a decreasing of density and a non-uniform VACNTs height.

Comparison of two samples with the same bilayer thickness (12 nm) but with different Pd/Co ratios 50/50 for figure 2.28(e) and 25/75 for figure 2.28(f) shows that a higher number of filled nanotubes is obtained for the 25/75 ratio as compared to 50/50 ratio. We can deduce that Pd/Co ratio plays a role in the quantitative filling aspect of the overall VACNTs assembly.

Comparison of two samples with the same Pd/Co ratio (25/75) but with different total bilayer thickness 8 nm for figure 2.28(b) and 12 nm for figure 2.28(f) show that a better filling state i.e. longer filling for VACNTs is obtained for the 12 nm ratio as compared to 8 nm. The same effect is also observed for two samples 40/60 Pd/Co ratio presented in 2.28(d) (10 nm) and 2.28(g) (15 nm). We can deduce that bilayer thickness plays a role in the qualitative filling aspect of VACNTs.

These conclusions explain why higher qualitative and quantitative filling that reaches to a length of 1 µm in some nanotubes is observed for the sample presented in figure 2.28(g), i.e. 6 nm Pd + 9 nm Co) that has a higher thickness and an adequate Pd/Co ratio.

The observations above lead us to believe that Pd do not participates to VACNTs growth by itself in these process conditions; rather, since CoPd are miscible alloys, adding Pd results in large size catalytic nanoparticles that nucleate large diameter VACNTs with large internal canals that are easier to fill. Further optimization of the process is needed to enhance alignment and morphology. For the next experiments, two samples were chosen in order to reduce the experimental workload: Pd 3nm / Co 6 nm and the Pd 6 nm / Co 9 nm deposited onto the TiSiN barrier.

2.4.5 Plasma power effect

In order to optimize the filling as well as the alignment of the grown VACNTs, we gradually increased the plasma power from 100 W to 150 W then to 200 W, keeping the temperature at 750°C and all other parameters the same. The results are presented in Figure 2.29 together with the ones obtained with 100 W, for comparison.

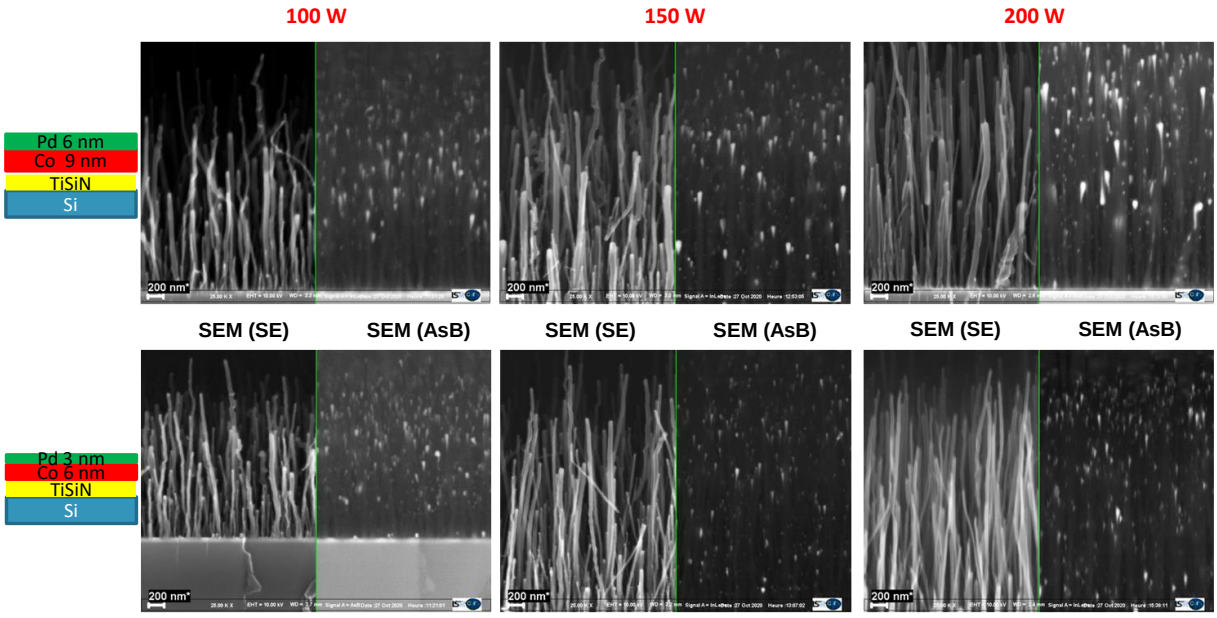

FIG. 2.29 SEM cross section view of the grown CNTs on TiSiN at 750°C on Pd 6 nm / Co 9 at different power. a) 100 W, b) 150 W, c) 200 W: on Pd 3 nm / Co 6 nm: d) 100 W, e) 150 W, f) 200 W.

With higher plasma power, higher VACNTs growth rate was observed as well as better alignment, this result was already discussed in the previous part of this chapter. We observe that increasing the plasma power leads to more elongated nanoparticles inside the CNTs, with larger diameter at the tip. Our results seem to indicate that the plasma power mainly acts on the alignment of the nanotubes but not much so on the filling rate of the nanotubes.

The conditions used in Thales reactor, namely: NH_3 ambient, aggressive ion bombardment, bias, higher temperature, than ones in LSPM reactor lead to a different VACNTs growth mechanism (tip growth) and to a different morphology (larger diameters, better alignment). Enlarged internal CNTs canals were obtained leading to a better filling rate and homogeneity.

In this optic, we performed further experiments to optimize the growth conditions, in order to better emphasize the role of the plasma as well as the temperature in the process of CNTs filling. Hence, the best conditions were obtained with a plasma power at maximum 200 W and a temperature at 950°C, as shown in Figure 2.29.

2.4.6 TiSiN barrier effect

In order to highlight the role of the barrier layer, VACNTs growth was performed for Pd 3 nm / Co 6 nm deposited onto TiSiN and SiO_2 barriers. The obtained results are presented in Figure 2.30.

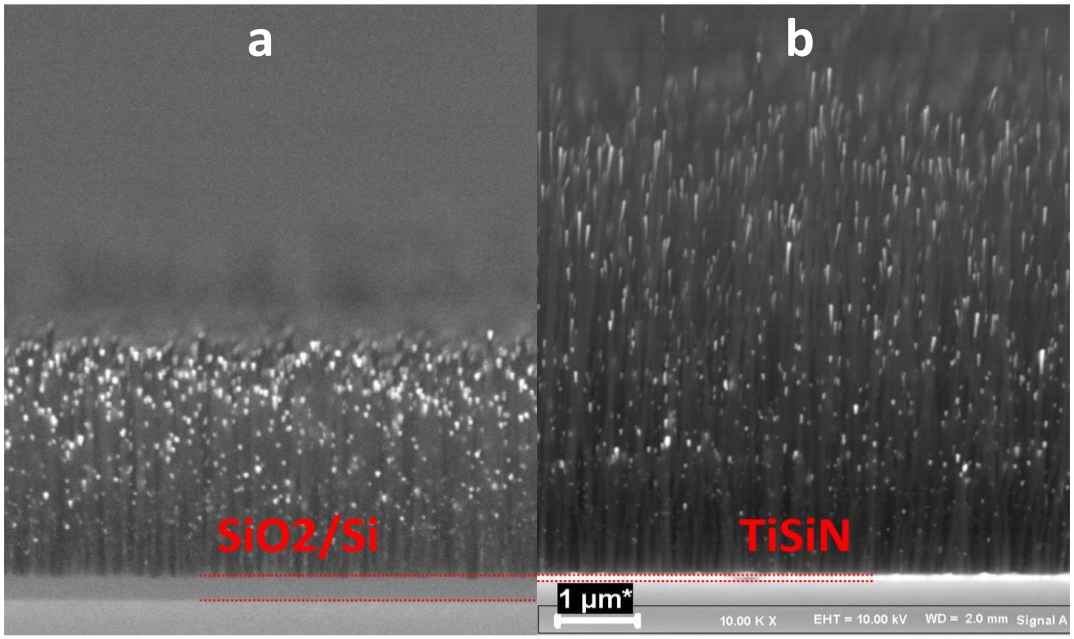

FIG 2.30 SEM (AsB) cross section view of the grown VACNTs from Pd 3 nm / Co 6 nm at 200 W - 950°C on: a) SiO_2, b) TiSiN.

Regarding to the CNTs grown directly onto SiO_2, the TiSiN barrier layer gave rise to longer VACNTs, approximately double, a better filling rate, and elongated nanoparticles. Conversely, spherical nanoparticles are observed in the case of VACNTs grown on SiO_2. This could be interpreted through interaction between Pd, and Si, observed earlier, that deactivates the role of Pd.

2.4.7 Palladium layer effect

One question that hasn't been answered yet is the role of Pd in enhancing the filling rate of VACNTs, is it the higher thickness resulted from the adding of few nm of Pd or the presence of Pd by itself? In order to analyze more concretely the role of Pd in the process of CNTs filling, we compared two systems: Co 9 nm and a stack with the same 9 nm thickness, namely 6 nm Co + 3 nm Pd. The results of the VACNTs growth on both samples using a TiSiN barrier layer are presented in Figure 2.31.

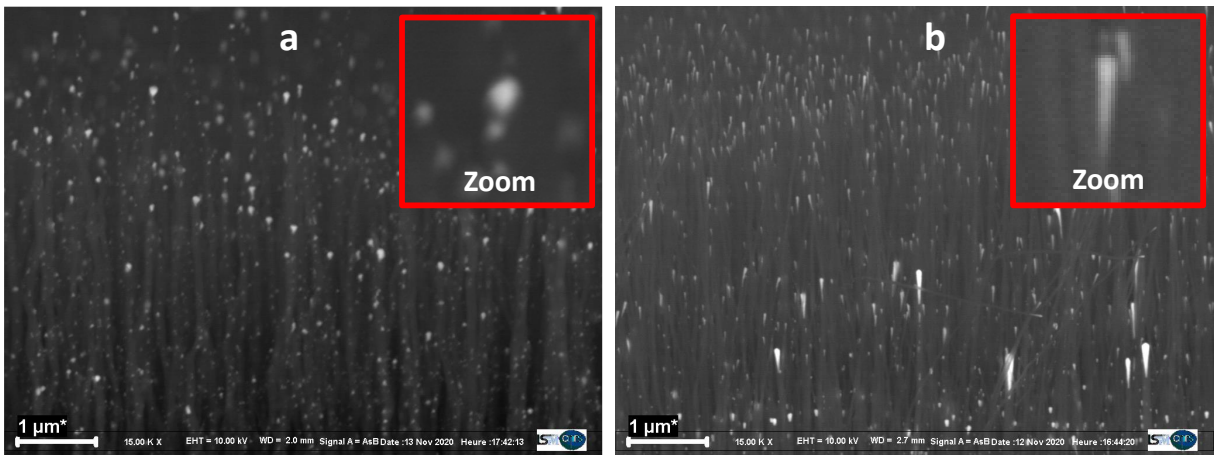

FIG 2.31 SEM (AsB) cross section view of the grown VACNTs at 200 W - 950°C on : a) Co 9 nm, b) Pd 3 nm / Co 6 nm.

As shown in the SEM images of Figure 2.31, the two samples present different nanoparticle morphologies ranging from spheroids to more elongated shapes. This is evidence that the presence of Pd itself enhances the VACNTs filling and leads to elongated shape metallic nanoparticles at the tip. As discussed in the introduction, this behaviour could be the result of the lowering of the melting point of the miscible system (Co + Pd) thus promoting the sliding in the internal canal.

2.4.8 Optimal VACNTs filling conditions

Using the optimized parameters: plasma power of 200 W of and temperature of 950°C, we proceeded to the growth of VACNTs, departing from a stack exhibiting higher Pd thickness and higher total thickness, namely: Pd 6 nm / Co 9 nm bilayer deposited onto Si substrates with pre-deposited TiSiN barrier layer. SEM images obtained with different angles and detectors are presented in Figure 2.32.

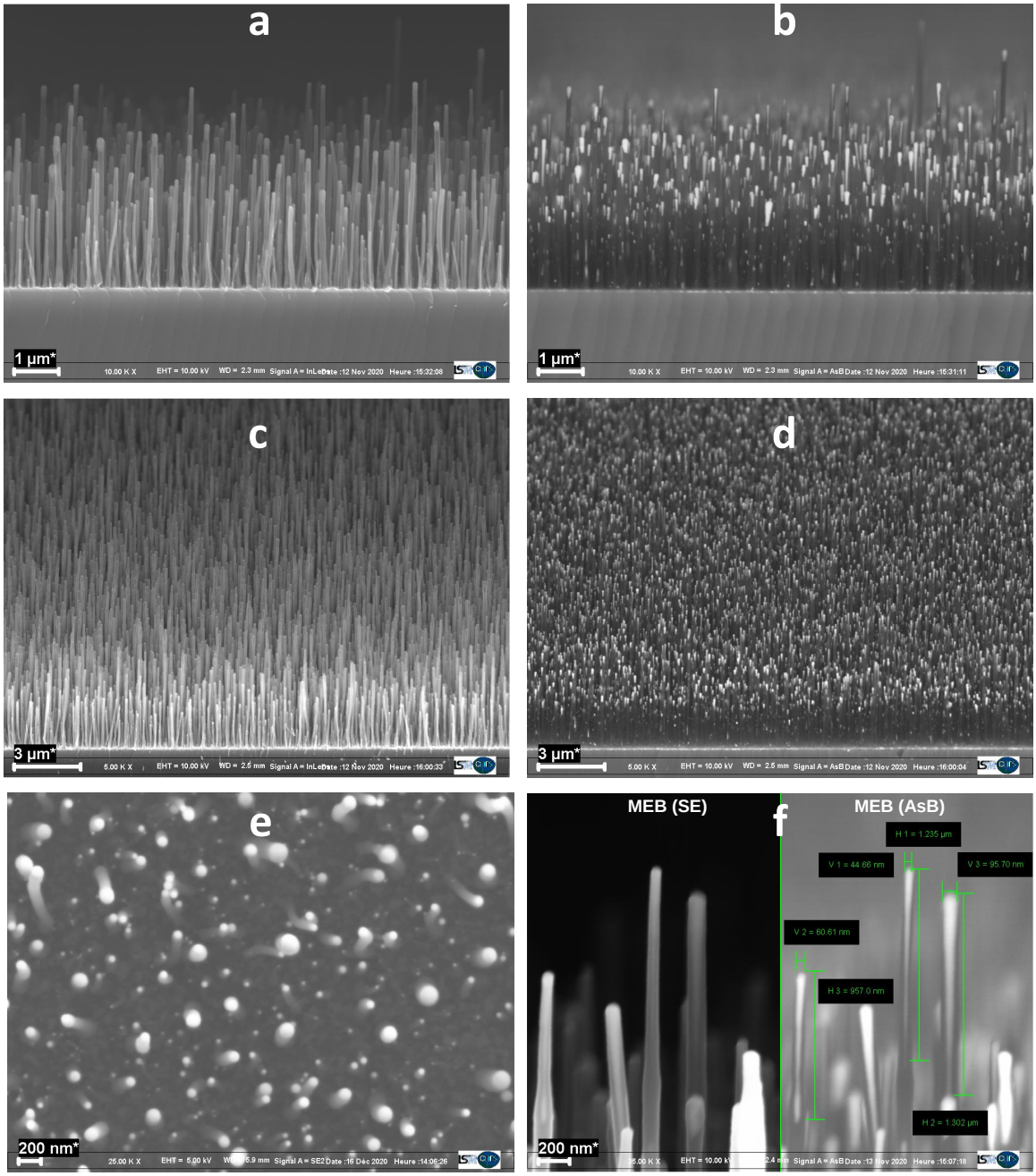

FIG 2.32: SEM images of the grown VACNTs at 200 W - 950°C Pd 6 nm / Co 9 nm / TiSiN. a) cross section SE b) cross section AsB , c) 20° angle view SE d) 20° angle view AsB e) Top view SE f) cross section SE + AsB.

As shown in Figure 2.32 a and Figure 2.32 b, highly aligned VACNTs with high filling density are synthesized. The Pd/Co ratio and the higher thickness of the configuration (Pd 6 nm / Co 9 nm) allowed obtaining nanotubes with larger diameters, thus larger internal canal that allowed the encapsulation of micrometer-long metallic nanowires, as shown in Figure 2.32 f. The higher thickness in this case, could be also responsible for the abundance of more metallic

matter on the substrate surface which is needed for the VACNTs filling. SEM angle views in Figure 2.32 c and Figure 2.32 d show a homogeneous distribution and a reproducibility of the synthesized VACNTs along the substrate surface, while the top SEM view in Figure 2.32 e shows good verticality of the VACNTs.

2.4.9 Statistical study

To get a clear idea on the filling state of the CNTs, a statistical study was performed, in order to evaluate the distribution of area, diameter, spacing and aspect ratio of the nanowires or the nanoparticles encapsulated in the VACNTs. For this purpose, the CNTs were placed in ethanol and underwent an ultrasonic bath for 20 min in order to detach the filled VACNTs from the substrate. After this protocol, the solution was dispersed on a Si wafer in order to take SEM images on isolated VACNTs, as presented in the Figure 2.33.

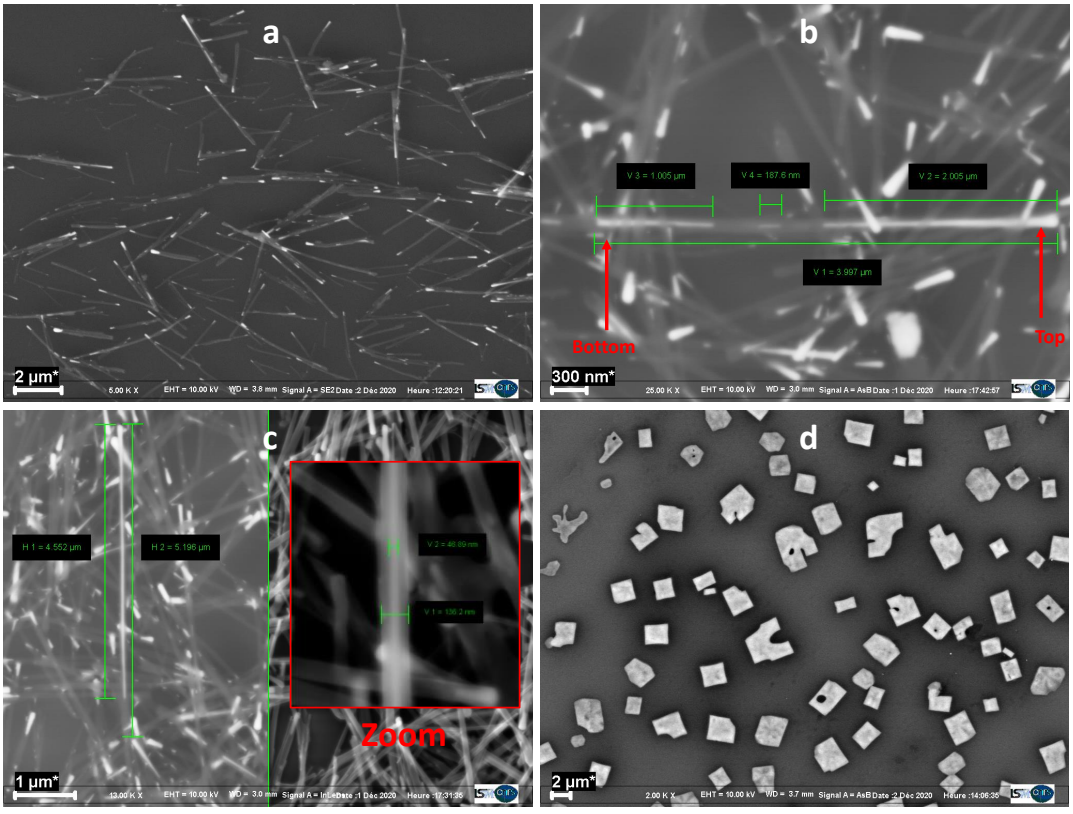

FIG 2.33 SEM images of the dispersed filled VACNTs and nanoparticles synthesized at 200 W - 950°C on Pd 6 nm / Co 9 nm / TiSiN.

The dispersed filled VACNTs in Figure 2.33 (a, b, c) show various fillings. Remarkably, the image in Figure 2.33 b shows a discontinuity in the filling of the VACNTs from the bottom (left) to the tip of the nanotube (right). This behaviour is a signature of atomic diffusion. The filling mechanism is complex including the filling of the nanotube from the bottom where there is an abundance of the metallic matter but could include also the elongation of the nanoparticle

situated in the superior part. This later hypothesis is diclined by observing the filled VCNTs shown in image in Figure 2.33 c; the encapsulated nanowire measures more than 4.5 µm in length and 46 nm in diameter. Such nanowire dimensions encapsulated in 5-micrometer long VACNTs can only be obtained through a continuous filling of the internal canal during the growth. Otherwise, the catalytic nanoparticle is either too small to be elongated to such length or too big to catalyse a 136 nm carbon nanotube diameter, as clearly shown in the zoom inserted in Figure 2.33 c.

Finally, Figure 2.33 d shows nanocube-shaped nanoparticles found in the proximity of the dispersed VACNTs. This could be indication that the deactivated catalyst nanoparticles left at the bottom. It would be interesting to know the composition of these nanocubes that might help to understand the filling mechanism better. Unfortunately, due to their small size ~5 to 10 µm, EDX measurements with the equipements at hand were not possible.

The VACNTs images were analysed using the software "image J". The derived distributions of total area, diameters, spacing and aspect ratio are summarized in the Table 2.5. The area and aspect ratio were estimated automatically from the software tools, whereas the diameter of the nanowires was measured one by one in order to consider the diameter in the vertical direction, meaning that the calculated diameter is a direct indication of the internal canal of the VACNTs. Finally, the spacing between VACNTs was also estimated one by one, using images of VACNTs before ultra-sonication.

The statistical study shows a large distribution in both area and diameter. This is an indication of the complex mechanism of the VACNTs filling that is not easily controlled. In term of size, the diameter distribution shows higher values that reaches 160 nm internal canal CNT diameter. This is expected considering the catalyst bilayer thickness (15 nm), especially considering the spacing between VACNTs that is equal to a mean 270 nm. Such large spacing between nanotubes is a result of the accumulation of catalyst nanoparticles that explains the higher size. Finally, the mean aspect ratio about 3 confirms that the VACNTs filling is not homogeneous throughout the sample and that not all VACNTs undergo a proper *in-situ* filling with metallic nanowires. Nevertheless, a maximum aspect ratio about 20 is observed on couple of nanowires which is considered a striking result of the filling experiment that needs more optimization.

Table 2.5: Area, diameter, spacing and aspect ratio distributions of the encapsulated metals inside dispersed VACNTs.

	Mean	**Minimum**	**Median**	**Maximum**
N total:	691 nanoparticles			
Area (nm^2)	19846	214	14640	175760
Diameter (nm)	71	33	70	162
Spacing (nm)	270	148	239	465
Aspect ratio	3	1	2	20

2.4.10 Structural observations of the filled CNTs

TEM images of VACNTs synthesized in optimal conditions (200 W - 950°C on Pd 6 nm / Co 9 nm / TiSiN) are presented in Figure 2.34. The upper part of the filled VACNTs show graphitic like curved planes surrounding the elongated metallic nanoparticle, where the tip of the nanoparticle is exposed.

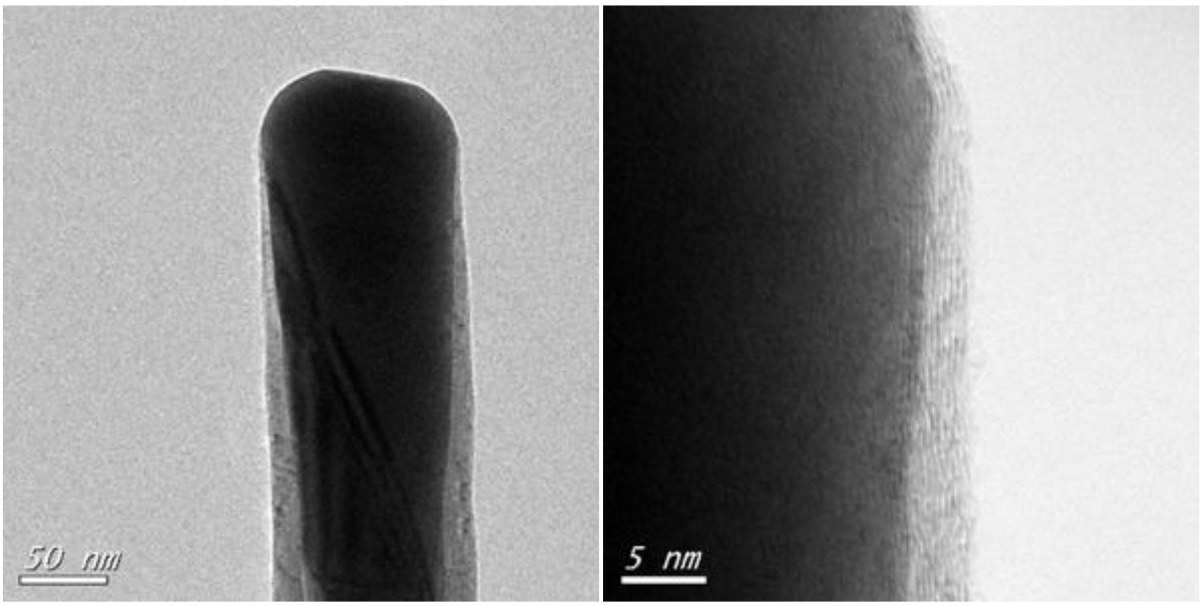

FIG 2.34 TEM images of the dispersed filled VACNTs synthesized at 200 W - 950°C on Pd 6 nm / Co 9 nm / TiSiN.

Chemical composition of the catalytic nanoparticle was investigated using spatially resolved electron energy loss spectroscopy (EELS). The obtained chemical contrast is presented in Figure 2.35. Electron energy loss spectroscopy images show that the filled nanotubes contain

mostly cobalt, the presence of Pd on the other hand is very limited inside the nanotubes. This might indicate that while Pd layer is indispensable for enhancing the filling state of VACNTs, Pd participates very weakly in the catalytic growth of VACNTs.

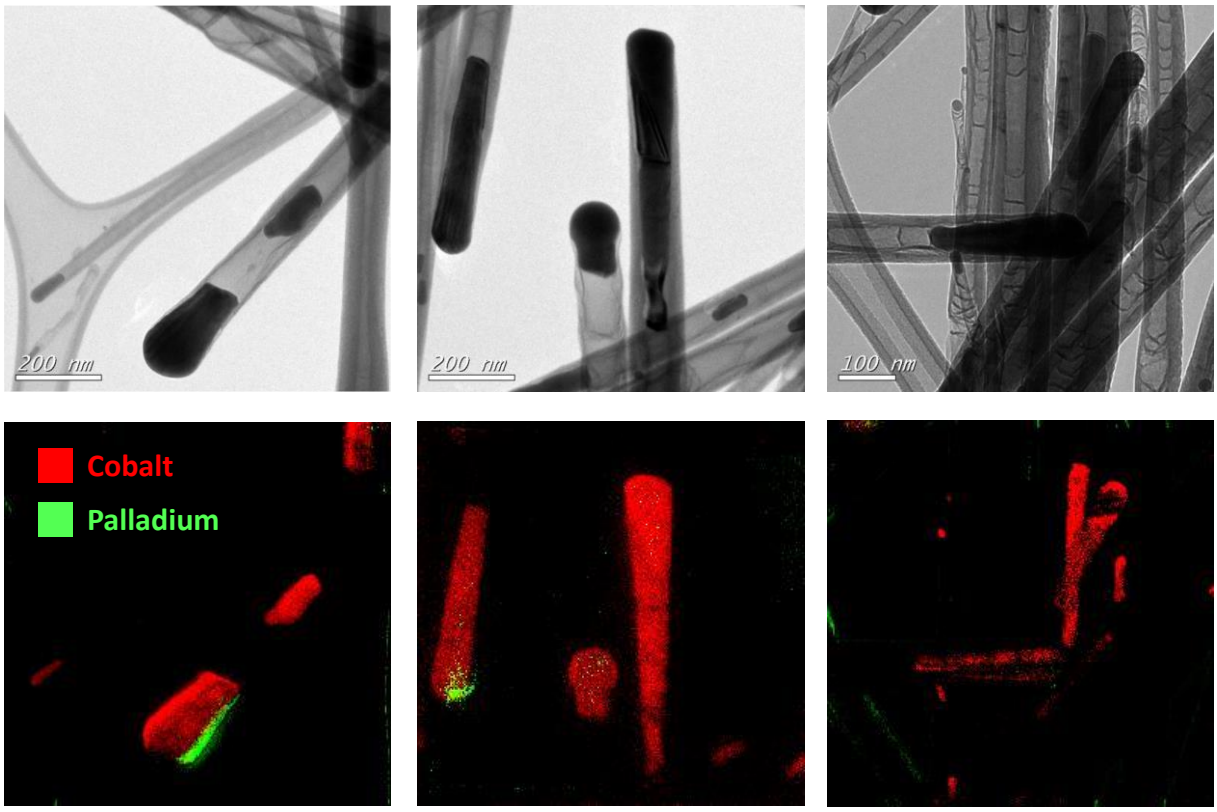

FIG 2.35 TEM images and their correspondent EELS images below of the dispersed filled VACNTs synthesized at 200 W - 950° C Pd 6 nm / Co 9 nm / TiSiN.

2.5 Conclusions

In this chapter, we first discussed the parameters that influence the solid dewetting of Co and Ni catalysts by an experimental study supported by the model of Zhong *et al.* stipulating a relationship between the height h of the catalyst film and the diameter of the particles D resulting from the solid dewetting. TiSiN barriers have proven to be particularly effective in stabilizing catalyst nanoparticles and best results were obtained by dewetting 3 nm cobalt film on TiSiN barriers. In the second part of this chapter, a parametric study was carried out on the most important growth parameters which allowed us to propose an optimal window for the growth of carbon nanotubes by PECVD on TiSiN barriers. Even if this study was conducted by trial-error methods, the results obtained are quite spectacular and deserve a more in-depth analysis, which we will conduct in **Chapter III**. Finally, the last part of **Chapter II** reports our

investigations of the routes to synthesize hybrid nanotubes composed by 1D nanocrystals/nanowires encapsulated in carbon nanotubes. Our experiments carried out in the Thales reactor were very conclusive. The use of the dewetted Co/Pd mixture on TiSiN barriers made it possible to fill the nanotubes during growth with up to 4.5 µm nanowires. The EELS analysis revealed that palladium only enters very little into the nanotubes which are mainly formed of cobalt. Investigations on the properties of Co/CNT hybrids are quite interesting since the inserted magnetic nanocrystals are aligned perpendicular to the substrate and their properties are expected to differ from that of the bulk material because of high anisotropy. This study will be presented in **Chapter IV**.

References

1. Lungu, C.P., et al., *Formation of nanostructured Re–Cr–Ni diffusion barrier coatings on Nb superalloys by TVA method.* Surface and Coatings Technology, 2005. **200**(1-4): p. 399-402.
2. V. Ciupina, R.V., C. P. Lungu, V. Dinca, M. Contulov, A. Mandes, P. Popov, G. Prodan *Investigation of the SiC thin films synthetized by Thermionic Vacuum Arc method (TVA).* The European Physical Journal D, 2012. **66**(4): p. 99.
3. Guha, S., et al., *Synthesis and characterization of Titanium Silicon Nitride (TiSiN) thin film: A review.* IOP Conference Series: Materials Science and Engineering, 2018. **377**: p. 012181.
4. E. J. Luber, et al., *Solid-state dewetting mechanisms of ultrathin Ni films revealed by combiningin situtime resolved differential reflectometry monitoring and atomic force microscopy.* Physical Review B, 2010. **82**(8): p. 085407.
5. Rose, F., et al., *Low surface energy and corrosion resistant ultrathin TiSiC disk overcoat.* Journal of Applied Physics, 2013. **113**(21): p. 213513.
6. Leroy, F., et al., *Influence of facets on solid state dewetting mechanisms: Comparison between Ge and Si onSiO2.* Physical Review B, 2013. **88**(3): p. 035306.
7. Zhang, C., et al., *Growth of vertically-aligned carbon nanotube forests on conductive cobalt disilicide support.* Journal of Applied Physics, 2010. **108**(2): p. 024311.
8. Yang, J., et al., *Comparison of carbon nanotube forest growth using AlSi, TiSiN, and TiN as conductive catalyst supports.* physica status solidi (b), 2014. **251**(12): p. 2389-2393.
9. Khalilov, U., et al., *Nanoscale mechanisms of CNT growth and etching in plasma envirement.* Journal of Physics D: Applied Physics, 2017. **50**(18): p. 184001.
10. Zhong, G., et al., *Growth of Ultrahigh Density Single-Walled Carbon Nanotube Forests by Improved Catalyst Design.* ACS Nano, 2012. **6**(4): p. 2893 – 2903.
11. Hofmann, S., et al., *Effects of catalyst film thickness on plasma-enhanced carbon nanotube growth.* Journal of Applied Physics, 2005. **98**(3): p. 034308.
12. Sugime, H., et al., *Ultra-long carbon nanotube forest via in situ supplements of iron and aluminum vapor sources.* Carbon, 2021. **172**: p. 772-780.
13. Andalouci, A., et al., *Morphological and magnetic study of plasma assisted solid-state dewetting of ultra-thin cobalt films on conductive titanium silicon nitride supports.* Thin Solid Films, 2020. **703**: p. 137973.
14. Byrne, E.M., et al., *Multiwall nanotubes can be stronger than single wall nanotubes and implications for nanocomposite design.* Phys Rev Lett, 2009. **103**(4): p. 045502.
15. Kuznetsov, V.L., et al., *Raman spectra for characterization of defective CVD multi-walled carbon nanotubes.* physica status solidi (b), 2014. **251**(12): p. 2444-2450.
16. Pimenta, M.A., et al., *Studying disorder in graphite-based systems by Raman spectroscopy.* Phys Chem Chem Phys, 2007. **9**(11): p. 1276-91.
17. Aqra, F. and A. Ayyad, *Surface energies of metals in both liquid and solid states.* Applied Surface Science, 2011. **257**(15): p. 6372-6379.
18. Jourdain, V. and C. Bichara, *Current understanding of the growth of carbon nanotubes in catalytic chemical vapour deposition.* Carbon, 2013. **58**: p. 2-39.
19. Joshi, R.K., Yoshimura, M., Tanaka, K., Ueda, K., Kumar, A., & Ramgir, N. , *Synthesis of vertically aligned Pd2Si nanowires in microwave plasma enhanced chemical vapor deposition system.* The Journal of Physical Chemistry C, 2008. **112**(36): p. 13901-13904.
20. Avigal, Y., & Kalish, R. , *Growth of aligned carbon nanotubes by biasing during growth.* Applied Physics Letters, 2001. **78**(16): p. 2291-2293.

Chapter III: VACNTs growth modeling

In this chapter, we investigate methodologies for modeling of Plasma Enhanced Chemical Vapor Deposition (PECVD) reactor used for vertically aligned carbon nanotube VACNTs growth. Different complementary modeling approaches will be proposed to explain the temperature-dependent growth kinetics, to identify the most important process parameters and their limits for nanotube formation thereby optimizing the process. The objective of this chapter is to provide comprehensive approaches to quantitatively correlate process parameters with growth conditions.

3.1 Modeling approach

Modeling is a useful tool to alleviate the economical and time burden required for sample preparation. In our specific PECVD reactor, a complete experiment including sample preparation, synthesis and characterization could last all day while simulating a synthesis condition would take from a few seconds to hundreds of minutes with the possibility to run multiple simulations simultaneously. However the main reasons for which we have developed modeling is to better understand VACNTs growth and to optimize the process. In PECVD, indeed, VACNTs growth has been hampered by the lack of quantitative understanding of gas and surface chemistries, at the scale and quality required for applications. Modeling hence offers more understanding of the underlying mechanisms responsible for carbon nanotubes growth, such as temperature and chemical species temporal and spatial profiles, reactions schemes, and most importantly since carbon nanotubes synthesis is a catalytic process, an insight into the heterogeneous phase chemistry that takes place between the gaseous chemical species and the catalyst nanoparticles leading to VACNTs nucleation and growth. This represents a major tool since in-situ diagnostic of such kinetic phenomenon on the nanoscale level requires cutting edge equipment. Hence the model is used to study the carbon precursors generated by the decomposition of methane in the presence of hydrogen and oxygen in the plasma, in order to identify the key species and the effect of different parameters in order to optimize the overall process.

A two-dimensional model of the PECVD process was implemented in axisymmetric configuration by using the commercial software ANSYS Fluent. Computational fluid dynamics (CFD) simulations with different operatory conditions were performed using this model in parallel to experiments in order to investigate the effect of each process parameter on gas temperature, gas and surface species distributions as well as VACNTs growth rate. For this purpose, we first build the reactor geometry, Then, in order to take in consideration, the

macroscopic phenomena such as fluid motion and energy and mass transfer, the reactor volume occupied by the fluids is divided into discrete cells, *via* meshing the entire geometry. This allows the governing equations to be solved in each discrete cell and then interpolated across the whole volume to display the results on the full reactor scale. Meshing is a critical step as it controls the model accuracy and convergence. The smaller the cells size, the more accurate the solution, however, the trade-off is that the higher the accuracy, the larger the computational times become. At this step, it must be noticed that the use of detailed chemistry can make the problem intractable due to the enormous computational cost. It should be noted that each species intervenes in its own partial differential equation. Reducing the number of species considerably reduces the calculation time. Hence, to obtain an optimal balance between accuracy and computational time, a sensitivity study was performed in a 0D model using CHEMM FORTRAN code [1] developed at LSPM. Due to its low computational demands, the 0D model is used in order to reduce the size of chemical scheme, *i.e.* reduce the number of species and reactions by the rapid identification of key species and dominant reactions. Finally, the reduced chemical set that includes only relevant species and reactions, thermodynamic properties and operatory conditions will be further introduced into the 2D Model in order to simulate the PECVD growth of VACNTs in the reactor.

3.1.1 Zero-dimension model formulation for nanotube growth

A non-equilibrium energy exchange and chemical reaction model was developed for specific hydrogen/methane/oxygen plasmas used in carbon nanotube growth. The aim is to simulate time-evolution bulk plasma properties like electron density, electron temperature and degree of dissociation, and to help understand how to optimize the process. In this direction, the general non-equilibrium three-temperature model is reduced to 0D in chemistry, vibrational and electronic energies. This extends the classical chemistry formulation to non-equilibrium plasma with three temperatures, namely gas temperature T, electron temperature Te and vibrational temperature Tv each describing a Maxwell/Boltzmann distribution for its respective energy mode as schematically shown in Figure 3.1. The plasma reactor is conFigured to form a microwave resonance cavity with an electric field distribution in the cavity. Due to their low mass and negative charge, electrons gain energy more easily from the electric field than neutral species and ions. This leads to a much higher electron temperature Te as compared to the gas temperature T. In addition, electron-vibration exchange allows the vibrational temperature to be slightly higher than gas temperature, as measured for pure hydrogen in our reactor by

Coherent anti-Stokes Raman scattering spectroscopy (CARS) [2]. The energy absorbed from the electric field is lost by electrons *via* collision processes involving the atoms and molecules and described in detail by Scott *et al.* in our previous work [2].

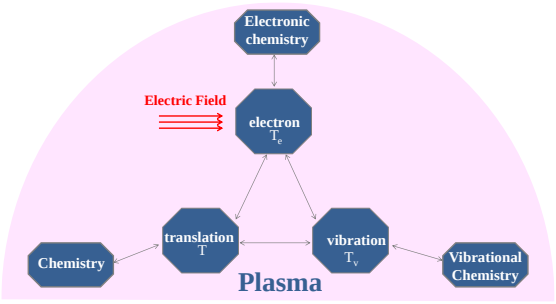

FIG 3.1 Three temperatures thermochemical model used to describe $H_2/CH_4/O_2$ plasma.

The electron energy balance is hence given by the net absorbed power from the microwave electromagnetic field and the exchange between various modes of energy and electrons as schematically represented in Figure 3.1. Subsequently, highly energetic electrons can activate the gas and initiate reactions by electron impact collisions. Mass balance equations for the different plasma species such as molecules, radicals, atoms, ions and electrons can be solved based on production and loss terms, as defined by chemical reactions. For nanotube growth, the chemical model is represented by various positive ions, H^+, H_2^+, H_3^+, CH_4^+, CH_3^+, CH_2^+, $C_2H_2^+$, $C_2H_4^+$ and $C_2H_5^+$, negative ion H^- and electrons compose the plasma. A large variety of neutral species, composed by hydrocarbon radicals and molecules, atomic hydrogen H and oxygenated radicals (O, OH ...) and molecules (H_2O, CO, CO_2 …) together with polycyclic aromatic hydrocarbons (PAHs) were considered in this model. The full model is composed by 134 species involved in 471 gas-phase reactions listed in Table S1 in **Appendix III (Table S1)** along with their corresponding rate coefficients. This makes the plasma a highly reactive, but extremely complex medium to calculate. In contrast, Khalilov *et al.* [3] used a computational approach supported by experiments to study the plasma-based formation of carbon nanotubes at the level of nickel nanoclusters. Since sampling the atomic positional fluctuations in a picosecond molecular dynamics simulations are computationally very expensive, only 9 plasma-generated carbon precursors (C, C_2, C_2H, CH_3, CH_4, C_2H_2, C_6H_6, C_7H_8, and C_8H_{10}) were considered by Khalilov *et al.* [3]. Nevertheless, to initiate CNT growth, the most efficient intermediates are expected to be first produced in the gas phase and then diffuse on the catalyst surface to be chemisorbed and/or physisorbed to nucleate the nanotube [4]. In our approach, taking advantage of the low computational time involved in 0D thermochemical modeling, to better represent the number of carbon atoms provided for CNT

formation, the decomposition of methane coupled with oxygen is calculated with the largest variety possible of gas phase intermediates including reactive species, free radicals, organic compounds and PAHs. Indeed, the CNT growth efficiency in a microwave PECVD process strongly depends on their relative concentration and reactivity. Then, for more accurate engineering optimization in a larger multidimensional model, this mechanism could be easily reduced *via* sensitivity and uncertainty analyses. This allows the calculation of the overall uncertainty of simulation results and the identification of the most important input parameters to reduce the chemical system without losing important kinetic and dynamic details. In our 0D model, plasma reactions are composed by vibrational kinetics of H_2 molecules driven by vibrational temperature Tv and represented by the dissociative attachment (reaction 1 in Table S1 in **appendix B.1**. Electron-impact reactions are composed by ionization of atoms and molecules, dissociative attachment, dissociative recombination and electron detachment. Electron impact reactions with the various molecules and radicals, included in the model are treated by referenced rate coefficients driven by electron temperature Te with the assumption of the electron energy distribution function (EEDF). The reaction rates for ionization of H_2 and H by electrons are calculated from cross-sectional data from Buckman and Phelps [5] using integration over the electron energy distribution function that is assumed to be Boltzmannian at an electron temperature Te. Heavy particle reactions, including charge exchange and the recombination of atoms and ions and methane pyrolysis reactions with aliphatic, aromatic and polycyclic aromatic hydrocarbons (PAHs) ranging from two to five fused aromatic rings deduced from Marinov *et al.* [6] and calculated at gas temperature T.

The 0D model is described in detail in the *Supplementary information* of Pashova *et al.* for the growth of graphene from H_2/CH_4 mixture [7]. We report here the most important constitutive equations to facilitate the discussion. The model may address the state of homogeneous plasma in both transient and steady-state. Even in steady-state, the computational method requires a solution of the related transient algebraic differential equations. Therefore, the transient conservation equations are presented here. Uniform stagnation flow field is assumed to be present in the region between the plasma and the substrate. Since the flow is laminar with a Reynolds number < 2000, the viscous and diffusive effects are mostly located in a thin region near the substrate. In stagnation flow geometry, momentum and thermal boundary layers exist with a thickness denoted by δ and δ_T, respectively. Within the boundary layer, the velocity rapidly decreases to zero at the surface, and the gas temperature decreases from its plasma value to that of the temperature-controlled substrate. Outside the boundary

layers, the flow behaves as if it were nearly inviscid. The relative thickness of the boundary layers, δ/δ_T depends on the relative importance of viscous and thermal diffusion represented by Prandtl number Pr. In our conditions, we estimated the thermal boundary-layer thickness from CARS measurements in pure hydrogen at ~1.6 cm above the substrate [2]. According to Dandy and Yun [8], thermal boundary-layer thickness may be used directly as an approximate concentration boundary-layer thickness for many different chemical vapor deposition systems. For microwave plasma, transport of species is hence diffusion-limited near the substrate and estimate the boundary layer thickness is of the order of, but somewhat less than, the plasma ball dimension. In our approach, the plasma composed by ns species is represented by one point located at a distance of ~1.6 cm above the substrate. We can write for each species i composing the plasma, the related transient conservation equations as a balance between a chemical source term ω_ι and a loss term ξ_i due mainly to the diffusion from the center of the active plasma zone to the surface of the substrate, where the nanotubes grow. The mass balance is represented by the equation

$$\frac{dY_i}{dt} = (\omega_i - \xi_i)\frac{W_i}{\rho} \qquad \text{i=2,.., ns} \qquad (1)$$

where i is the species index and 1 is the index of the major species (which is supposed to be H_2 for nanotube growth), Y_i is the mass fraction of species i, ω_ι is the chemical molar production of species i ($mol.cm^{-3}.s^{-1}$), ξ_i is the chemical molar loss due to diffusion of species i ($mol.cm^{-3}.s^{-1}$), W_i is the molecular weight ($g.mol^{-1}$), ns is the total number of species, ρ is the total mass density ($g.cm^{-3}$) and t is the time (s). Note that chemical loss terms ξi are related to the recombination of H-atoms, hydrocarbon species and ions at the substrate wall. Equation (1) is solved in time until the steady state is reached. In addition, we imposed the normalization condition because the total mass fraction is given by the following summation equation

$$\sum_{i=1}^{ns} Y_i = 1 \qquad (2)$$

The steady state electron energy balance is given by the absorbed power from the microwave electromagnetic field and the exchange between various modes of energy and electrons. The loss term is associated with electron-ionization, electron-dissociation and molecular-atomic radiation:

$$P_{abs} - Q_{ev} - Q_{te} - Q_{ei} - Q_{ed} - Q_{ev}^{1e} = 0 \qquad (3)$$

where the subscripts e, v and t indicate the electronic, vibrational and translational modes of energy, respectively, $P_{abs} = \frac{P_{mw}}{V}$ is the net absorbed power in the plasma ($W.m^{-3}$), P_{mw} is the total input power (W), V is the plasma volume (m^3), Q_{te} is the exchange of electronic energy with translation/rotation for the major species H_2 and C_2H_2 ($W.m^{-3}$), Q_{ei} is the energy loss by electron ionization ($W.m^{-3}$), Q_{ed} is the energy loss by electron dissociation ($W.m^{-3}$), and Q^{1e}_{ev} is the electron energy loss by excitation to the H_2 singlet states $B_1\Sigma_\upsilon^+$ and $C^1\Pi_\upsilon$ ($W.m^{-3}$). The loss of energy occurs *via* collision processes involving the atoms and molecules. Because of the predominance of hydrogen in the system, the energy exchange model includes only hydrogen, whereas the chemical reaction model includes both hydrocarbon and hydrogen. The vibrational energy balance is provided by the exchange between various modes of energy and vibration:

$$Q_{tv} + Q_{ev} + Q^{1v}_{ev} = 0 \qquad (4)$$

where Q_{tv} is the exchange of vibrational energy with translation/rotation ($W.m^{-3}$), Q_{ev} is the direct exchange of vibrational energy with electrons ($W.m^{-3}$) and Q^{1v}_{ev} is the vibrational excitation of ground-state H_2 by electrons via excitation of singlet electronic states ($W.m^{-3}$).

The total energy-conservation equation is given by:

$$\rho\left[\bar{c}_p\left(1-Y_e\right)\frac{dT}{dt} + \bar{c}_{pe}Y_e\frac{dT_e}{dt}\right] = P_{abs} - Qev - Qte - Qei - Qed - Q^{1e}_{ev} - Ah(T - T_0) - \sum_{i=1}^{ns} h_i\,\omega_i W_i \qquad (5)$$

where ρ is the total gas density; $\bar{c}_p$ is the mean gas specific heat, excluding the electronic contribution because the electron temperature is assumed to substantially differ from the gas temperature; Y_e is the mass fraction of electrons in the plasma; and $\bar{c}_{pe}$ is the electron specific heat. The right-hand terms in Eq. (5) account for the energy balance with the same terms developed in Eqs. (3) and (4). The heat released by convection is considered using a heat transfer convection coefficient h between the plasma gas mixture and the surrounding reactor wall with a surface area A and a temperature T_0. The last term on the right-hand side of Eq. (5) accounts for the accumulated heat release from the gas phase, where h_i, ω_i and W_i are the specific enthalpy, chemical molar production and molecular weight of species i, respectively. Individual species thermodynamic properties were calculated using the NASA seven-coefficient polynomial fits format. The heat released from surface reactions was neglected in the 0D model. Energy exchange terms in Eqs. (3-5) are explained in detail in Scott *et al.* [2]. Chemical source terms in Eq. (1) describe the chemical kinetics of non-equilibrium $H_2/CH_4/O_2$

plasma and are calculated according to the kinetics scheme of the table in **appendix B.1**, with electronic reactions driven by T_e and the rest of the reactions driven by gas temperature T. The FORTRAN computer code developed to solve the set of differential algebraic equations (DAE) uses a backward differentiation formula (BDF) method implemented in the LSODI package which is specifically adapted to stiff problems such as chemical kinetics [9]. The 0D model was used to perform a global sensitivity analysis in order to identify the key species and reactions necessary for CNT growth, thereby reducing the chemical scheme with the idea to use it in a higher two-dimensional model.

3.1.2 Two-dimension model formulation for nanotube growth

As mentioned before, the 0D model was also used to perform a global sensitivity analysis in order to identify the key species and reactions necessary to CNT growth by involving gas-phase and surface reaction mechanisms, thereby reducing the schematic scheme introduced in a higher dimensional model, the 2D PECVD model is a steady state (2D) computational fluid dynamics (CFD) model where fluid motion and energy transfer equation are resolved in order to take in consideration the macroscopic phenomena. Both geometry description and theoretical assumptions are well detailed in [10]. In this work, an optimization of the model was implemented in order to introduce oxygenated species in the reactional mechanism of CNT growth; the considered gas phase chemistry involves 23 neutral species and 100 reactions. The gas phase chemistry model describes homogeneous reactions that influence the species concentration distribution near the deposition surface through the production/destruction of chemical species in the gas phase. Each reaction is assumed to be reversible. The temperature dependence of the forward rate constants is usually described through a modified Arrhenius type expression.

The reactor set-up is showed in Figure 3.2 a. Only the quartz bell whose halot is visible in the Figure 3.2 b has been modeled. The rest of the reactor such as the Faraday cage, the antennas etc. which are important for the establishment of the electromagnetic field are not concerned by the reactive gas flow and are therefore ignored. The reactor geometry was introduced in the software using ANSYS Design Modeler. Axisymmetric 2D computation field was created as represented in Figure 3.2 c. The mesh was implemented using ANSYS Meshing application with Quad/Tri cells in all zones, with a total number of 3944 cell and 4177 nodes. Meshing was refined as we get closer to the substrate due to the strong gradients of temperature

and concentrations as represented in Figure 3.2. Both reactor geometry and meshing model are described in detail in Hinkov *et al* [10, 11].

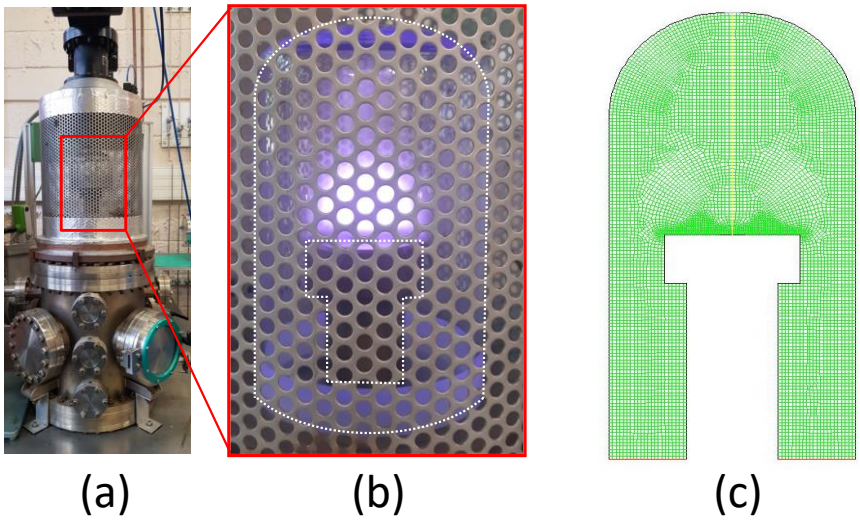

FIG 3.2 Bell Jar reactor (a) Photography of the set-up ; (b) Quartz reactor through Faraday cage **; (c)** Geometry and mesh modeling obtained by ANSYS meshing software.

Meshing allows the governing equations to be solved in each discrete cell and then interpolated across the whole volume to display the results on the full reactor scale; these equations include the conservation equations of momentum, mass, and energy, as well as the continuity equation and the ideal gas equation of state. Finally the boundary and the initial conditions were defined: the temperature of the reactor walls and of the substrate holder was set at 300 K. The substrate surface was fixed at 1 cm^2 corresponding to the area of the catalyst exposed to the flux from the plasma. Inlet velocity was calculated according the gas flow rates of the mixture and the section of the inlet tubes. A convergence criterion of 10^{-3} was imposed on the residuals of the continuity and momentum equations, while the value of 10^{-6} is considered for the residuals of the energy equation.

In order to reduce the complexity and computational burden of the 2D model, some assumptions were considered: (i) the plasma is in Local Thermodynamic Equilibrium (LTE). This assumption allows us to define a unique temperature of all plasma species in localized areas in the plasma, fluid motion is considered in laminar flow since it is small inlet flow rates are characterized by relatively low values of the Reynolds number; (ii) The plasma is modeled using a steady state time formulation; Axisymmetric physical domain; (iii) The radiative losses are neglected; (iv) only neutral species are involved in the gas-phase and surface chemistry.

The low ionization rate of the plasma and the relatively high growth rate of the nanotubes suggest that the contribution of the ions to the CNTs growth is of the second order.

In the gas phase reaction model we describe the dissociation of $CH_4/H_2/O_2$ in the plasma by electron impact. Totally, 23 species are incorporated in the model including 8 oxygenated species (H, H_2, CH_4, CH_3, CH_2, CH_2*, CH, C, C_2H_6, C_2H_5, C_2H_4, C_2H_3, C_2H_2, C_2H, C_2, O, O_2, OH, H_2O, HO_2, H_2O_2, CO et CO_2) governed by 100 reactions as listed in **Appendix B.2**, the reaction rate are considered as a modified Arrhenius equation that is temperature dependent, the gas phase reactions are presented in Table SII, including: The addition and dissociation reaction of atomic hydrogen with hydrocarbon species , the recombination of carbon radicals and the reaction of oxygenated species with hydrogen and hydrocarbon species.

3.1.3 Surface chemistry

Another valuable insight provided by the 2D model is an estimation of CNT growth rate on the ($Co/TiSiN/SiO_2/Si$) surface. This was achieved by incorporating specific surface chemistry in the 2D model. Since nanotube surface chemistry is controlled by the local terminated bond and not by the bulk bond, only terminal cobalt atoms attached to nanotubes will be considered in our surface chemistry model. For this purpose, a surface nucleation density value is needed in order to define the geometrical space where surface reactions take place to grow nanotubes. A value of the molar surface site density Γ (moles.cm^{-2}) is introduced to represent the carbon moles attached to the cobalt surface per 1 cm^2 of the substrate. To estimate Γ, we first assume that the surface of the substrate is entirely covered with cobalt atoms. Hence we introduce a first correction through a fraction ϕ_1 due to solid dewetting of the cobalt. A final correction *via* the factor ϕ_2 is necessary to consider only the cobalt atoms attached to a multi-walled nanotube of given inside (d) and outside (D) nanotube diameters. This analysis aims to provide a roadmap for estimating asymptotic values of Γ to be used in the surface chemistry model. For a fully covered substrate with cobalt, the surface density of terminated cobalt atoms can be simply deduced from crystallographic and geometric considerations. For the face-centered cubic fcc-cobalt, the surface density is given in the three crystallographic orientations (111), (100) and (110) by repectively:

$$\frac{4}{\sqrt{3}a_0^2}\ for\ Co(111),\quad \frac{4}{a_0^2}\ for\ Co(100),\quad and\quad \frac{4}{\sqrt{2}a_0^2}\ for\ Co(110) \qquad (6)$$

Where a_0 is the cobalt lattice parameter a_0=3.54 Å. Application of Equation (6) leads to surface site densities $\Gamma_{111}=3.06\times10^{-9}$ moles/cm^2, $\Gamma_{100}=2.65\times10^{-9}$ moles/cm^2 and $\Gamma_{110}=1.87\times10^{-9}$ moles/cm^2. These values would thus constitute maximum limit values if the entire substrate

were covered with cobalt. Solid dewetting induces shrinkage of the covered surface by generating isolated cobalt nanoparticles of diameter D. Assuming uniform diameter, the fraction of circles of diameter D on the plane due to solid dewetting is ϕ_1 =0.907 for a compact hexagonal lattice and ϕ_1 =0.82 for random packing [12]. Compact stacking is the way of arranging these particles in order to have the maximum density of nanoparticles N_{max} in the plane. Hence, in a compact hexagonal lattice arrangement:

$$N_{max} = \frac{2}{\sqrt{3}\,D^2} \quad (7)$$

The density of nanoparticles is minored by the de-wetting limit N_{dew} that depends on the diameter of the catalyst nanoparticles D and the contact angle θ between the catalyst and the support as estimated by the Robertson *et al*. model, [13]

$$N_{dew} = \frac{4\,(1+\cos(\theta))}{\pi D^2(2+\cos(\theta))} \quad (8)$$

For cobalt and nickel de-wetted on standard oxide surfaces, a typical value of θ=90° leads to $N_{dew}=0.6/D^2$. Indeed, the driving force of de-wetting is the difference in surface energy between the metal and the support. Experimental surface energies expressed in J/m^2 reported by Robertson *et al.* [13] are: Co(2.22) and Ni(2.08) much higher than for $TiSi_2$(0.8-0.9) or SiO_2(0.043-0.106). Rose *et al*. (see [5] in Chapter II] reported low surface energy of 0.6 J/m^2 for TiSiN. We can then extrapolate this model to de-wetting cobalt on TiSiN. In Figure 3.3, particle density is plotted versus the initial catalyst thickness h and the nanoparticle diameter D~6×h in fully compact and de-wetting limits together with the measured value $N_{exp}=1.2 \times 10^{11} \pm 0.1$ cm^{-2} typical for de-wetting of 3 nm Co on TiSiN substrates in our conditions [14, 15].

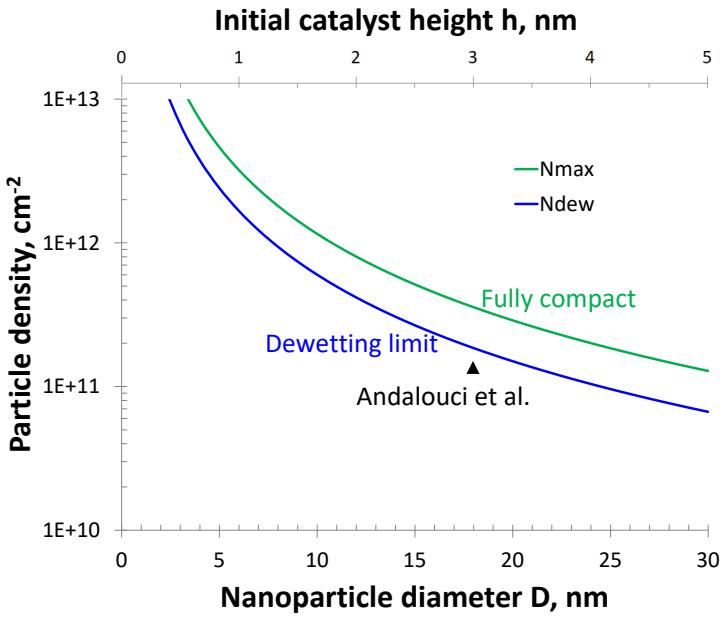

FIG 3.3 Catalyst particle density estimated theoretically in fully compact arrangement and de-wetting limit. The initial catalyst film thickness is h and the nanoparticle diameter is D. Experimental value for h=3 nm by Andalouci *et al*. [14, 15].

Thus, as schematically shown in Figure 3.4 a, correcting the data obtained from equation 6 by the factor ϕ_1, Γ varies between 1.54×10^{-9} moles/cm^2 for a random arrangement of Co(110) and 2.78×10^{-9} moles/cm^2 for a compact hexagonal arrangement of Co(111). In addition, as shown in Figure. 3.4 b, a second correction by a factor ϕ_2 is necessary to consider only the cobalt atoms attached to the nanotubes. This is estimated by projecting the CNTs structure on the plane and by counting the number of atoms ending the nanotube. Multiplying the carbon atoms per nanoparticle by the density of nanoparticles and dividing by the Avogadro number leads to the final site density Γ, thereby allowing calculating the deposition rate of CNT as shown in Figure 3.4 c.

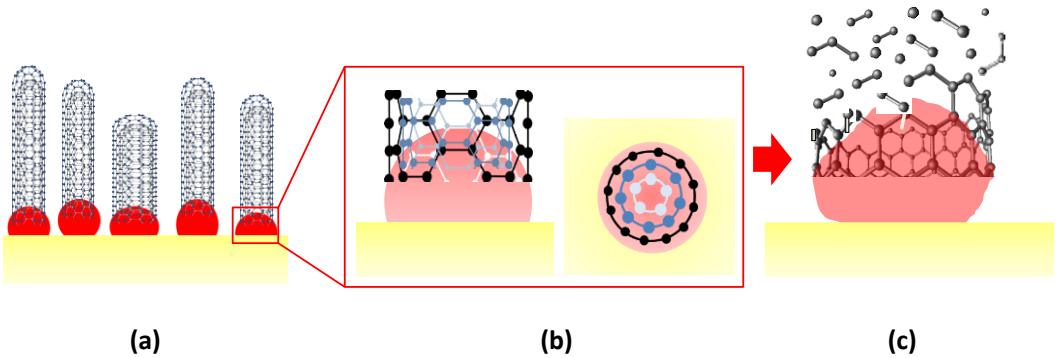

FIG. 3.4 Nucleation density estimation: (a) statistical analysis of VACNTs density, (b) atom number projected on the nanoparticle surface, (c) estimation of CNT deposition rate.

Based on our HRTEM measurements of multi-walled nanotubes, internal diameter varies from 4 to 8 nm and external diameter varies from 12 to 17 nm. For these conditions, the number of walls was found to vary from 11 to 17 walls. Hence an average number of walls of 14 ± 3 were defined. In reality, a multi-walled carbon nanotube (MWCNT) is a complex interlocking of several chiralities and circumferences of successive cylinders. In addition, the structure of constitutive tubes is incommensurate in the sense that the ratio between the periods of tubes in the axis direction is irrational, indicating that there is no translational symmetry [16]. Thus, to facilitate the reasoning, we will study only the two limiting cases of MWCNT exclusively made up of zig-zag (n, 0) or armchair (n, n) nanotubes following Hamada indexes. In order to calculate the number of carbon atoms projected on the surface of cobalt nanoparticle for each nanotube wall with a certain diameter, the software «nanotube modeler» developed by © JCrystalSoft, 2005-2018 was used. To simplify the problem, two configurations were chosen either armchair or zig zag for which the number of atoms as a function of nanotube wall number starting from a first nanotube wall with 4 nm diameter is represented in Figure 3.5. From this Figure we can see that the zig zag structure offers less atom number projected on the surface as compared to the armchair structure.

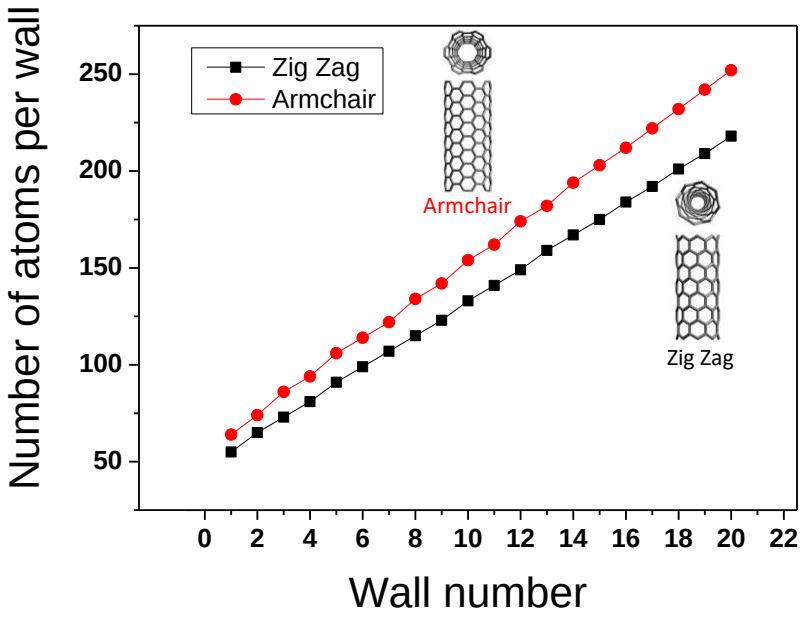

FIG 3.5 Number of atoms per wall as a function of wall number in MWCNT with internal diameter of 4 nm.

Starting from the measured particle density $N_{exp}=1.2 \times 10^{11} \pm 0.1$ cm^{-2} and taking into account the number of projected atoms given in Figure 3.5, we can propose the domain of variation of the nucleation site density Γ for both armchair and zig zag nanotubes. As shown in

Figure 3.6, for a MWCNT with 11 to 17 walls and internal diameter of 4 nm, the nucleation site density is bounded in the interval $2.0\times 10^{-10} < \Gamma(\text{moles/cm}^2) < 5.3 \times 10^{-10}$.

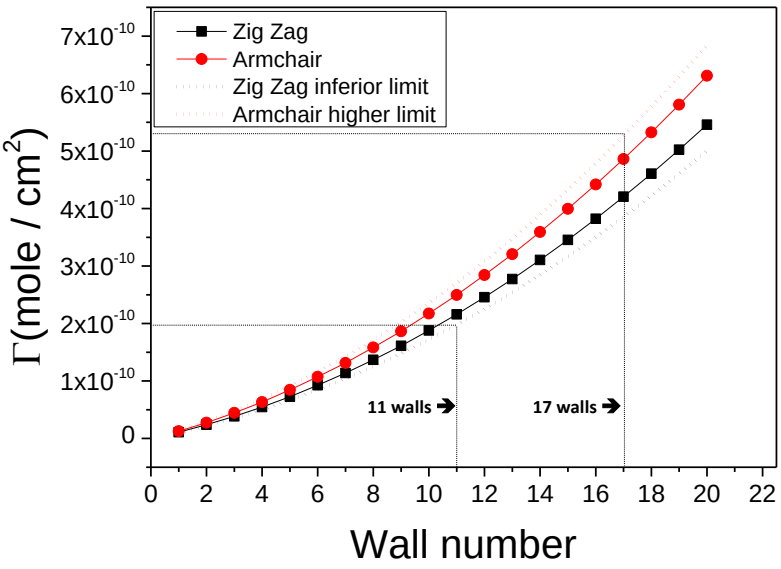

FIG 3.6 Nucleation site density as a function of wall number for MWCNT with internal diameter of 4 nm.

On the surface sites, we need to describe the chemical state in terms of surface species site fractions that become dependent variables in the chemically reacting-flow problem. The mechanism proposed here includes both gaseous species impacting the surface, adsorbed molecules, atoms and free sites. It consists of 60 heterogeneous reactions involving 14 surface species _Co(S), H(S), CH_3(S), C_2H_2(S), CH_4(S), O(S), H_2O(S), CO_2(S), CO(S), OH(S), HCO(S), CH(S), CHH(S) and C_2(S) and 9 gaseous species namely H, H_2, CH_3, C_2H_2, CH_4, O_2, H_2O, CO_2 and CO. The scheme is listed in Table of **Appendix B.3**. Where _Co(S) represents the cobalt-free site and "CNT" is the single solid carbon phase representing carbon nanotubes. The conservation of cobalt atom is guaranteed by the scheme because, as a catalyst, cobalt should not be created or consumed by surface reactions. Several possible interactions between the considered species were taken into account. The mechanism includes adsorption and desorption reactions, reactions between adsorbed species, removal and addition of atomic hydrogen, and radical recombination reactions. The last five reactions represent the growth of the nanotubes. The temperature dependence of the rate coefficients has been described by an Arrhenius-type expression. The development of this surface reaction mechanism is based on the theoretical studies and the previous models developed for the chemical vapor deposition of carbon nanotubes on cobalt [17, 18] and on nickel substrates [10]. Oxygen surface reaction kinetics data were obtained from the oxidation of methane over nickel-based catalysts [19, 20].

3.2 Zero-dimension model Results

First, the 0D model was solved under the reactor conditions of Table 1 by varying only oxygen flowrate. Time evolution of some representative species mole fractions calculated without and with 2 sccm O_2 in the inlet is plotted in Figure. 3.7. We can clearly see that the steady-state solution is reached within 0.1 to 10 seconds. Atomic hydrogen H is created after few milliseconds and the discharge is dominated by molecular hydrogen H_2. Indeed, microwave plasma is known to improve hydrogen dissociation *via* electronic processes. In the absence of oxygen in the inlet, we can clearly see from Figure. 3.7 a that acetylene is the major carbon species formed in the plasma from the methane dissociation by the following global reaction: 2 $CH_4 \rightarrow C_2H_2 + 3\ H_2$. By adding O_2 in the inlet gas, the two major carbon species in molar fraction become CO (3.4%) and C_2H_2 (2.5%) as shown in Figure 3.7 b.

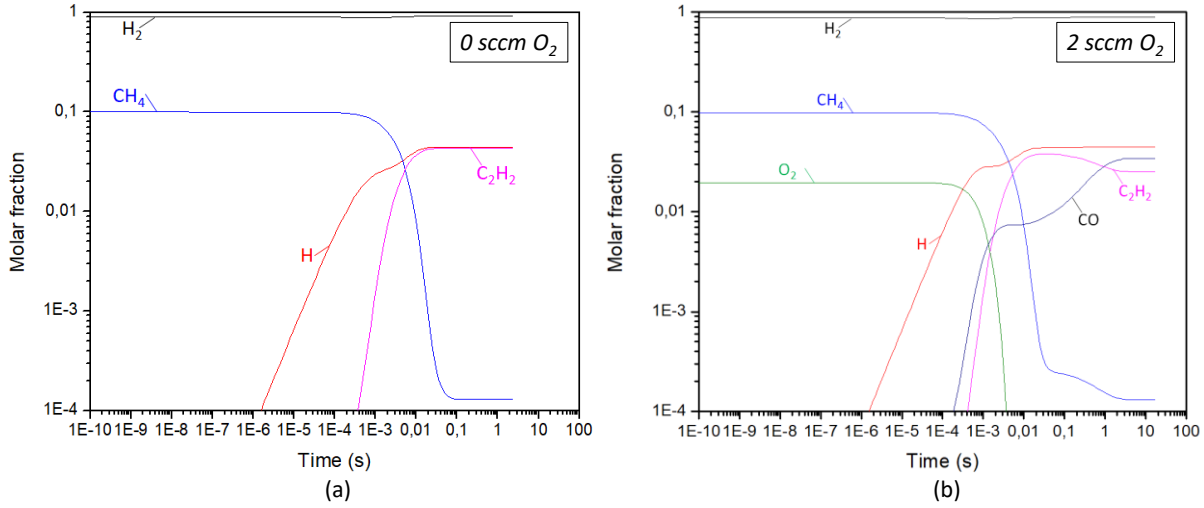

FIG 3.7 Time evolution of the major species in the plasma calculated using the 0D model. (a) Without oxygen; (b) With 2 sccm of O_2 added in the inlet gas.

When analyzing the entire oxygenated species molar fraction, we can notice, from Figure 3.8 a, that most of the introduced oxygen is transformed into water in few milliseconds. Water has already been proposed as an amorphous carbon etchant during water-assisted vertically aligned CNT growth (also called super growth) to synthesize densely packed and ultra-long (~2.5 mm) carbon nanotube (CNT) forests. Indeed, introducing a small and controlled amount of water enhances the activity and the lifetime of the catalyst particles [21, 22]. Moreover, Chang *et al.* included water flowrate as a parameter in their autonomous closed-loop experimentation combined with machine learning to understand input-to-output correlations during nanotube CVD growth [23]. In our conditions, the small amount of O_2 (2

sccm) can produce (~0.7 ppm) water *in-situ* thereby improving catalyst activity and the removal of amorphous carbon. However, as the system reachs an equilibrium state in few tenths of seconds; most of water is transformed into CO. In the same time, Figure 3.8 b shows that most of the introduced methane is transformed to acetylene with the major hydrocarbon species in this order C_2H_2>CH_4>CH_3. By compiling all the simulations from 0D model, we can clearly see that the addition of O_2 is manifested by a competition between CO and C_2H_2 formation in the plasma. As the inlet oxygen fraction is increased, an increase in the molar fraction of CO at the expense of that of C_2H_2 is obtained. This competition is marked by a cross-section in the vicinity of 2 sccm of oxygen shown in Figure 3.9 suggesting a change in the growth mechanism of carbon nanotubes when oxygen is added.

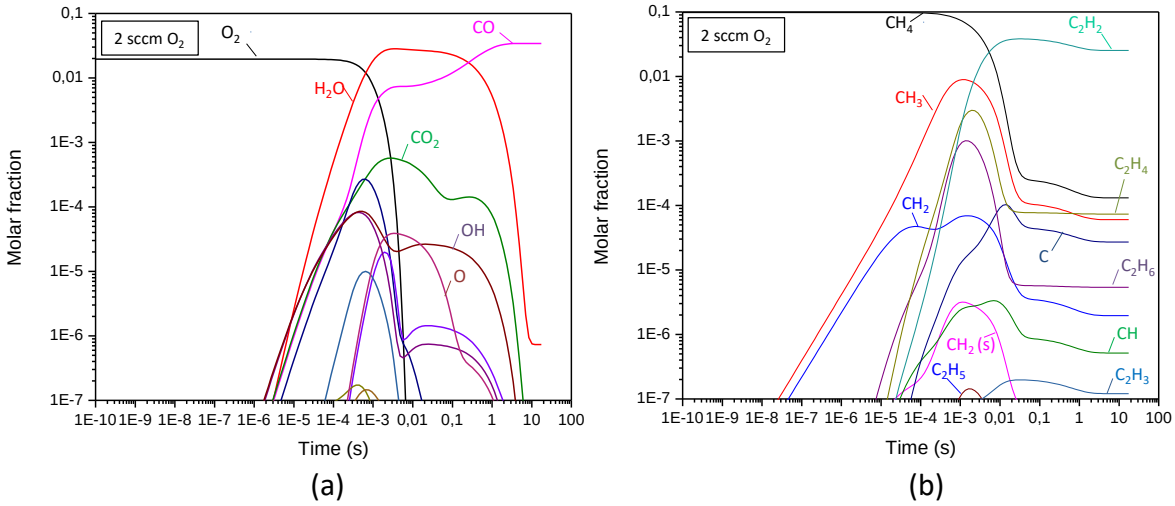

FIG 3.8 Time evolution of the major species with 2 sccm of O_2 added in the inlet gases. (a) Oxygenated species. (b) Major C_1 and C_2 species.

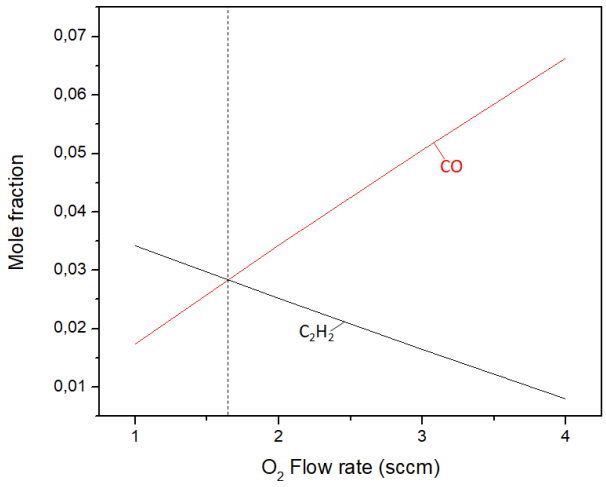

FIG 3.9 Mole fraction of CO and C_2H_2 versus oxygen flowrate in the inlet.

Another important aspect brought by the solution of the 0D model concerns the energy exchange processes in the plasma. The energy exchange dynamics discussed in Eqs (3-5) is illustrated in Figure 3.10 representing the time evolution of gas T and electron Te temperatures for a condition without O_2. Stationary conditions are reached faster than for species at about 0.1 s with Te= 16,920 K (~1.46 eV) and T= 1540 K. Note the robustness of the BDF integration method which makes it possible to incorporate variables with very disparate orders of magnitude and time constants.

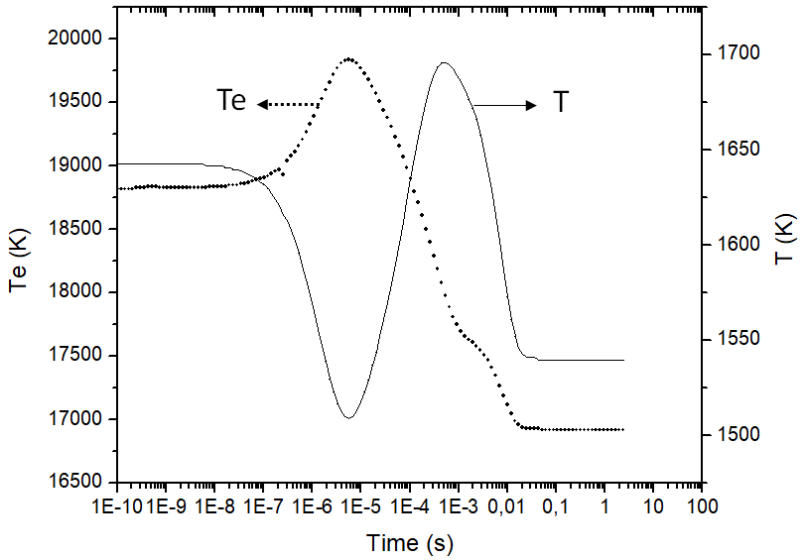

FIG 3.10 Time evolution of the electron Te and gas T temperatures calculated without oxygen.

The steady state solution obtained by solving energy exchanges in the plasma is summarized in in Figure 3.11. High electron temperatures 16,920 K (1.46 eV) facilitate the direct dissociation of molecules and heating of the gas. The calculated gas temperature is T = 1540 K and a small vibrational disequilibrium of ~123 K is present with a vibrational temperature Tv ~ 1663 K. This disequilibrium contributes to anion formation by dissociative attachment, which is known to depend on the vibrational excitation. When few oxygen is added in the inlet, gas temperature T slightly increases from 1540 K (0 sccm O_2) to ~1565 K (4 sccm O_2) suggesting that the presence of a small amount of oxygen does not affect energy exchanges in the plasma. Figure 3.11 also provides the details of the power deposition obtained at the steady-state converged solution. The power absorbed from the microwaves by the electrons P_{abs} is transferred to the neutral gas during collisions primarily by dissociation through the channel Q_{ed} (39.6%), followed by electron-vibration exchanges Q_{ev} (29.6%), electron-translation

exchanges Q_{et} (19.9%), electron energy loss by excitation of singlet H_2 states, $Q^{1e}{}_{ev}$ (10.7%) and ionization, Q_{ei} (0.7%).

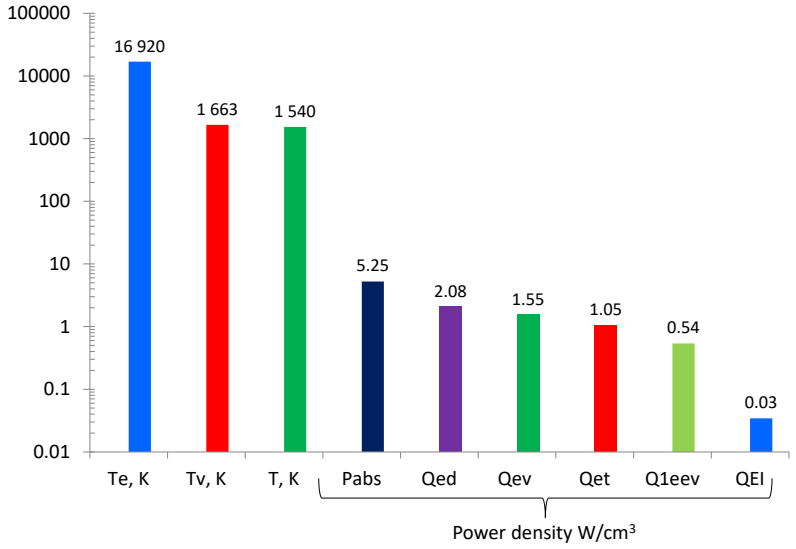

FIG 3.11 Electron, gas and vibration temperatures together with absorbed power and electron and vibration energy exchanges calculated from 0D model for Table 1 conditions without oxygen.

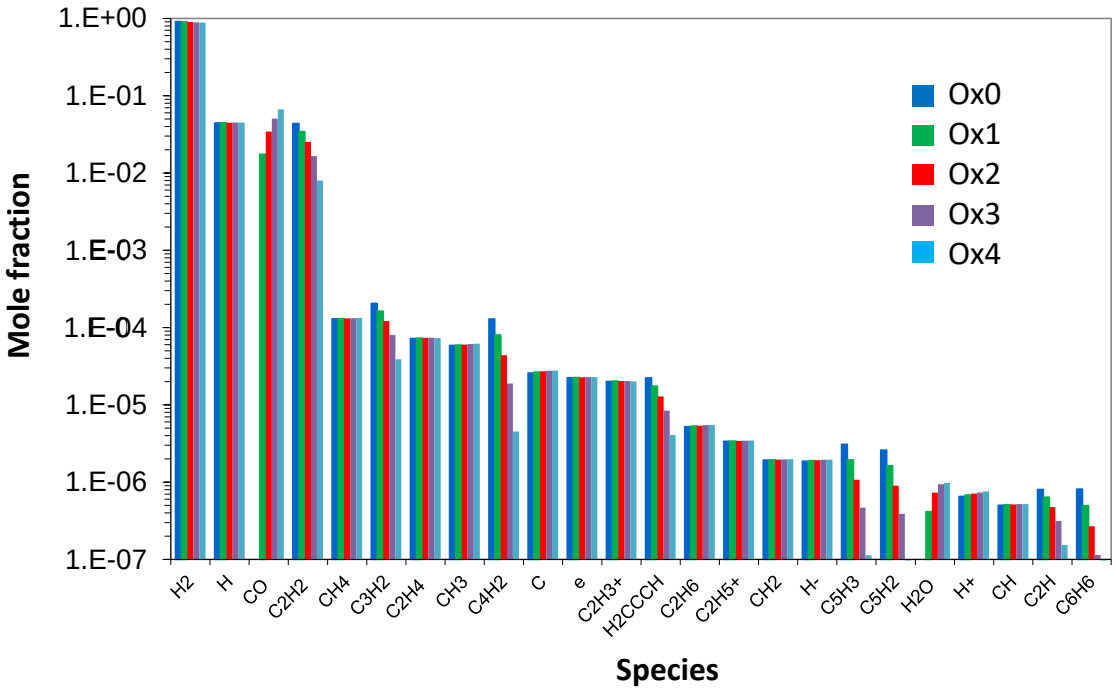

FIG 3.12 Major species ions and electrons calculated by the 0D plasma model for different oxygen flow rates in the inlet.

Figure 3.12 gives the major species in the plasma as predicted by the 0D model for different oxygen flowrates in the input. This list was classified in descending order starting from H_2 and stopped at the 24 most important species with a composition greater than 0.1 ppm. Major carbon species are by far CO and C_2H_2 that can likely contribute to nanotube growth. We can notice that an increase in the flow of oxygen leads to an increase in the molar fraction of CO at the expense of that of C_2H_2. Without the presence of oxygen, acetylene is the predominant carbon precursor. Beyond 2 sccm of O_2, carbon monoxide becomes dominant. From Figure 3.12, the atomic hydrogen mole fraction (~4.4%) is not affected by oxygen content. Regarding the kinetics model, acetylene is produced *via* fast the two processes: $C_2H_3 + H \rightarrow C_2H_2 + H_2$ and $C_2H_4 + M \rightarrow C_2H_2 + H_2 + M$. Acetylene is consumed primarily by ion-neutral reactions $H_3^+ + C_2H_2 \rightarrow C_2H_3^+ + H_2$. Due to the reaction $H_3^+ + C_2H_2 \rightarrow C_2H_3^+ + H_2$, $C_2H_3^+$ is the major cation in the plasma. Major charged species follow the order $e^- > C_2H_3^+ > C_2H_5^+ > H^- > H^+$.

3.3 Two-dimension model Results

After having studied in detail the thermochemical phenomena and the mechanisms of energy exchange in 0D plasma, we extend the study to 2D. In order to make the kinetic scheme compatible with CFD calculations, it is first necessary to reduce it. For this purpose, Chemkin Pro software was used through a sensitivity analysis. When using full chemical scheme, reaction pathways showed that H_2O and OH are the dominant oxygenated species. In addition, atomic hydrogen is the key element in carbon precursors cycling. The sensitivity analysis allowed the reduction of the kinetic scheme from 471 reactions to 100 reactions and the selection of 23 species out of 134 as detailed in the sensitivity analysis presented in the **Appendix B.4**. A 2D steady-state reactor simulation was performed by CFD code ANSYS Fluent incorporating homogeneous and heterogeneous kinetic data from respectively Table B.2 and Table B.3 in Appendix B. This makes it possible to reproduce very faithfully the temperature distribution inside the reactor as represented in the temperature profile of Figure 3.13. The maximum gas temperature of 1550°C is located at a distance δ_T of 1.6 cm above the substrate in good agreement with the boundary-layer thickness used previously in the 0D model. The temperature decreases gradually in the direction of the substrate. As clearly shown in the 1D profile along the centerline of the reactor (see Figure. 3.13 right), there is a steep temperature gradient between the plasma center and the substrate on one side and the gas inlet on the other.

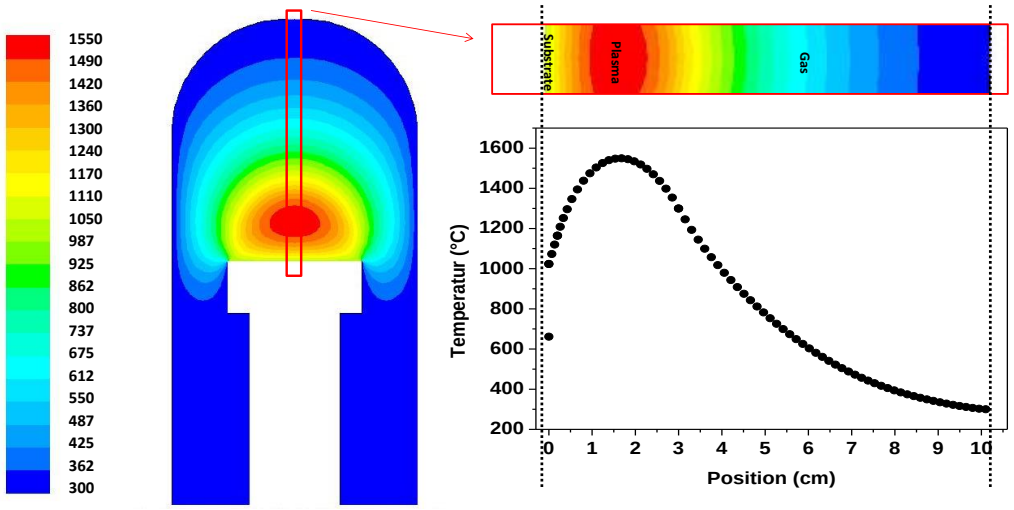

FIG 3.13 Simulated temperature profile inside the reactor (left) and corresponding 1D temperature profile along the centerline of the reactor (right).

3.3.1 Effect of Oxygen

O_2 flowrate was varied from 0 sccm down to 4 sccm under constant CH_4 and H_2 flowrates. Table 3.1 is a reminder of the inlet composition and conditions used in this study.

Table 3.1 Parameters used to investigate H_2 flowrate in the inlet

Experiment	Substrate temperature	Pressure	Plasma power	CH4 flow rate	H2 flow rate	O2 flow rate
Ox0	750°C	10 mbar	340 Watt	10 sccm	90 sccm	**0 sccm**
Ox1	750°C	10 mbar	340 Watt	10 sccm	90 sccm	**1 sccm**
Ox2	750°C	10 mbar	340 Watt	10 sccm	90 sccm	**2 sccm**
Ox3	750°C	10 mbar	340 Watt	10 sccm	90 sccm	**3 sccm**
Ox4	750°C	10 mbar	340 Watt	10 sccm	90 sccm	**4 sccm**

By gradually increasing the oxygen flow at the reactor inlet, the distribution of the H, OH and H_2O species is given in Figure 3.14 for the 5 simulations representing the experiments of Table 1. From this Figure, we can see that the maximum atomic hydrogen concentration is located in the center of the plasma. Nevertheless, contrary to the results of the 0D model shown in Figure 3.10, in 2D the molar composition of H is affected by the amount of O_2 introduced in the inlet. This is probably due to H-atom diffusion and thermal diffusion in the reactor volume together with the surface chemistry that are considered in the 2D model. We can clearly distinguish the imprint of the surface chemistry located in the central part of the substrate on

the shape of H and OH species profiles. Thus, it is interesting to compare the effect of oxygen on all the profiles under 2D calculation conditions.

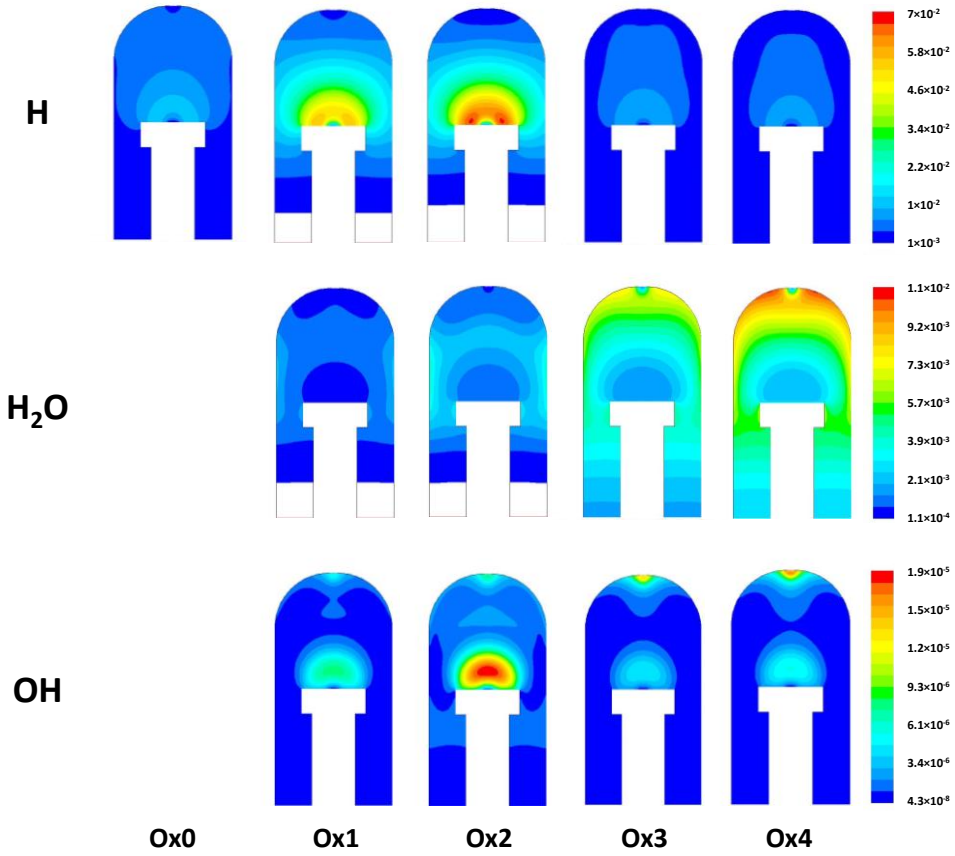

FIG 3.14 Distribution profile of H, H_2O and OH for different oxygen inlet rates.

For each species in Figure 3.14, the scales have been normalized to be able to compare the effect of oxygen addition. At first glance, using 2 sccm of O_2 in the inlet (Ox2) leads to more H and OH in the plasma center. Whereas, the amount of water increases with the amount of oxygen added and tends to accumulate outside the plasma ball, where the temperature is lower. The addition of more oxygen in the inlet induces a drastic decrease of atomic hydrogen in Ox3 and Ox4 even as compared to Ox0. The molar fraction of atomic hydrogen has a direct link to the formation of OH and H_2O according to the following reaction:

$$H_2O + H = H_2 + OH$$

The formation of oxygenated species at small rate leads to forming more atomic hydrogen as a result of the reaction of OH radicals with molecular hydrogen in the plasma (Ox1 and Ox2), however, after a certain threshold, the addition of more oxygen results in the formation of large quantities of H_2O at the entry of the reactor, leading to a depletion of oxygen, thereby, less oxygenated species needed for the plasma composition reactivity are formed such

as OH radicals, as represented in Figure 3.14, less OH radicals are formed in the plasma in Ox3 and Ox4 as compared to Ox1 and Ox2.

This plasma composition changes regarding atomic hydrogen as well as oxygenated species is expected to affect the carbon precursor formation which might explain the evolution of the growth rate of CNT. To explore this, chemical species distribution in the plasma is presented in detail in Figure 3.15.

Figure 3.15 shows the major species formed in the plasma, by considering the previously discussed results concerning methane and oxygen dissociation as well as atomic hydrogen formation; we can see that gas-phase kinetics produces numerous hydrocarbons and oxygenated species in the discharge dominated by the presence of molecular hydrogen followed by atomic hydrogen, and then CH_4, C_2H_2 and CH_3 smaller with 2 orders of magnitudes compared to atomic H. This is in well accordance with previous studies on methane-hydrogen gas mixture [24, 25] as we can observe, adding oxygen in the inlet mixture under the same operating conditions changes the plasma composition, it is interesting to find that H_2O is formed in the plasma with the same order of magnitude of CH_4, and C_2H_2 and CH_3 radicals.

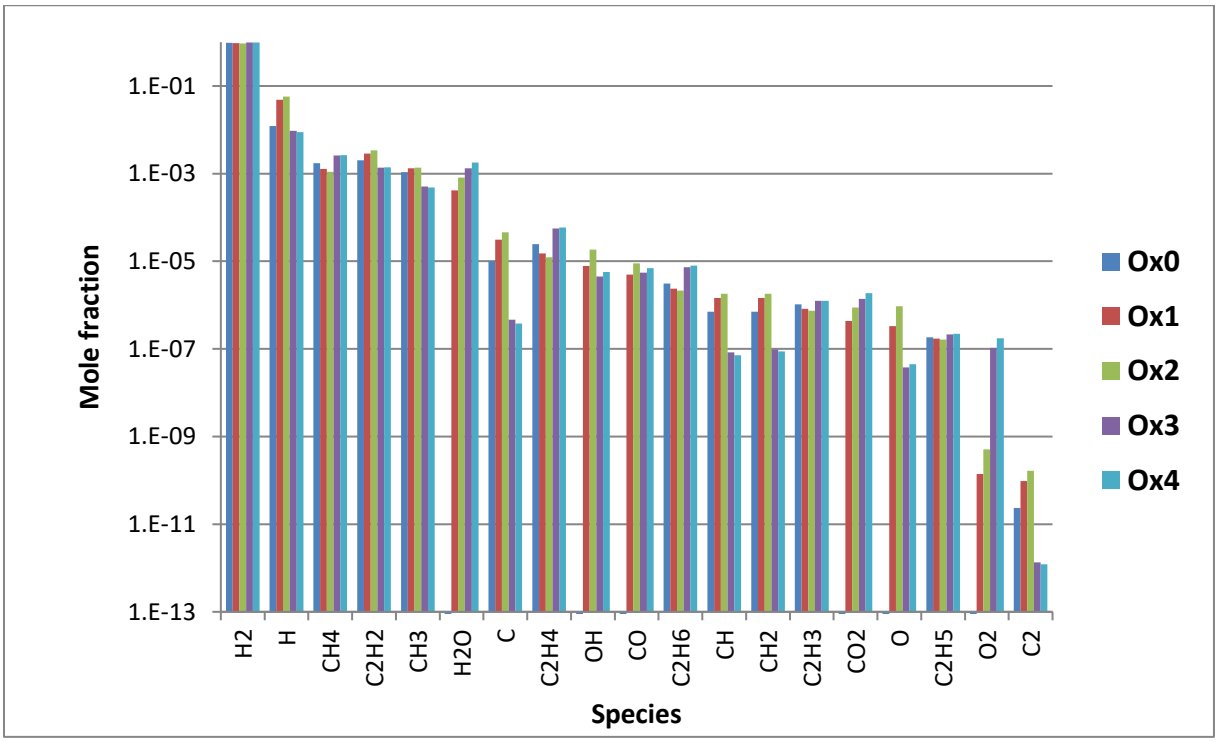

FIG 3.15 Molar fraction of chemical species at the center of the plasma for different oxygen inlet rates ranging from 0 to 4 sccm.

According to 2D calculations, H_2O become the dominant oxygenated specie in the plasma for all four experiments where oxygen is added. In this direction, M Jiménez-Redondo *et al*. [26] have reported by diagnostic supported by modeling the production of appreciable

amount of water, much higher than OH radical, even by adding small quantities of oxygen in hydrogen plasma discharge. From Figure 3.15, the observation of the molar fraction of the four dominating species (CH_4, C_2H_2, CH_3 and H_2O) shows that for gas mixtures with inlet oxygen less or equal to 2 sccm, C_2H_2 and CH_3 radicals have higher molar fraction than CH_4 and H_2O. These species are incorporated in chemisorption to the catalyst surface and subsequent reactions responsible for carbon nanotubes growth described in **Appendix B.5.**

Once we have better understood the role of oxygen in bulk chemistry, we are interested in what follows in its effect on the growth mechanism of nanotubes on the substrate. We first plotted in Figure 3.16 the axial evolution of some species from the center of the plasma to the substrate. The simulated species profiles presented in Figure 3.16 show that C_2H_2, CH_3 and CH_4 are important species that may significantly contribute to carbon nanotubes growth. There is a region of uniform C_2H_2, CH_3 and CH_4 distribution where CNTs were synthesized for the experiments, showing a relatively broader region close to the substrate surface. Other species such as atomic carbon and hydrogen have also a rather important contribution. Finally, simulation shows that large amounts of H_2 are produced in the gas phase, but H_2 production arises also from the surface desorption.

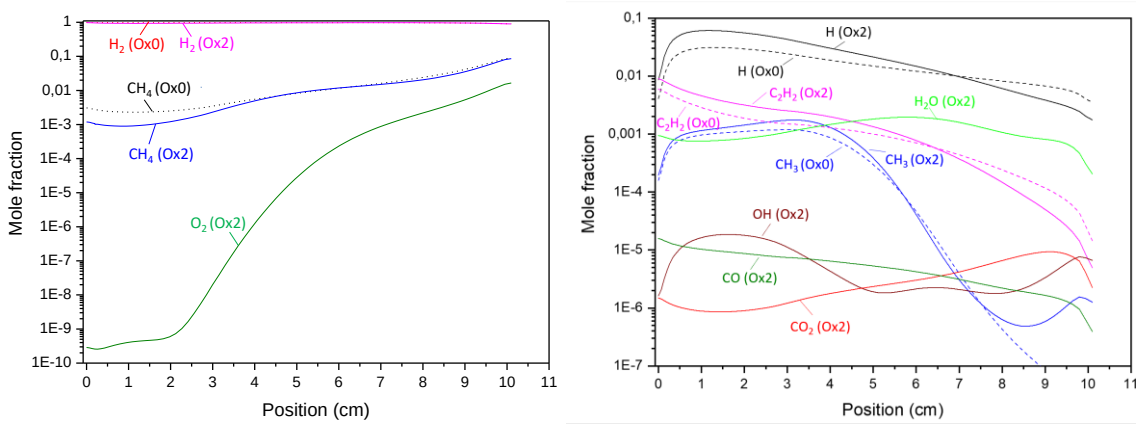

FIG 3.16 Simulated 1D profile issued from (2D) model of the H_2, CH_4, O_2 (left) and H, CH_3, C_2H_2, H_2O, CO_2 and CO (right) mole fractions along the centerline of the reactor without oxygen (Ox0) and with 2 sccm O_2 (Ox2) added in the inlet.

Once these species diffuse to the surface, we can then define the chemical state of the substrate in terms of surface species site fractions, often referred to as “site coverages”, involving the 14 surface species and the 9 gaseous species described above. We first intend to study the effect of oxygen added in the inlet gas on those site coverages. The site fractions are estimated based on our actual understanding of the surface chemistry and they are normalized

such that their sum is equal to 1.0. Figure 3.17 shows the cobalt surface coverage obtained by varying the oxygen flowrate in the simulations. The surface sites are occupied by any of 14 surface species, where _Co(S) is the open cobalt site, and the other surface species represent any atoms, or molecules, or radicals adsorbed on the cobalt surface. The results of Figure 3.17 indicate that regardless of the oxygen added, more than half the cobalt nanoparticle (~60%) remains attached free from any radical or molecule. This is the direct consequence of the nucleation density that we introduced above and that we will justify later. In addition, as expected, atomic hydrogen H is the first cobalt spanning species. Indeed H-atoms are the dominant radicals in the plasma and the most reactive species at the cobalt surface. However, it is interesting to note that carbon monoxide CO is the second dominant species adsorbed on the cobalt surface. To date, we have no evidence that a part of CO could be involved in the growth of nanotubes on cobalt surfaces at such low pressures of 10 mbar. A recent study by Luo *et al*. [27] showed the growth of single-walled carbon nanotubes (SWCNTs) from CO decomposition on cobalt nanoparticles. Nevertheless, as for high-pressure carbon monoxide (HiPco) [28], high pressure of 6 atm was necessary for CO disproportionation on cobalt *via* the Boudouard reaction. From Figure 3.17 we can see that the surface site fraction of C_2H_2 remains important in spite of its implication in the growth of the nanotubes. Hence, if we exclude the involvement of carbon monoxide, acetylene C_2H_2 due to its strong presence on the catalyst surface would be the most important precursor in the nanotube growth. From Figure 3.17, a detailed analysis of the effect of oxygen on the surface site coverage of CNTs shows a better efficiency at 2 sccm of O_2 (see CNT columns in the histogram of Figure 3.17). This logically reproduces the effect of oxygen on the distribution of species in the volume discussed in Figure 3.15 and Figure 3.16. From Figure 3.17 we can see that the cobalt surface is covered by oxygenated species such as O, H_2O and OH which could participate in the etching of the amorphous carbon. Even if these reactions are not yet incorporated in our model, these results provide interesting guidelines for future improvements of the nanotube surface chemistry.

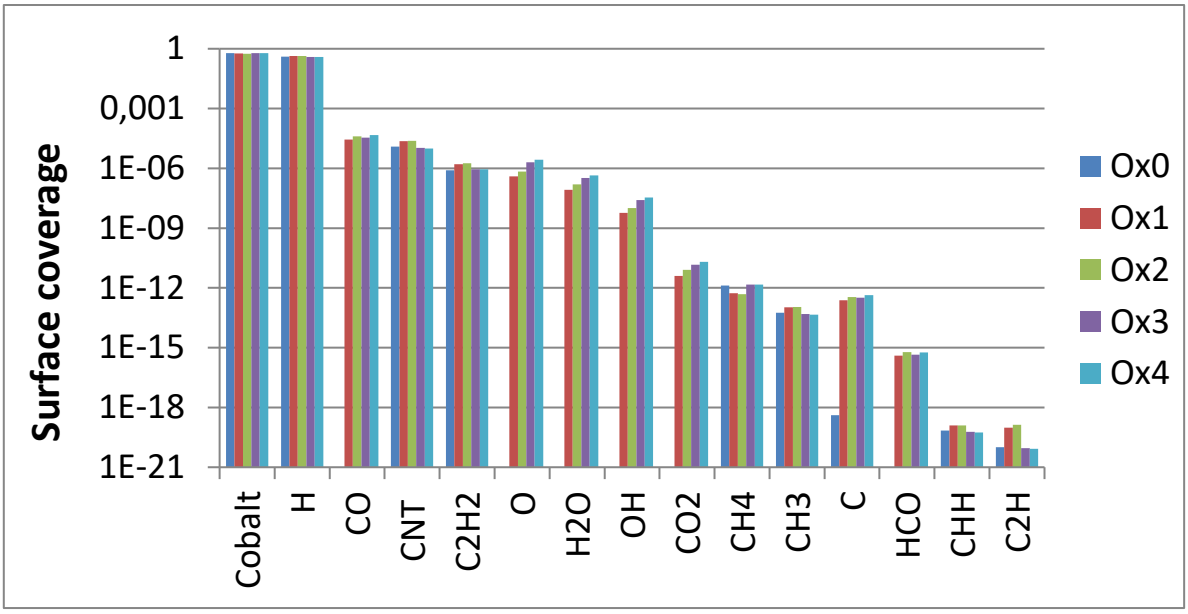

FIG 3.17 Surface coverage of a cobalt for different oxygen inlet rates ranging from 0 to 4 sccm.

To analyze the radial evolution of the site fraction surface, we plotted in Figure 3.18 their radial evolution on 1 cm of the substrate, indexed from -0.5 to +0.5 cm with the axis of the reactor located in the center. The result confirms a uniform distribution of species over the extent of the substrate. Since surface chemistry is a thermally activated process, this result is attributed to the uniformity of temperature across the substrate. The rare inhomogeneity which is manifested by profiles sometimes concave, sometimes convex is attributed to the diffusion of the species in the immediate vicinity of the substrate. Note also that at 4 sccm of O_2, the O surface site fraction exceeds that of C_2H_2 at any point of the substrate.

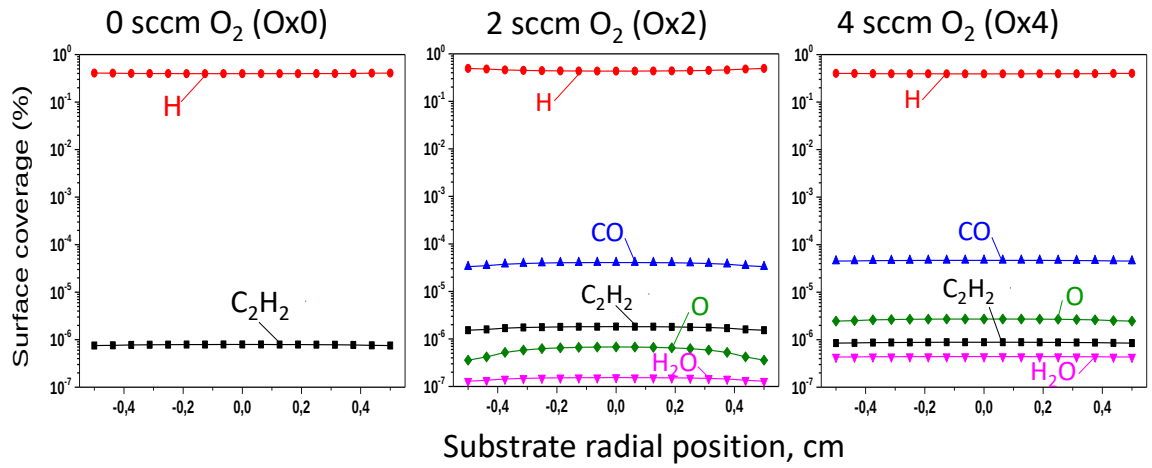

FIG 3.18 Radial evolution of the calculated surface site coverage on 1 cm cobalt substrate on either side of the reactor axis located at 0 cm. Gas inlet oxygen flowrate was varied with the indicated oxygen flowrates.

Finally, the estimation of the overall nanotube growth rate was obtained by combining all the homogeneous and heterogeneous reactions of the model. According to the Surface Chemkin formalism [29], the calculated rate of production expressed in moles.cm^{-2} s^{-1} is converted to linear nanotube growth rate G in µm/min by using nanotube bulk mass density ρ_{CNT} = 2.20 g/cm^{-3}. Nevertheless, nanotube growth rate G depends on the nucleation site density Γ. For this reason, and because there are variabilities in this parameter, we adjusted Γ within a parametric study. First, the nucleation site density Γ was varied in a large domain of two orders of magnitude between 3.6×10^{-11} and 1×10^{-9} moles.cm^{-2} and nanotube growth rate G is plotted versus Γ in Figure 3.19. According to our calculations shown in Figure 3.5, the lower limit of the nucleation site density corresponds to Zig Zag structure for 11 walls nanotubes with Γ_{min}= 2×10^{-10} moles.cm^{-2} while the maximum value of Γ_{max}= 5.3×10^{-10} moles.cm^{-2} corresponds to the armchair structure for 17 walls. Once the effect of the nucleation density on the growth rate of the nanotubes has been studied, we can reasonably set Γ to a value of 3.6×10^{-10} moles.cm^{-2}. This value corresponds to the calculation of a mixture of Zig Zag and armchair nanotubes with between 11 and 17 walls, as statistically observed in our growth experiments. To study the effect of oxygen on the growth of the nanotubes, we have thus set Γ = 3.6×10^{-10} moles.cm^{-2} in all the simulations. The standard deviation on the calculated values of the growth rate would then correspond to ±0.26 µm/min and was applied to the model growth rates reported in Figure 3.20.

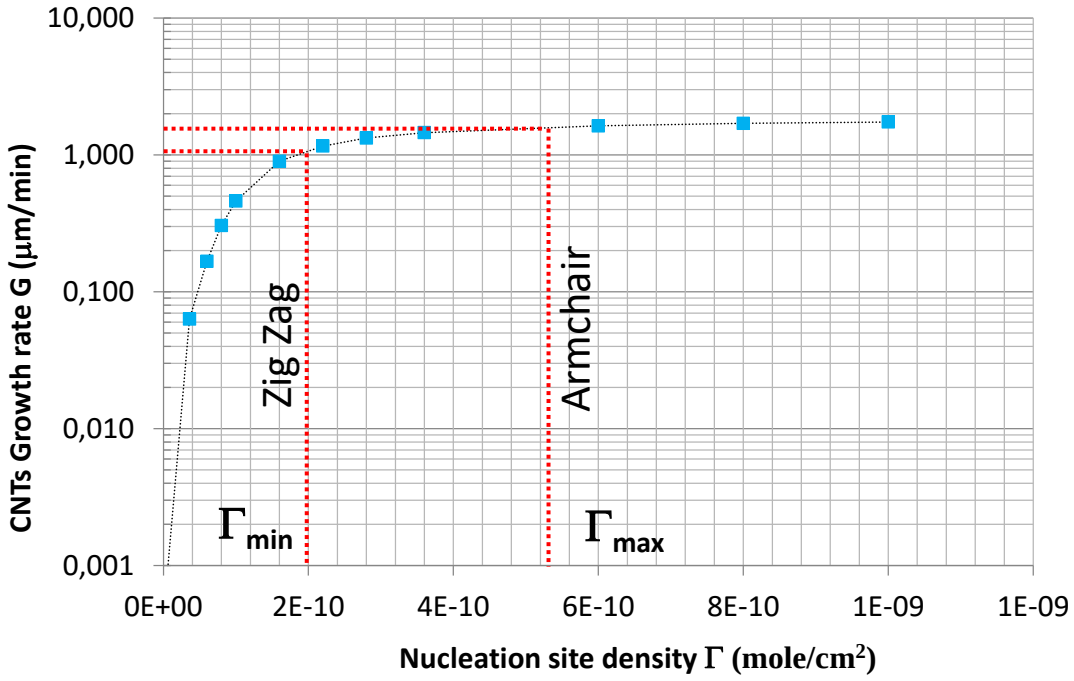

FIG 3.19 Effect of nucleation site density on carbon nanotube growth rate. Nucleation site lower limit and higher limits corresponds to Zig Zag and Armchair nanotubes structures respectively.

The calculated growth rates obtained from both experiment and simulation are displayed as a function of oxygen inlet rate in Figure 3.20.

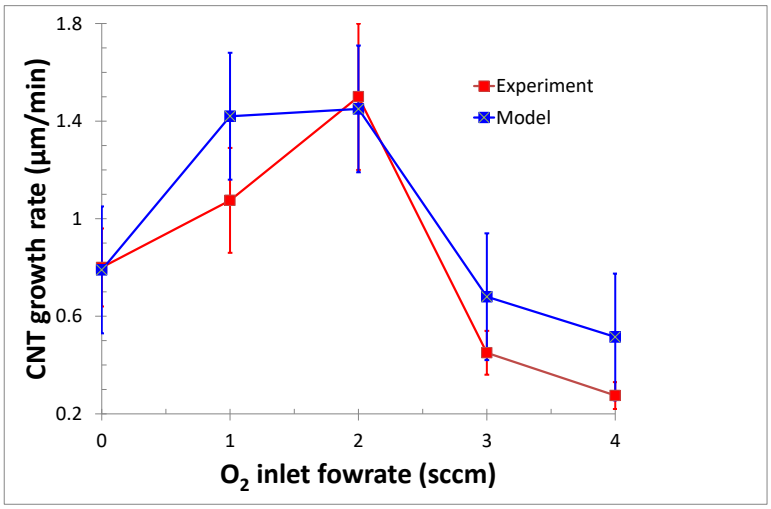

FIG 3.20 Simulated and experimental nanotube growth rate for different oxygen flow rates. A standard deviation of ±0.26 µm/min was applied to the model growth rates to take into account the possible effect of nanotube chirality and number of walls in surface site density estimation.

The experimental growth rate of the nanotube forest was estimated from the measured nanotube height divided by a net growth time. An incubation time of ~1 min was chosen to adjust the model and the experiment without adding oxygen. This could fairly correspond to the time taken by the methane to move from the feed valve to the nanoparticle including the transport by convection in the pipe and in the bulk of the plasma as well as the homogeneous reaction and diffusion times in the boundary layer in the vicinity of the substrate. The agreement between modeling and experimental results is fairly good, reasonably reproducing the behavior of the growth rates as a function of oxygen.

3.3.2 Effect of hydrogen

Another set of simulations was conducted to investigate the effect of H_2 flowrate that was varied from 90 sccm down to 10 sccm under constant CH_4 and O_2 flowrates. Table 3.2 shows the inlet composition and process conditions used in this study.

Table 3.2 Parameters used to investigate H_2 flowrate in the inlet

Experiment	Substrate temperature	Pressure	Plasma power	CH4 flow rate	H2 flow rate	O2 flow rate
H1	750°C	10 mbar	340 Watt	10 sccm	**90 sccm**	2 sccm
H2	750°C	10 mbar	340 Watt	10 sccm	**60 sccm**	2 sccm
H3	750°C	10 mbar	340 Watt	10 sccm	**30 sccm**	2 sccm
H4	750°C	10 mbar	340 Watt	10 sccm	**20 sccm**	2 sccm
H5	750°C	10 mbar	340 Watt	10 sccm	**10 sccm**	2 sccm

For these calculations, nucleation sites density was attributed the same value as the precedent series. Calculated and experimental nanotube growth rate are represented in Figure 3.21 as a function of the percentage of molecular oxygen in the inlet.

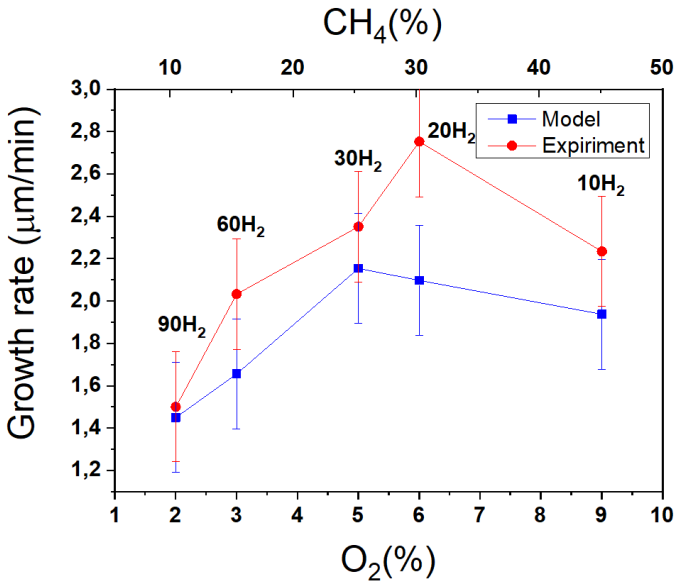

FIG 3.21 Simulation and experiment growth rate results of carbon nanotube growth as a function of oxygen percentages of molecular oxygen in the inlet for different hydrogen flow rates expressed in sccm.

As represented in Figure 3.21, by reducing H_2 inlet and subsequently increasing O_2 and CH_4 percentage in the inlet, the growth rate shows a maximum. This behavior is similar to the one observed in Figure 3.19 confirming that a threshold of O_2 percentage in the inlet is always advised for an optimal growth rate. Growth rate trends for both modeling and experiments are in good agreement with yet an optimal nanotube growth rate of ~ 2.2 µm/min, obtained for 5 to 6% of oxygen. By comparing this optimal point to precedent results, multiple observations can be extracted:

i) Decreasing hydrogen inlet improves nanotube growth rate up to 2.15 µm/min in the model and 2.75 µm/min in experiment.

ii) Although oxygen percentage in the inlet is further increased than 2% (here O_2%=5%), growth rate is enhanced significantly. This result could be related to the fact that CH_4 percentage is increasing too in the inlet. Hence, since they are involved in a complex chemical scheme, the three compositions of H_2, CH_4 and O_2 must be optimized simultaneously by considering carbon/hydrogen ratios in the inlet. For this purpose, further simulations were performed to differentiate the effect of hydrogen decrease in the system before going back to investigate the effect of oxygen in a high carbon/hydrogen ratios.

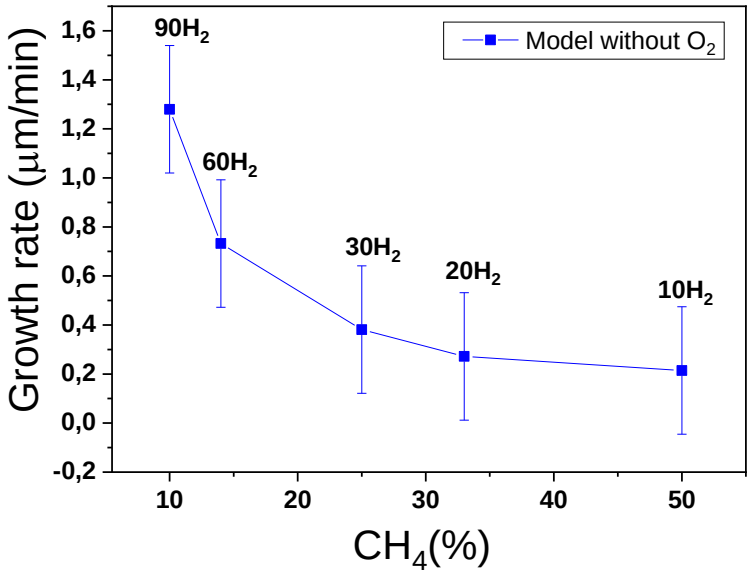

FIG 3.22 Effect of %CH_4 in the inlet on the calculated nanotube growth rate without adding oxygen.

Figure 3.22 presents the calculated growth rate as a function of methane percentage in the inlet as hydrogen inlet is decreased from 90 sccm to 10 sccm in the absence of oxygen. The growth rate decreases with decreasing hydrogen to reach a plateau at lower hydrogen values. This clearly demonstrates that a rich carbon plasma environment is not necessarily favorable for carbon nanotube growth in the bell jar reactor. This result is in concordance with the previous findings[10]. This drastic decrease of VACNTs growth rate and stabilization is an indication of the stagnation of the reactional system at low atomic H concentrations [10].

Now that we have confirmed that lowering H_2 inlet and increasing CH_4 percentage is not the reason behind the increase of growth rate values in the simulation series represented in Figure 3.28. It is clear that the increase in O_2 percentage has in fact enhanced growth rate to a certain threshold then decreased, this confirms again what has been demonstrated above, the shifting of optimal growth rate point toward higher oxygen percentages (H3, O_2%=5%) as compared to optimal values of the first series (Ox2 , O_2%=2%) can be investigated by analyzing the gas phase composition of species in the center of the plasma represented in Figure 3.23.

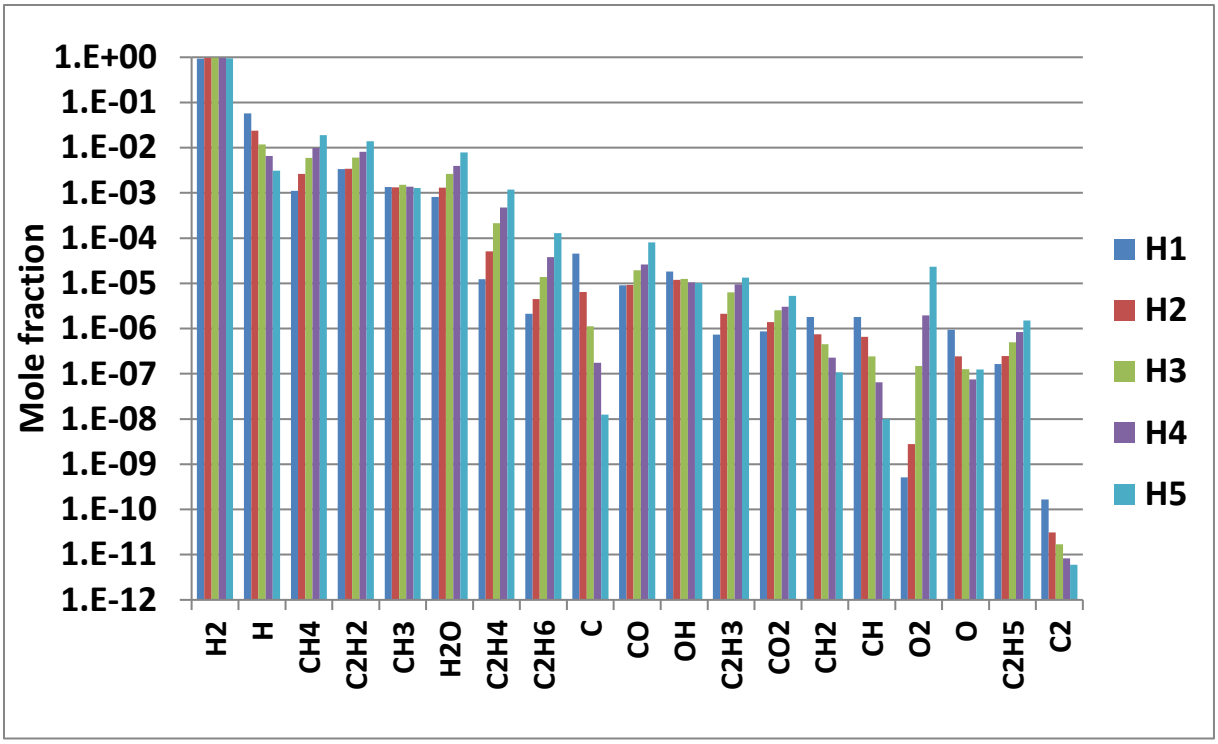

FIG 3.23 Mole fraction of chemical species at the center of the plasma for different H_2 flow rates in the inlet. H1: 90 sccm - H2: 60 sccm – H3: 30 sccm – H4: 20 sccm and H5: 10 sccm.

From Figure 3.23, the distribution of molar fraction in the center of the plasma indicates a dominant presence of H_2 even when the initial inlet was decreased to 10 sccm. Moreover, higher hydrogen mole fraction value is identified at the point H3. This is a direct result of methane dissociation that produce H_2 [30]. However, as expected, atomic hydrogen is decreased by one order of magnitude as hydrogen inlet is decreased from 90 sccm to 10 sccm and is surpassed by other species such as CH_4 , C_2H_2 and H_2O. This switch of the plasma chemical composition is identified at the experiment H4 which is the point where growth rate decreases after reaching a peak in the model. The predominant presence of both C_2H_2 and CH_4 is a result of atomic H decline. This evolution of the reactional composition is characterized by the increase of C_2H_x species mole fraction such C_2H_2, C_2H_3, C_2H_4, C_2H_5, C_2H_6 probably at the expense of the recombination of hydrocarbon radicals that decreases including C, CH_2, CH and C_2. As for oxygenated species, an increase of mole fraction of stable oxygenated molecules such as H_2O, CO, CO_2 and O_2 is observed; this is in agreement with the increase of the oxygen inlet percentage. The only three radicals in the plasma that do not follow a monotonous trend are CH_3, OH and O. First it is important to note that the growth rate of VACNTs does not follow the increase of C_2H_2 mole fraction, indicating that C_2H_2 is probably not the key precursor. On the other hand, CH_3 radical's molar fraction exhibits a similar evolution to VACNTs growth

rate and peaks similarly at the point H3. This implies that CH_3 is probably the main precursor for VACNTs growth, at least from the analysis of gas phase composition of the plasma. In addition, the non-monotonous evolution of both OH and O might be an indication of the role of these two species in hydrocarbon dissociation and in CH_3 formation. This means that in the presence of O_2, atomic H is not the only key species in hydrocarbon dissociation. Other species such as O and OH could induce dissociation of CH_4 through the two reactions:

$$CH_4+O=CH_3+OH$$

$$CH_4+OH=CH_3+H_2O$$

However, according to [31], the hydroxyl radical OH seems to have more implication in the forming of CH_3 than atomic oxygen O. They attribute this higher reactivity to the higher oxidative potential of OH.

To investigate the effect of H_2 flowrate on surface chemistry, cobalt surface coverage was plotted for different simulated conditions and shown in Figure 3.24.

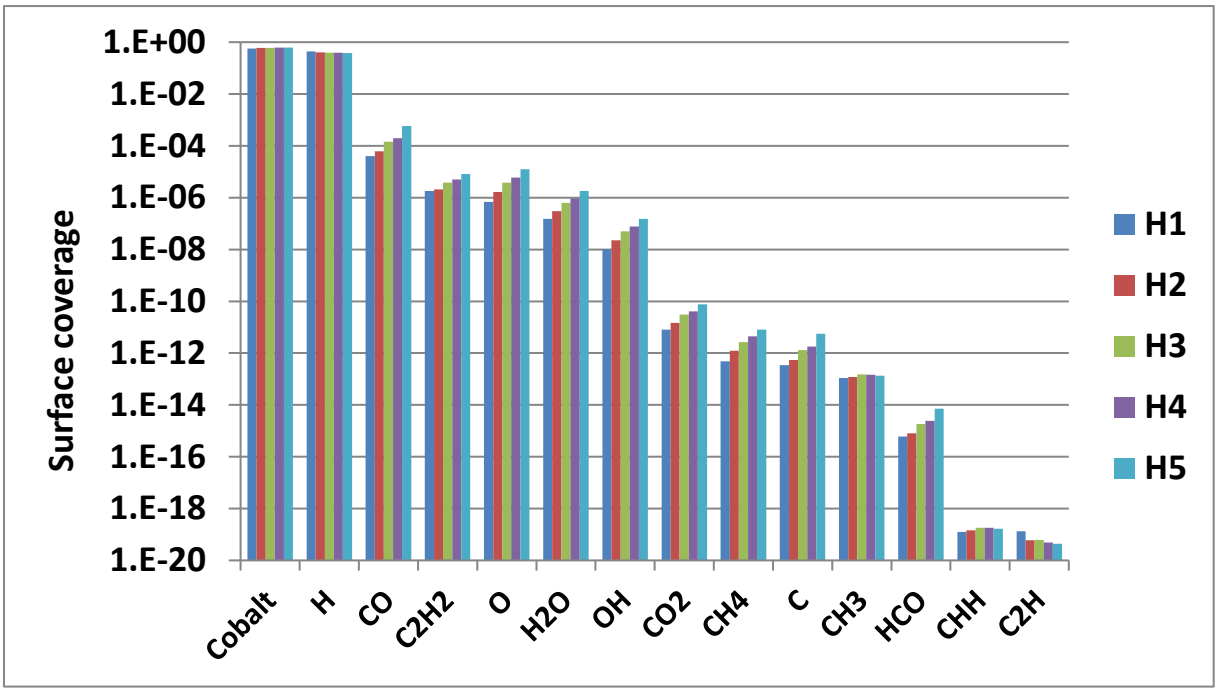

FIG 3.24 Surface coverage of cobalt nanoparticle for different Hydrogen inlet rates.

Even by decreasing atomic hydrogen by almost one order of magnitude (90 sccm to 10 sccm) while decreasing Q_{H2}, we can clearly notice from Figure 3.24 that cobalt coverage is not affected thereby demonstrating that the incorporation of H atoms on the cobalt surface is kinetically controlled rather than obeying to diffusion limited process. In the opposite, all the

other species (CO, C_2H_2, O, H_2O …) increase as their plasma composition increases. This is an indication of diffusion limited process.

Furthermore, as represented in Figure 3.23 (ou Figure 3.24?), all surface species express a monotonous trend when decreasing H_2 inlet except CH_3, CHH, and C_2H. CH_3 and CHH express specifically the same trend as growth rate by peaking at H3 then decreasing, this is a conclusive evident that CH_3 more than any other hydrocarbon (since it has higher surface coverage than CHH) is the key species in VACNTs growth.

3.3.3 Discussion

In a ternary system (CH_4, H_2, O_2), simultaneous optimization for each gas inlet fraction is needed, hence as proved in this second part , the optimum percentage of oxygen inlet depends highly on the percentage of the other two gases, by increasing CH_4 inlet , VACNTs growth rate is enhanced at higher O_2% = 5%, the decrease of growth rate after reaching the optimum is mainly related to the saturation of the plasma with carbon species, this translates to the surface of the catalyst by the fluctuation of the CH_3 coverage, indeed CH_3 is suspected to be the main precursor for VACNTs growth, this is highlighted in Figure 3.25 and Figure 3.26.

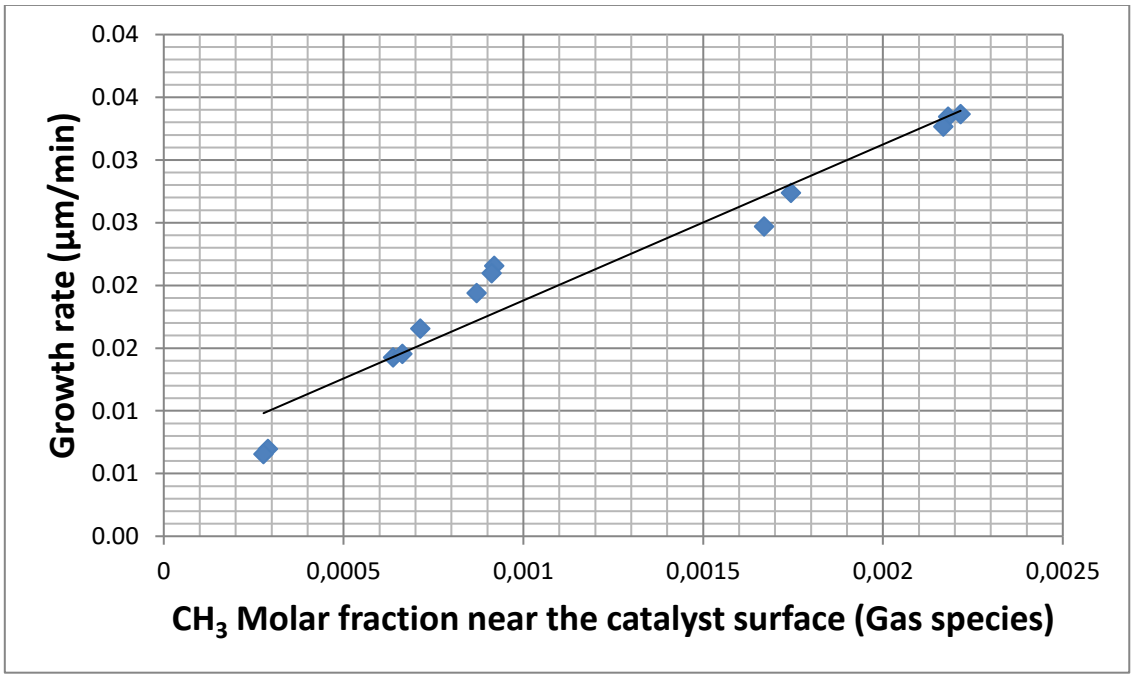

FIG 3.25: calculated nanotube growth rate as a function of CH3 molar fraction

In Figure 3.25 the calculated growth rate of all the simulations (3 series) is plotted as a function of CH_3 molar fraction near the catalyst surface, as we can see, the growth rate show

an almost linear dependency on the presence of CH_3 near the substrate, whether there is O_2 or not, and no matter what percentage is chosen for the ternary system. This dependency is translated directly to the surface chemistry of carbon nanotubes growth.

In Figure 3.26 the calculated growth rate of all the simulations (3 series) is plotted as a function of CH_3 surface coverage on the catalyst, the plot however changes to an exact linear dependency confirming that CH_3 that is attached on the catalyst surface is the species that controls the VACNTs growth, this show the importance of surface chemistry in VACNTs growth simulations since VACNTs growth is a heterogeneous mechanism, but most importantly this confirms that surface chemistry in the model is a kinetically controlled mechanism that is not limited to species diffusion and gas transport processes.

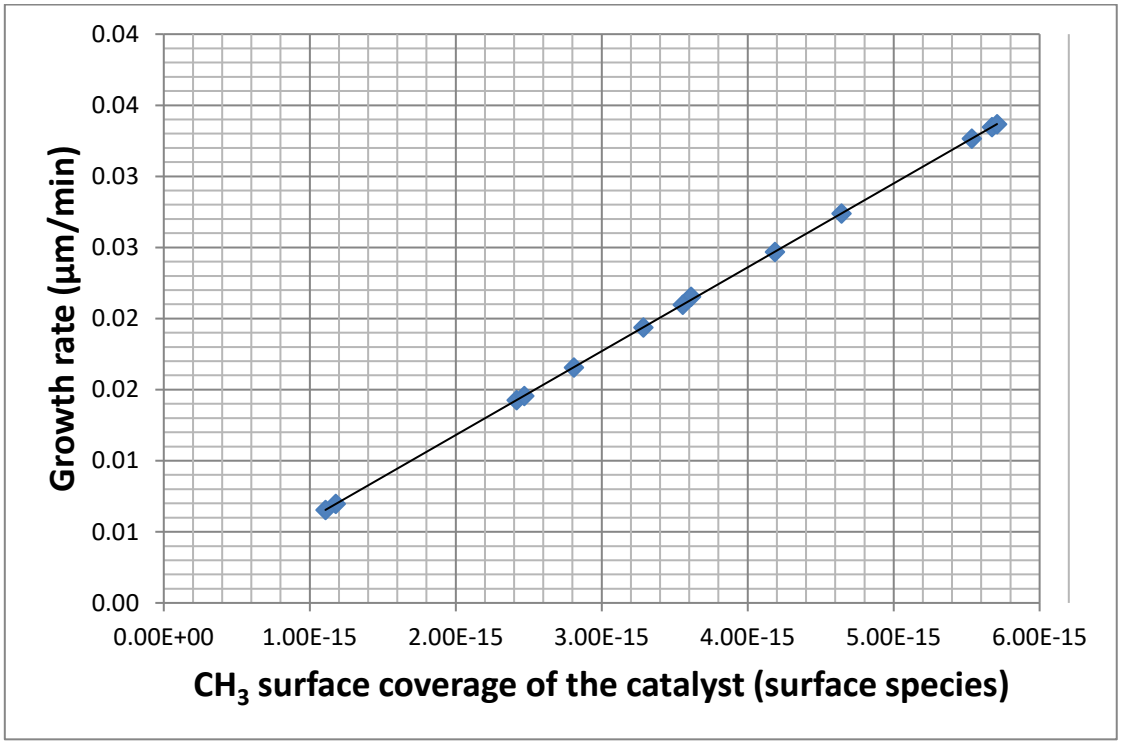

FIG 3.26: calculated nanotube growth rate as a function of CH3 surface coverage

3.4 Conclusion

In conclusion of this chapter, we can draw the most important results in modeling. First, as evidenced by SEM analysis, the use of TiSiN barriers made it possible that experiments are then more reproducible rending it possible to study the role of the addition of O_2. According to our experiments, the addition of 2 sccm of O_2 in H_2/CH_4 plasma at moderate pressure improves the nanotube growth rate nearly twofold. In addition, the stabilization of the catalyst nanoparticle on the substrate constitutes an ideal situation for the analysis of the thermo-kinetic processes of the growth of nanotubes by modeling. In this direction, we first studied thermo-kinetic processes using a 0D plasma model. The plasma is described by spatially averaged bulk properties, and the species compositions are determined using a complete chemical scheme in the transient zero-dimensional 0D configuration. The advantage of this approach lies in its small computational demands, which enable rapid evaluation of the effects of oxygen and permit the identification of dominant reactions and key species during nanotube growth. A sensitivity analysis then allowed reducing the kinetic scheme while incorporating the phenomena of convection, diffusion and surface chemistry within the framework of a 2D model. This model was used to investigate the global composition of the plasma over the whole range of $H_2/CH_4/O_2$ mixtures experimentally studied by incorporating specific surface chemistry reproducing nanotube growth. The growth rates obtained by varying oxygen flowrate in the inlet from both experiment and simulation are in fairly good agreement. Even if surface reaction mechanisms still contain larger uncertainties in reaction-rate coefficients and surface site density estimation, we developed a comprehensive model to estimate surface site density from HRTEM analysis of the structure of the nanotubes. In addition, we estimated surface kinetic parameters from published data for cobalt and nickel catalytic systems. We have checked and referenced all of our data sources that are grouped in tables and constitute a valuable source of information for future development of nanotube growth chemistry.

References

1. Farhat, S., *CHEMM a FORTRAN computer code developed at LSPM to solve plasma chemistry problems for nanotubes and graphene growth.* 2010.
2. Scott, C.D., Farhat, S., Gicquel, A., Hassouni, K., & Lefebvre, M., *Determining electron temperature and density in a hydrogen microwave plasma. .* Journal of thermophysics and heat transfer, 1996. **10**(3): p. 426-435.
3. Khalilov, U., et al., *Nanoscale mechanisms of CNT growth and etching in plasma envirement.* Journal of Physics D: Applied Physics, 2017. **50**(18): p. 184001.
4. Skukla, B., et al., *Interdependency of Gas Phase Intermediates and Chemical Vapor Deposition Growth of Single Wall Carbon Nanotubes.* Chemistry of Materials, 2010. **22**(22): p. 6035-6043.
5. Buckman, S.J., *Tabulations of Collision Cross Sections and Calculated Transport and Reaction Coefficients for Electrons in H2 and D2. .* JILA Data Center Report, 1985. **27**.
6. Marinov, N.M., Pitz, W. J., Westbrook, C. K., Vincitore, A. M., Castaldi, M. J., Senkan, S. M., & Melius, C. F, *Aromatic and polycyclic aromatic hydrocarbon formation in a laminar premixed n-butane flame.* Combustion and flame, 1998. **114**(1-2): p. 192-213.
7. Pashova, K., et al., *Graphene synthesis by microwave plasma chemical vapor deposition: analysis of the emission spectra and modeling.* Plasma Sources Science and Technology, 2019. **28**(4): p. 045001.
8. Dandy, D.S., & Yun, J. , *Momentum and thermal boundary-layer thickness in a stagnation flow chemical vapor deposition reactor.* Journal of materials research, 1997. **12**(4): p. 1112-1121.
9. Vichnevetsky, R., & Vignes, J., *IMACS transactions on scientific computation-85.* 1986.
10. Hinkov, I., et al., *Microwave Plasma Enhanced Chemical Vapor Deposition of Carbon Nanotubes.* Journal of Surface Engineered Materials and Advanced Technology, 2014. **04**(04): p. 196-209.
11. Hinkov, I., K. Pashova, and S. Farhat, *Modeling of plasma-enhanced chemical vapor deposition growth of graphene on cobalt substrates.* Diamond and Related Materials, 2019. **93**: p. 84-95.
12. Kausch, H.H., Fesko, D. G., & Tschoegl, N. W., *The random packing of circles in a plane.* Journal of Colloid and Interface Science, 1971. **37**(3): p. 603-611.
13. Robertson, J., et al., *Applications of Carbon Nanotubes Grown by Chemical Vapor Deposition.* Japanese Journal of Applied Physics, 2012. **51**(1): p. 01AH01.
14. Andalouci, A., et al., *Morphological and magnetic study of plasma assisted solid-state dewetting of ultra-thin cobalt films on conductive titanium silicon nitride supports.* Thin Solid Films, 2020. **703**: p. 137973.
15. Andalouci, A., et al., *Low frequency vibrations observed on assemblies of vertical multiwall carbon nanotubes by Brillouin light scattering: determination of the Young modulus.* Phys Condens Matter, 2020. **32**(45): p. 455701.
16. Uryu, S. and T. Ando, *Electronic intertube transfer in double-wall carbon nanotubes.* Physical Review B, 2005. **72**(24).
17. Grujicic, M., Cao, G., & Gersten, B., *Optimization of the chemical vapor deposition process for carbon nanotubes fabrication.* Applied surface science 2002. **191**(1-4): p. 223-239.
18. Grujicic, M., Cao, G., & Gersten, B. , *An atomic-scale analysis of catalytically-assisted chemical vapor deposition of carbon nanotubes.* Materials Science and Engineering: B, 2002. **94**((2-3)): p. 247-259.
19. Maier, L., et al., *Steam Reforming of Methane Over Nickel: Development of a Multi-Step Surface Reaction Mechanism.* Topics in Catalysis, 2011. **54**(13-15): p. 845-858.
20. Delgado, K., et al., *Surface Reaction Kinetics of Steam- and CO2-Reforming as Well as Oxidation of Methane over Nickel-Based Catalysts.* Catalysts, 2015. **5**(2): p. 871-904.
21. Futaba, D.N., et al., *Kinetics of water-assisted single-walled carbon nanotube synthesis revealed by a time-evolution analysis.* Phys Rev Lett, 2005. **95**(5): p. 056104.
22. Futaba, D.N., Hata, K., Namai, T., Yamada, T., Mizuno, K., Hayamizu, Y., ... & Iijima, S., *84% Catalyst Activity of Water-Assisted Growth of Single Walled Carbon Nanotube Forest*

Characterization by a Statistical and Macroscopic Approach. Journal of Physical Chemistry 2006. **110**(15): p. 8035-8038.

23. Chang, J., et al., *Efficient Closed-loop Maximization of Carbon Nanotube Growth Rate using Bayesian Optimization.* Sci Rep, 2020. **10**(1): p. 9040.
24. Garg, R.K., et al., *Effects of feed gas composition and catalyst thickness on carbon nanotube and nanofiber synthesis by plasma enhanced chemical vapor deposition.* J Nanosci Nanotechnol, 2008. **8**(6): p. 3068-76.
25. Hosseini, M.R., N. Jalili, and D.A. Bruce, *A time-dependent multiphysics, multiphase modeling framework for carbon nanotube synthesis using chemical vapor deposition.* AIChE Journal, 2009. **55**(12): p. 3152-3167.
26. Jimenez-Redondo, M., et al., *Chemistry in glow discharges of H2 / O2 mixtures. Diagnostics and modelling.* Plasma Sources Sci Technol, 2015. **24**(1).
27. Luo, Y.C., et al., *Selective growths of single walled carbon nanotubes from mesoporous supports via CO disproportionation.* Journal of the Chinese Chemical Society, 2021. **68**(3): p. 491-499.
28. Gangoli, V.S., Godwin, M. A., Reddy, G., Bradley, R. K., & Barron, A. R. , *The state of HiPco single-walled carbon nanotubes in 2019.* C, 2019. **5**(4): p. 65.
29. ANSYS 2020. ANSYS Chemkin-Pro Theory Manual, R.R., January 2020.
30. Jasiński, M., M. Dors, and J. Mizeraczyk, *Production of hydrogen via methane reforming using atmospheric pressure microwave plasma.* Journal of Power Sources, 2008. **181**(1): p. 41-45.
31. Chen, Q., et al., *The role of hydroxyl and atomic oxygen in multiwall carbon nanotube growth.* Frontiers of Materials Science in China, 2008. **2**(1): p. 20-25.

Chapter IV: Physical characterizations of nanoparticles and VACNTs.

After analyzing and optimizing the growth of nanotubes in the previous chapters, we investigate in this chapter some physical properties of the dewetted nanoparticles and synthesized VACNTs. Vibrating sample magnetometry (VSM) and Brillouin light scattering (BLS) techniques were used to study both their static and dynamic magnetic behaviors as well as the VACNTs mechanical properties.

We first performed VSM measurements on dewetted cobalt nanoparticles. The measurements obtained from the assembly of cobalt nanoparticles were analyzed by means of nanoparticle size distribution. VSM measurements were also performed on VACNTs and filled VACNTs to point out the shape anisotropy contribution to the magnetic behavior of these VACNTs with different filling forms, the analysis was reinforced with a statistical study of shape descriptors of encapsulated nanoparticles.

Second, BLS measurements were monitored to assess the effective optical properties of the nanoparticles comparing to that observed on the native layer, in order to explain the observed reversed height asymmetry of the magnons lines between the two systems. Indeed, the assembly of nanoparticles behaves as an effective magnetic and optical medium where these properties can be tuned by the elaboration process.

Finally, the mechanical elastic behavior of VACNTs assemblies has been studied, also, by means of BLS by investigating the phonons behavior. The measured inelastic light scattering from the VACNTs is attributed to bending vibrations of the nanotubes, considered as dense effective media. The observed phonons frequencies are compatible with an effective Young modulus of 850 GPa.

4.1 Magnetic properties of Co nanoparticles

Dealing with Co magnetic nanomaterials as catalyst for carbon nanotubes growth, they are characterized by the value of their remnant magnetization and that of their coercive field. The remnant magnetization is determined by the spontaneous magnetization of the material. Coercivity is linked in particular to magnetic anisotropy that is mainly dictated by shape anisotropy of the nanomaterial. Different shapes of Co nanoparticles were obtained from the dewetting process, as presented in Chapter II. In this section, growth and filling of the VACNTs, VSM characterization of the static magnetic properties of the Co nanoparticles are presented and discussed.

4.1.1 Experiments

VSM measurements were taken at SATIE laboratory (ENS Cachan, now at Paris Saclay University) using a vibrating sample magnetometer (VSM) Lakeshore 7400 that records the magnetization M versus the applied magnetic field H, using an electromagnet providing a magnetic field up to 20 kOe. It high sensitivity (10^{-7} emu) enables to record extremely low magnetic signal. VSM hysteresis curves for the as-deposited continuous native layer and the assembly of nanodots obtained after the solide-state dewetting process, presented in Figure 2(b), were measured in the configuration where the magnetic field is applied in the plane of the films.

4.1.2 Magnetic properties of dewetted cobalt nanoparticles

We focus in this section on the static magnetic properties of the 3 nm-thick Co films deposited on TiSiN that give a better signal-to-noise ratio than lower Co thicknesses. Figure 4.1 shows the normalized hysteresis curves for the as-deposited film (a), and for the dewetted films, after the thermal reduction (b) and after association of the thermal reduction to the plasma treatment (c). The corresponding assemblies of nanoparticles are shown in the attached SEM images. We analyze here the effect of the thermal treatment on one side (b) and the combination of thermal and plasma treatments on the other side (c). Therefore, the magnetic behavior is widely discussed based on size and shape distribution of Co nanoparticles.

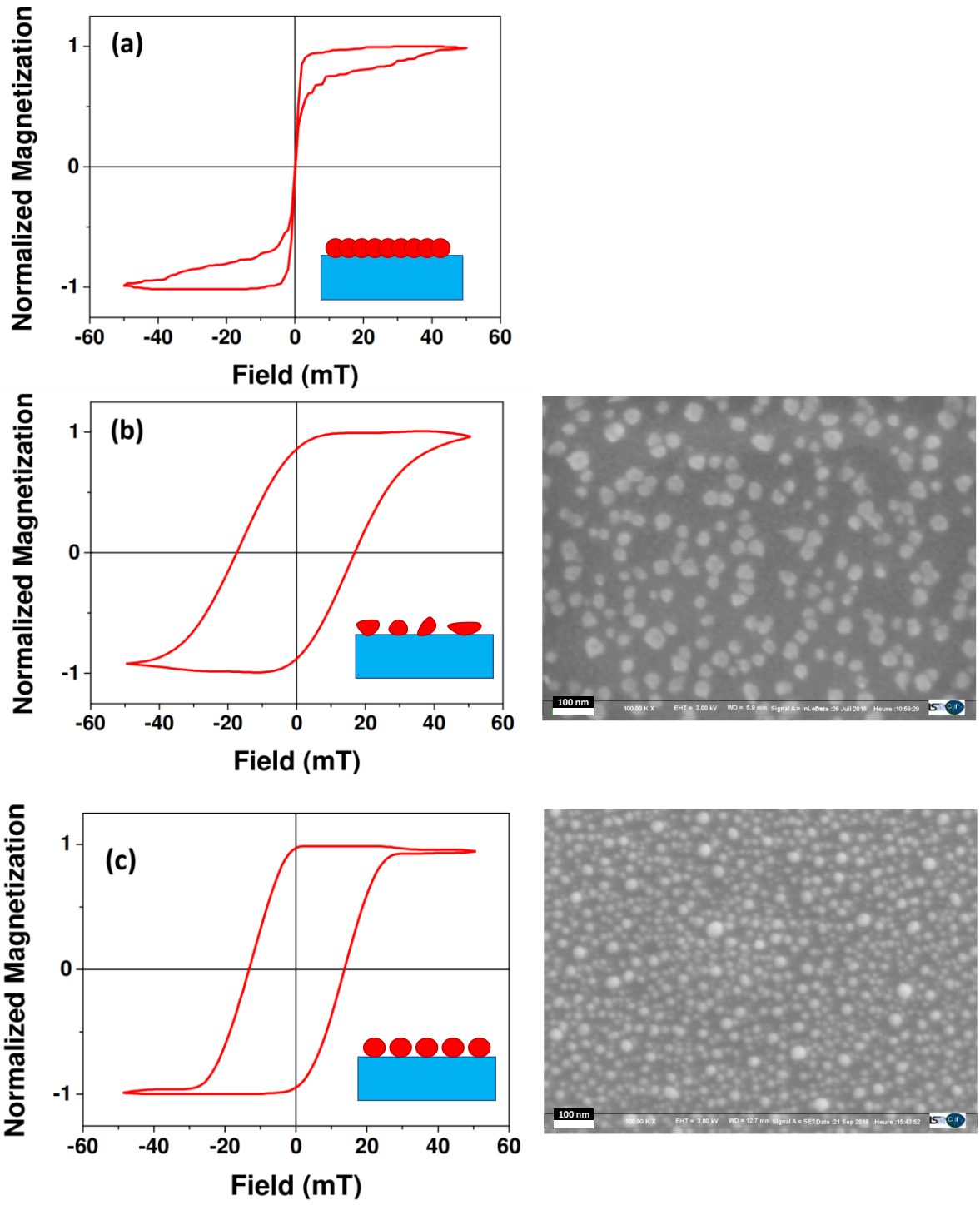

FIG 4.1. Hysteresis cycles of 3 nm-thick cobalt films deposited on TiSiN: a) as-deposited b) after thermal treatment, c) after thermal and plasma treatments. Inserts in hysteresis schematically shows the state of the cobalt on the top of the substrate. SEM images are shown on the right for dewetted films.

The as-deposited Cobalt film presents a narrow hysteresis curve with a weak coercive field H_c about 0.6 mT. This small coercivity is probably associated with domain wall motion across grains boundaries [1]. After preforming the thermal reduction, H_c increases to about 17 mT. As we perform combination of thermal and plasma treatments, its value slightly decreases to 14 mT. The increase of the coercive field in the first protocol is due to the nanostructuring of the continuous film into nanoparticles which completely modify the magnetization reversal process regarding to the continuous film. As a general trend, the coercivity is found to increase up to a maximum and then to decrease to zero with decreasing the particle size [2]. It exists a critical size, lying in the range of few tens of nanometers, which separates different magnetization behaviors. It depends on the material nature and on its micromagnetic parameters. For spherical particles, the critical diameter below which a single-domain state exists is reached when the domain-wall energy and the magnetostatic energy are equal [3]. As discussed above, introducing the plasma treatment after the thermal one produces narrow particle size distribution with higher density. This diminishes the geometrical dispersion introduced by the thermal treatment by exhibiting less particles side defects and more homogeneous size distribution leading to a slightly lower coercive field.

4.1.3 Discussion

Considering the cobalt nanoparticles studied in this section, the size distribution provides an average size of 29 nm (with 79% of nanoparticles size above 24 nm) after preforming thermal treatment, and an average diameter of 18 nm (with 80% of nanoparticles size below 24 nm) after combination with the plasma one. We can thus infer that these nanoparticles are mostly quasi-uniformly magnetized. The squarness S (M_r/M_s) exhibits values higher than 0.8. Various mechanisms can be responsible for the magnetization reversal that can correspond to coherent rotation, curling or domain wall motion. In the case of a spherical nanoparticle of diameter D, Aharoni has shown that the process of magnetization reversal by coherent rotation is ensured for up to a diameter such that $D < D_c = 7.21\ L$, L being the exchange length given by $(A/2\pi M_s^2)^{1/2}$; with A the exchange stiffness constant [4]. Namely, using the usual cobalt bulk material parameters ($A = 1.8\times10^{-6}$ erg.cm^{-1} and $4\pi M_s = 17.6$ kOe), one finds $L \approx 4$ nm in good agreement with literature [5]. We can conclude that the homogeneous rotation is then operative up to approximately a particle diameter of about 30 nm. The opening of the hysteresis cycles after thermal treatment and after combination with plasma one could be mainly attributed to a slight shift to sphericity (ellipsoidal nanoparticles). It is to mention that in the case of

polycrystalline nanoparticles, which is our case, an effective magnetic anisotropy can be introduced due to the fact that each nanoparticle can be represented as an assembly of monocrystalline grains of different sizes, close to the single-domain diameter, having a random distribution of their easy anisotropy [6, 7]. However, such effective anisotropy is significantly less than the anisotropy of the crystallites constituent the nanoparticle. Complex microstructure in polycrystalline nanoparticles has been presented at the origin of reduced coercive field compared with that expected from randomly oriented assembly of single-crystal nanoparticles [8]. Note also that the nanoparticles issued from the two treatments exhibit sizes enough large to ensure that the thermal agitation does not overcome magnetic anisotropy energy; otherwise, this would have led to a superparamagnetic state where the magnetization becomes unstable above the blocking temperature, leading to lack of coercivity.

4.1.4 Partial conclusion

Magnetic properties have been discussed within the frame of magnetic anisotropy introduced by a small deviation to sphericity of the nanoparticles. Our results also proved that the solid-state dewetting on TiSiN is a reliable and non-expensive approach to elaborate controlled size and distribution assembly of metal nanoparticles.

4.2 Magneto optical properties of cobalt nanoparticles

4.2.1 Experiments

The magnetization dynamics of Co nanoparticles has been investigated through the study of the spin waves (SWs) modes with nonzero wave-vector values by means of BLS technique. In the BLS set-up, the SWs characterized by a wave number (k_{sw}) up to 20 μm $^{-1}$ (depending on the incidence angle θ: $k_{sw} = \frac{4\pi}{\lambda}\sin\theta$ in backscattering configuration), are probed by illuminating the sample with a laser having a wavelength λ = 532 nm. The magnetic field is applied perpendicular to the incidence plane allowing for probing SWs propagating along the in-plane direction perpendicular to the applied field i.e. the so-called Damon-Eshbach (DE) geometry [9-12]. The Stokes (S, negative frequency shift relative to the incident light) and anti-Stokes (AS, positive frequency shift relative to the incident light) frequencies are simultaneously detected. Typical BLS spectra for the initial continuous film and for the

assembly of nanodots are presented in Figure 4.2.

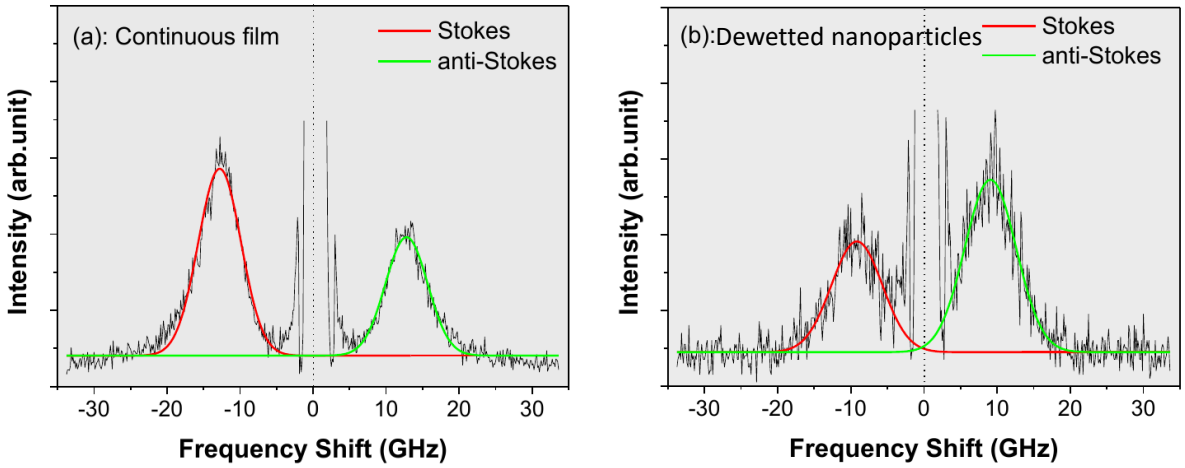

FIG 4.2 Typical BLS spectra obtained for (a) the continuous film and (b) the assembly of cobalt nanodots with an applied field of 2 kOe and an angle of incidence of 30 ^{o}. Notice the reversed Stokes/anti-Stokes line height asymmetry between the two spectra.

4.2.2 Results

The properties of the initial film are typical for an easy in-plane magnetization. It means that the magnetic anisotropy K is inferior to the shape anisotropy $2\pi M^2$ (where M is the magnetisation). Assuming $M = 1400$ emu/cc, one can fit the film frequency variation with respect to the applied field by taking $K = 8.05$ Merg/cc as shown in Figure 4.3 (a). The frequency is derived from the usual formula [13]

$$F = \frac{\gamma}{2\pi}\sqrt{(H + \frac{2A}{M}k^2 + 4\pi M(1-G))(H + \frac{2A}{M}k^2 + 4\pi MG - \frac{2K}{M})} \qquad (1)$$

where γ, H, A, k, t, G are the gyromagnetic factor, the external field, the exchange constant, the wave vector, the thickness and the factor giving account of the dynamic field associated to the magnetization oscillation. For a thin film, this latter parameter reads $G = \frac{1-exp(-|kt|)}{|kt|}$. The parameters values are $\frac{\gamma}{2\pi}$ = 2.95 GHz/kOe , A = 1.8 μerg/cm, which are typical values for cobalt, k = 11.8 μm $^{-1}$, corresponding to the used angle of incidence 30 ^{o}, t = 3 nm, is the thickness of the as-deposited cobalt film.

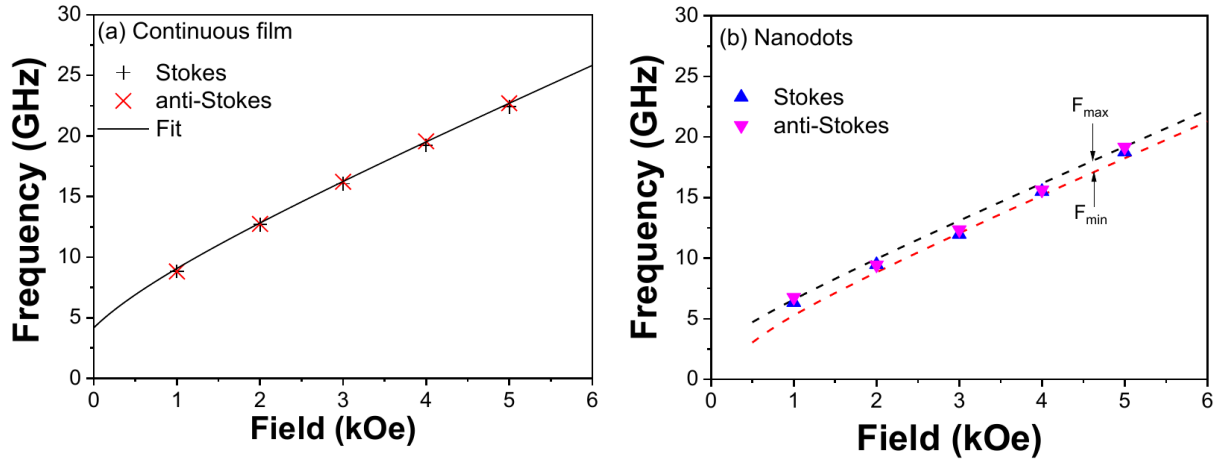

FIG 4.3: Variation of the spin waves frequency versus the applied magnetic field for (a) the continuous film and (b) for the assembly of nanoparticles. The measurements for the film can be fitted with $K = 8.05$ Merg/cc, those for the assembly of nanodots are fitted if each dot can be regarded as an ellipsoid with a thickness 7.8 nm and two diameters 18.4 nm and 17.6 nm, the dipolar interaction being characterized by the demagnetizing factor $N'_3 = 4$.

The microscopy images show nearly circular dots with an average diameter of 18 nm. The corresponding hysteresis loop exhibits a coercive field. Consequently the dot volume and the magnetic anisotropy allow for stabilizing the magnetization direction. As discussed above, we can assume that the static magnetization is uniform in each dot. In order to interpret the coercive field revealed by magnetometry, we assume that the dots are not perfectly circular. Let d_1 be the larger diameter of a dot, d_2 the smaller in-plane diameter and d_3 the thickness. Let N_1, N_2 and N_3 be the demagnetizing factors. The dots are randomly oriented in plane. Thus the coercive field corresponds to dots whose larger diameter is aligned along the field direction $i.e.$

$$H_c = (N_2 - N_1)M \tag{2}$$

We assume that the dot thickness can be evaluated from the cobalt conservation

$$d_3 = d_{film}\left(\frac{\ell}{d_{mean}}\right)^2 \tag{3}$$

where $d_{film} = 3$ nm is the film thickness, $\ell = 29$ nm is the average distance between dots and $d_{mean} = 18$ nm is the mean dot diameter. The dot thickness is thus estimated to $d_3 = 7.8$ nm. Fitting the coercive field value by the expression (2) allows for deriving the maximal d_1 and minimal d_2 in-plane dot diameter values and associated demagnetizing factors:

$d_1 =$	18.36 nm	$N_1 =$	2.65
$d_2 =$	17.64 nm	$N_2 =$	2.79
$d_3 =$	7.79 nm	$N_3 =$	7.12

N_1, N_2 and N_3 are calculated by numerical integration. For instance

$$N_3 = \int_0^{\pi} \int_0^{2\pi} \frac{d_1 d_2 d_3 \cos^2(\theta)\sin(\theta) d\theta d\varphi}{((d_1\sin(\theta)\cos(\varphi))^2+(d_2\sin(\theta)\sin(\varphi))^2+(d_3\cos(\theta))^2)^{3/2}} \quad (4)$$

is evaluated by the Simpson approximation with $d\theta = d\varphi = \pi/1000$

As the dots are randomly oriented, the dipolar interactions between dots are characterized by an out-of-plane demagnetizing factor N'_3 and two equal in-plane factors $N'_1 = N'_2$. While the sum of the demagnetizing factors is equal to 4π, the sum of the dipolar interaction factors is null, thus $N'_1 = N'_2 = -N'_3/2$ [13]. Considering that the dot size is much lower than the light wave, $d << \lambda$, we can assume that the probed mode by BLS is uniform in each dot. Thus the Kittel formula giving the frequency of the uniform mode [14] can be used. It is derived from the following energy:

$$E_M = -\vec{H}.\vec{M} + \frac{1}{2}(N_1 M_1^2 + N_2 M_2^2 + N_3 M_3^2) - \frac{K}{M^2} M_3^2 \quad (5)$$

$$+(N_{1'} M_1 M_{1'} + N_{2'} M_2 M_{2'} + N_{3'} M_3 M_{3'})$$

where $\vec{M}$ is the magnetization in a dot, $\vec{M'}$ is the magnetization in other dots. In other words, the effective field in each dot reads:

$$-\nabla_M E_M = \vec{H} - (N_1 M_1 \vec{e}_1 + N_2 M_2 \vec{e}_2 + N_3 M_3 \vec{e}_3) \quad (6)$$

$$+\frac{2K}{M^2} M_3 \vec{e}_3 - (N_{1'} M_{1'} \vec{e}_1 + N_{2'} M_{2'} \vec{e}_2 + N_{3'} M_{3'} \vec{e}_3)$$

where $\vec{e}_1$, $\vec{e}_2$ are the two in-plan unit vectors and $\vec{e}_3$ is the normal to the dot plane.
Finally the Kittel formula for a dot whose larger diameter lies along the applied field is

$$F_{max} = \frac{\gamma}{2\pi}\sqrt{(H + (N_2 - N_1)M)(H + (N_3 - N_1)M + 3N'_3 M/2 - 2K/M)} \quad (7)$$

and the Kittel formula for a dot whose smaller in-plane diameter lies along the applied field is

$$F_{min} = \frac{\gamma}{2\pi}\sqrt{(H + (N_1 - N_2)M)(H + (N_3 - N_2)M + 3N'_3M/2 - 2K/M)} \quad (8)$$

The two calculated assembly frequencies displayed in Figure 4.3(b) correspond to dots whose larger diameter is parallel or perpendicular to the applied field. These calculated frequencies are the maximal and minimal values for the eigen frequency of randomly in plane oriented dots. These two limits frame the experimental frequencies represented by the symbols in Figure 4.3(b). The fitting parameter is $N'_3 = 4$. If the dots were flat, N'_3 would be close to $4\pi(\frac{d_{mean}}{\ell})^2 = 4.84$. As they are not flat this demagnetizing factor is reduced. It is to notice that the spin waves frequencies are lower in the case of the assembly of nanodots compared to the frequencies of the continuous film. In fact, in this latter case, the probed mode corresponds to the so-called Damon-Eshbach propagating spin wave while the uniform mode is probed in the case of nanodots as discussed above ; consequently there is no influence of the wave vector. Moreover the shape anisotropies are different in the two cases. As the film thickness is low, the most important parameter modifying the frequency is the shape anisotropy. Thus, the models used for analyzing the film and the dots assembly results differ.

Concerning the BLS line height reversed asymmetry observed on assembly spectra, this phenomenon has already been evidenced on ultra thin magnetic wire assemblies [15] and has been attributed to the peculiar light polarization inside the magnetic nano-objects. We can speculate that for our ultra narrow dot assembly, the light polarization is also peculiar making this assembly interesting for their optical properties. In order to elucidate the reversed asymmetry, we use the Maxwell Garnett approximation to derive the assembly optical properties: as the dot diameter is much lower than the wavelength of the probing light, we can use the electrostatic approximation to derive the field inside each dot. Inside each dot the electric field is deduced from the one existing in the gap from the relations

$$E_{//}^{dot} = E_{//}^{gap}/(1 + N_{//}(\varepsilon_{dot} - 1)/(4\pi)) \quad (9)$$

$$E_{\perp}^{dot} = E_{\perp}^{gap}/(1 + N_{\perp}(\varepsilon_{dot} - 1)/(4\pi)) \quad (10)$$

where $N_{//}$ and $N_{\perp}$ are the depolarizing factors. As we intend to derive the optical properties of the assembly, we take $N_{//} = \frac{1}{2}(N_1 + N_2)$ and $N_{\perp} = N_3$. The effective in-plane and out-of-plane permittivities of the assembly are thus

$$\varepsilon_{//} = \frac{(1-f)E_{//}^{gap} + f\varepsilon_{dot}E_{//}^{dot}}{(1-f)E_{//}^{gap} + fE_{//}^{dot}} \quad (11)$$

$$\varepsilon_{\perp} = \frac{(1-f)E_{\perp}^{gap} + f\varepsilon_{dot}E_{\perp}^{dot}}{(1-f)E_{\perp}^{gap} + fE_{\perp}^{dot}} \quad (12)$$

where $f = (d_{mean}/\ell)^2$. Taking into account the assembly optical property, we derive the electric field using the Maxwell boundary conditions at the interface air/assembly

$$E_{//}^{inc} + E_{//}^{ref} = E_{//}^{+} + E_{//}^{-} \tag{13}$$

$$E_{\perp}^{inc} + E_{\perp}^{ref} = \varepsilon_{\perp}(E_{\perp}^{+} + E_{\perp}^{-}) \tag{14}$$

and at the interface assembly/substrate

$$E_{//}^{tra} = E_{//}^{+}\exp(i\phi) + E_{//}^{-}\exp(-i\phi) \tag{15}$$

$$\varepsilon^{sub}E_{\perp}^{tra} = \varepsilon_{\perp}(E_{\perp}^{+}\exp(i\phi) + E_{\perp}^{-}\exp(-i\phi)) \tag{16}$$

where ε^{sub} is the permittivity of the substrate, $\phi = k_{\perp}^{assembly}d_3$ is the phase related to the assembly thickness, $E_{//}^{inc}$ and $E_{\perp}^{inc}$ are the incident field components, $E_{//}^{ref}$ and $E_{\perp}^{ref}$ are the reflected field components, $E_{//}^{+}$, $E_{//}^{-}$ and $E_{\perp}^{+}$, $E_{\perp}^{-}$ are field components inside the assembly, $E_{//}^{tra}$ and $E_{\perp}^{tra}$ are the field components inside the substrate as well as the relations deduced from the Maxwell equations

$$\varepsilon_{//}^{\alpha}E_{//}^{\alpha}k_{//}^{\alpha} + \varepsilon_{\perp}^{\alpha}E_{\perp}^{\alpha}k_{\perp}^{\alpha} = 0 \tag{17}$$

$$\frac{(k_{//}^{\alpha})^2}{\varepsilon_{\perp}^{\alpha}} + \frac{(k^{\alpha}\perp)^2}{\varepsilon_{//}^{\alpha}} = (\frac{2\pi}{\lambda})^2 \tag{18}$$

where λ is the laser wavelength and $\alpha \in \{air, assembly, substrate\}$

The coupling of light ($E_{//}^{dot}$, $E_{\perp}^{dot}$) and dynamic magnetization ($m_{//}$, $m_{\perp}$) yields a scattered light whose intensities is proportional to [8]

$$I = |E_{//}^{dot}m_{\perp} - E_{\perp}^{dot}m_{//}|^2 \tag{19}$$

From the Landau Lifshitz equation, we deduce $m_{\perp}/m_{//} = -H/(i\frac{2\pi F}{\gamma})$, thus the ratio between Stokes and anti Stokes intensity can be written as

$$\frac{I_{St}}{I_{aSt}} = \left|\frac{i\frac{2\pi F}{\gamma}E_{\perp}^{dot} - HE_{//}^{dot}}{-i\frac{2\pi F}{\gamma}E_{\perp}^{dot} - HE_{//}^{dot}}\right|^2 \tag{20}$$

Using the optical parameters of cobalt $\varepsilon = -10 + 15i$ and of the titanium $\varepsilon = -5 + 17i$ [16],we derive the intensity ratio as a function of the incidence angle θ as displayed in Figure 4.4. In the case of the film this ratio is greater than 1 and increases with θ while for the dot assembly it is inferior to 1 and decreases with the incidence angle. Finally the effective optical properties of the assembly combined with the relation between mean field and inside dot field can explain the observed reversed height asymmetry. Interestingly the most influencing parameters on the effective optical properties are the nano object shape and density. In the range of the metal refractive index for visible light, this parameter plays a secondary role on the effective properties.

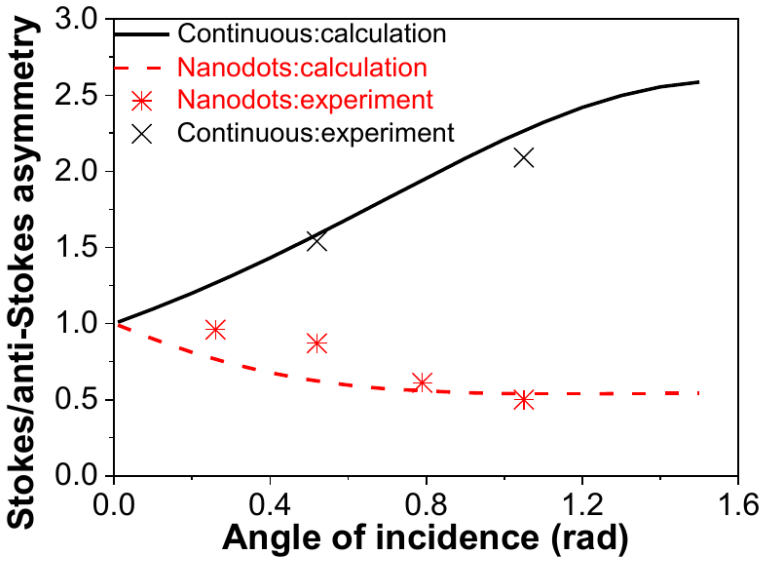

FIG 4.4: Stokes anti-Stokes asymmetry vs incidence angle for the continuous film and the assembly of nanodots.

4.2.3 Partial conclusion

We studied the static and dynamic magnetic properties of an ultra narrow nanoparticles assembly obtained from solid-state dewetting of a 3 nm-thick native cobalt layer, using vibrating sample magnetometry (VSM) and Brillouin light scattering (BLS) techniques. The dewetting approach proves effective and not very constraining to obtain assemblies of nanoparticles with well-controlled size and distribution. The VSM static measurements were satisfactorily analyzed by means of assembly of nearly circular dots (ellipsoid) in which the

magnetization is stable. The BLS measurements revealed a peculiar magneto-optical behaviour and that the light polarization inside the nanodots can be deduced from averaged optical properties. Such assembly of nanodots behaves as an effective magneto-optical material with tunable properties.

It is worth highlighting the importance of the following. Usually, the Brillouin spectroscopy is regarded as a tool for investigation of magnetic properties, while the optical properties are supposed to be known. Studying effective materials opens a new promising alternative in the BLS technique: investigation of their highly non-trivial optical and magneto-optical features, taking advantage of the knowledge of the magnetic dynamics.

4.3 Magnetic properties of VACNTs and Filled VACNTs

4.3.1 Magnetic properties of VACNTs

Hysteresis loop measurements were performed on VACNTs obtained from 3 nm Co catalyst, presented in Figure 2.13, by using the LSPM reactor. Figure 4.5 presents the cycles obtained at room temperature with a magnetic field applied in the film plane (perpendicular to the VACNTs axis) and perpendicular to the film plane (parallel to the VACNTs axis), respectively.

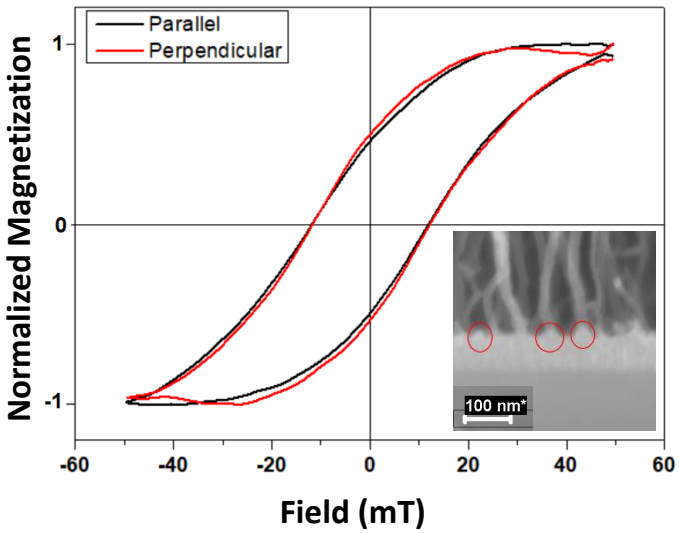

FIG. 4.5. Hysteresis cycles of VACNTs issued from 3 nm-thick cobalt films deposited on TiSiN (see Figure. 2.13) with a field applied parallel (black) or perpendicular (red) to the VACNTs axis.

No significant difference is observed between the two directions with a coercive field H_c about 12 mT, sensitively higher than those reported for thick cobalt layers, about 1 mT [1].

The two hysteresis loops exhibits the same squareness S, defined as the ratio of remnant magnetization Mr and of saturation magnetization Ms, suggesting that there is no contribution of a shape anisotropy associated to the Co nanoparticles that catalysed the growth of the VACNTs, between the perpendicular and the parallel configurations. This is indication that the nanoparticles are mainly spherical, as displayed in the insert of Figure 4.5, and enough distant to cancel dipolar coupling.

We notice that the H_c value seems to be only slightly lower than that of the ones measured for dewetted nanoparticles after the thermal followed by plasma protocols, indicating that the dewetted nanoparticles are preserved during VACNTs growth process.

4.3.2 Magnetic properties of filled VACNTs

Hysteresis loop measurements at room temperature were also conducted, at ITODYS laboratory of University Paris Diderot, on filled VACNTs elaborated in section 2.4 of chapter II, using the Thales reactor operating with a bias. Four samples were chosen:

- filled VACNTs on Co 9 nm under 950° C and 200 W (see Figure 2.32 a)
- filled VACNTs on Pd 6 nm / Co 9 nm under 750° C and 200 W (see Figure 2.30 c)
- filled VACNTs on Pd 6 nm / Co 9 nm under 950° C and 200 W (see Figure 2.33)
- filled VACNTs on Pd 3 nm / Co 6 nm under 950° C and 200 W (see Figure 2.31 b)

Along with magnetic measurements, statistical analysis of the encapsulated magnetic nanoparticles was done in order to correlate magnetic response to the filling state of the nanotubes. For this purpose, ImageJ software was used to obtain the following shape descriptors:

- Nanoparticle diameter: since all the four samples have vertically aligned carbon nanotubes, diameter of nanoparticles was obtained by measuring the longest distance in the horizontal axis for each nanoparticle.
- Nanoparticle Height: represents the length of the longest distance in the vertical axis for each nanoparticle
- Aspect ratio: calculated for each nanoparticle by dividing its height by its diameter

Moreover, according to EELS results (Chapter II, Figure 2.35), the chemical composition characterization attests that encapsulated nanoparticles are predominantly cobalt, thus , the following discussion is carried out assuming that the encapsulated nanoparticles are mainly Cobalt.

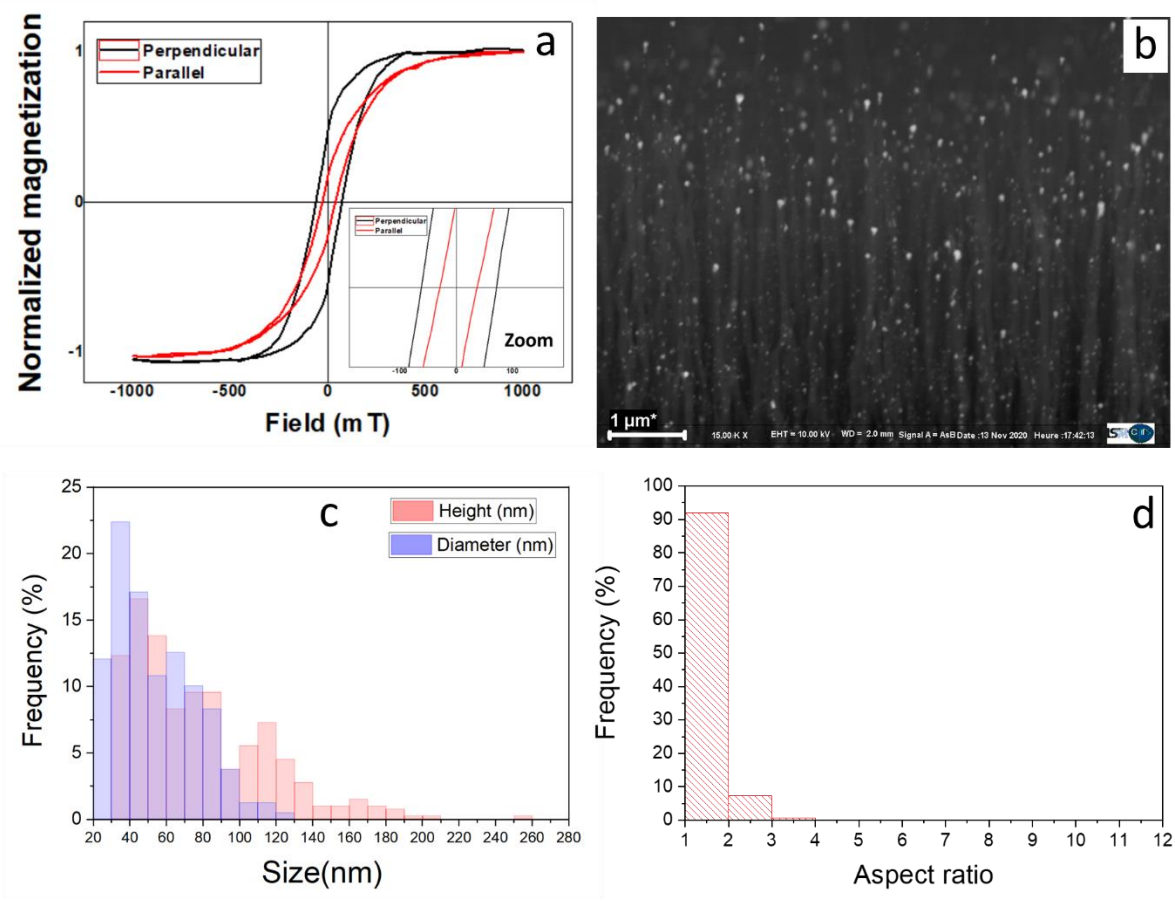

FIG. 4.6. Filled VACNTs issued from Co 9 nm films (950° C, 200 W): a) Magnetic hysteresis cycles with a magnetic field applied parallel (black) or perpendicular (red) to the VACNTs axis, b) SEM image, c) Nanoparticles diameter and height distribution, d) Nanoparticles aspect ratio distribution.

The hysteresis loop measurements of filled VACNTs on Co 9 nm are presented in Figure 4.6 a. This magnetic response might correspond to the cobalt nanoparticles encapsulated inside the internal canal of nanotubes as observed in the SEM image (Figure 4.6 b). An open cycle corresponding to a ferromagnetic response is observed. The coercive field H_c in the perpendicular configuration (parallel to the VACNTs growth axis) is about 66 mT which is the double of the value in the parallel configuration (perpendicular to the VACNTs growth axis), about 33 mT. Such difference cannot be explained by a plane assembly of spherical nanoparticles (see aspect ratio in Figure. 4.6 d), because in that case, the in-plane direction (parallel to the substrate) will be the easy direction for magnetization. One can assume, at first glance, that a shape anisotropy associated to vertical assemblies of spherical nanoparticles (encapsulated and/or decorating the vertical nanotubes) could contribute to this variation.

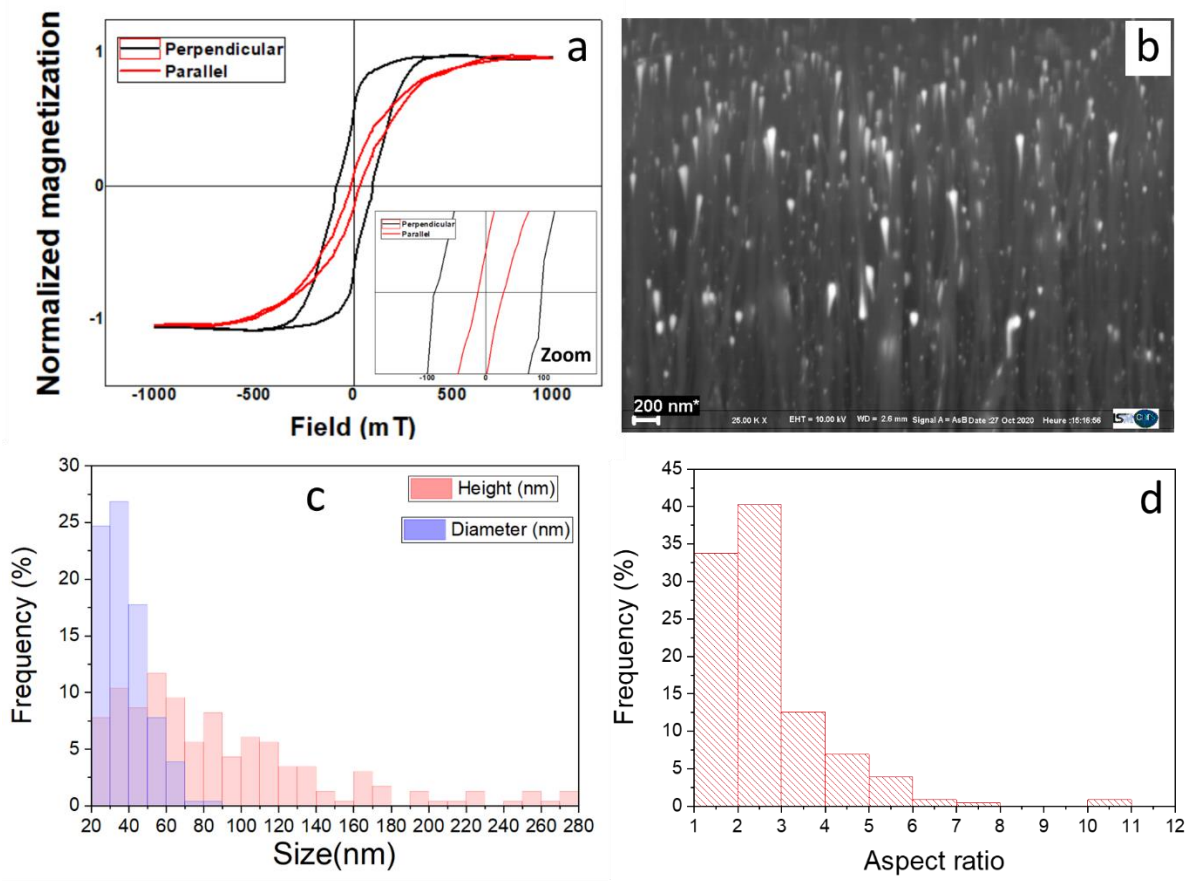

FIG. 4.7. Filled VACNTs issued from Pd 6 nm / Co 9 nm films (750°C, 200W)/ a) Magnetic hysteresis cycles with a field applied parallel (black) or perpendicular (red) to the VACNTs axis, b) SEM image, c) Nanoparticles diameter and height distribution, d) Nanoparticles aspect ratio distribution.

The hysteresis loop measurements of filled VACNTs on Pd 6 nm / Co 9 nm obtained at lower plasma temperature (750°C, 200 W) are presented in Figure 4.7 a. This measurement corresponds to the elongated Co nanoparticles presented in Figure 4.7 b. as compared to the spherical ones observed for the previous Co 9 nm sample. We observe a lower H_c value (22.5 mT) in the parallel configuration (field applied in the substrate plane; i.e. perpendicular to the VACNTs axis compared to the perpendicular configuration (field along the VACNTs axis), about 92.5 mT. This variation of coercive field can be attributed to a contribution of a shape anisotropy associated to the elongated shape of the nanoparticles, in the form of nails, i.e. with an apex. Figure 4.7 c shows the diameter and height distribution values of these nanoparticles, indicating smaller diameter values of the nanoparticles top (20-80 nm) and larger height values (20–280 nm), as compared to the previous Co sample. Along with changes in size distribution, shape anisotropy has also been enhanced as longer steep nanoparticles ending are observed.

The signature of the shape anisotropy is confirmed by the aspect ratio calculation presented in Figure 4.7 d. Higher aspect ratio values are obtained; 66% of nanoparticles have at least an aspect ratio of 2. Due to this enhancement in shape anisotropy, the ratio between in-plane and out-of-plane coercive field values is about 4.

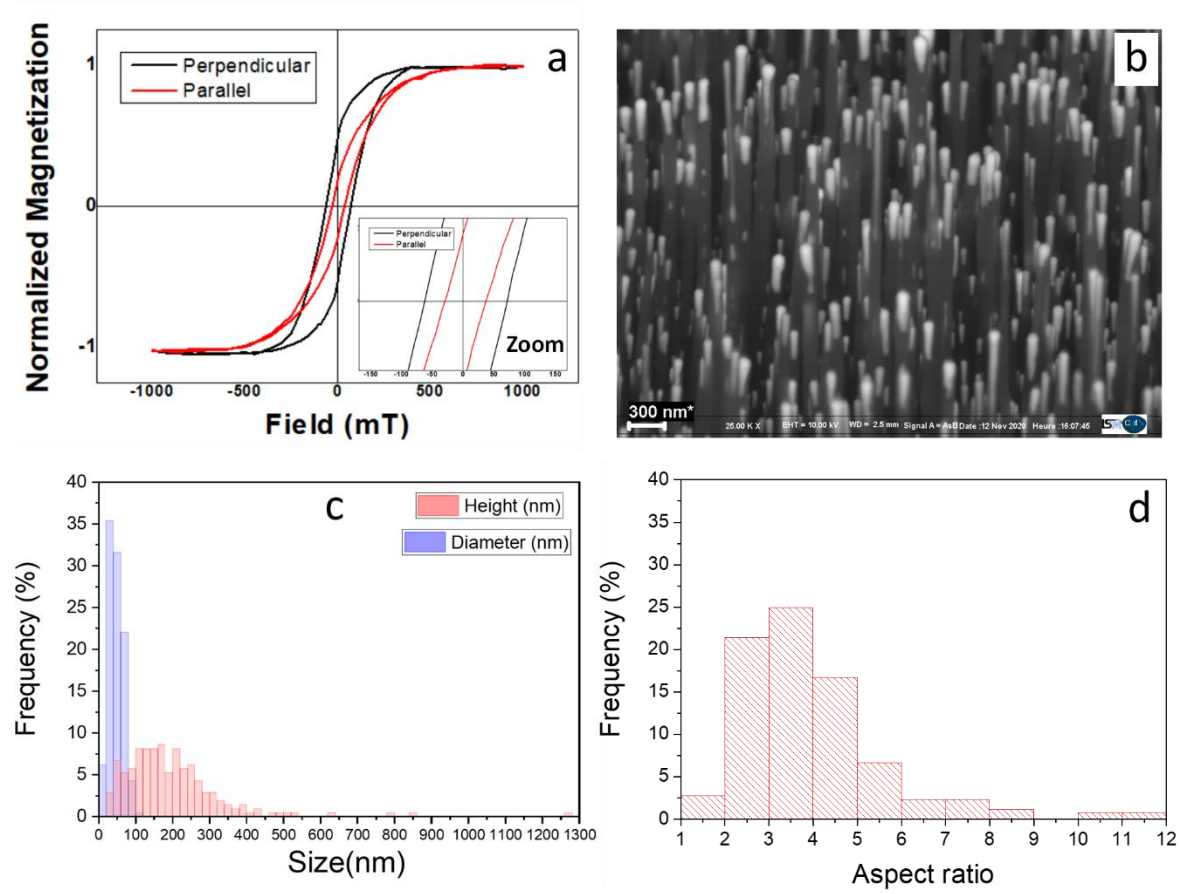

FIG. 4.8. Filled VACNTs issued from Pd 6 nm / Co 9 nm films (950° C, 200W)/ a) Magnetic hysteresis cycles with a field applied parallel (black) or perpendicular (red) to the VACNTs axis, b) SEM image, c) Nanoparticles diameter and height distribution, d) Nanoparticles aspect ratio distribution.

Magnetic hysteresis measurements and SEM image of Pd 6 nm / Co 9 nm sample at optimal filling conditions (950°C, 200 W) are presented in the Figures 4.8 a and 4.8 b, respectively. Although the same Pd/Co ratio is used for both samples, elaborated (@950°C) and (@750°C, respectively, lower H_c values are observed for the @950°C sample. Indeed, we obtain a coercive field about 33 mT in the parallel configuration (field applied in the substrate plane, i.e. perpendicular to the VACNTs axis), and about 67 mT in the perpendicular one (i.e. field parallel to VACNTs axis). These coercive field values are similar to those obtained for the

mainly spherical Co nanoparticles presented in Figure 4.6, in spite of clear shape anisotropy and better filling state between the two samples. This signs a similar magnetization reversal in these cases. The difference between the coercive field behavior of the two samples @950°C and (@750°C can be explained from the diameter and height size distribution presented in Figure 4.8.c. Indeed, higher diameter (20 –100 nm), and heights (20-500 nm) are obtained for the one @950°C. Moreover, aspect ratio is also better than the one @750°C, with 75% of nanoparticles having at least an aspect ratio of 3. We can conclude that despite the better shape anisotropy, the higher diameter distribution of elongated nanoparticles has decreased the magnetic response and consequently the H_c ratio between the parallel and the perpendicular configurations (2 for Pd6/Co9 @950°C (cylinders), as compared to 4 for Pd6/Co9 @750°C (nails). Such behaviour can be attributed to the absence of apex for the embedded nanoparticles obtained from Pd6/Co9 @950°C, thus reducing the coercive field.

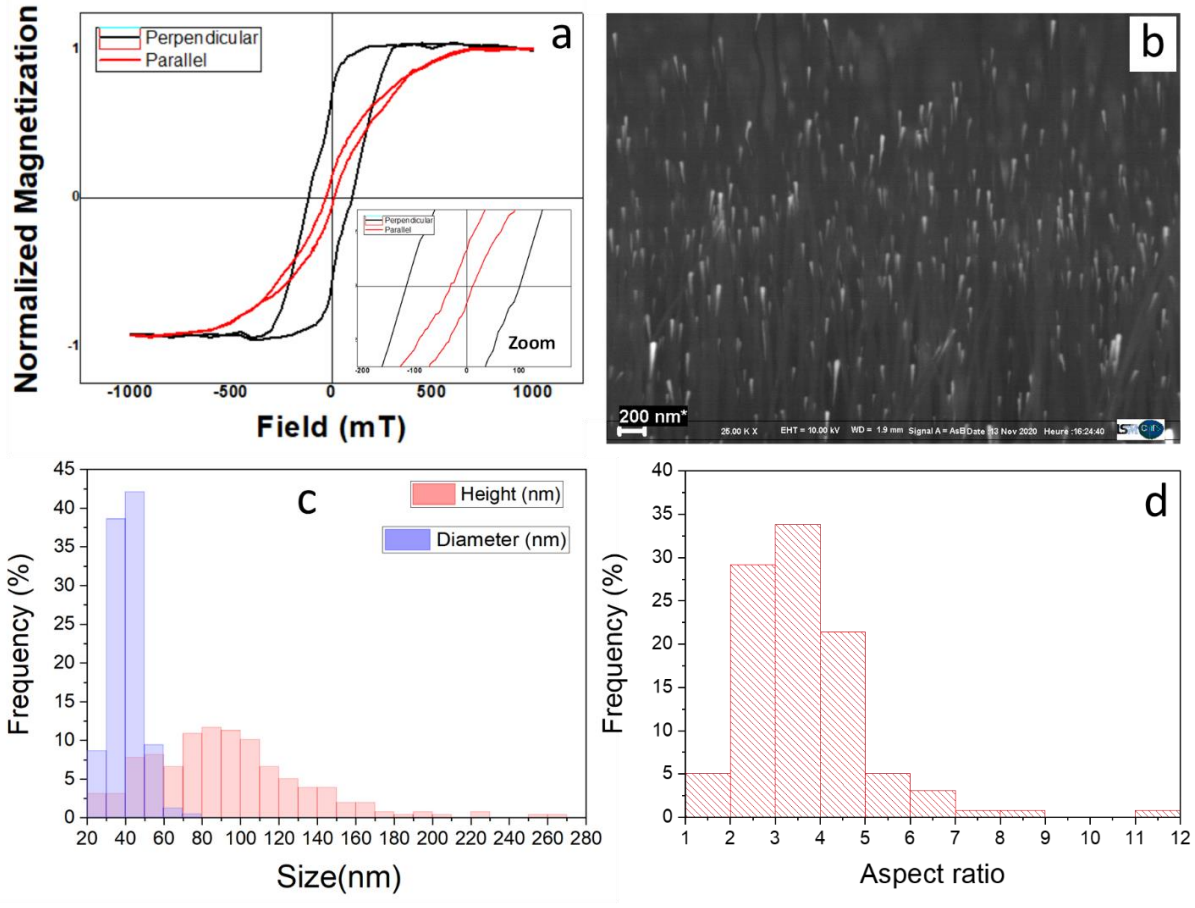

FIG. 4.9. Filled VACNTs issued from Pd 3 nm / Co 6 nm films (950°C , 200 W): a) Magnetic hysteresis cycles, b) SEM image, c) nanoparticles diameter and height distribution , d) Nanoparticles aspect ratio distribution.

Magnetic hysteresis measurements and SEM image of Pd 3 nm / Co 6 nm sample at optimal filling conditions (950° C, 200 W) are presented in the Figure 4.9 a and 4.9 b

respectively. The coercive field values are about 95 mT and 20 mT, in the perpendicular and parallel configurations, respectively. Size nanoparticles distribution presented in Figure 4.9 c shows a very good homogeinity of the nanoparticles diameters (90% of nanoparticles between 20-50 nm) the nanoparticles height is still similar to the previous samples (20-260 nm). Aspect ratio evaluation presented in Figure 4.9 d shows also better homogeneity with 65% of the nanoparticles showing an aspect ratio higher than 3. The combination of small diameter, better homogeneity and high aspect ratios has resulted better magnetic response. This is also translated with higher ratio of coercitive field values between out-of-plane (field parralel to VACNTs axis) and in-plane (field perpendicular to VACNTs axis) measurements, equal to 5. It's worth noticing that the coercive fields for this sample are very close to the ones obtained for Pd6/Co9 @750°C one, indicating quite similar magnetization reversal ; their shapes being close with marked apex.

4.3.3 Qualitative discussion

In order to qualitatively discuss the above results, a summary of the measured coercive fields H_c as well as squarnesses value S are summarized in Table 4.1.

Table 4.1: Co filled VACNTs magnetic measurements

Catalyst	**Co 9 nm**		**Pd 6 nm / Co 9 nm**		**Pd 6 nm / Co 9 nm**		**Pd 3 nm / Co 6 nm**	
Plasma	**200 W**		**200 W**		**200 W**		**200 W**	
Temperature	**950° C**		**750° C**		**950° C**		**950° C**	
Shape								
Applied field direction with respect to VACNTs axis	//	⊥	//	⊥	//	⊥	//	⊥
H_c (mT)	**66**	**33**	**92.5**	**22.5**	**67**	**33**	**95**	**20**
S = Mr/Ms	**0.521**	**0.228**	**0.611**	**0.149**	**0.525**	**0.119**	**0.683**	**0.128**

The first point to highlight from the S values is the presence, in all cases, of easy and hard axes. Namely, the vertical direction of the VACNTs is the easy axis for magnetization. It

is to notice that the ratios S, between easy and hard axes, are more pronounced in the case of nanoparticles showing nail shape. This can be explained qualitatively considering the magnetization reversal process that can operate through coherent rotation, curling or domain-wall motion.

Indeed, let us consider cylindrical nanowires, a macrospin reversal (coherent reversal), for the configuration parallel to the nanowires, will be entirely determined by the shape anisotropy. The coercive field H_c is then equal to (1/2) $\mu_0 M$ = 880 mT, with M being the saturation magnetization for cobalt. The observed coercive fields, in our case, are always about 10 times lower. We can thus infer that the involved magnetization reversal process is not uniform. The curling reversal is effective if the diameter is larger than the exchange length, estimated above about 4 nm. In the case of such reversal, the coercive field reads as $(1.84)^2$ $2A/(MR^2)$ [17], where R is the nanowire radius and A ($=10^{-9}$ J/m^2) is the exchange constant. Taking R = 30 nm, representative of our nanoparticles, we obtain a coercive field of 80 mT. This value well agrees with the measured ones along the easy direction. We now discuss the measurement by considering a mean radius R_m. In the cases of nanoparticles exhibiting sphere or cylinder shapes, R_m is the real radius, while for nail shaped nanoparticles it is inferior to the head radius. Consequently, the coercive field is higher, as we experimentally observed. The obtained H_c values are comparable to those reported in literature dealing with filled CNTs using different synthesis approaches [18, 19]. In many cases, the reported results correspond to individual filled nanotubes or assemblies of VACNTs with less degree of verticality than those reported in our study.

Note that the effect of dipolar interactions should not be ignored depending on the VACNT packing density and the degree of filling with ferromagnetic materials. In the case of non-interacting encapsulated nanowires, hysteresis loops obtained from magnetometry measurements corresponds to a response from many individual nanowires, averaged or integrated over a broad distribution of nanowire lengths, diameters, shapes and deviations from parallel alignment.

4.3.4 Partial conclusion

We have synthesized hybrid carbon nanotubes by means of plasma enhanced chemical vapor deposition (PECVD). The use of a bias in the elaboration process leads to better verticality and filling of the CNTs, especially by using a Pd/Co bilayer as catalyst, compared to Co catalyst. Indeed, the addition of a palladium layer as a catalyst with cobalt leads to a marked

improvement in the density, the filling and the alignment of the nanotubes. Hysteresis cycles measurements exhibited a ferromagnetic behaviour with coercive field H_c values well above those usually reported for continuous layers. It is also observed to be higher when the filled nanoparticles exhibit nail shape than spherical or cylindrical one due to a lower mean diameter. This shape aspect influences the nature of the magnetization reversal probably operating through curling process. These results indicate that tuning the magnetic properties of the filled VACNTs is possible by controlling the growth conditions, which is suitable for many applications.

4.4 Mechanical elastic properties of VACNTs

We present in this section, BLS measurements of acoustic vibrational modes from arrays of high density vertically aligned multiwalled VACNTs. These VACNTs are the ones elaborated and discussed in section 2.3.2 of **Chapter II**. The VACNTs assembly issued from Co catalyst is denser than the one obtained with Ni catalyst. The inelastic light scattering was used to evidence VACNTs vibrations and to determine an associated Young modulus by considering the VACNTs assemblies as dense effective media.

4.4.1 Experiments

In our BLS set-up, an incident laser beam is focused on the sample and the backscattered light is collected and analyzed through a Sandercock tandem Fabry Perot interferometer that was set so that it can evidence a frequency shift between incident and scattered lights ranging from -45 to +45 GHz [9]. The laser beam wavelength is 532 nm, much smaller than the length of the VACNTs. Consequently the studied VACNTs can be considered as infinite, regarding to the laser wavelength. Then, the observed vibrations are waves propagating along the VACNTs. Vibrations of the nanotubes propagating in the opposite direction of the incident light are coupled to the incident light. This induces scattered light in the opposite direction of the incident light with a shifted frequency. This scattering process is sketched in Figure 4.10. The frequency shift is negligible compared to the light frequency. Consequently the observed vibration has a wave vector k_{vib} equal to $-2k_{inc}$.

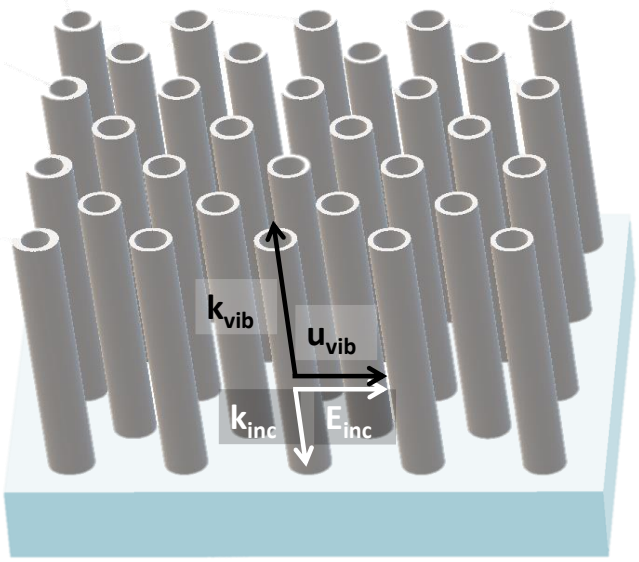

FIG 4.10 Sketch of inelastic scattering by VACNTs.

4.4.2 VACNTs vibration modes

In nanotubes, the longitudinal elastic waves, which are wave motion in which the particles displacement occurs in the direction of the wave vector, are conditioned by stretching (compression) deformations. The torsional (or twisting) elastic wave is the mode related to a twisting motion around the nanotube axis, where the particles displacement is in the tube wall perpendicular to the nanotube axis. Moreover, bending strains in tubular nanostructures cause the existence of transverse (flexural) elastic waves[20-22]. In addition to this, it exist a radial breathing mode, in which all particles oscillate perpendicular to the axis simultaneously, that exhibits a strong dependence on tube diameter[22]. We recall in the following the characteristics and frequency expressions of these vibrations modes within the framework of the elastic continuum model which considers the long wavelength acoustic vibrations. In this approach, the acoustic characteristics (directions of pure waves, propagation velocities) of any crystalline structures can be derived from its elastic properties (the components of the elastic tensor, Young modulus) and density.

a) Bending mode

Let the z axis be the direction of the nanotube. A bending mode is associated to a small displacement along the x axis for instance. Let u be this displacement. The movement equation for this displacement is

$$EI\frac{\partial^4 u}{\partial z^4} = -\rho S\frac{\partial^2 u}{\partial t^2} \quad (21)$$

E is the Young modulus, $I = \frac{\pi}{4}(R_e^4 - R_i^4)$ where R_e is the external radius and R_i is the internal radius , $S = \pi(R_e^2 - R_i^2)$ is the cross section area, ρ is the mass per volume unit. For $u = u_0 e^{ikz-i\omega t}$,

$$EIk^4 = \rho S\omega^2 \quad (22)$$

b) Stretching mode

A stretching mode is associated to a small displacement along the z axis. Let w be this displacement. The movement equation for this displacement is

$$ES\frac{\partial^2 w}{\partial z^2} = \rho S\frac{\partial^2 w}{\partial t^2} \quad (23)$$

For $w = w_0 e^{ikz-i\omega t}$,

$$Ek^2 = \rho\omega^2 \quad (24)$$

c) Twisting mode

A twisting mode is associated to a rotation around the z axis. The corresponding angle is ϕ. The movement equation is

$$\mu J\frac{\partial^2 \phi}{\partial z^2} = \rho J\frac{\partial^2 \phi}{\partial t^2} \quad (25)$$

where μ is the shear modulus and $J = \frac{\pi}{2}(R_e^4 - R_i^4)$. For $\phi = \phi_0 e^{ikz-i\omega t}$,

$$\mu k^2 = \rho\omega^2 \quad (26)$$

d) Breathing mode

Let us consider r, θ, z, the cylindrical coordinates associated to the nanotube. A breathing mode corresponds to a radial displacement depending only on r : $(r, \theta, z) \mapsto (r + u(r), \theta, z)$. The movement equation for this displacement is

$$\left(\frac{\partial^2 u}{\partial r^2} + \frac{1}{r}\frac{\partial u}{\partial r} - \frac{u}{r^2}\right)\frac{E}{1-\nu^2} = \rho\frac{\partial^2 u}{\partial t^2} \quad (27)$$

where ν is the Poisson ratio. For $u = f(r)e^{-i\omega t}$,

$$r^2 f''(r) + rf'(r) - f + q^2 r^2 f(r) = 0 \quad (28)$$

with $q^2 = \rho\omega^2\frac{1-\nu^2}{E}$. Consequently $f(r)$ is a linear combination of $J_1(qr)$ and $Y_1(qr)$ where J_1 and Y_1 are Bessel's functions. The boundary conditions read

$$\sigma_{rr}(R_i) = \sigma_{rr}(R_e) = 0 \quad (29)$$

where $\sigma_{rr} = \frac{E}{1-\nu^2}(f'(r) + \frac{\nu}{r}f(r))e^{-i\omega t}$. As $J_1(\xi)$ and $Y_1(\xi)$ are oscillating within a characteristic range of 3 for ξ inferior to 20, the boundary conditions allow to evaluate the order of magnitude of q corresponding to the lowest frequency from the approximate relation:

$$qR \approx 3 \tag{30}$$

with $R = \frac{R_i+R_e}{2}$

4.4.3 Morphology

The two samples elaborated in **Chapter II** are named VACNT/Co for the assembly issued from Co catalyst and VACNT/Ni, for the one issued from Ni catalyst represented in Figure 4.11 .

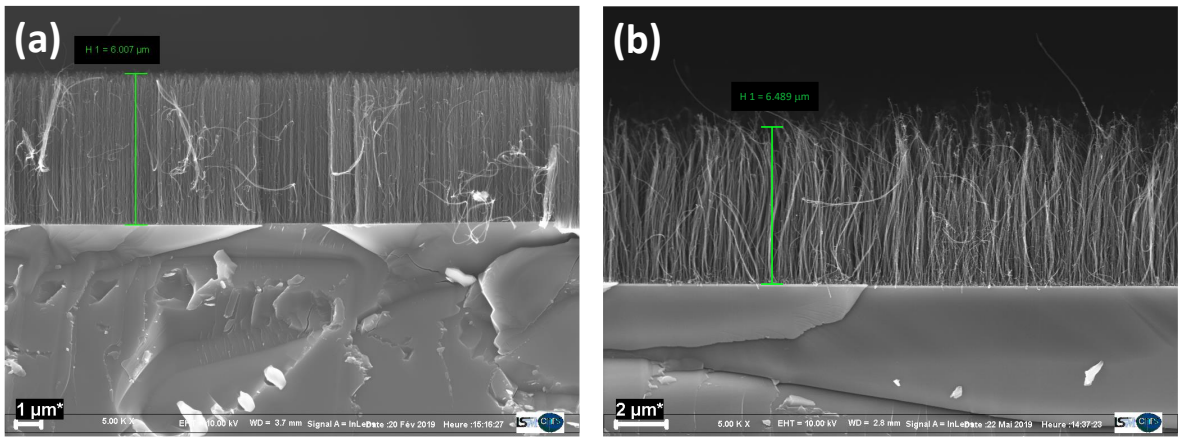

FIG 4.11. SEM images of assemblies of VACNTs from: (a) Co catalyst layer (VACNT/Co) and (b) Ni catalyst layer (VACNT/Ni).

In order to analyze BLS measurements of the VACNTs assemblies, areal density values are needed for both samples. For this purpose, high magnification SEM images of the VACNTs were used to determine the number of nanotubes in each image as presented in Figure 4.12. The square of this number is calculated to estimate the areal density of nanotubes for a surface equal to the images (framed parts), and then multiplied according to the scale in order to estimate the areal density per square centimeter. The estimated values of the density for each assembly of VACNTs are presented in the table of Figure 4.12.

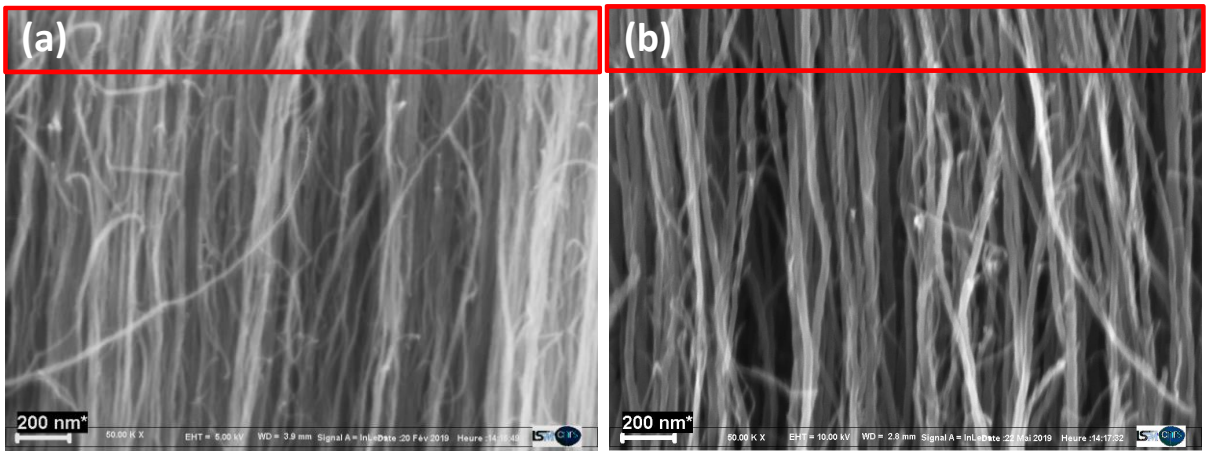

		VCNT / image	VCNT / area (length^2)	VCNT / cm^2
(a)	CNT / Co	75	5625	1.3×10^{11}
(b)	CNT / Ni	36	1296	3×10^{10}

FIG 4.12 Magnified SEM images of VACNT from: (a) Co catalyst layer (VACNT/Co) and (b) Ni catalyst (VACNT/Ni)

4.4.4 Effective Young modulus estimation

Spectra obtained from areas covered by the VACNTs grown from Co or Ni nanoparticles and from a nanotubes free area, are presented in Figure 4.13. The scattering by the VACNTs (Figures 4.13Aa, Ba) largely increases the measured intensity near the central line. This effect is larger for the denser VACNTs issued from Co catalyst (Figure 4.13Aa). The narrow lines indicated by the arrows at 25 GHz and 34 GHz correspond to vibration modes of the substrate.

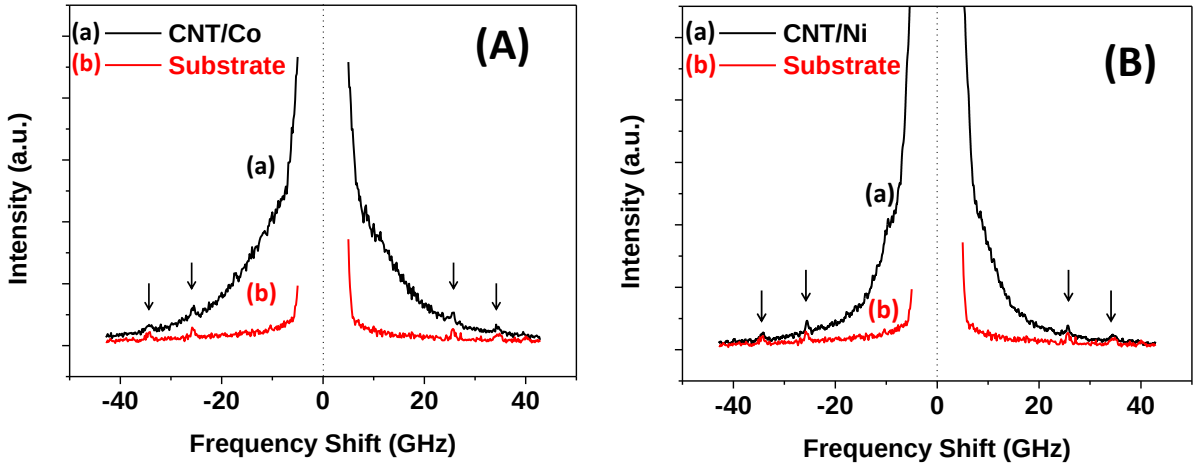

FIG 4.13: BLS Spectra obtained with Co catalyst (A) and Ni catalyst (B) for both assemblies of VACNTs (a) and the substrate layer (b). Arrows indicate the frequency positions of vibration modes of the substrate material.

The spectra presented in Figure 4.13 clearly show that the nanotubes enhance the elastic scattering $i.e.$ without frequency shift. Nevertheless they also contribute to inelastic scattering. In order to evidence this inelastic contribution, the elastic background, assumed to be lorentzian, was substracted to the raw data (see Figure 4.14). In order to analyze the inelastic scattering by nanotubes, we assume that the involved vibrations are parallel to the optical electric field as shown in Figure 4.10. Such vibrations modulate the permittivity in the direction of the optical electric field thus yielding an electric polarization that generates the inelastic scattered light. Consequently the involved vibrations are polarized perpendicularly to the nanotubes. This means that the observed vibrations are related to bending modes. Thus, for such vibrations the dispersion law is given by the following expression [23]:

$$EIk_{vib}^4 = \rho S \omega_{vib}^2 \tag{31}$$

E is the Young modulus. $I = \frac{\pi}{4}(R_e^4 - R_i^4)$ is the geometrical factor associated to bending of a nanotube. R_e is the external radius and R_i is the internal radius of the nanotube. $S = \pi(R_e^2 - R_i^2)$ is the nanotube cross section. ρ is the mass density. ω_{vib} is equal to $2\pi f_{vib}$ where f_{vib} is the frequency of the vibration.

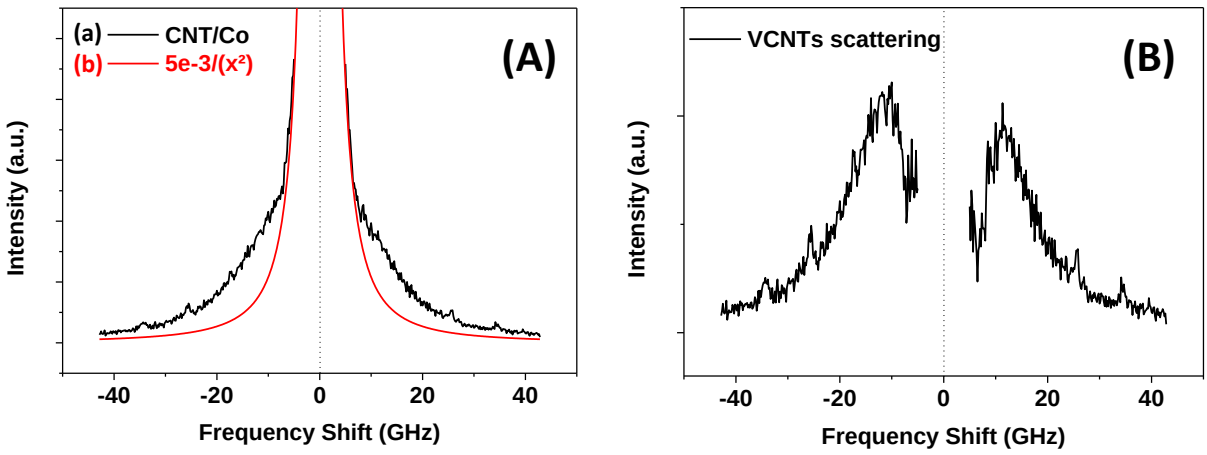

FIG 4.14 (A) BLS spectrum of VACNTs obtained with Co catalyst (a) in the presence of the elastic background represented by a lorentzian fit function (b). (B) BLS spectrum of VACNTs after substraction of the elastic background contribution

We will use equation (31) to estimate the Young modulus of the VACNTs issued from Co catalyst. We assume the mass density is close to the one of the graphite $\rho = 2100$ kg/m ^{3} [24]. From microscopy observations, we estimate $R_e = 8.5$ nm and $R_i = 3.5$ nm (see Figure 2.18 , C**hapter II**). From the spectra in Figure 4.14, we measure the frequency $f_{vib} = 12$ GHz. The last parameter to be estimated is the wave vector k_{vib}. Because of momentum conservation it is related to the light wave vector inside the nanotube assembly: $k_{vib} = -2k_{inc}$. This latter parameter is $k_{inc} = \frac{2\pi n}{\lambda_{air}}$ where $\lambda_{air} = 532$ nm is the laser wave length and n is the refractive index of light inside the nanotube assembly. Figure 4.10 clearly shows that the VACNTs assembly has to be considered as an effective medium. As this medium is made of dense packed cylinders, one can use the dedicated Bruggeman method[25], allowing for deriving the effective permittivity and consequently the refractive index. Therefore we calculate the effective refractive index from the equation:

$$r\frac{n^2-n_1^2}{n^2+n_1^2} + (1-r)\frac{n^2-n_2^2}{n^2+n_2^2} = 0 \qquad (32)$$

where r is the ratio between the nanotube section area and the area containing one nanotube, $n_1 = 2.4$ is the refractive index of graphite, $n_2 = 1$ is the refractive index of air. The ratio r is equal to S/d^2 where $d = 28$ nm is the mean distance between nanotubes as deduced from the microscopy images. Using $R_e = 8.5$ nm and $R_i = 3.5$ nm, we deduce $r = 0.24$. Equation (32) yields $n = 1.21$. It is worth mentioning that the refractive index should be as precise as possible because the Young modulus estimation from equation (31) involves the fourth power of this index. For instance taking $n = 1$ as in the air would yield a twice higher value for the Young

modulus. Finally from equation (31) we obtain $E = 850$ GPa. This estimation represents the effective value of the Young modulus. It is in agreement with the values reported in several studies by means of various techniques represented in the table 4.2.

Table 4.2: measured young modulus and techniques in the literature

CNTs type	Technique		Young modulus	Reference
SWCNTs	Experimental	DLS	1 TPa	[26]
MWCNTs		TEM	1.8 ± 0.9 TPa	[27]
MWCNTs		AFM	1.25 TPa	[28]
MWCNTs		AFM	270 to 950 GPa	[29]
MWCNTs		AFM	350 GPa	[30]
SWCNTs	Modeling	Tight-binding model	0.94 TPa	[31]
SWCNTs		*ab initio* calculation	0.92 TPa	[32]

Interestingly, disregarding the coupling mechanism between light and nanotube vibrations, we could have inferred that the observed mode would have been associated to stretching or torsion modes. In these cases the corresponding frequencies would have been given by the following expressions:

$$f_{stre,vib} = \frac{1}{2\pi} k_{vib} \sqrt{\frac{E}{\rho}} \tag{33}$$

$$f_{tors,vib} = \frac{1}{2\pi} k_{vib} \sqrt{\frac{G}{\rho}} \tag{34}$$

where G is the shear modulus. Considering the measured frequency f_{vib} = 12 GHz, we would have obtained E or G equal to 14.6 GPa. Such a low value is not expected for multiwall carbon nanotubes[27-29, 33]. Keeping our first interpretation, the frequency of stretching vibrations is $f_{stre,vib} = 92$ GHz. The shear modulus is lower than the Young modulus but the ratio G/E is likely greater than ¼ [34, 35]. Consequently the torsion mode frequency $f_{tors,vib}$ is higher than $\frac{1}{2} f_{stre,vib} = 46$ GHz. No evidence of such modes have been observed using a larger frequency range. This supports our interpretation about the scattering mechanism. The light is more likely scattered by bending modes than by stretching or torsion modes.

Finally, we will also exclude the possibility that the observed line would be associated to a breathing mode. Breathing is associated to swelling-shrinking periodic

movement. The lowest frequency is related to the Young modulus, Poisson ratio ν, mass density, inner and outer radii by the approximate relation $qR \approx 3$ where $q^2 = \rho\omega^2 \frac{1-\nu^2}{E}$ and $R = \frac{R_i+R_e}{2}$. Taking the previously used parameters, we obtain $\frac{E}{1-\nu^2} \approx 0.05$ GPa. This value is much too low.

As the VACNTs issued from Ni catalyst exhibit similar structural quality to VACNTs from Co catalyst, we can assume that their elastic constant is close to that deduced from frequency measurements on VACNTs assembly issued from Co catalyst. The observed spectrum from VACNTs/Ni can be explained as the effect of reduced nanotube density. This reduction yields a lower refractive index, a lower vibration wave vector and eventually a lower frequency. Using $d = 58$ nm as the mean distance between nanotubes (Figure 4.12), we deduce $r = 0.056$. Equation (32) yields $n = 1.04$. Assuming $E = 850$ GPa, we estimate the frequency from equation (31) $f_{vib} = 8.9$ GHz. This estimation is in agreement with our BLS measurements: we can suspect the presence of a shoulder around 9 GHz on spectrum displayed in Figure 4.13 B (plot a).

4.4.5 Intermediate conclusion

Vertical multiwall carbon nanotubes assemblies have been grown on Co or Ni islands obtained by dewetting initial 3 nm-thick layers deposited on a TiSiN layer acting as a barrier avoiding the diffusion of the metal into the silicon substrate. From high resolution transmission electron microscopy observations, the mean distance between nanotubes grown on cobalt is estimated to 28 nm while the nanotubes grown on nickel are 58 nm distant. The nanotube inner radius is about 4 nm and its outer radius is about 8 nm. Consequently, the assembly grown on Ni islands is less dense than that grown on Co islands. According to Raman measurements, the structural quality is found similar for both assemblies. The assemblies of vertical nanotubes have been studied by Brillouin light scattering technique. The inelastic light scattering from the nanotubes has been attributed to bending vibrations of the nanotubes. The measured frequencies for both assemblies are compatible with an effective Young modulus of 850 GPa. The differences observed between the Brillouin spectra of the assemblies of nanotubes grown on Co and Ni are attributed to the variation of the nanotubes density. This value of Young modulus obtained by the Brillouin light scattering (BLS) technique represents an average over a very large number of nanotubes. Thus, BLS appears to be an effective tool capable of providing a reliable statistical value of the Young modulus of assemblies of vertically ordered CNTs that hold greater promise for many applications.

4.5 Conclusions

We are interested in this chapter to study some physical properties of the assemblies of nanoparticles resulting from the dewetting process and the vertically aligned carbon nanotubes (VACNTs) subsequently grown from these nanoparticles. We have shown that controlling the synthesis parameters allows obtaining assemblies of self organised nanoparticles that behave as effective magnetic and optical media where these properties can be tuned by the elaboration process.

We have also succesfully synthesised assemblies of VACNTs filled with ferromagnetic material. The obtained structures correpond to nanowires or nanomagnets inside the carbon nanotube. The interest of studying VACNTs goes beyond the strict stage of applications but encompasses a fundamental scientific interest related to the effects of confinement and dimensionality reduction of encapsulated magnetic materials. Indeed, compared to bulk material, they often exhibit new magnetic properties, which originate from their low dimensionality and large geometric aspect ratio, such as enhancement of coercivity and magnetic anisotropy. These effetcs have been highlighted from some examples presented in this chapter.

The inelastic light scattering measurements, using Brillouin light scattering (BLS) technique, evidenced VACNTs vibrations that allow determining an associated Young modulus by considering the VACNTs assemblies as dense effective media. Thus, BLS appears to be an effective tool capable of providing a reliable statistical value of the Young modulus of assemblies of vertically ordered CNTs that hold greater promise for many applications.

Refrences

1. Kharmouche, A., et al., *Structural and magnetic properties of evaporated Co/Si(100) and Co/glass thin films.* Journal of Physics D: Applied Physics, 2004. **37**(18): p. 2583-2587.
2. Lee, J.S., et al., *Magnetic multi-granule nanoclusters: A model system that exhibits universal size effect of magnetic coercivity.* Sci Rep, 2015. **5**: p. 12135.
3. Batlle, X. and A.L. Labarta, *Finite-size effects in fine particles:magnetic and transport properties.* Journal of Physics D: Applied Physics, 2002. **35**(6): p. R15-R42.
4. Aharoni, A., *Introduction to the Theory of Ferromagnetism.* Clarendon Press, 2000. **109**.
5. Mee, C.D. and E.D. Daniel, *Magnetic Recording.* McGraw Hill, New York, 1987. **1**: p. 99–243.
6. Herzer, G., *Grain structure and magnetism of nanocrystalline ferromagnets.* IEEE Transactions on Magnetics 1989. **25**(5): p. 3327-3329.
7. Herzer, G., *Anisotropies in soft magnetic nanocrystalline alloys.* Journal of Magnetism and Magnetic Materials, 2005. **294**(2): p. 99-106.
8. Bautin, V.A., et al., *Magnetic properties of polycrystalline cobalt nanoparticles.* AIP Advances, 2017. **7**(4): p. 045103.
9. Chérif, S.M., Roussigné, Y., & Moch, P, *Effect of anisotropy on Brillouin spectra of stripe-structured cobalt layers.* Physical Review B, 1999. **59**(14): p. 9482.
10. Demokritov, S., & Tsymbal, E., *Light scattering from spin waves in thin films and layered systems.* Journal of Physics: Condensed Matter, 1994. **6**(36): p. 7145.
11. Stamps, R.L. and B. Hillebrands, *Dipolar interactions and the magnetic behavior of two-dimensional ferromagnetic systems.* Phys Rev B Condens Matter, 1991. **44**(22): p. 12417-12423.
12. Zighem, F., et al., *Spin wave modelling in arrays of ferromagnetic thin stripes: application to Brillouin light scattering in permalloy.* J Phys Condens Matter, 2007. **19**(17): p. 176220.
13. Carignan., L.P., *Modélisation, développement et caractérisation de matériaux magnétiques à base de nanofils ferromagnétiques pour les technologies hyperfréquences.* Université de Montréal, 2012.
14. Kittel, C., *On the Theory of Ferromagnetic Resonance Absorption.* Physical Review, 1948. **73**(2): p. 155-161.
15. Stashkevich, A.A., et al., *Anomalous polarization conversion in arrays of ultrathin ferromagnetic nanowires.* Physical Review B, 2015. **92**(21).
16. Johnson, P. and R. Christy, *Optical constants of transition metals: Ti, V, Cr, Mn, Fe, Co, Ni, and Pd.* Physical Review B, 1974. **9**(12): p. 5056-5070.
17. Aharoni, A. and S. Shtrikman, *Magnetization Curve of the Infinite Cylinder.* Physical Review, 1958. **109**(5): p. 1522-1528.
18. Weissker, U., et al., *Carbon Nanotubes Filled with Ferromagnetic Materials.* Materials (Basel), 2010. **3**(8): p. 4387-4427.
19. Poudel, Y.R. and W. Li, *Synthesis, properties, and applications of carbon nanotubes filled with foreign materials: a review.* Materials Today Physics, 2018. **7**: p. 7-34.
20. Popov, V.N., Van Doren, V. E., & Balkanski, M. , *Elastic properties of single-walled carbon nanotubes.* Physical Review B, 2000. **61**(4): p. 3078.
21. Mahan, G.D. and G.S. Jeon, *Flexure modes in carbon nanotubes.* Physical Review B, 2004. **70**(7).
22. Li, C. and T.-W. Chou, *Elastic wave velocities in single-walled carbon nanotubes.* Physical Review B, 2006. **73**(24).
23. McLachlan, N.W., *Theory of vibrations New York, USA.* Dover Publications Inc, 1951.
24. Poncharal, P., Wang, Z. L., Ugarte, D., & De Heer, W. A., *Electrostatic deflections and electromechanical resonances of carbon nanotubes.* science, 1999. **283**(5407): p. 1513-1516.
25. Bruggeman, V.D.B.v.p.K.v.h.S.I.D.u.L.d.M.a.i.S.A.d.p., 416(7), 636-664.
26. Bottani, C.E., et al., *Dynamic light scattering from acoustic modes in single-walled carbon nanotubes.* Physical Review B, 2003. **67**(15).

27. Treacy, M.J., Ebbesen, T. W., & Gibson, J. M. , *Exceptionally high Young's modulus observed for individual carbon nanotubes.* nature, 1996. **381**(6584): p. 678-680.
28. Salvetat, J.P., Bonard, J. M., Thomson, N. H., Kulik, A. J., Forro, L., Benoit, W., & Zuppiroli, L., *Mechanical properties of carbon nanotubes.* Applied Physics A, 1999. **69**(3): p. 255-260.
29. Yu, M.F., Lourie, O., Dyer, M. J., Moloni, K., Kelly, T. F., & Ruoff, R. S, *Strength and breaking mechanism of multiwalled carbon nanotubes under tensile load.* Science, 2000. **287**(5453): p. 637-640.
30. Guhados, G., et al., *Simultaneous measurement of Young's and shear moduli of multiwalled carbon nanotubes using atomic force microscopy.* Journal of Applied Physics, 2007. **101**(3): p. 033514.
31. Farajian, A.A., & Mikami, M. , *Electronic and mechanical properties of C60-doped nanotubes.* Journal of Physics: Condensed Matter, 2001. **13**(35): p. 8049.
32. Sánchez-Portal, D., Artacho, E., Soler, J. M., Rubio, A., & Ordejón, P, *Ab initio structural, elastic, and vibrational properties of carbon nanotubes.* Physical Review B, 1999. **59**(19): p. 12678.
33. A. Sakharova, N., et al., *Developments in the evaluation of elastic properties of carbon nanotubes and their heterojunctions by numerical simulation.* AIMS Materials Science, 2017. **4**(3): p. 706-737.
34. Li, C., *Elastic moduli of multi-walled carbon nanotubes and the effect of van der Waals forces.* Composites Science and Technology, 2003. **63**(11): p. 1517-1524.
35. Fan, C.W., Y.Y. Liu, and C. Hwu, *Finite element simulation for estimating the mechanical properties of multi-walled carbon nanotubes.* Applied Physics A, 2009. **95**(3): p. 819-831.

General Conclusions

The understanding and modeling of the growth of carbon nanotubes with a view to controlling their selective synthesis remain a great challenge towards the development of new materials for emergent applications. Due to its practicality and scalability, chemical vapor deposition (CVD) process has become the reference technique. Nevertheless, carbon nanotube synthesis by CVD process implies a huge number of interdependent variables, making the process optimization in such high-dimensional space-exploration very complex. In addition, the lack of a quantitative understanding of the gas-phase chemistry, as well as the growth mechanism, limited the approaches of so-called knowledge modelling.

For these reasons, we propose in this thesis, as a complementary alternative, to develop a knowledge-based engineering modelling to assess the intrinsic parameters of nanotube growth. This approach supported by experiments is illustrated by studying the role of oxygen in carbon nanotube growth during the PECVD process. It is especially important to understand how species behave upon their entrance into the plasma active zone down to the substrate and which processes control the nanotube growth rate.

The major contributions of this thesis are summarized in the following:

(i) We have mastered the solid dewetting stage of the catalyst thanks to diffusion barriers in the form of TiSiN. We have, in accordance with the work published in the literature, correlated the size of the nanoparticles D issued from de-wetting with the initial height of the catalyst, *i.e.* D~6 h.

(ii) We have experimentally demonstrated that the addition of 2 sccm of O_2 enhances the nanotube growth rate nearly twofold. The results indicated a connection between the flow patterns and the kinetics.

(iii) Since one of plasma's distinctive characteristics is the large number of types of species it comprises, to explain the role of oxygen, we developed a thermo-chemical model in transient zero-dimensional (0D) including three temperatures, 134 species involved in 471 gas-phase reactions. The specific role of generated oxygenated species such as H_2O, OH, CO and O is found to be decisive.

(iv) To consider transport and surface reactions, two-dimensional model (2D) is proposed with reducing gas chemistry via sensitivity analysis and considering surface reactions through site fraction and surface molar concentrations. The nanotube growth rate is then obtained by compiling the effects of gas and surface reactions at the gas /substrate interface using surface CHEMKIN software.

(v) There was good agreement between experimental and the modeling results, providing an insight into optimizing PECVD CNT growth.

(vi) We have checked and referenced all of our sources of the data that are grouped in tables in Annexes and constitute a valuable source of information for future development of PECVD in CNT synthesis context.

(vii) Thanks to the negative bias available in the Thales reactors, we successfully synthesised vertically aligned multiwalled carbon nanotubes (MWCNTs) filled with Co magnetic nanowires. Co and Pd bilayer, both of nanometric thicknesses, deposited onto 50 nm TiSiN serving as a diffusion barrier was used as catalysts for nanotube growth. Acetylene was used as the carbon source, which is balanced by ammonia. A 6 mbar growth atmosphere combined with 200 W plasma permitted to achieve simultaneously the growth, alignment and filling of carbon. Structural investigations of metal nanowires were carried out by scanning electron microscopy (SEM) and high-resolution transmission electron microscopy (HRTEM) to elucidate the growth mechanisms. Statistical analysis performed on the nanotubes torn from the forest and scattered on a flat substrate revealed that cobalt fills the nanotubes to heights up to 1.4 µm. Spatially resolved electron energy loss spectroscopy (EELS) and energy filtered elemental mapping revealed that the nanotubes are mainly filled with cobalt. These results open up the potential for one step growth, alignment and filling of carbon nanotubes with potential applications as spintronic devices.

Regarding to physical properties:

(Viii) we have shown that controlling the synthesis parameters allows obtaining assemblies of self organised dewetted nanoparticles behaving as effective magnetic and optical media, where the magneto-optical properties can be tuned by the elaboration process.

(Viiii) the assemblies of VACNTs are filled with ferromagnetic structures correponding to nanowires or nanomagnets inside the carbon nanotube. Compared to bulk material, they exhibit new magnetic properties, which originate from their low dimensionality and large geometric aspect ratio, such as enhanced coercivity and magnetic anisotropy. These effetcs have

been highlighted from some examples presented in this thesis.

(iX) We have shown that the Brillouin light sacttering technique is an effective tool, capable of providing a reliable statistical value of the Young modulus of assemblies of vertically aligned CNTs, considered as dense effective media, that holds greater promise for many applications.

As a perspective of this work, the modelling of the nanotube growth from other carbon sources such as C_2H_2/NH_3 could be achieved to better understand the intrinsic mechanisms leading to the nanotube growth and filling. Indeed, several carbon sources have historically been proposed for the growth of CNTs including but not restricted to gaseous, liquid hydrocarbons, alcohols, aromatics as well as natural carbon sources. Methane, acetylene, carbon monoxide and ethanol are currently the most frequent precursors. These gaseous carbon precursors carry not only carbon but also other elements such as hydrogen and/or oxygen. These elements are obviously not necessary for the growth of the CNTs because the latter grow from pure carbon as in the process by electric arc or by laser ablation. However, they can affect thermochemical processes and precursors distribution in the reactor. Indeed, the precursor gases are always mixed with a diluent such as dihydrogen and a very reactive additive gas such as dioxygen or ammonia whose role is to etch the amorphous carbon co-deposited with the CNTs. The chemistry of the system including the elements C, H, N, O and e- then very quickly become very complex due to the combinatorial explosion of several hundred neutral species, ionic radicals liable to form by thermal or plasma activation.

This perspective is already under study at LSPM and at list of 142 including [NH3 NH2 NH N NH4+ NH3+ NH2+ NH+ N+ N2 N2+ N2H+ H2 H H+ H2+ H3+ H- E NH3 NH2 NH N N2 N2H4 N2H3 N2H2 NNH etc…

Promising findings related to the filling of VACNTs using CoPd bilayers have also been reported. There are still several potential avenues which can be further explored for future works. There are still a lot to be understood about the mechanism of filling and how to homogenize the filling state of VACNTs assembly. It might be useful to vary parameters such as film thickness and growth time. For example, thicker film can be used to obtain nanowires with higher aspect ratios, on the other hand, growth time can be prolonged or shortened to eliminate the fragmented nature of the encapsulated metallic nanowires, on top of this further

characterization should be performed to investigate the chemical composition of the nanowires, this could help us to identify the role of Pd in the filling of VACNTs.

Appendix

Appendix A: Dewetting, synthesis and filling of VACNTs

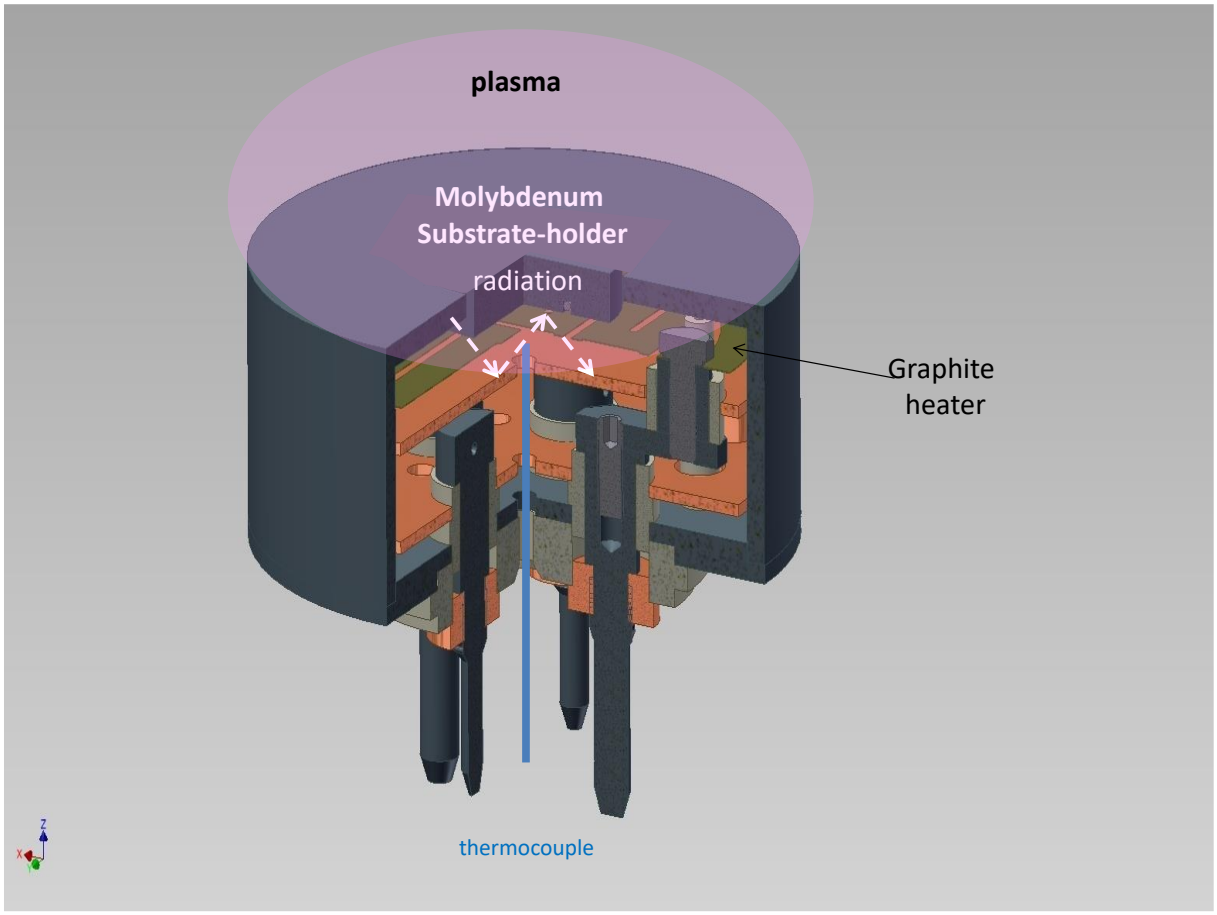

FIG A.1: Design of the PECVD heater. Radiation between molybdenum and hated graphite susceptor can increase the temperature of the substrate-holder face exposed to the plasma

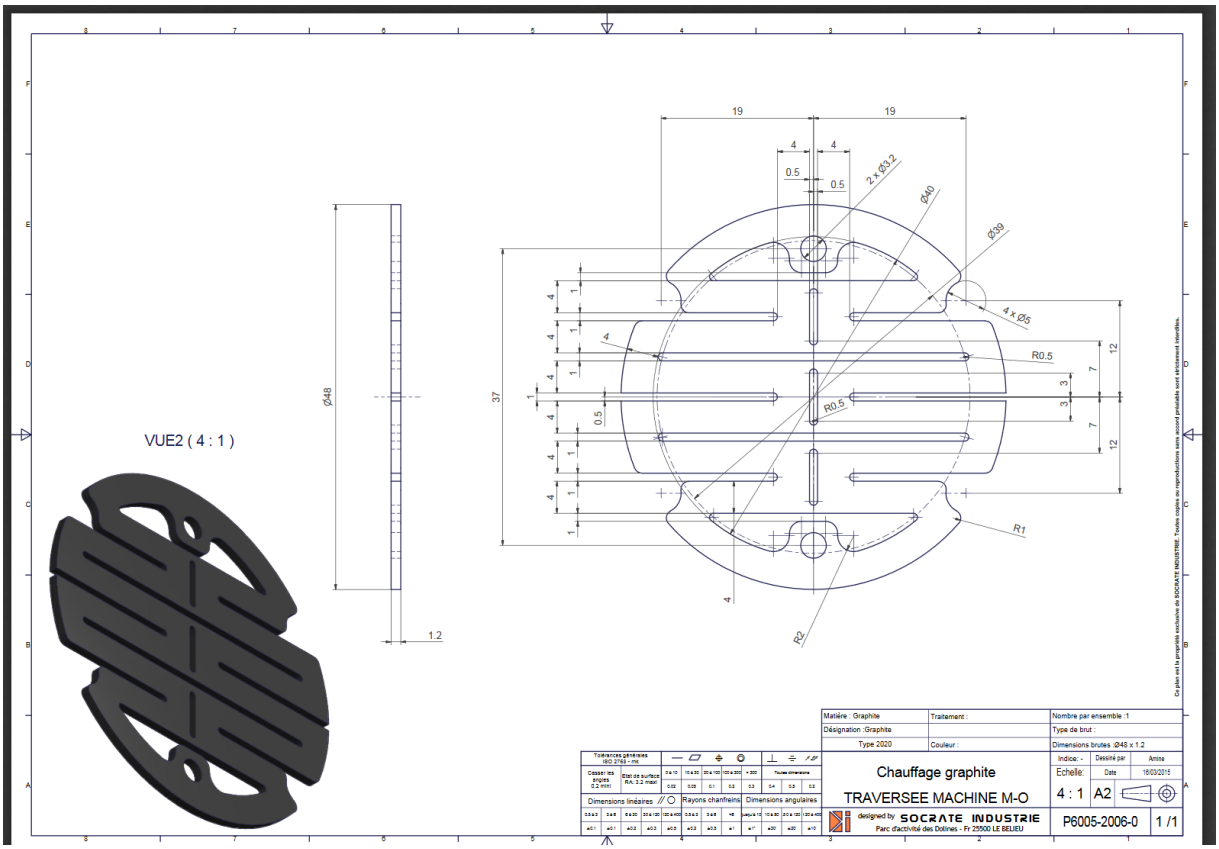

FIG A.2: Design of the graphite susceptor inserted in the body of the heater

Appendix B: VACNTs growth modeling

Table B.1 Full chemical scheme used for CNT growth in (0D) model*

N°	Gas Phase Reactions	A_r	β	E_r	Ref.
	electron-heavy particles				
1.	$e + H2(v>4) \rightarrow H + H^-$	2.24E+22	-1.4	19049.712	[1]
2.	$e + H3^+ \rightarrow 3H$	8.00E+17	-0.4	0.0	[1]
3.	$e + H3+ \rightarrow H2 + H$	3.20E+17	-0.4	0.0	[1]
4.	$e + H3^+ \rightarrow e + H^+ + 2H$	1.22E+17	0.0	356248.68	[1]
5.	$e + H2 \rightarrow 2e + H2^+$	1.18E+16	0.0	380281.266	[2]
6.	$e + H2^+ \rightarrow e + H^+ + H$	1.46E+17	0.0	74395.56	[1]
7.	$e + H2^+ \rightarrow 2H$	9.44E+18	-0.6	0.0	[1]
8.	$e + H^- \rightarrow 2e + H$	1.34E+13	0.9	45082.2	[1]
9.	$e + H \rightarrow 2e + H^+$	1.08E+16	0.0	353925.06	[3]
10.	$e + H2 \rightarrow e + 2H$	1.20E+16	0.0	225411	[2]
11.	$e + H^+ \rightarrow H + hv$	1.46E+14	-0.7	0.0	[4]
12.	$2e + H^+ \rightarrow e + H$	3.63E+37	-4.0	0.0	[5,6]
13.	$2e + H2^+ \rightarrow e + 2H$	3.17E+21	-4.5	0.0	[7]
14.	$2e + H3^+ \rightarrow e + H + H2$	3.17E+21	-4.5	0.0	[7]
15.	$e + CH4 \rightarrow e + CH3 + H$	1.24E+16	0.0	210516.0	[8]
16.	$e + CH4 \rightarrow e + CH2 + H2$	1.14E+16	0.0	232362.0	[8]
17.	$e + CH4 \rightarrow 2e + CH4^+$	1.82E+11	1.0	288367.2	[8]
18.	$e + CH4 \rightarrow 2e + CH3^+ + H$	2.72E+12	0.8	327690.0	[8]
19.	$e + C2H2 \rightarrow e + C2H + H$	4.07E+14	-0.5	230376.0	[8]
20.	$e + C2H2 \rightarrow 2e + C2H2^+$	3.71E+14	-0.5	230376.0	[8]
21.	$e + C2H4 \rightarrow 2e + C2H4^+$	4.33E+14	-0.5	236334.0	[8]
22.	$e + C2H6 \rightarrow e + C2H4 + H2$	4.94E+14	-0.5	234348.0	[8]
23.	$e + C2H6 \rightarrow 2e + C2H6^+$	1.69E+14	-0.5	262152.0	[8]
24.	$e + C2H6 \rightarrow 2e + C2H5^+ + H$	1.57E+14	-0.5	278040.0	[8]
25.	$e + C2H6 \rightarrow 2e + C2H4^+ + H2$	3.37E+14	-0.5	278040.0	[8]
26.	$e + C2H4 \rightarrow e + C2H2 + H2$	4.80E+14	-0.5	230376.0	[8]
27.	$e + CH4 \rightarrow 2e + CH2^+ + H2$	1.04E+14	-0.5	347550.0	[8]
	Ion-neutral				
28.	$H^+ + H2 \rightarrow H + H2^+$	1.90E+14	0.0	43497.372	[9]
29.	$H2^+ + H \rightarrow H^+ + H2$	3.85E+14	0.0	0.0	[10]
30.	$H2^+ + H2 \leftrightarrow H3^+ + H$	1.27E+15	0.0	0.0	[10]
31.	$H + H^- \rightarrow e + 2H$	4.50E+08	1.5	1386.228	[1]
32.	$H + H^- \rightarrow e + H2$	1.43E+15	-0.1	0.0	[1]
33.	$H^+ + H^- \leftrightarrow 2H$	1.78E+17	0.0	3511.248	[1]
34.	$H^+ + 2H2 \rightarrow H3^+ + H2$	1.95E+20	-0.5	0.0	[7]
35.	$H^- + H2^+ \rightarrow H2 + H$	2.08E+18	-0.5	0.0	[7]
36.	$H^- + H3^+ \rightarrow H2 + H2$	2.08E+18	-0.5	0.0	[7]

37.	$CH_4^+ + CH4 \rightarrow CH_5^+ + CH3$	5.21E+13	0.5	0.0	[11]
38.	$CH_3^+ + CH4 \rightarrow C2H_5^+ + H2$	4.17E+13	0.5	0.0	[11]
39.	$H_3^+ + CH4 \rightarrow CH_5^+ + H2$	5.56E+13	0.5	0.0	[11]
40.	$H_3^+ + C2H2 \rightarrow C2H_3^+ + H2$	6.74E+13	0.5	0.0	[11]
41.	$H_3^+ + C2H4 \rightarrow C2H_5^+ + H2$	6.60E+13	0.5	0.0	[11]
42.	$CH_5^+ + C2H6 \rightarrow C2H_5^+ + H2 + CH4$	1.74E+13	0.5	0.0	[11]
43.	$CH_4^+ + H_2 \rightarrow CH_5^+ + H$	1.15E+12	0.5	0.0	[11]
44.	$CH_3^+ + CH4 \rightarrow CH4^+ + CH3$	4.73E+12	0.5	0.0	[11]
45.	$CH2^+ + H2 \rightarrow CH_3^+ + H$	5.56E+13	0.5	0.0	[11]
46.	$CH2^+ + CH4 \rightarrow C2H_5^+ + H$	1.25E+13	0.5	0.0	[11]
47.	$CH2^+ + CH4 \rightarrow C2H_3^+ + H2 + H$	8.03E+12	0.5	0.0	[11]
48.	$CH2^+ + CH4 \rightarrow C2H2^+ + 2H2$	1.38E+13	0.5	0.0	[11]
49.	$CH2^+ + CH4 \rightarrow CH_3^+ + CH3$	4.80E+12	0.5	0.0	[11]
50.	$C2H_3^+ + C2H4 \rightarrow C2H_5^+ + C2H2$	7.99E+12	0.5	0.0	[11]
51.	$C2H2^+ + CH4 \rightarrow C2H_3^+ + CH3$	1.43E+14	0.5	0.0	[11]
52.	$H^- + CH_5^+ \rightarrow CH4 + H2$	2.08E+18	-0.5	0.0	[b]
53.	$H^- + CH4^+ \rightarrow CH4 + H$	2.08E+18	-0.5	0.0	[b]
54.	$H^- + CH_3^+ \rightarrow CH4$	2.08E+18	-0.5	0.0	[b]
55.	$H^- + CH2^+ \rightarrow CH3$	2.08E+18	-0.5	0.0	[b]
56.	$H^- + C2H6^+ \rightarrow C2H6 + H$	2.08E+18	-0.5	0.0	[b]
57.	$H^- + C2H_5^+ \rightarrow C2H6$	2.08E+18	-0.5	0.0	[b]
58.	$H^- + C2H4^+ \rightarrow C2H5$	2.08E+18	-0.5	0.0	[b]
59.	$H^- + C2H_3^+ \rightarrow C2H4$	2.08E+18	-0.5	0.0	[b]
60.	$H^- + C2H2^+ \rightarrow C2H2 + H$	2.08E+18	-0.5	0.0	[b]
	neutral-neutral				
61.	H + H + H2 ↔ H2 + H2	9.20E+16	-0.6	0.0	[12]
62.	CH4 + H ↔ CH3 + H2	2.20E+04	3.0	8750.0	[13]
63.	CH3 + H ↔ CH2 + H2	9.00E+13	0.0	15100.0	[13]
64.	CH3 + M ↔ CH + H2 + M	6.90E+14	0.0	82469.0	[14]
65.	CH2 + H ↔ CH + H2	1.00E+18	-1.6	0.0	[13]
66.	CH2 + CH3 ↔ C2H4 + H	4.00E+13	0.0	0.0	[5]
67.	CH2 + CH2 ↔ C2H2 + H + H	4.00E+13	0.0	0.0	[13]
68.	CH2 + C2H2 ↔ H2CCCH + H	1.20E+13	0.0	6600.0	[13]
69.	CH2* + CH4 ↔ CH3 + CH3	4.00E+13	0.0	0.0	[13]
70.	CH2* + C2H6 ↔ CH3 + C2H5	1.20E+14	0.0	0.0	[13]
71.	CH2* + H2 ↔ CH3 + H	7.00E+13	0.0	0.0	[13]
72.	CH2* + C2H2 ↔ H2CCCH + H	1.50E+14	0.0	0.0	[13]
73.	CH2* + C2H4 ↔ aC3H5 + H	1.30E+14	0.0	0.0	[13]
74.	CH2* + H ↔ CH + H2	3.00E+13	0.0	0.0	[13]
75.	CH2* + CH3 ↔ C2H4 + H	2.00E+13	0.0	0.0	[13]
76.	CH + H ↔ C + H2	1.50E+14	0.0	0.0	[13]
77.	CH + C2H2 ↔ C3H2 + H	1.00E+14	0.0	0.0	[13]
78.	CH + CH2 ↔ C2H2 + H	4.00E+13	0.0	0.0	[13]
79.	CH + CH3 ↔ C2H3 + H	3.00E+13	0.0	0.0	[13]
80.	CH + CH4 ↔ C2H4 + H	6.00E+13	0.0	0.0	[13]
81.	C + CH3 ↔ C2H2 + H	5.00E+13	0.0	0.0	[13]
82.	C + CH2 ↔ C2H + H	5.00E+13	0.0	0.0	[13]
83.	C2H6 + CH3 ↔ C2H5 + CH4	5.50E-01	4.0	8300.0	[13]
84.	C2H6 + H ↔ C2H5 + H2	5.40E+02	3.5	5210.0	[13]

85.	C2H5 + H ↔ C2H4 + H2	1.25E+14	0.0	8000.0	[14]
86.	C2H5 + H ↔ CH3 + CH3	3.00E+13	0.0	0.0	[15]
87.	C2H5 + H ↔ C2H6	1.00E+14	0.0	0.0	[14]
88.	C2H4 + H ↔ C2H3 + H2	3.36E-07	6.0	1692.0	[16]
89.	C2H4 + CH3 ↔ C2H3 + CH4	6.62E+00	3.7	9500.0	[14]
90.	C2H3 + H ↔ C2H2 + H2	4.00E+13	0.0	0.0	[13]
91.	C2H3 + C2H ↔ C2H2 + C2H2	3.00E+13	0.0	0.0	[13]
92.	C2H3 + CH ↔ CH2 + C2H2	5.00E+13	0.0	0.0	[13]
93.	C2H3 + CH3 ↔ aC3H5 + H	4.73E+02	3.7	5677.0	[17]
94.	C2H3 + CH3 ↔ C3H6	4.46E+56	-13.0	13865.0	[17]
95.	C2H3 + CH3 ↔ C2H2 + CH4	2.00E+13	0.0	0.0	[17]
96.	C2H3 + C2H2 ↔ CH2CHCCH + H	2.00E+12	0.0	5000.0	[17]
97.	C2H3 + C2H4 ↔ CH2CHCHCH2 + H	5.00E+11	0.0	7304.0	[17]
98.	C2H3 + C2H3 ↔ CH2CHCCH2 + H	7.00E+13	0.0	0.0	[17]
99.	C2H3 + C2H3 ↔ C2H4 + C2H2	1.45E+13	0.0	0.0	[18]
100.	C2H2 + CH3 ↔ C2H + CH4	1.81E+11	0.0	17289.0	[14]
101.	C2H + H2 ↔ C2H2 + H	4.09E+05	2.4	864.3	[19]
102.	C2H + C2H2 ↔ C4H2 + H	9.64E+13	0.0	0.0	[19]
103.	C2H + C2H4 ↔ CH2CHCCH + H	1.20E+13	0.0	0.0	[19]
104.	C2 + H2 ↔ C2H + H	4.00E+05	2.4	1000.0	[19]
105.	C3H8 (+M) ↔ C2H5 + CH3 (+M)	7.90E+22	-1.8	88629.0	[18]
	Low pressure limit: 0.72370E+28 -0.28800E+01 0.67448E+05				
	TROE centering: 0.10000E+01 0.10000E-14 0.15000E+04 0.10000E+16				
	H2/2.0/				
106.	C3H8 + H ↔ iC3H7 + H2	1.30E+06	2.4	4471.0	[17]
107.	C3H8 + H ↔ nC3H7 + H2	1.33E+06	2.5	6756.0	[17]
108.	C3H8 + CH3 ↔ nC3H7 + CH4	9.04E-01	3.6	7153.0	[17]
109.	C3H8 + CH3 ↔ iC3H7 + CH4	1.51E+00	3.5	5480.0	[17]
110.	C3H8 + C2H3 ↔ iC3H7 + C2H4	1.00E+03	3.1	8830.0	[17]
111.	C3H8 + C2H3 ↔ nC3H7 + C2H4	6.00E+02	3.3	10500.0	[17]
112.	C3H8 + C2H5 ↔ iC3H7 + C2H6	1.51E+00	3.5	7470.0	[17]
113.	C3H8 + C2H5 ↔ nC3H7 + C2H6	9.03E-01	3.6	9140.0	[17]
114.	C3H8 + aC3H5 ↔ C3H6 + nC3H7	2.35E+02	3.3	19842.0	[17]
115.	C3H8 + aC3H5 ↔ C3H6 + iC3H7	7.83E+01	3.3	18169.0	[17]
116.	nC3H7 (+M) ↔ C2H4 + CH3 (+M)	1.23E+13	-0.1	30202.0	[17]
	Low pressure limit: 0.54850E+50 -0.10000E+02 0.35766E+05				
	TROE centering: 0.21700E+01 0.10000E-14 0.25100E+03 0.11850E+04				
	H2/2.0/				
117.	C3H6 + H (+M) ↔ iC3H7 (+M)	5.70E+09	1.2	874.0	[17]
	Low pressure limit: 0.16400E+55 -0.11100E+02 0.93640E+04				
	TROE centering: 0.10000E+01 0.10000E-14 0.26000E+03 0.30000E+04				
	H2/2.0/				
118.	iC3H7 + H ↔ C2H5 + CH3	5.00E+13	0.0	0.0	[17]
119.	nC3H7 + H ↔ C2H5 + CH3	1.00E+14	0.0	0.0	[17]
120.	C3H6 ↔ pC3H5 + H	7.58E+14	0.0	101300.0	[17]
121.	C3H6 ↔ sC3H5 + H	1.45E+15	0.0	98060.0	[17]
122.	C3H6 ↔ C2H2 + CH4	2.50E+12	0.0	70000.0	[17]
123.	C3H6 ↔ aC3H4 + H2	3.00E+13	0.0	80000.0	[17]
124.	C3H6 + H ↔ C2H4 + CH3	7.23E+12	0.0	1302.0	[17]

125.	C3H6 + H ↔ aC3H5 + H2	1.73E+05	2.5	2492.0	[17]
126.	C3H6 + H ↔ sC3H5 + H2	4.09E+05	2.5	9794.0	[17]
127.	C3H6 + H ↔ pC3H5 + H2	8.04E+05	2.5	12284.0	[17]
128.	C3H6 + CH3 ↔ aC3H5 + CH4	2.22E+00	3.5	5675.0	[17]
129.	C3H6 + CH3 ↔ sC3H5 + CH4	8.43E-01	3.5	11656.0	[17]
130.	C3H6 + CH3 ↔ pC3H5 + CH4	1.35E+00	3.5	12848.0	[17]
131.	aC3H5 + H ↔ aC3H4 + H2	5.00E+13	0.0	0.0	[17]
132.	aC3H5 + H ↔ C3H6	1.88E+26	-3.6	5468.0	[17]
133.	aC3H5 + CH3 ↔ aC3H4 + CH4	3.02E+12	-0.3	-131.0	[17]
134.	aC3H5 + C2H2 ↔ c-C5H6 + H	2.95E+32	-5.8	25733.0	[17]
135.	aC3H5 + CH3 ↔ C4H8-1	1.76E+50	-11.0	18600.0	[17]
136.	aC3H5 + C2H3 ↔ c-C5H6 + H + H	1.59E+65	-14.0	61265.0	[17]
137.	pC3H5 + H ↔ pC3H4 + H2	2.00E+13	0.0	0.0	[17]
138.	pC3H5 + H ↔ aC3H5 + H	1.00E+14	0.0	0.0	[17]
139.	sC3H5 + H ↔ aC3H5 + H	1.00E+14	0.0	0.0	[17]
140.	sC3H5 + H ↔ pC3H4 + H2	4.00E+13	0.0	0.0	[17]
141.	aC3H4 + H ↔ H2CCCH + H2	2.00E+07	2.0	5000.0	[17]
142.	aC3H4 + CH3 ↔ H2CCCH + CH4	1.50E+00	3.5	5600.0	[17]
143.	aC3H4 ↔ pC3H4	1.48E+13	0.0	60401.0	[17]
144.	pC3H4 + H ↔ H2CCCH + H2	2.00E+07	2.0	5000.0	[17]
145.	pC3H4 + CH3 ↔ H2CCCH + CH4	1.50E+00	3.5	5600.0	[17]
146.	pC3H4 + H ↔ CH3 + C2H2	5.12E+10	1.0	2060.0	[17]
147.	pC3H4 + H (+M) ↔ sC3H5 (+M)	6.50E+12	0.0	2000.0	[17]
	Low pressure limit: 0.84500E+40 -0.72700E+01 0.65770E+04				
148.	aC3H4 + H (+M) ↔ aC3H5 (+M)	1.20E+11	0.7	3007.0	[17]
	Low pressure limit: 0.55600E+34 -0.5000E+01 0.44480E+04				
149.	aC3H4 + H (+M) ↔ sC3H5 (+M)	8.49E+12	0.0	2000.0	[17]
	Low pressure limit: 0.11100E+35 -0.50000E+01 0.65770E+04				
150	H2CCCH + H ↔ C3H2 + H2	5.00E+13	0.0	3000.0	
151	H2CCCH + C2H3 ↔ c-C5H5 + H	9.63E+40	-7.8	28820.0	[17]
152	H2CCCH + CH3 ↔ CH3CHCCH2	5.00E+12	0.0	0.0	[17]
153	H2CCCH + CH3 ↔ CH3CH2CCH	5.00E+12	0.0	0.0	[17]
154	H2CCCH + CH ↔ HCCHCCH + H	7.00E+13	0.0	0.0	[17]
155	H2CCCH + CH ↔ H2CCCCH + H	7.00E+13	0.0	0.0	[17]
156	H2CCCH + H (+M) ↔ aC3H4 (+M)	1.66E+15	-0.4	0.0	[17]
	Low pressure limit: 0.33600E+46 -0.85200E+01 0.62930E+04 H2/2.0/				
157.	H2CCCH + H (+M) ↔ pC3H4 (+M)	1.66E+15	-0.4	0.0	[17]
	Low pressure limit: 0.87800E+46 -0.89000E+01 0.79740E+04 H2/2.0/ C2H2/2.0/				
158.	H2CCCH + H2CCCH ↔ C6H6	5.56E+20	-2.5	1692.0	[17]
159.	H2CCCH + aC3H5 ↔ fulvene + H + H	5.56E+20	-2.5	1692.0	[17]
160.	H2CCCH + H2CCCH ↔ C6H5 + H	2.00E+12	0.0	0.0	[17]
161.	C4H10 ↔ C2H5 + C2H5	2.00E+16	0.0	81300.0	[17]
162.	C4H10 ↔ nC3H7 + CH3	1.74E+17	0.0	85700.0	[17]
163.	C4H10 ↔ pC4H9 + H	1.00E+14	0.0	100000.0	[17]
164.	C4H10 ↔ sC4H9 + H	1.00E+14	0.0	100000.0	[17]
165.	C4H10 + aC3H5 ↔ pC4H9 + C3H6	7.94E+11	0.0	20500.0	[17]
166.	C4H10 + aC3H5 ↔ sC4H9 + C3H6	3.16E+11	0.0	16400.0	[17]

167.	C4H10 + CH3 ↔ pC4H9 + CH4	5.00E+11	0.0	13600.0	[17]
168.	C4H10 + CH3 ↔ sC4H9 + CH4	4.30E+11	0.0	10500.0	[17]
169.	C4H10 + H ↔ pC4H9 + H2	2.84E+05	2.5	6050.0	[17]
170.	C4H10 + H ↔ sC4H9 + H2	5.68E+05	2.4	3765.0	[17]
171.	sC4H9 (+M) ↔ C3H6 + CH3 (+M)	2.14E+12	0.7	30856.0	[17]
	Low pressure limit: 0.63230E+59 -0.1285E+02 0.35567E+05				
	H2/2.0/				
172.	sC4H9 ↔ C4H8-1 + H	2.00E+13	0.0	40400.0	[17]
173.	sC4H9 ↔ C4H8-2 + H	5.01E+12	0.0	37900.0	[17]
174.	pC4H9 (+M) ↔ C2H5 + C2H4 (+M)	1.06E+13	0.0	27828.0	[17]
	Low pressure limit: 0.18970E+56 -0.1191E+02 0.32263E+05				
	H2/2.0/				
175.	pC4H9 ↔ C4H8-1 + H	1.26E+13	0.0	38600.0	[17]
176.	C4H8-1 ↔ C2H3 + C2H5	1.00E+19	-1.0	96770.0	[17]
177.	C4H8-1 ↔ H + C4H7	4.11E+18	-1.0	97350.0	[17]
178.	C4H8-1 + CH3 ↔ C4H7 + CH4	1.00E+11	0.0	7300.0	[17]
179.	C4H8-1 + H ↔ C4H7 + H2	5.00E+13	0.0	3900.0	[17]
180.	C4H8-1 + aC3H5 ↔ C4H7 + C3H6	7.90E+10	0.0	12400.0	[17]
181.	C4H8-2 ↔ H + C4H7	4.11E+18	-1.0	97350.0	[17]
182.	C4H8-2 + CH3 ↔ C4H7 + CH4	1.00E+11	0.0	8200.0	[17]
183.	C4H8-2 + H ↔ C4H7 + H2	5.00E+13	0.0	3800.0	[17]
184.	C4H7 ↔ CH2CHCHCH2 + H	1.00E+14	0.0	55000.0	[17]
185.	C4H7 + CH3 ↔ CH2CHCHCH2 + CH4	8.00E+12	0.0	0.0	[17]
186.	C4H7 + aC3H5 ↔ C3H6 + CH2CHCHCH2	6.31E+12	0.0	0.0	[17]
187.	C4H7 + H ↔ CH2CHCHCH2 + H2	3.16E+13	0.0	0.0	[17]
188.	CH2CHCHCH2 + H ↔ CH2CHCHCH + H2	3.00E+07	2.0	13000.0	[17]
189.	CH2CHCHCH2 + H ↔ CH2CHCCH2 + H2	3.00E+07	2.0	6000.0	[17]
190.	CH3CH2CCH + H ↔ C2H5 + C2H2	1.00E+14	0.0	3000.0	[17]
191.	CH3CHCCH2 + H ↔ CH2CHCCH2 + H2	5.00E+07	2.0	5000.0	[17]
192.	CH3CHCCH2 + H ↔ CH3CCCH2 + H2	1.50E+07	2.0	6000.0	[17]
193.	CH3CHCCH2 + H ↔ CH3CHCCH + H2	3.00E+07	2.0	6500.0	[17]
194.	CH3CHCCH2 + H ↔ CH3 + aC3H4	2.00E+13	0.0	2000.0	[17]
195.	CH3CHCCH + H ↔ CH3 + H2CCCH	1.00E+14	0.0	0.0	[17]
196.	CH2CHCCH2 + H ↔ CH3 + H2CCCH	1.00E+14	0.0	0.0	[17]
197.	CH2CHCCH2 + H ↔ CH3CCCH2 + H	3.00E+13	0.0	0.0	[17]
198.	CH2CHCCH2 + C2H2 ↔ C6H6 + H	3.00E+11	0.0	14900.0	[17]
199.	CH3CCCH2 + H ↔ CH3 + H2CCCH	1.00E+14	0.0	0.0	[17]
200.	CH3CCCH2 + H ↔ H2CCCCH2 + H2	1.00E+14	0.0	8000.0	[17]
201.	CH2CHCHCH + H ↔ CH2CHCCH2 + H	1.00E+14	0.0	0.0	[17]
202.	CH2CHCHCH + H ↔ CH2CHCCH + H2	3.00E+07	2.0	1000.0	[17]
203.	CH2CHCHCH + C2H2 ↔ C6H6 + H	1.60E+16	-1.3	5400.0	[17]
204.	CH3CHCCH (+M) ↔ CH2CHCCH + H (+M)	1.00E+13	0.0	49000.0	[17]
	Low pressure limit: 0.20000E+15 0.00000E+00 0.41000E+05				
205.	CH3CCCH2 (+M) ↔ H2CCCCH2 + H (+M)	1.00E+13	0.0	56000.0	[17]
	Low pressure limit: 0.20000E+15 0.00000E+00 0.48000E+05				
206.	CH2CHCCH2 (+M) ↔ CH2CHCCH + H (+M)	1.00E+14	0.0	50000.0	[17]
	Low pressure limit: 0.20000E+16 0.00000E+00 0.42000E+05				
207.	CH2CHCHCH (+M) ↔ CH2CHCCH + H (+M)	1.00E+14	0.0	37000.0	[17]
	Low pressure limit: 0.10000E+15 0.00000E+00 0.30000E+05				

208.	CH3CCCH2 + H2CCCH ↔ C6H5CH2 + H	3.00E+12	0.0	0.0	[17]
209.	CH3CHCCH + H2CCCH ↔ C6H5CH2 + H	3.00E+12	0.0	0.0	[17]
210.	CH3CCCH2 + CH3CCCH2 ↔ CH3C6H4CH2 + H	3.00E+12	0.0	0.0	[17]
211.	CH3CHCCH + CH3CHCCH ↔ CH3C6H4CH2 + H	3.00E+12	0.0	0.0	[17]
212.	H2CCCCH2 + H ↔ H2CCCCH + H2	3.00E+07	2.0	6000.0	[17]
213.	CH2CHCCH + H ↔ HCCHCCH + H2	2.00E+07	2.0	15000.0	[17]
214.	CH2CHCCH + H ↔ H2CCCCH + H2	3.00E+07	2.0	5000.0	[17]
215.	HCCHCCH + H ↔ H2CCCCH + H	1.00E+14	0.0	0.0	[17]
216.	HCCHCCH + C2H2 ↔ C6H5	9.60E+70	-17.8	31300.0	[17]
217.	H2CCCCH + H ↔ C4H2 + H2	5.00E+13	0.0	0.0	[17]
218.	H2CCCCH + CH2 ↔ aC3H4 + C2H	2.00E+13	0.0	0.0	[17]
219.	H2CCCCH + C2H2 ↔ C6H5	3.00E+11	0.0	14900.0	[17]
220.	H2CCCCH (+M) ↔ C4H2 + H (+M)	1.00E+14	0.0	47000.0	[17]
	Low pressure limit: 0.20000E+16 0.00000E+00 0.40000E+05				
221.	C4H2 + CH2 ↔ C5H3 + H	1.30E+13	0.0	4326.0	[17]
222.	C4H2 + CH ↔ C5H2 + H	1.00E+14	0.0	0.0	[17]
223.	C4H2 + CH2* ↔ C5H3 + H	3.00E+13	0.0	0.0	[17]
224.	C4H2 + C2H ↔ C6H2 + H	9.60E+13	0.0	0.0	[17]
225.	l-C5H8 + H ↔ l-C5H7 + H2	7.00E+06	2.0	5000.0	[17]
226.	l-C5H8 + H ↔ aC3H5 + C2H4	3.35E+08	1.5	2000.0	[17]
227.	c-C5H7 ↔ c-C5H6 + H	3.16E+15	0.0	36000.0	[17]
228.	c-C5H7 ↔ l-C5H7	3.16E+15	0.0	39500.0	[17]
229.	l-C5H7 + H ↔ l-C5H8	1.00E+14	0.0	0.0	[17]
230.	c-C5H6 + H ↔ c-C5H5 + H2	2.19E+08	1.8	3000.0	[17]
231.	c-C5H6 + CH3 ↔ c-C5H5 + CH4	3.11E+11	0.0	5500.0	[17]
232.	c-C5H6 + C2H3 ↔ c-C5H5 + C2H4	6.00E+12	0.0	0.0	[17]
233.	c-C5H6 + CH2CHCHCH ↔ c-C5H5 + CH2CHCHCH2	6.00E+12	0.0	0.0	[17]
234.	c-C5H5 + H ↔ c-C5H6	2.00E+14	0.0	0.0	[17]
235.	c-C5H5 + c-C5H5 ↔ C10H8 + H + H	2.00E+13	0.0	8000.0	[17]
236.	C6H6 + H ↔ C6H5 + H2	3.03E+02	3.3	5690.0	[17]
237.	C6H5 + H ↔ C6H6	8.00E+13	0.0	0.0	[17]
238.	C6H5 + C2H4 ↔ C6H5C2H3 + H	7.23E+01	3.5	8345.0	[17]
239.	C6H5 + C2H2 ↔ C6H5C2H + H	3.98E+13	0.0	10099.0	[17]
240.	C6H5 + C6H5 ↔ biphenyl	5.00E+12	0.0	0.0	[17]
241.	C6H5 + C6H6 ↔ biphenyl + H	4.00E+11	0.0	4000.0	[17]
242.	C6H5CH3 ↔ C6H5 + CH3	1.40E+16	0.0	99800.0	[17]
243.	C6H5CH3 + H ↔ C6H5CH2 + H2	3.98E+02	3.4	3120.0	[17]
244.	C6H5CH3 + H ↔ C6H6 + CH3	1.20E+13	0.0	5148.0	[17]
245.	C6H5CH3 + CH3 ↔ CH4 + C6H5CH2	3.16E+11	0.0	9500.0	[17]
246.	C6H5CH3 + C6H5 ↔ C6H6 + C6H5CH2	2.10E+12	0.0	4400.0	[17]
247.	C6H5CH2 + H ↔ C6H5CH3	1.80E+14	0.0	0.0	[17]
248.	C6H5CH2 + CH3 ↔ C6H5C2H5	1.19E+13	0.0	221.0	[17]
249.	C6H5CH2 + H2CCCH ↔ C10H10	1.00E+10	0.0	0.0	[17]
250.	C6H5CH2 + C2H2 ↔ indene + H	3.20E+11	0.0	7000.0	[17]
251.	C6H5C2H5 + H ↔ C6H5C2H3 + H2 + H	8.00E+13	0.0	8235.0	[17]
252.	C6H5C2H3 + H ↔ C6H4C2H3 + H2	3.03E+02	3.3	5690.0	[17]
253.	C6H5C2H3 + H ↔ C6H5CCH2 + H2	2.00E+07	2.0	6000.0	[17]
254.	C6H5CHCH + H ↔ C6H5CCH2 + H	1.00E+14	0.0	0.0	[17]

255.	C6H5CCH2 + H ↔ C6H5C2H + H2	5.00E+13	0.0	0.0	[17]
256.	C6H5C2H + H ↔ C6H4C2H + H2	3.03E+02	3.3	5690.0	[17]
257.	C6H5C2H + CH3 ↔ C6H4C2H + CH4	1.67E+12	0.0	15057.0	[17]
258.	C6H4C2H + C2H2 ↔ C10H7	1.07E+04	2.3	-657.3	[17]
259.	C6H4C2H3 + CH3 ↔ indene + H + H	2.00E+13	0.0	0.0	[17]
260.	CH3C6H4CH3 + H ↔ CH3C6H4CH2 + H2	3.98E+02	3.4	3120.0	[17]
261.	CH3C6H4CH2 + C2H2 ↔ C10H10 + H	3.20E+11	0.0	7000.0	[17]
262.	CH3C6H4CH2 + C2H2 ↔ CH3indene + H	3.20E+11	0.0	7000.0	[17]
263.	CH3C6H4CH2 + H ↔ CH3C6H4CH3	7.46E+13	0.0	78.0	[17]
264.	CH3C6H4CH2 + CH3 ↔ CH3C6H4C2H5	6.00E+12	0.0	221.0	[17]
265.	indene + H ↔ indenyl + H2	2.19E+08	1.8	3000.0	[17]
266.	indenyl + H ↔ indene	2.00E+14	0.0	0.0	[17]
267.	indenyl + c-C5H5 ↔ phnthrn + H + H	1.00E+13	0.0	8000.0	[17]
268.	CH3C6H4C2H5 + H ↔ CH3C6H4C2H3 + H2 + H	8.00E+13	0.0	8235.0	[17]
269.	CH3C6H4C2H3 + H ↔ indene + H + H2	3.98E+02	3.4	3120.0	[17]
270.	CH3indene + H ↔ CH3indenyl + H2	2.19E+08	1.8	3000.0	[17]
271.	CH3indene + H ↔ indene + CH3	1.20E+13	0.0	5200.0	[17]
272.	CH3indenyl + H ↔ CH3indene	2.00E+14	0.0	0.0	[17]
273.	CH3indenyl + c-C5H5 ↔ CH3phnthrn + H + H	1.00E+13	0.0	8000.0	[17]
274.	C10H10 + H ↔ C10H9 + H2	2.00E+05	2.5	2500.0	[17]
275.	C10H9 + H ↔ C10H10	1.00E+14	0.0	0.0	[17]
276.	C10H8 + H ↔ C10H9	5.00E+14	0.0	5000.0	[17]
277.	C10H8 + H ↔ C10H7 + H2	4.55E+02	3.3	5690.0	[17]
278.	C10H7 + H ↔ C10H8	1.00E+14	0.0	0.0	[17]
279.	C10H7 + CH3 ↔ C10H7CH2 + H	2.00E+13	0.0	0.0	[17]
280.	C10H7 + C2H2 ↔ acenphthln + H	1.00E+20	-2.1	12000.0	[17]
281.	C10H7 + C2H2 ↔ C10H7CCH + H	1.17E-07	5.2	-9482.0	[17]
282.	C10H7 + C6H5 ↔ flrnthn + H + H	5.00E+12	0.0	0.0	[17]
283.	C10H7 + C6H6 ↔ flrnthn + H + H2	4.00E+11	0.0	4000.0	[17]
284.	C10H7CH3 + H ↔ C10H7CH2 + H2	3.98E+02	3.4	3120.0	[17]
285.	C10H7CH3 + H ↔ C10H8 + CH3	1.20E+13	0.0	5148.0	[17]
286.	C10H7CH2 + H ↔ C10H7CH3	1.00E+14	0.0	0.0	[17]
287.	C10H7CH2 + C2H2 ↔ bz(a)ndene + H	3.20E+11	0.0	7000.0	[17]
288.	C10H7CH2 + CH3 ↔ C10H7C2H5	1.19E+13	0.0	221.0	[17]
289.	C10H7C2H5 + H ↔ C10H7C2H3 + H2 + H	8.00E+13	0.0	8235.0	[17]
290.	C10H7C2H3 + H ↔ C10H7CCH2 + H2	2.00E+07	2.0	6000.0	[17]
291.	C10H7CCH2 + H ↔ C10H7CCH + H2	5.00E+13	0.0	0.0	[17]
292.	C10H7CCH + H ↔ C10H6CCH + H2	3.03E+02	3.3	5690.0	[17]
293.	C10H7CCH + H ↔ acenphthln + H	8.46E+21	-2.6	7062.6	[17]
294.	C10H6CCH + C2H2 ↔ phnthryl-1	1.07E+04	2.3	-657.3	[17]
295.	fluorene + H ↔ fluoryl + H2	2.19E+08	1.8	3000.0	[17]
296.	fluoryl + H ↔ fluorene	2.00E+14	0.0	0.0	[17]
297.	bz(a)ndnyl + H ↔ bz(a)ndene	2.00E+14	0.0	0.0	[17]
298.	bz(a)ndene + H ↔ bz(a)ndnyl + H2	2.19E+08	1.8	3000.0	[17]
299.	bz(a)ndnyl + c-C5H5 ↔ bz(a)phnthrn + H + H	1.00E+13	0.0	8000.0	[17]
300.	phnthrn + H ↔ phnthryl-1 + H2	4.04E+02	3.3	5690.0	[17]
301.	phnthrn + H ↔ phnthryl-9 + H2	1.01E+02	3.3	5690.0	[17]

302.	anthracn ↔ phnthrn	8.00E+12	0.0	65000.0	[17]
303.	phnthryl-1 + H ↔ phnthrn	8.00E+13	0.0	0.0	[17]
304.	phnthryl-9 + H ↔ phnthrn	8.00E+13	0.0	0.0	[17]
305.	phnthryl-1 + C2H2 ↔ pyrene + H	3.49E+10	0.6	5658.0	[17]
306.	phnthryl-1 + CH3 ↔ HC4-p(def)pthn + H + H	2.00E+13	0.0	0.0	[17]
307.	CH3phnthrn + H ↔ HC4-p(def)pthn + H2 + H	3.98E+02	3.4	3120.0	[18]
308.	CH3phnthrn + H ↔ phnthrn + CH3	1.20E+13	0.0	5148.0	[17]
309.	HC4-p(def)pthn + H ↔ HC4-p(def)pthyl + H2	2.19E+08	1.8	3000.0	[17]
310.	HC4-p(def)pthyl + H ↔ HC4-p(def)pthn	2.00E+14	0.0	0.0	[17]
311.	bz(a)phnthrn + H ↔ bz(ghi)fln + H2 + H	3.03E+02	3.3	5690.0	[17]
312.	H2CCCH + CH2 ↔ CH2CHCCH + H	4.00E+13	0.0	0.0	[17]
313.	c-C5H 5+ CH3 ↔ CH3cy24pd	1.76E+50	-11.0	18600.0	[17]
314.	CH3cy24pd + H ↔ c-C5H6 + CH3	1.00E+13	0.0	1300.0	[17]
315.	C6H6 + H ↔ CH3cy24pd1	2.39E+27	-3.9	29200.0	[17]
316.	cyC6H7 ↔ CH3cy24pd1	5.00E+12	0.0	38100.0	[17]
317.	CH3cy24pd1 + H ↔ CH3cy24pd	1.00E+14	0.0	0.0	[17]
318.	CH3cy24pd1 + H ↔ c-C5H5 + CH3	1.00E+14	0.0	0.0	[17]
319.	cyC6H7 ↔ CH3dcy24pd	5.50E+10	0.0	23500.0	[17]
320.	C6H6 + H ↔ cyC6H7	4.87E+56	-12.7	26800.0	[17]
321.	CH3dcy24pd + H2 ↔ CH3cy24pd + H	4.00E+12	0.0	15000.0	[17]
322.	fulvene ↔ C6H6	9.84E+37	-7.4	76979.0	[17]
323.	fulvene + H ↔ C6H6 + H	3.00E+12	0.5	2000.0	[17]
324.	fulvene + H ↔ fulvenyl + H2	3.03E+02	3.3	5690.0	[17]
325.	fulvenyl + H ↔ C6H5 + H	1.00E+14	0.0	0.0	[17]
326	H2 + O ↔ OH + H	5.12E+04	2.7	3158.7	[20]
327	H2 + OH → H2O + H	1.02E+08	1.6	1659.9	[20]
328	H2O + H → H2 + OH	4.52E+08	1.6	9271.1	[20]
329	CH4 + O2 ↔ CH3 + HO2	3.97E+13	0.0	28631.0	[20]
330	CH4 + O ↔ CH3 + OH	7.23E+08	1.6	4270.0	[20]
331	CH4 + OH ↔ CH3 + H2O	1.57E+07	1.8	1400.0	[20]
332	CH4 + HO2 ↔ CH3 + H2O2	9.03E+12	0.0	12440.0	[20]
333	C2H2 + O2 ↔ C2H + HO2	1.20E+13	0.0	37527.0	[20]
334	C2H2 + H (+M) ↔ C2H3 (+M)	8.43E+12	0.0	1300.0	[20]
	Low pressure limit: 0.34300E+19 0.00000E+00 0.61500E+01				
	TROE centering: 0.10000E+01 0.10000E+01 0.10000E+01 0.12310E+04				
	O2/0.4/ CO/0.75/ CO2/1.5/ H2O/6.5/ CH4/3.0/ C2H6/3.0/				
335	C2H3 (+M) ↔ C2H2 + H (+M)	2.00E+14	0.0	20001.0	[20]
	Low pressure limit: 0.11900E+43 -0.75000E+01 0.19040E+03				
	TROE centering: 0.10000E+01 0.10000E+01 0.10000E+01 0.15750E+04				
	O2/0.4/ CO/0.75/ CO2/1.5/ H2O/6.5/ CH4/3.0/ C2H6/3.0/				
336	C2H2 + O ↔ CH2 + CO	2.17E+06	2.1	790.0	[20]
337	C2H2 + O ↔ HCCO + H	5.06E+06	2.1	790.0	[20]
338	C2H2 + OH ↔ C2H + H2O	6.00E+13	0.0	6500.0	[20]
339	C2H2 + M ↔ C2H + H + M	1.14E+17	0.0	53765.0	[20]
	O2/0.4/ CO/0.75/ CO2/1.5/ H2O/6.5/ CH4/3.0/ C2H6/3.0/				
340	C2H4 + H (+M) → C2H5 (+ M)	3.97E+09	1.3	650.0	[20]
	Low pressure limit: 0.13500E+20 0.00000E+00 0.31600E+01				

	TROE centering: 0.76000E+00 0.40000E+02 0.10250E+04				
	O2/0.4/ CO/0.75/ CO2/1.5/ H2O/6.5/ CH4/3.0/ C2H6/3.0/				
341	C2H5 (+M) → C2H4 +H (+ M)	8.20E+13	0.0	20071.0	[20]
	Low pressure limit: 0.34000E+18 0.00000E+00 0.31968E+03				
	TROE centering: 0.7000E+00 0.97000E+02 0.13790E+04				
	O2/0.4/ CO/0.75/ CO2/1.5/ H2O/6.5/ CH4/3.0/ C2H6/3.0/				
342	C2H4 + O ↔ H + CH2HCO + H2	4.74E+06	1.9	90.0	[20]
343	C2H4 + O ↔ CH3 + HCO	8.13E+06	1.9	90.0	[20]
344	C2H4 + O ↔ CH2CO + H2	6.80E+05	1.9	90.0	[20]
345	C2H4 + O ↔ C2H3 + H2O	2.05E+13	0.0	2990.0	[20]
346	C2H4 + M ↔ C2H2 + H2 + M	9.97E+16	0.0	36002.0	[20]
	O2/0.4/ CO/0.75/ CO2/1.5/ H2O/6.5/ CH4/3.0/ C2H6/3.0/				
347	C2H4 + M ↔ C2H3 + H + M	7.14E+17	1.5	48604.0	[20]
	O2/0.4/ CO/0.75/ CO2/1.5/ H2O/6.5/ CH4/3.0/ C2H6/3.0/				
348	C2H6 + O ↔ C2H5 + OH	1.00E+09	1.5	2920.0	[20]
349	C2H6 + OH ↔ C2H5 + H2O	7.23E+06	2.0	435.0	[20]
350	C2H6 + HO2 ↔ H2O2 + C2H5	1.32E+13	0.0	10299.0	[20]
351	C4H2 + O ↔ C3H2 + CO	7.89E+12	0.0	678.0	[20]
352	C4H2 + OH ↔ C3H2 + HCO	6.68E+12	0.0	-206.0	[20]
353	O2 + CO ↔ CO2 + O	1.26E+13	0.0	23683.0	[20]
354	O2 + CH2O ↔ HCO + HO2	6.02E+13	0.0	20461.0	[20]
355	O2 + C ↔ CO + O	1.20E+14	0.0	2010.0	[20]
356	O2 + H + M ↔ HO2 + M	2.10E+18	-0.8	0.0	[20]
	O2/0.4/ CO/0.75/ CO2/1.5/ H2O/6.5/ CH4/3.0/ C2H6/3.0/				
357	O2 + H + H2O ↔ HO2 + H2O	6.89E+15	0.0	-1050.0	[20]
358	O2 + H → OH + O	9.76E+13	0.0	7471.0	[20]
359	OH + O → O2 + H	1.45E+13	0.0	354.0	[20]
360	O2 + CH ↔ CO + OH	1.66E+13	0.0	0.0	[20]
361	O2 + CH ↔ CO2 + H	1.66E+13	0.0	0.0	[20]
362	O2 + CH2 ↔ CO2 + H2	5.43E+12	0.0	751.0	[20]
363	O2 + CH2 ↔ CO2 + H + H	5.43E+12	0.0	751.0	[20]
364	O2 + CH2 ↔ CO + OH + H	8.15E+12	0.0	751.0	[20]
365	O2 + CH2 ↔ CO + H2O	1.48E+12	0.0	751.0	[20]
366	O2 + CH2 ↔ CH2O + O	4.20E+12	0.0	751.0	[20]
367	O2 + CH2* ↔ CO + OH + H	3.13E+13	0.0	0.0	[20]
368	O2 + CH3 ↔ CH2O + OH	3.31E+11	0.0	4501.0	[20]
369	O2 + C2H ↔ HCCO + O	9.05E+12	0.0	0.0	[20]
370	O2 + C2H ↔ CO2 + CH	9.05E+12	0.0	0.0	[20]
371	O2 + C2H3 ↔ C2H2 + HO2	5.42E+12	0.0	0.0	[20]
372	O2 + C2H5 ↔ C2H4 + HO2	1.02E+12	0.0	-1101.0	[20]
373	O2 + C3H2 ↔ HCO + HCCO	1.00E+13	0.0	0.0	[20]
374	O2 + H2CCCH ↔ CH2CO + HCO	3.01E+10	0.0	1443.0	[20]
375	O2 + HCO ↔ HO2 + CO	3.01E+12	0.0	0.0	[20]
376	O2 + CH3O ↔ CH2O + HO2	2.17E+10	0.0	880.0	[20]
377	O2 + CH2OH ↔ CH2O + HO2	1.57E+15	-1.0	0.0	[20]
	Declared duplicate reaction…				
378	O2 + CH2OH ↔ CH2O + HO2	7.23E+13	0.0	1801.0	[20]
	Declared duplicate reaction…				
379	O2 + HCCO ↔ CO + CO + OH	1.63E+12	0.0	431.0	[20]

380	H2O2 + H ↔ HO2 + H2	1.69E+12	0.0	1890.0	[20]
381	H2O2 + H ↔ OH + H2O	1.02E+13	0.0	1801.0	[20]
382	H2O2 + O ↔ OH + HO2	6.62E+11	0.0	2000.0	[20]
383	H2O2 + OH ↔ H2O + HO2	7.83E+12	0.0	670.0	[20]
384	H2O2 (+ M) → OH + OH (+ M)	3.00E+14	0.0	24401.0	[20]
	Low pressure limit: 0.30000E+18 0.00000E+00 0.19040E+03				
	TROE centering: 0.10000E+01 0.10000E+01 0.10000E+01 0.10400E+04				
	O2/0.4/ CO/0.75/ CO2/1.5/ H2O/6.5/ CH4/3.0/ C2H6/3.0/				
385	OH + OH (+ M) → H2O2 (+ M)	7.23E+13	-0.4	0.0	[20]
	Low pressure limit: 0.55300E+20 -0.76000E+00 0.00000E+00				
	TROE centering: 0.10000E+01 0.10000E+01 0.10000E+01 0.10400E+04				
	O2/0.4/ CO/0.75/ CO2/1.5/ H2O/6.5/ CH4/3.0/ C2H6/3.0/				
386	CO + O + M ↔ CO2 + M	1.54E+15	0.0	1511.0	[20]
	O2/0.4/ CO/0.75/ CO2/1.5/ H2O/6.5/ CH4/3.0/ C2H6/3.0/				
387	CO + OH ↔ CO2 + H	1.66E+07	1.3	-385.0	[20]
388	CO + HO2 ↔ CO2 + OH	1.51E+14	0.0	11910.0	[20]
389	CO + CH ↔ HCCO	2.77E+11	0.0	-860.0	[20]
390	CO2 + CH ↔ HCO + CO	3.43E+12	0.0	345.0	[20]
391	CO2 + CH2 ↔ CH2O + CO	2.35E+10	0.0	0.0	[20]
392	CH2O + H ↔ HCO + H2	1.26E+08	1.6	1090.0	[20]
393	CH2O + CH ↔ CH2 + HCO	9.64E+13	0.0	-260.0	[20]
394	CH2O + CH3 ↔ CH4 + HCO	7.83E-08	6.1	990.0	[20]
395	CH2O + O ↔ HCO + OH	4.16E+11	0.6	1390.0	[20]
396	CH2O + OH ↔ HCO + H2O	3.43E+09	1.2	-225.0	[20]
397	CH2O + HO2 ↔ H2O2 + HCO	3.01E+12	0.0	6580.0	[20]
398	CH2O + M ↔ HCO + H + M	1.40E+36	-5.5	48662.0	[20]
	O2/0.4/ CO/0.75/ CO2/1.5/ H2O/6.5/ CH4/3.0/ C2H6/3.0/				
399	CH2O + M ↔ H2 + CO + M	3.26E+36	-5.5	48662.0	[20]
	O2/0.4/ CO/0.75/ CO2/1.5/ H2O/6.5/ CH4/3.0/ C2H6/3.0/				
400	CH2CO + H ↔ CH3 + CO	1.81E+13	0.0	1700.0	[20]
401	CH2CO + O ↔ CH2 + CO2	1.33E+12	0.0	6800.0	[20]
402	CH2CO + O ↔ CH2O + CO	4.58E+11	0.0	6800.0	[20]
403	CH2CO + O ↔ HCO + H + CO	2.52E+11	0.0	6800.0	[20]
404	CH2CO + O ↔ HCO + HCO	2.52E+11	0.0	6800.0	[20]
405	CH2CO + OH ↔ CH3 + CO2	2.52E+12	0.0	0.0	[20]
406	CH2CO + OH ↔ CH2OH + CO	4.68E+12	0.0	0.0	[20]
407	CH2CO + M ↔ CH2 + CO +M	6.57E+15	0.0	28991.0	[20]
	O2/0.4/ CO/0.75/ CO2/1.5/ H2O/6.5/ CH4/3.0/ C2H6/3.0/				
408	CH2CO + M ↔ HCCO + H +M	1.14E+09	0.0	0.0	[20]
	O2/0.4/ CO/0.75/ CO2/1.5/ H2O/6.5/ CH4/3.0/ C2H6/3.0/				
409	C + OH ↔ CO + H	5.00E+13	0.0	0.0	[20]
410	H + H + M ↔ H2 + M	1.87E+18	-1.0	0.0	[12]
	O2/0.4/ CO/0.75/ CO2/1.5/ H2O/6.5/ CH4/3.0/ C2H6/3.0/				
411	H + CH3 (+ M) ↔ CH4 (+ M)	1.69E+14	0.0	0.0	[20]
	Low pressure limit: 0.14000E+25 -0.18000E+01 0.00000E+00				
	TROE centering: 0.37000E+00 0.33150E+04 0.61000E+02				
	O2/0.4/ CO/0.75/ CO2/1.5/ H2O/6.5/ CH4/3.0/ C2H6/3.0/				
412	CH4 (+ M) ↔ CH3 + H (+ M)	2.40E+16	0.0	52804.0	[20]
	Low pressure limit: 0.12000E+19 0.00000E+00 0.37997E+03				

	TROE centering: 0.00000E+00 0.13500E+04 0.10000E+01 0.78300E+04				
	O2/0.4/ CO/0.75/ CO2/1.5/ H2O/6.5/ CH4/3.0/ C2H6/3.0/				
413	CH4 (+ CH4) ↔ CH3 + H (+ CH4)	2.40E+16	0.0	52804.0	[20]
	Low pressure limit: 0.84300E+18 0.00000E+00 0.37997E+03				
	TROE centering: 0.69000E+00 0.90000E+02 0.22100E+04				
414	H + O + M ↔ OH + M	1.18E+19	-1.0	0.0	[20]
	O2/0.4/ CO/0.75/ CO2/1.5/ H2O/6.5/ CH4/3.0/ C2H6/3.0/				
415	H + OH + M ↔ H2O + M	5.53E+22	-2.0	0.0	[20]
	O2/0.4/ CO/0.75/ CO2/1.5/ H2O/6.5/ CH4/3.0/ C2H6/3.0/				
416	H + HO2 ↔ H2 + O2	4.28E+13	0.0	710.0	[20]
417	H + HO2 ↔ OH + OH	1.69E+14	0.0	440.0	[20]
418	H + HO2 ↔ H2O + O	3.01E+13	0.0	866.0	[20]
419	H + HCO ↔ CO + H2	9.03E+13	0.0	0.0	[20]
420	H + CH3O ↔ CH2O + H2	1.81E+13	0.0	0.0	[20]
421	H + CH2OH ↔ CH3 + OH	1.02E+13	0.0	0.0	[20]
422	H + CH2OH ↔ CH2O + H2	3.08E+13	0.0	0.0	[20]
423	H + HCCO ↔ CH2 + CO	1.15E+14	0.0	0.0	[20]
424	CH + O ↔ CO + H	3.97E+13	0.0	0.0	[20]
425	CH + OH ↔ HCO + H	3.00E+13	0.0	0.0	[20]
426	CH + HCCO ↔ C2H2 + CO	5.00E+13	0.0	0.0	[20]
427	CH2 + O ↔ CO + H + H	7.20E+13	0.0	0.0	[20]
428	CH2 + O ↔ CO + H2	4.80E+13	0.0	0.0	[20]
429	CH2 + OH ↔ CH2O + H	1.81E+13	0.0	0.0	[20]
430	CH2 + HCO ↔ CH3 + CO	1.81E+13	0.0	0.0	[20]
431	CH2 + HCCO ↔ C2H3 + CO	3.00E+13	0.0	0.0	[20]
432	CH2 + HCCO ↔ C2H + CH2O	1.00E+13	0.0	1007.0	[20]
433	CH2* + M ↔ CH2 + M	1.51E+13	0.0	0.0	[20]
	O2/0.4/ CO/0.75/ CO2/1.5/ H2O/6.5/ CH4/0.48/ C2H2/3.2/ C2H4/1.6/ C2H6/1.44/				
434	CH3 + CH3 (+ M) → C2H6 (+ M)	3.61E+13	0.0	0.0	[20]
	Low pressure limit: 0.36300E+42 -0.70000E+01 0.11560E+02				
	TROE centering: 0.62000E+00 0.73000E+02 0.11800E+04				
	O2/0.4/ CO/0.75/ CO2/1.5/ H2O/6.5/ CH4/3.0/ C2H6/3.0/				
435	C2H6 (+ M) → CH3 + CH3 (+ M)	1.80E+21	-1.2	45702.0	[20]
	Low pressure limit: 0.18900E+50 -0.82400E+01 0.39153E+02				
	TROE centering: 0.62000E+00 0.73000E+02 0.11800E+04				
	O2/0.4/ CO/0.75/ CO2/1.5/ H2O/6.5/ CH4/3.0/ C2H6/3.0/				
436	CH3 + O ↔ CH2O + H	8.43E+13	0.0	0.0	[20]
437	CH3 + OH ↔ CH2* + H2O	7.23E+13	0.0	1400.0	[20]
438	CH3 + HO2 ↔ CH3O + OH	1.80E+13	0.0	1400.0	[20]
439	CH3 + HCO ↔ CH4 + CO	1.20E+14	0.0	0.0	[20]
440	CH3 + M ↔ CH2 + H + M	2.91E+16	0.0	45603.0	[20]
	O2/0.4/ CO/0.75/ CO2/1.5/ H2O/6.5/ CH4/3.0/ C2H6/3.0/				
441	C2H + O ↔ CH + CO	1.00E+13	0.0	0.0	[20]
442	C2H + OH ↔ HCCO + H	2.00E+13	0.0	0.0	[20]
443	C2H + OH ↔ CH2 + CO	1.81E+13	0.0	0.0	[20]
444	C2H3 + O ↔ CO + CH3	3.00E+13	0.0	0.0	[20]
445	C2H3 + OH ↔ C2H2 + H2O	5.00E+12	0.0	0.0	[20]
446	C2H5 + O ↔ CH2O + CH3	6.62E+13	0.0	0.0	[20]
447	H2CCCH + O ↔ C2H2 + CO + H	1.39E+14	0.0	0.0	[20]

448	H2CCCH + OH ↔ C3H2 + H2O	2.00E+13	0.0	0.0	[20]
449	H2CCCCH + M ↔ C4H2 + H + M	1.12E+16	0.0	23409.0	[20]
	O2/0.4/ CO/0.75/ CO2/1.5/ H2O/6.5/ CH4/3.0/ C2H6/3.0/				
450	O + O + M ↔ O2 + M	5.40E+13	0.0	-900.0	[20]
	O2/0.4/ CO/0.75/ CO2/1.5/ H2O/6.5/ CH4/3.0/ C2H6/3.0/				
451	O + HO2 ↔ O2 + OH	3.19E+13	0.0	0.0	[20]
452	O + HCO ↔ CO + OH	3.01E+13	0.0	0.0	[20]
453	O + HCO ↔ CO2 + H	3.01E+13	0.0	0.0	[20]
454	O + CH3O → O2 + CH3	1.33E+13	0.0	0.0	[20]
455	O2 + CH3 → CH3O + O	4.40E+13	0.0	15801.0	[20]
456	O + CH3O ↔ CH2O + OH	1.81E+12	0.0	0.0	[20]
457	O + CH2OH ↔ CH2O + OH	9.03E+13	0.0	0.0	[20]
458	O + HCCO ↔ H + CO + CO	9.64E+13	0.0	0.0	[20]
459	OH + OH ↔ O + H20	1.51E+09	1.1	51.0	[20]
460	OH + HO2 ↔ H20 + O2	2.89E+13	0.0	-250.0	[20]
461	OH + HCO ↔ H2O + CO	1.02E+14	0.0	0.0	[20]
462	OH + CH3O ↔ CH2O + H2O	1.81E+13	0.0	0.0	[20]
463	OH + CH2OH ↔ CH2O + H2O	2.41E+13	0.0	0.0	[20]
464	OH + HCCO ↔ HCO + HCO	1.00E+13	0.0	0.0	[20]
465	OH + HCCO ↔ CH2O + CO	1.00E+13	0.0	0.0	[20]
466	HO2 + HO2 ↔ H2O2 + O2	4.22E+14	0.0	6031.0	[20]
	Declared duplicate reaction…				
467	HO2 + HO2 ↔ H2O2 + O2	1.32E+11	0.0	-820.0	[20]
	Declared duplicate reaction…				
468	HCO + HCO ↔ CH2O + CO	3.01E+13	0.0	-820.0	[20]
469	HCO + M → H+ CO + M	4.49E+14	0.0	7930.0	[20]
	O2/0.4/ CO/0.75/ CO2/1.5/ H2O/6.5/ CH4/3.0/ C2H6/3.0/				
470	H + CO + M → HCO + M	5.49E+14	0.0	370.0	[20]
	O2/0.4/ CO/0.75/ CO2/1.5/ H2O/6.5/ CH4/3.0/ C2H6/3.0/				
471	CH3O + M → CH2O + H + M	1.55E+14	0.0	6791.0	[20]
	O2/0.4/ CO/0.75/ CO2/1.5/ H2O/6.5/ CH4/3.0/ C2H6/3.0/				

[a] A_r (or A_{re}) units mole-cm-sec-K and E_r (or E_{re}) units cal/mol

$k_{1re}=A_{re}T_e^{\beta_{re}}\exp(\frac{-E_{re}}{R_{univ}.T_e})$; $k_{1r}=A_rT^{\beta_r}\exp(\frac{-E_r}{R_{univ}.T})$

[b] estimated in this study by extrapolating Matveyev and Silakov data [7].

[*] A units mole-cm-sec-K and E units cal/mol – The first 27 reactions in Table B.1 are driven by electron temperature Te and the rest by gas temperature T.

Formalism in chemical plasma model

Plasma reactions are composed by vibrational kinetics of H_2 molecules driven by vibrational temperature Tv and represented by the dissociative attachment (reaction 1 in Table B.1). Electron-impact reactions are composed by ionization of atoms and molecules, dissociative attachment, dissociative recombination and electron detachment. Electron impact reactions

with the various molecules and radicals, included in the model are treated by referenced rate coefficients driven by electron temperature Te with the assumption of the electron energy distribution function (EEDF). The reaction rates for ionization of H_2 and H by electrons are calculated from cross-sectional data from Buckman and Phelps [2] using integration over the electron energy distribution function that is assumed to be Boltzmannian at an electron temperature Te. Heavy particle reactions, including charge exchange and the recombination of atoms and ions and methane pyrolysis reactions with aliphatic, aromatic and polycyclic aromatic hydrocarbons (PAHs) ranging from two to five fused aromatic rings deduced from Marinov *et al.* [3-5] and calculated at gas temperature T. The *R* elementary reversible or irreversible reactions involve ns chemical species and include reactions between heavy species and electrons.

$$\sum_{i=1}^{ns} \nu'_{ir} A_i \underset{2}{\overset{1}{\leftrightarrow}} \sum_{i=1}^{ns} \nu''_{ir} A_i \qquad (r = 1, ...,R) \qquad (E1)$$

Where ν'_{ir} and ν''_{ir} are stochiometric coefficients and Ai is the chemical symbol for the i^{th} species. The chemical production rate ω_i of i^{th} species can be written as a summation of the rate-of-progress variables for electronic and non-electronic reactions involving the i^{th} species.

$$\omega_i = \sum_{r=1}^{Re} \nu_{ir} q_{re} + \sum_{r=Re+1}^{R} \nu_{ir} q_r \qquad (i=1,...,ns) \qquad (E2)$$

where $\nu_{ir} = \nu_{ir}$ » - ν_{ir}'

The rate-of-progress variables q_{re} and q_r for the r^{th} reaction is given by the difference of the forward rates 1 and the reverse rates 2 as:

$$q_{re}=k_{1re}\prod_{i=1}^{ns}C_i^{\nu'_{ir}}-k_{2re}\prod_{i=1}^{ns}C_i^{\nu''_{ir}} \qquad (r = 1, ...,Re) \qquad (E3)$$

$$q_r=k_{1r}\prod_{i=1}^{ns}C_i^{\nu'_{ir}}-k_{2r}\prod_{i=1}^{ns}C_i^{\nu''_{ir}} \qquad (r = Re +1, ...,R) \qquad (E4)$$

Where k_{1re} , k_{2re} , k_{1r} and k_{2r} are the forward and reverse rate constants of the r^{th} electronic and non-electronic reactions and C_i is the molar concentration of i^{th} species. Reverse reactions are written explicitly in the forward sense. The forward rate constants are calculated for the electronic reactions assuming Maxwell electron energy distribution function (EEDF) and Arrhenius electron temperature dependence:

$$k_{1re}=A_{re}T^{\beta_{re}}\exp(\frac{-E_{re}}{R.T_e}) \qquad (r = 1, ...,Re) \qquad (E5)$$

where A_{re} is the pre-exponential factor, β_{re} is the electron temperature exponent and E_{re} is the activation energy. The forward rate constants are calculated for the non-electronic reactions assuming Arrhenius temperature dependence:

$$k_{1r}=A_rT^{\beta_r}\exp(\frac{-E_r}{R.T}) \qquad (r = Re +1, ...,R) \qquad (E6)$$

The rate-of-progress variables q_{re} and q_r are computed using CHEMKIN format.

Table B.2 Reduced gas-phase reactions

N°	Gas phase reaction	A*	β	Ea	Ref.
1	H + H + M ↔ H2 + M	1.00E+18	−1.0	0.0	[12]
	H2/2.0/				
2	H + H + H2 ↔ H2 + H2	9.20E+16	−0.6	0.0	[12]
3	CH3 + CH3 ↔ C2H6 (+M)	9.20E+16	−1.174	636.0	[14]
	Low pressure limit: 1.14000E+36 –5.24600E+00 1.70500E+03				
	TROE centering: 4.05000E-01 1.12000E+03 6.96000E+01 1.00000E+15				
	H2/2.0/				
4	CH3 + H (+M) ↔ CH4 (+M)	2.14E+15	−0.4	0.0	[19]
	Low pressure limit: 3.31E+30 –4.00000E+00 2.10800E+03				
	TROE centering: 0.00000E+00 1.00000E–15 1.00000E–15 4.00000E+01				
	H2/2.0/				
5	CH4 + H ↔CH3 + H2	2.20E+04	3.0	8750.0	[13]
6	CH3 + H ↔ CH2 + H2	9.00E+13	0.0	15100.0	[13]
7	CH3 + M ↔ CH + H2 + M	6.90E+14	0.0	82469.0	[21]
8	CH3 + M ↔ CH2 + H + M	1.90E+16	0.0	91411.0	[21]
9	CH2 + H ↔ CH + H2	1.00E+13	−1.56	0.0	[13]
10	CH2 + CH3 ↔ C2H4 + H	4.00E+13	0.0	0.0	[13]
11	CH2 + CH2 ↔ C2H2 + H + H	4.00E+13	0.0	0.0	[13]
12	CH2* + M ↔ CH2 + M	1.00E+13	0.0	0.0	[13]
	H2/12.0/ C2H2/4.0/				
13	CH2* + CH4 ↔ CH3 + CH3	4.00E+13	0.0	0.0	[13]
14	CH2* + C2H6 ↔ CH3 + C2H5	1.20E+14	0.0	0.0	[13]
15	CH2* + H2 ↔ CH3 + H	7.00E+13	0.0	0.0	[13]
16	CH2* + H ↔ CH + H2	3.00E+13	0.0	0.0	[13]
17	CH2* + CH3 ↔ C2H4 + H	2.00E+13	0.0	0.0	[13]
18	CH + H ↔ C + H2	1.50E+14	0.0	0.0	[13]
19	CH + CH2 ↔ C2H2 + H	4.00E+13	0.0	0.0	[13]
20	CH + CH3 ↔ C2H3 + H	3.00E+13	0.0	0.0	[13]
21	CH + CH4 ↔ C2H4 + H	6.00E+13	0.0	0.0	[13]
22	C + CH3 ↔ C2H2 + H	5.00E+13	0.0	0.0	[13]
23	C + CH2 ↔ C2H + H	5.00E+13	0.0	0.0	[13]
24	C2H6 + CH3 ↔ C2H5 + CH4	5.50E-01	4.0	8300.0	[13]
25	C2H6 + H ↔ C2H5 + H2	5.40E+02	3.5	5210.0	[13]
26	C2H5 + H ↔ C2H4 + H2	1.25E+14	0.0	8000.0	[12]
27	C2H5 + H ↔ CH3 + CH3	3.00E+13	0.0	0.0	[22]
28	C2H5 + H ↔ C2H6	1.00E+14	0.0	0.0	[12]
29	C2H4 + H ↔ C2H3 + H2	3.36E-07	6.0	1692.0	[15]
30	C2H4 + CH3 ↔ C2H3 + CH4	6.62E+00	3.7	9500.0	[14]
31	C2H4 + H (+M) ↔ C2H5 (+M)	1.08E+12	0.5	1822.0	[16]
	Low pressure limit: 1.11200E+34 –5.00000E+00 4.44800E+03				
	TROE centering: 1.00000E+00 1.00000E–15 9.50000E+00 2.00000E+02				
	H2/2.0/				
32	C2H4 (+M) ↔ C2H2 + H2 (+M)	1.80E+13	0.0	76000	[23]
	Low pressure limit: 1.50000E+15 0.00000E+00 5.54430E+04				[24]
33	C2H4 (+M) ↔ C2H3 + H (+M)	2.00E+16	0.0	110000	[25]

	Low pressure limit: 1.40000E+15 0.00000E+00 8.18330E+04				[24]
34	C2H3 + H ↔ C2H2 + H2	4.00E+13	0.0	0.0	[13]
35	C2H3 + C2H ↔ C2H2 + C2H2	3.00E+13	0.0	0.0	[13]
36	C2H3 + CH ↔ CH2 + C2H2	5.00E+13	0.0	0.0	[13]
37	C2H3 + CH3 → C2H2 + CH4	2.00E+13	0.0	0.0	[18]
38	C2H3 + C2H3 → C2H4 + C2H2	1.45E+13	0.0	0.0	[18]
39	C2H2 + CH3 ↔ C2H + CH4	1.81E+11	0.0	17289.0	[19]
40	C2H2 + M ↔ C2H + H + M	4.20E+16	0.0	107000.0	[13]
41	C2H2 +H (+M) ↔ C2H3 (+M)	3.11E+11	0.6	2589.0	[26]
	Low pressure limit: 2.25000E+40 –7.26900E+00 6.57700E+03				
	TROE centering: 1.00000E+00 1.00000E–15 6.7500E+02 1.00000E+15				
	H2/2.0/				
42	C2H + H2 ↔ C2H2 + H	4.09E+05	2.39	864.3	[13]
43	C2 + H2 ↔ C2H + H	4.09E+05	2.4	1000	[13]
44	H2 + O ↔ OH + H	5.12E+04	2.7	3158.7	[20]
45	H2 + OH ↔ H2O + H	1.02E+08	1.6	1659.9	[20]
46	H2O + H ↔ H2 + OH	4.52E+08	1.6	9271.1	[20]
47	CH4 + O2 ↔ CH3 + HO2	3.97E+13	0.0	28631.0	[20]
48	CH4 + O ↔ CH3 + OH	7.23E+08	1.6	4270.0	[20]
49	CH4 + OH ↔ CH3 + H2O	1.57E+07	1.8	1400.0	[20]
50	CH4 + HO2 ↔ CH3 + H2O2	9.03E+12	0.0	12440.0	[20]
51	C2H2 + O2 ↔ C2H + HO2	1.20E+13	0.0	37527.0	[20]
52	C2H4 + OH ↔ C2H3 + H2O	2.05E+13	0.0	2990.0	[20]
53	C2H6 + O ↔ C2H5 + OH	1.00E+09	1.5	2920.0	[20]
54	C2H6 + OH ↔ C2H5 + H2O	7.23E+06	2.0	435.0	[20]
55	C2H6 + HO2 ↔ H2O2 + C2H5	1.32E+13	0.0	10299.0	[20]
56	O2 + CO ↔ CO2 + O	1.26E+13	0.0	23683.0	[20]
57	O2 + C ↔ CO + O	1.20E+14	0.0	2010.0	[20]
58	O2 + H +M ↔ HO2 + M	2.10E+18	-0.8	0.0	[20]
	O2/0.4/ CO/0.75/ CO2/1.5/ H2O/0.0/ CH4/3.0/ C2H6/3.0/				
59	O2 + H + H2O ↔ HO2 + H2O	6.89E+15	0.0	-1050.0	[20]
60	O2 + H ↔ OH + O	9.76E+13	0.0	7471.0	[20]
61	OH + O ↔ O2 + H	1.45E+13	0.0	354.0	[20]
62	O2 + CH ↔ CO + OH	1.66E+13	0.0	0.0	[20]
63	O2 + CH ↔ CO2 + H	1.66E+13	0.0	0.0	[20]
64	O2 + CH2 ↔ CO2 + H2	5.43E+12	0.0	751.0	[20]
65	O2 + CH2 ↔ CO2 + H + H	5.43E+12	0.0	751.0	[20]
66	O2 + CH2 ↔ CO + OH + H	8.15E+12	0.0	751.0	[20]
67	O2 + CH2 ↔ CO + H2O	1.48E+12	0.0	751.0	[20]
68	O2 + CH2* ↔ CO + OH + H	3.13E+13	0.0	0.0	[20]
69	O2 + C2H ↔ CO2 + CH	9.05E+12	0.0	0.0	[20]
70	O2 + C2H3 ↔ C2H2 + HO2	5.42E+12	0.0	0.0	[20]
71	O2 + C2H5 ↔ C2H4 + HO2	1.02E+10	0.0	-1101.0	[20]
72	H2O2 + H ↔ HO2 + H2	1.69E+12	0.0	1890.0	[20]
73	H2O2 + H ↔ OH + H2O	1.02E+13	0.0	1801.0	[20]
74	H2O2 + O ↔ OH + HO2	6.62E+11	0.0	2000.0	[20]
75	H2O2 + OH ↔ H2O + HO2	7.83E+12	0.0	670.0	[20]
76	H2O2 (+M) ↔ OH + OH (+M)	3.00E+14	0.0	24401.0	[20]
	Low pressure limit: 0.30000E+18 0.00000E+00 0.19040E+03				

	TROE centering: 0.10000E+01 0.10000E+01 0.10000E+01 0.10400E+04				
	O2/0.4/ CO/0.75/ CO2/1.5/ H2O/6.5/ CH4/3.0/ C2H6/3.0/				
77	OH + OH (+M) ↔ H2O2 (+M)	7.23E+13	-0.4	0.0	[20]
	Low pressure limit: 0.55300E+20 -0.76000E+00 0.00000E+00				
	TROE centering: 0.10000E+01 0.10000E+01 0.10000E+01 0.10400E+04				
	O2/0.4/ CO/0.75/ CO2/1.5/ H2O/6.5/ CH4/3.0/ C2H6/3.0/				
78	CO + O + M ↔ CO2 + M	1.54E+15	0.0	1511.0	[20]
	O2/0.4/ CO/0.75/ CO2/1.5/ H2O/6.5/ CH4/3.0/ C2H6/3.0/				
79	CO + OH ↔ CO2 + H	1.66E+07	1.3	-385.0	[20]
80	CO + HO2 ↔ CO2 + OH	1.51E+14	0.0	11910.0	[20]
81	C + OH ↔ CO + H	5.00E+13	0.0	0.0	[20]
82	H + O + M ↔ OH + M	1.18E+19	-1.0	0.0	[20]
	O2/0.4/ CO/0.75/ CO2/1.5/ H2O/6.5/ CH4/3.0/ C2H6/3.0/				
83	H + OH + M ↔ H2O + M	5.53E+22	-2.0	0.0	[20]
	O2/0.4/ CO/0.75/ CO2/1.5/ H2O/2.55/ CH4/3.0/ C2H6/3.0/				
84	H + HO2 ↔ H2 + O2	4.28E+13	0.0	710.0	[20]
85	H + HO2 ↔ OH + OH	1.69E+14	0.0	440.0	[20]
86	H + HO2 ↔ H2O + O	3.01E+13	0.0	866.0	[20]
87	CH + O ↔ CO + H	3.97E+13	0.0	0.0	[20]
88	CH2 + O ↔ CO + H + H	7.20E+13	0.0	0.0	[20]
89	CH2 + O ↔ CO + H2	4.80E+13	0.0	0.0	[20]
90	CH3 + OH ↔ CH2* + H2O	7.23E+13	0.0	1400.0	[20]
91	C2H + O ↔ CH + CO	1.00E+13	0.0	0.0	[20]
92	C2H + OH ↔ CH2 + CO	1.81E+13	0.0	0.0	[20]
93	C2H3 + O ↔ CO + CH3	3.00E+13	0.0	0.0	[20]
94	C2H3 + OH ↔ C2H2 + H2O	5.00E+12	0.0	0.0	[20]
95	O + O + M ↔ O2 + M	5.40E+13	0.0	-900.0	[20]
	O2/0.4/ CO/0.75/ CO2/1.5/ H2O/6.5/ CH4/3.0/ C2H6/3.0/				
96	O + HO2 ↔ O2 + OH	3.19E+13	0.0	0.0	[20]
97	OH + OH ↔ O + H2O	1.51E+09	1.1	51.0	[20]
98	OH + HO2 ↔ H2O + O2	2.89E+13	0.0	-250.0	[20]
99	HO2 + HO2 ↔ H2O2 + O2	4.22E+14	0.0	6031.0	[20]
	Declared duplicate reaction				
100	HO2 + HO2 ↔ H2O2 + O2	1.32E+11	0.0	-820.0	[20]

Table B.3 Surface reactions for nanotube growth on cobalt

N°	Surface reaction	A[a]	β	Ea	Ref.
1	2_Co(S) + H2 → 2H(S)	0.01*	0.000	0.0	[27]
2	2H(S) → H2 + 2_Co(S)	2.545E+19	0.000	19379.3	[27]
3	_Co(S) + H → H(S)	1.00*	0.000	0.0	[28]
4	H(S) → _Co(S) + H	6.000E+13	0.000	60762.0	[28]
5	_Co(S) + CH3 → CH3(S)	1.00*	0.000	0.0	[28]
6	CH3(S) → _Co(S) + CH3	1.000E+13	0.000	38931.0	[28]
7	_Co(S) + C2H2 → C2H2(S)	0.05*	0.000	0.0	[29]
8	C2H2(S) → _Co(S) + C2H2	1.000E+12	0.000	13996.0	[29]
9	_Co(S) + CH4 → CH4(S)	0.008*	0.000	0.0	[29]
10	CH4(S) → CH4 + _Co(S)	8.705E+15	0.000	8949.8	[29]
11	2_Co(S) + O2 → 2O(S)	0.01*	0.000	0.0	b
12	2O(S) → O2 + 2_Co(S)	4.283E+23	0.000	113340.7	b
13	_Co(S) + H2O → H2O(S)	0.1*	0.000	0.0	b
14	H2O(S) → H2O + _Co(S)	3.732E+12	0.000	14510.6	b
15	_Co(S) + CO2 → CO2(S)	0.00001*	0.000	0.0	b
16	CO2(S) → CO2 + _Co(S)	6.447E+07	0.000	6205.2	b
17	_Co(S) + CO → CO(S)	0.5*	0.000	0.0	b
18	CO(S) → CO + _Co(S)	3.563E+11	0.000	26563.1	b
	Oxygen surface reactions				
19	H(S) + O(S) → _Co(S) + OH(S)	5.000E+22	0.000	23365.0	b
20	_Co(S) + OH(S) → H(S) + O(S)	1.781E+21	0.000	8615.7	b
21	H(S) + OH(S) → _Co(S) + H2O(S)	3.000E+20	0.000	42.7	b
22	_Co(S) + H2O(S) → H(S) + OH(S)	2.271E+21	0.000	10190.8	b
23	2OH(S) → H2O(S) + O(S)	3.000E+21	0.000	23866.2	b
24	H2O(S) + O(S) → 2OH(S)	6.373E+23	0.000	50333.8	b
25	C(S) + O(S) → _Co(S) + CO(S)	5.200E+23	0.000	35345.8	b
26	_Co(S) + CO(S) → C(S) + O(S)	1.354E+22	-3.000	27708.6	b
27	CO(S) + O(S) → _Co(S) + CO2(S)	2.000E+19	0.000	29498.6	b
28	_Co(S) + CO2(S) → CO(S) + O(S)	4.653E+23	-1.000	21312.5	b
29	_Co(S) + HCO(S) → H(S) + CO(S)	3.700E+21	0.000	0.0	b
30	H(S) + CO(S) → _Co(S) + HCO(S)	4.019E+20	-1.000	31551.1	b
31	_Co(S) + HCO(S) → CH(S) + O(S)	3.700E+24	-3.000	22863.8	b
32	CH(S) + O(S) → _Co(S) + HCO(S)	4.604E+20	0.000	26252.8	b
33	OH(S) + CH3(S) → CH4(S) + O(S)	9.876E+022	0.000	7255.3	b
34	CH3(S) + O(S) → OH(S) + CHH(S)	3.700E+024	0.000	31049.9	b
35	OH(S) + CHH(S) → CH3(S) + O(S)	4.607E+021	0.000	5632.4	b
36	CHH(S) + O(S) → OH(S) + CH(S)	3.700E+024	0.000	30262.3	b
37	OH(S) + CH(S) → CHH(S) + O(S)	1.457E+023	0.000	11240.9	b
38	CH(S) + O(S) → OH(S) + C(S)	3.700E+021	0.000	11479.6	b
39	OH(S) + C(S) → CH(S) + O(S)	1.625E+021	0.000	30691.9	b
	C+H surface reactions				
40	CH4(S) + _Co(S) → CH3(S) + H(S)	1.548E+21	0.087	13317.4	[30]
41	CH3(S) + H(S) → CH4(S) + _Co(S)	1.443E+22	-0.087	15131.2	[30]
42	CH3(S) + _Co(S) → CHH(S) + H(S)	1.548E+24	0.087	23412.8	[30]
43	CHH(S) + H(S) → CH3(S) + _Co(S)	3.091E+23	-0.087	13651.5	[30]

44	CHH(S) + _Co(S) → CH(S) + H(S)	3.700E+24	0.087	22720.7	[30]
45	CH(S) + H(S) → CHH(S) + _Co(S)	9.774E+24	-0.087	19331.6	[30]
46	CH(S) + _Co(S) → C(S) + H(S)	9.888E+20	0.500	5226.7	[30]
47	C(S) + H(S) → CH(S) + _Co(S)	1.707E+24	-0.500	37684.8	[30]
	Hydrogen-abstraction reactions				
48	H(S) + H → _Co(S) + H2	1.100E+12	0.000	7300.0	[27]
49	CH3(S) + H → CHH(S) + H2	2.800E+07	2.000	7700.0	[27,28]
50	CHH(S) + H → _Co(S) + CH3	3.000E+13	0.000	0.0	[30]
51	CHH(S) + H → CH(S) + H2	2.800E+07	2.000	7700.0	[27,28]
52	CH(S) + H → C(S) + H2	2.800E+07	2.000	7700.0	[27,28]
53	C2H2(S) + H → C2H(S) + H2	9.000E+06	2.000	5000.0	[29]
54	C2H(S) + H → C2(S) + H2	9.000E+06	2.000	5000.0	[29]
	Nanotube growth				
55	CH(S) → _Co(S) + CNT + H	5.000E+15	0.000	0.0	b
56	CHH(S) → _Co(S) + CNT + 2H	5.000E+15	0.000	0.0	b
57	CH3(S) → _Co(S) + CNT + 3H	5.000E+15	0.000	0.0	b
58	C2H(S) → _Co(S) + 2CNT + H	5.000E+15	0.000	0.0	b
59	C2(S) → _Co(S) + 2CNT	1.300E+12	0.000	31104.0	[28]
60	C(S) → _Co(S) + CNT	1.300E+12	0.000	31104.0	[28]

* Sticking coefficient

a Surface reaction mechanism rate coefficients as $K_f = A T^{\beta} * \exp(-E / RT)$ where A is the pre-exponential factor, β is the temperature exponent, and E is the activation energy. (Units are defined in terms of moles, cubic centimeters, seconds, Kelvins and calories per mole)

b Estimated in this work

c Data extrapolated from Ni

B.4 Sensitivity analysis

Sensitivity analysis was performed in order to reduce the kinetic scheme responsible for the dissociation of the mixture gas ($CH_4 + H_2 + O_2$) under CNT growth conditions; such a complex system is characterized by the competition of 471 chemical reactions given in Table B.1 as well as the huge number of parameters that describe the chemistry of CNT nucleation. Hence, a smaller chemical set is selected by identifying the dominant reaction and key species in order to consume less computational effort in higher dimensional models while preserving the same correct predictions. The identification of the dominant reactions and active species is enabled by the visualization of chemical pathways as well as the rate of production (ROP) for each reaction in CHEMKIN Reaction Path Analyzer; the rate of production is an indication of the reaction speed in $mol.cm^{-3}.s^{-1}$. The chemical pathways as well as all the reactions involving 4 species: OH, H_2O, O, CO, are represented in Fig. S1 where the four oxygenated species represented are identified as the key species according to their higher ROP values. The sensitivity analysis shown in Fig. S1 gives evidence that H_2O and OH are the dominant oxygenated species in the mechanism. Indeed, both H_2O and OH are produced and consumed in the same reversible reaction with the highest ROP:

$$H_2O + H \leftrightarrow OH + H_2$$

This is followed by CO hydrogenation on the catalyst surface into HCO and O_2 hydrogenation:

$$CO + H + M \leftrightarrow HCO + M$$

$$O_2 + H \leftrightarrow OH + O$$

We note that atomic H is involved in these three dominant reactions thereby underling the importance of this chemical element in PECVD growth of carbon nanotubes; in the generation

of oxygenated enhancers as well as the reactions of hydrocarbon dissociation represented in Fig. S2.

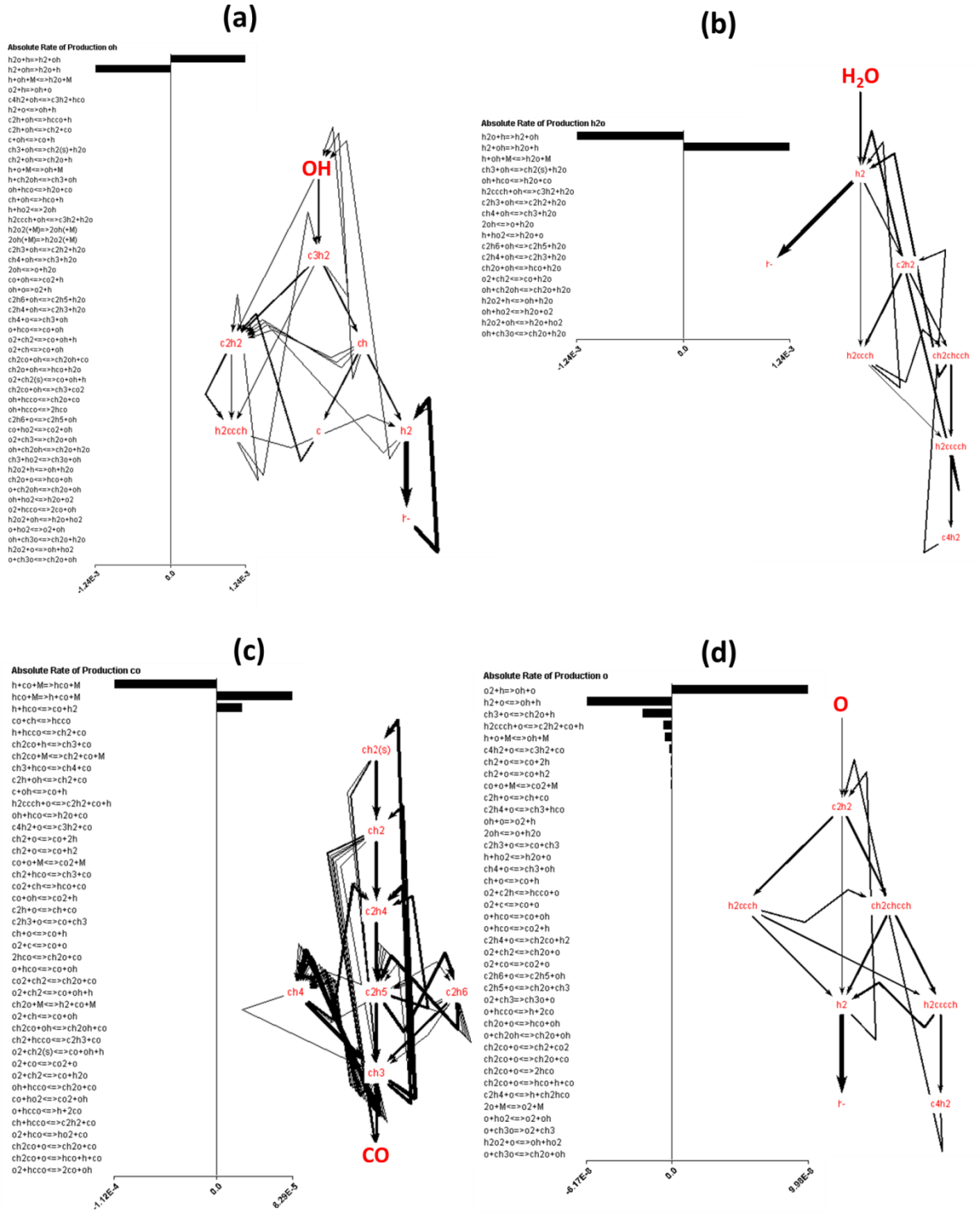

Fig. B.4 Chemical pathways for the formation and consumption of a) OH, b) H_2O, c) CO, d) O under the full chemical model of Table B.1.

B.5 Reduced scheme restricted to C1 and C2 species

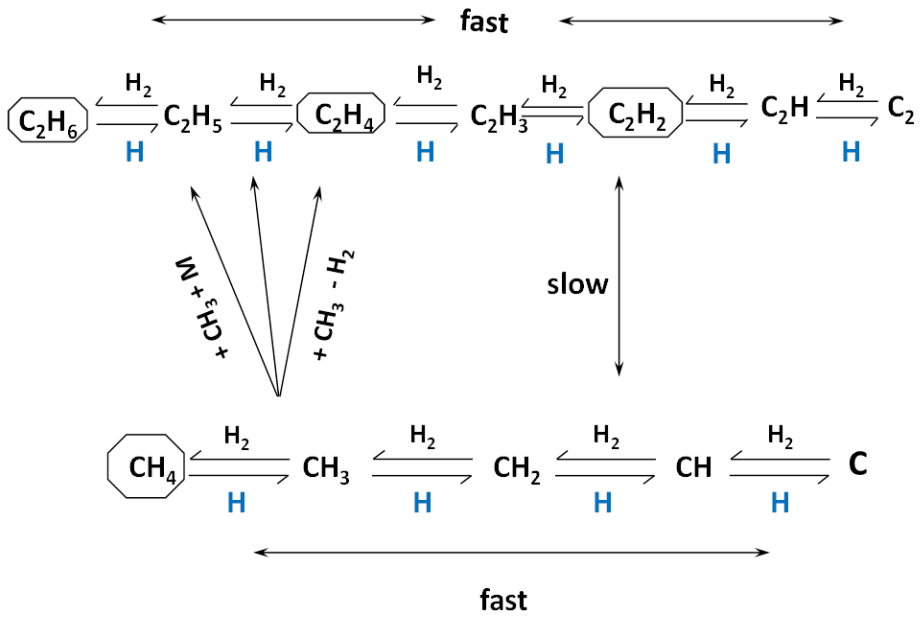

Fig. B.5 Schematic cycling of carbon precursors by the mediation of atomic H restricted to C1 and C2 species under the reduced chemical model of Table B.2.

References

[1] Janev RK, Langer WD, Evans Jr K, Post Jr DE (1987) Elementary processes in hydrogen-helium plasmas. Springer-Verlag, Berlin
[2] Buckman SJ, Phelps AV (1985) Tabulations of collision cross sections and calculated transport and reaction coefficients for electrons in H2 and D2, University of Colorado, JILA Information Center Rept. 27, Boulder, CO
[3] Takayanage K, Suzuki H (1978) Cross sections for atomic processes, Vol. 1, Research Information Center, Nagoya University, Chikusa-Ku, Nagoya
[4] Massy HSW (1969) Electronic and ionic impact phenomena, Vol. II, Electron collisions with molecules and photo-ionization, Oxford
[5] Johnson LC, Hinnov E (1973) Ionization, recombination, and population of excited levels in hydrogen plasmas. J Quant Spectrosc Radiat Transf 13:333-358
[6] Johnson LC, Hinnov E (1969) Rates of electron-impact transitions between excited states of helium. Phys Rev 187:143-152
[7] Matveyev AA, Silakov VP (1994) Reprint n°8, Russian Academy of Sciences, Moscow
[8] Tahara H, Minami K, Murai A, Yasui T, Yoshikawa T (1995) Diagnostic experiment and kinetic model analysis of microwave CH4/H2 plasmas for deposition of diamondlike carbon films. Jpn J Appl Phys 34:1972-1979
[9] Phelps AV (1990) Cross sections and swarm coefficients for H+, H2+, H3+, H, H2, and H− in H2 for energies from 0.1 eV to 10 keV. J Phys Chem Ref Data 19:653-675
[10] Karpas Z, Anicivh V, Huntress Jr WT (1991) An ion cyclotron resonance study of reactions of ions with hydrogen atoms. J Chem Phys 70:2877-2881
[11] Cohen N, Westerberg KR (1983) Chemical kinetic data sheets for high-temperature chemical reactions. J Phys Chem Ref Data 12:531-564
[12] Marinov NM, Malte PC (1995) Ethylene oxidation in a well-stirred reactor. Int J Chem Kinet 27:957-986
[13] Miller JA, Melius CF (1992) Kinetic and thermodynamic issues in the formation of aromatic compounds in flames of aliphatic fuels. Combust Flame 91:21-39
[14] Walter D, Grotheer HH, Davies JW, Pilling MJ, Wagner AF (1990) Experimental and theoretical study of the recombination reaction CH3+CH3→C2H6. Symp Int Combust Proc 23:107-114
[15] Dagaut P, Cathonnet M, Aboussi B, Boettner JC (1990) Allene oxidation in jet-stirred reactor: a kinetic modeling study. J Chim Phys 87:1159-1172
[16] Feng Y, Niiranen JT, Bencsura A, Knyazev VD, Gutman D, Tsang W (1993) Weak collision effects in the reaction ethyl radical .dblarw. ethene + hydrogen. J Phys Chem 97:871-880
[17] Marinov NM, Pitz WJ, Westbrook CK, Castaldi MJ, Senkan SM, Melius CF (1998) Aromatic and polycyclic aromatic hydrocarbon formation in a laminar premixed n-butane flame. Combust Flame 114:192-213
[18] Fahr A, Laufer A, Klein R, Braun W (1991) Reaction rate determinations of vinyl radical reactions with vinyl, methyl, and hydrogen atoms. J Phys Chem 95:3218-3224
[19] Tsang W, Hampson RF (1986) Chemical kinetic data base for combustion chemistry. Part I. Methane and related compounds. J Phys Chem Ref Data 15:1087-1279
[20] Marinov NM (1999) A detailed chemical kinetic model for high temperature ethanol oxidation. Int J Chem Kinet 31:183-220
[21] Markus MW, Woiki D, Roth P (1992) Two-channel thermal decomposition of CH3. Symp (Int) Combust 24:581-588
[22] Warnatz J (1984). Rate coefficients in the C/H/O system. In: Gardiner WC (ed) Combustion chemistry. Springer, New York
[23] Towell GD Martin J (1961) Kinetic data from nonisothermal experiments: thermal decomposition of ethane, ethylene, and acetylene. AIChE J 7:693-698

[24] Kiefer JH, Kapsalis SA, Al-Alami MZ, Budach KA (1983) The very high temperature pyrolysis of ethylene and the subsequent reactions of product acetylene. Combust Flame 51:79-93
[25] Dean AM (1985) Predictions of pressure and temperature effects upon radical addition and recombination reactions. J Phys Chem 89:4600-4608
[26] Knyazev VD, Bencsura A, Stoliarov SI, Slagle IR (1996) Kinetics of the C2H3 + H2 ⇄ H + C2H4 and CH3 + H2 ⇄ H + CH4 Reactions. J Phys Chem 100:11346-11354
[27] Maier L, Schädel B, Delgado KH, Tischer S, Deutschmann O (2011) Steam reforming of methane over nickel: development of a multi-step surface reaction mechanism. Top Catal 54:845-858
[28] Grujicic M, Cao G, Gersten B (2002) Optimization of the chemical vapor deposition process for carbon nanotubes fabrication. Appl Surf Sci 191:223-239
[29] Grujicic M, Cao G, Gersten B (2002) An atomic-scale analysis of catalytically-assisted chemical vapor deposition of carbon nanotubes. Mat Sci Eng B 94:247-259
[30] Delgado KH, Maier L, Tischer S, Zellner A, Stotz H, Deutschmann O (2015) Surface reaction kinetics of steam- and CO2-reforming as well as oxidation of methane over nickel-based catalysts. Catalysts 5:871-904

Abstract:

Optimization of carbon nanotubes synthesis by microwave plasma-enhanced chemical vapor deposition: experiments and modeling

This thesis is dedicated to a better understanding of the growth of carbon nanotubes by a chemical vapor deposition process assisted by microwave plasma developed at the Laboratory of Processes and Materials Sciences (LSPM). First, we studied the solid de-wetting of thin cobalt films on a TiSiN surface used as a diffusion barrier. This made it possible in particular to correlate the size D of the catalytic nanoparticles resulting from the de-wetting with the initial height of the cobalt layer h via the relation D~6h in agreement with the results of the bibliography. Then, we conducted growth experiments by varying the parameters of the growth process and those of the de-wetting. A combination of our parameters allowed obtaining forests of dense and perfectly aligned nanotubes perpendicular to the substrate. In particular, we demonstrated that the addition of a small amount of oxygen doubled the growth rate of the nanotubes. Modeling work including homogeneous and heterogeneous chemistry confirmed these results and elucidated the role of oxygen. experiments were also carried out at Thales TRT as part of the DEFIS nanotubes project of the Labex Seam have made it possible, by applying a negative bias, to fill the nanotubes with cobalt nanowires over lengths greater than one micrometer while preserving alignment and verticality. Finally, the synthesized nanoparticles, carbon nanotubes and nanowires have been subjected to physical characterization, their remarkable properties open the way to applications in particular in spintronics and in field emission.

Keywords: PECVD, carbon nanotubes, de-wetting, growth, filling, modeling

Résumé :

Optimisation de la synthèse de nanotubes de carbone par dépôt chimique en phase vapeur assisté par micro-ondes: expérience et modélisation

Cette thèse est dédiée à une meilleure compréhension de la croissance des nanotubes de carbone par un procédé de dépôt chimique en phase vapeur assisté par plasma micro-ondes développé au Laboratoire des Sciences des Procédés et des Matériaux (LSPM). D'abord, nous avons étudié le démouillage solide de films minces de cobalt sur une surface de TiSiN utilisée comme barrière de diffusion. Ceci a permis en particulier de corréler la taille D des nanoparticules issues du démouillage à la hauteur initiale de la couche de cobalt h *via* la relation D~6h en accord avec les résultats de la bibliographie. Ensuite, nous avons conduit des expériences de croissance en variant les paramètres du procédé de croissance et ceux du démouillage. Une combinaison de nos paramètres à permis d'obtenir des forêts de nanotubes denses et parfaitement alignés perpendiculairement au substrat. En particulier, nous avons démontré que l'ajout d'une faible quantité d'oxygène permettait de doubler la vitesse de croissance des nanotubes. Des travaux de modélisation incluant une chimie homogène et hétérogène ont confirmé ces résultats et ont permis d'élucider le rôle de l'oxygène. Des expériences menées à Thales TRT dans le cadre du projet DEFIS nanotubes du Labex Seam ont permis en appliquant un bias négatif de remplir les nanotubes par des nanofiles de cobalt sur des longueurs supérieures au micromètre tout en préservant l'alignement et la verticalité. Enfin, les nanoparticules, nanotubes et les nanofiles synthétisés ont subi des caractérisations physiques, leurs propriétés remarquables ouvrent ainsi la voie à des applications notamment en spintronique et en émission sous champ.

Mots clés : PECVD, nanotubes de carbone, démouillage, croissance, remplissage, modélisation